THE DEVELOPMENT OF A NEAR INFRARED SPECTROSCOPY SYSTEM AND ITS APPLICATION FOR NON INVASIVE MONITORING OF CEREBRAL BLOOD AND TISSUE OXYGENATION IN THE NEWBORN INFANTS.

Mark Cope, B.Sc.(Eng)

Thesis submitted for the Degree of
Doctor of Philosophy (Ph.D.)
of the University of London

Department of Medical Physics and Bioengineering,
University College London

April, 1991

Dedicated to my wife, Alison, and my parents who have encouraged me throughout the time taken to complete this thesis.

ACKNOWLEDGEMENTS

I am particularly indebted to my Supervisor, Dr. David T. Delpy, for providing direction, enthusiasm and encouragement throughout this project. Also to clinical colleagues, especially Prof. E.O.R. Reynolds, Dr. J.S. Wyatt and Dr. A.D. Edwards without whom this work would have had no purpose and who have educated me in paediatric medicine. I also have to thank Dr. Susan Wray, Dr. M.T. Wilson (Essex Univ.) and Dr. G.C. Brown for their patience in tutoring me in physiology and biochemistry. Dr. S.R. Arridge and Pieter van der Zee are two other physicists who are part of the group working on near infrared monitoring and without whose specialities I would not have gained my current level of understanding of this field. Thanks also go to Prof. E.R. Pike (Kings College, London) for all the helpful discussions we have had over the years. The project has involved a number of animal experiments which could not have been carried out without the expertise of Dr. Susan Wray, Dr. David Delpy and the clinical staff.

I am grateful for the financial support of the Wolfson Foundation both for enabling the project to get started and for funding my current Fellowship. To Hamamatsu Photonics (System Div), Japan for their excellent financial and technical support over many years, and which is still continuing. Finally to the Wellcome Trust for providing the group with a substantial equipment grant for both the picosecond laser system and the CCD spectrophotometer.

Thanks also go to Matthias Essenpreis for preparing a number of diagrams in this thesis and to David Delpy, John Wyatt, Guy Brown and Clare Elwell who have taken time to read it and make comments.

PREFACE

This project had two main objectives. The first of these was to design and construct a spectroscopic instrument to monitor small changes in optical transmission across an infant's head at several near infrared wavelengths resulting from changes in the cerebral oxygenation status. The overall attenuation of light by brain tissue is very high and is dominated by the scattering properties of the tissue. Hence a major requirement of the instrument was the ability to measure spectral changes at very low light levels. Once the instrument was available, the second objective was to convert the measured changes in optical transmission into changes in the concentration of the naturally occurring chromophores oxyhaemoglobin, deoxyhaemoglobin and oxidised and reduced cytochrome c oxidase. An important aspect of the work was that the chromophore concentration measurements should be quantified in non-arbitrary units.

Medical Physics is, by its nature, highly interdisciplinary and this is reflected in the introductory chapter which briefly covers the clinical problems, the medical science background and the technical aspects of monitoring the cerebral oxygenation status of newborn infants. The second and third chapters examine those constituents of brain tissue which absorb and scatter light and how the complication of multiple scattering can be dealt with in performing quantitative spectroscopy.

The fourth and fifth chapters describe the technical details of the instrument design and construction from the initial step of setting its design specifications to the final testing of its performance.

The sixth chapter examines the absorption characteristics of the main chromophores of interest namely oxyhaemoglobin, deoxyhaemoglobin and the cytochrome enzymes of the respiratory chain within the brain cells. A discussion on the interpretation of the redox state of the respiratory enzymes in terms of the metabolic state of the brain is also included.

The final chapter describes the data analysis methods, the measurement of optical pathlengths in scattering media and introduces a non-linear modification to the Beer-Lambert law which improves the accuracy of the spectroscopic measurements in highly scattering media.

Table of Contents

List of Figures

List of Tables

GLOSSARY

2,3-DPG	2,3 diphosphoglycerate.
ADP	Adenosine diphosphate.
ATP	Adenosine triphosphate.
B	Differential pathlength factor (DPF).
β	Differential pathlength (DP).
BPD	Bi-parietal diameter.
CBF	Cerebral blood flow (ml/100 g tissue/min).
CBV	Cerebral blood volume (ml/100 g tissue).
CLVHR	Cerebral to large vessel haematocrit ratio.
CRBCV	Cerebral red blood corpuscle volume (ml RBC/ 100 g tissue).
CSF	Cerebrospinal fluid.
Cu_A	The low potential copper centre of cytochrome c oxidase.
Cu_B	The high potential copper centre of cytochrome c oxidase.
Cyt a	The low potential haem metal centre of cytochrome c oxidase.
Cyt a_3	The high potential haem metal centre of cytochrome c oxidase.
DH	Double heterostructure.
DP	Differential pathlength.
DPF	Differential pathlength factor.
EC	Enzyme classification (an International standard).
EPR	Electron paramagnetic resonance.
F_iO_2	Inspired oxygen concentration (%).
FWHM	Full wide half maximum, describing a pulse.
GaAs	Gallium Arsenide, a photo multiplier tube photocathode material.
Haematocrit	Fractional volume of blood occupied by red blood cells, sometimes quoted as a percentage.

Hb	Deoxy-haemoglobin.
Hb A_2	Haemoglobin ($\alpha\delta$ chains).
Hb A	Adult haemoglobin ($\alpha\beta$ chains).
Hb F	Fetal haemoglobin ($\alpha\gamma$ chains).
HbCO	Carboxy-haemoglobin.
HbO_2	Oxy-haemoglobin.
Hb_t	Haemoglobin concentration in tissue (moles/litre tissue).
Hi	Haemiglobin (also called met-haemoglobin).
HiCN	Haemiglobincyanide.
LED	Light emitting diode.
lg	Logarithm (base 10).
ln	Natural logarithm (base e).
M	Molar (gram molecule/litre).
MCHC	Mean red blood corpuscle haematocrit concentration.
MCV	Mean red blood corpuscle volume.
MOCVD	Metal oxide chemical vapour deposition.
MOSFET	Metal oxide field effect transistor.
MW	Molecular weight.
NA	Numerical aperture.
NADH	Nicotinamide adenine dinucleotide.
NMR	Nuclear magnetic resonance.
NIR	Near infrared.
NIRS	Near infrared spectroscopy.
OD	Optical density.
OER	Oxygen extraction ratio.
P_{50}	Haemoglobin half saturation partial pressure (kPa).
p_aCO_2	Arterial partial pressure of carbon dioxide.
p_aO_2	Arterial partial pressure of oxygen.
PCr	Phosphocreatine.
PCV	Packed cell volume.
PDE	Phosphodiesters.
PET	Positron emission tomography.
P_i	Inorganic phosphate.

Pig-tailed	A method of direct coupling laser diodes to optical fibres.
PME	Phosphomonoesters.
PMT	Photo multiplier tube.
PVH	Periventricular haemorrhage.
PVL	Periventricular leukomalacia.
RBC	Red blood corpuscle.
S_aO_2	Arterial haemoglobin saturation.
S_vO_2	Venous haemoglobin saturation.
SCBU	Special care baby unit.
SH	Single heterostructure.
SHb	Sulfhaemoglobin.
SNR	Signal to noise ratio.
SO_2	Haemoglobin saturation.
SPECT	Single photon emission computed tomography.
TCA	Tricarboxylic acid cycle.
THb	Total haemoglobin concentration in large blood vessels (g/dl).
TMPD	Tetramethyl-p-phenylenediamine dihydrochloride.
TPSF	Temporal point spread function.
TTL	Transistor transistor logic.

CHAPTER 1

INTRODUCTION

This chapter discusses the clinical need for cerebral oxygenation monitoring of the newborn infant and introduces both optical and other monitoring techniques that can be applied to the problem. In addition to discussing the paediatric motivation for the work, both the clinical and medical science background are briefly outlined, as these predict the form of the oxygenation dependent optical signals which may be observed.

1.1 CLINICAL NEED FOR CEREBRAL OXYGENATION MONITORING

Noninvasive examination of the oxygenation of living tissue in-vivo is of general interest in many areas of medicine and physiology. The work described in this thesis was however originally undertaken to assist in the study of one small field of medicine, the cause of neurodevelopmental problems in newborn infants, both those born very premature, or at normal or late gestations[†]. There are a number of clinical situations in which damage to the

[†] Recently other areas of clinical interest have been studied with the instruments developed in this work. These include the examination of patients who have had treatment by radiotherapy for cancer of the mandible and the examination of muscle oxygenation in patients

brain of the infant is thought to occur as a result of the separate or combined effects of low arterial blood oxygenation and abnormal cerebral blood flow. Firstly let the problem be put into perspective.

Special Care Baby Units (SCBU) admit between 1% and 3% of all newborn infants for some degree of intensive care, for example mechanical ventilation, oxygen therapy, maintenance of nutrition and acid-base balance. The majority of these infants develop into normal children, a small group do not survive and a further small group survive with some degree of severe or minor neurodevelopmental impairment. It is the latter group which create the largest concern especially as there is evidence that despite an increase in the number of newborn infants surviving, the numbers with some degree of neurodevelopmental impairment are static[1]. The most "at risk" groups of infants are very preterm infants (defined as less than 33 weeks gestation), very low birth weight infants (defined as less than 1500 grams) and term infants with growth retardation or birth asphyxia.

1.1.1 Very preterm infants

Follow up studies of the neurodevelopmental outcome of very preterm infants have been performed at a number of centres[1 2 3 4]. One such study covered all 158 very preterm infants admitted to University College Hospital, London (UCH) in 1979-80[5]. The outcome of these infants, followed up until the age of 16-23 months is given in Table 1.i.

The infants found to be most at risk were those of less than 1250 g birth weight, and any infant requiring mechanical ventilation. In this study, the brains of all infants less than 33 weeks gestation were examined by ultrasound for evidence of both haemorrhage and ventricular dilatation and comparisons were made with neurodevelopmental outcome based upon clinical developmental quotients. Haemorrhage was graded according to the degree of bleeding. The results in Table 1.i showed the magnitude of the problem in very preterm infants. The data indicated that the sensitivity of uncomplicated periventricular haemorrhage (PVH, grade II or higher), as detected by ultrasound examination, at picking up neurological problems in later life was 77% (17 out of 22). The specificity of detecting normal outcome on the same basis was 66% (57 out of 87). The rather poor specificity indicated above was greatly improved when the normal group included those infants with abnormal ultrasound

---

suffering from peripheral vascular disease.

Table 1.i Results of ultrasound scans on the 109 surviving very preterm infants admitted to University College Hospital, London in 1979-80[5].

Ultrasound appearance	No of infants	Neurodevelopmental abnormality		
		Major No (%)	Minor No (%)	Total No (%)
Normal	62	2 (3)	3 (5)	5 (8)
Abnormal				
Haemorrhage				
PVH grade I	21[2]	2[1] (10)	2[1] (10)	4[2] (20)
PVH grade II	12	2 (17)	1 (8)	3 (25)
PVH grade III	5	1 (20)	1 (20)	2 (40)
PVH grade IV	4[4]	4[4] (100)	0	4[4] (100)
Intradural	1	0	0	0
No haemorrhage				
Mild ventricular distension (transient)	1	0	1	1
Cerebral atrophy	3	1 (33)	2 (67)	3 (100)

PVH-Periventricular haemorrhage.
Numbers in superscript are infants where haemorrhage was complicated by cerebral atrophy.

scans indicating periventricular haemorrhage uncomplicated by ventricular enlargement, hydrocephalus or cerebral atrophy. Then, specificity was improved to 93% (81 out of 87) with a small loss in sensitivity to 68% (15 out of 22). This result, together with additional data in the paper indicated that uncomplicated PVH was not a good predictor of poor neurodevelopmental outcome.

Each of the 22 infants who showed abnormal sequelae were tabulated together with their ultrasound appearance and neurodevelopmental status. The minor neurodevelopmental impairment cases mainly involved loss of muscle tone, predominantly affecting the legs, while spastic diplegia, quadriplegia and hearing loss were common outcomes in the group with major neurodevelopmental impairment.

The conclusions drawn from this study were that PVH was extremely common in very preterm infants, however it was not the major cause of neurodevelopmental impairment. Hypoxic ischaemic damage was considered to be the major cause, but it could only be detected reliably by ultrasound as cerebral atrophy (loss of brain tissue), at which point it was

too late for clinical intervention. In a few infants, ventricular dilatation could be detected by ultrasound sufficiently early to allow clinical intervention. A method of detecting hypoxic ischaemic damage reliably before cerebral atrophy has occurred was obviously desirable.

1.1.2 Term infants

The number of neurodevelopmentally impaired children resulting from severe birth asphyxia in term infants is three times the number in the preterm infant group[6]. Just as in the preterm infant population where damage to the brain is thought to be caused by hypoxic ischaemic injury, it is extremely difficult to predict impairment following birth asphyxia in the first few days of life. Standard clinical indicators involve measuring fetal heart rate as a sign of fetal distress, the Apgar score at birth, and data from umbilical cord blood samples. However more reliable monitoring techniques are sought. Although the data is still controversial, hypoxic ischaemic brain injury is thought to be the cause of damage in up to 20% of all moderate and severely impaired children. Congenital and hereditary disorders are the largest cause of impairment in the newborn infant[6].

1.2 THE MEDICAL SCIENCE BACKGROUND

This section is included to provide some background information on the characteristics of the oxygenation changes that are to be likely to be observed in the brain of normal and brain injured newborn infants. These characteristics include signal magnitudes, the spatial distribution of oxygenation and the rate of change of both cerebral oxygenation and blood volume.

1.2.1 Clinical anatomy of the developing brain

The structure of the newborn brain is complex and this complexity increases as the brain continues to develop even after the normal 40 weeks of gestation. The brain and the intercranial volume increases by a factor of 2 between 28 and 40 weeks of gestation,

corresponding to an increase in the average occipitofrontal head circumference from 26.8 to 33.5 cm[7].

The brain is comprised of the forebrain, midbrain and hindbrain and small individual volumes are known to be responsible for specific functions such as auditory or visual sensation or certain motor functions. The brain tissue consists of both grey matter, containing the cell bodies of neurones, and the white matter comprised mainly of axons and dendrites which communicate between neurones. The grey matter is mainly located on the surface of both the forebrain and hindbrain (the cortex) and varies in thickness between 1 and 4 mm. As the brain develops the surface becomes highly convoluted with about two thirds of its surface area hidden in folds. There are also small nuclei of grey matter deep within the midbrain. Cerebrospinal fluid (CSF) flows around the spinal cord and the ventricles, a system of connected cavities within the brain. It is a pale yellow clear liquid produced within the lateral ventricles.

It is into the ventricles and their surrounding white matter, the periventricular region, that the majority of haemorrhages occur in preterm infants. As already discussed, ultrasound is extensively used in the diagnosis of periventricular haemorrhage and ventricular dilation. Eighty percent of these periventricular haemorrhages occur in an area called the germinal layer matrix, lining the lateral ventricle. The period of highest risk occurring between 26 and 32 weeks gestation when this region is characterised by very immature, friable blood vessels. From 32 to 34 weeks changes in the pattern of cerebral vasculature occur with the disappearance of the germinal matrix together with rapid growth of the cortex and white matter.

In addition to haemorrhagic damage, cerebral underperfusion related to the immaturity of the vascular supply can occur in other periventricular regions (those more distal to the ventricle walls). Periventricular leukomalacia (PVL) is an ischaemic lesion which occurs in preterm infants at gestations up to 30 weeks, in areas of terminal distribution of the arterial supplies, the so called arterial watershed regions[8]. The damage affects the periventricular white matter under conditions of hypotension or hypoxia. The commonest neurodevelopmental problems which are observed in the later life of preterm infants reflect the role of this periventricular white matter. This area normally develops into motor neurones conducting messages to the trunk, legs and arms, while posteriorly the neurones make connections to the auditory and visual centres. One or more of these functions can be impaired in infants who have sustained neurological damage following preterm birth.

Various patterns of cerebral damage arise in the mature infant, usually as a consequence of birth asphyxia. In these infants the anatomy of the brain is well developed but the process of myelination is continuing together with modification of the venous drainage system. Observed sequelae are: tissue necrosis, frequently associated with cerebral oedema, compressed ventricles and flattening of the convolutions of the brain. The cerebral cortex, basal ganglia, cerebellum and brainstem appear to be the most vulnerable areas at this age.

1.2.2 Haemoglobin and the red blood cell

Non-invasive optical monitoring systems detect changes in optical attenuation caused by naturally existing chromophores, the most important of which is haemoglobin. Haemoglobin is a iron containing protein with a molecular weight of 64450 and consists of 4 subunits made up of 4 possible protein chains, α, β, δ and γ. In adults 97% is found in the HbA form ($\alpha\beta$ chains) with approximately 2.5% in the HbA_2 form ($\alpha\delta$ chains) and less than 1% in the fetal HbF form ($\alpha\gamma$ chains). In the newborn infant at birth the amount of HbF is 60-80%, HbA 20-40% and HbA_2 is 0.2%. These ratios gradually change towards the adult values, with HbF 10-15%, HbA 82-87% and HbA_2 0.5% at 4 months of age, finally approaching adult values at 1 year[9].

The main function of haemoglobin is to carry oxygen from the lungs to the tissues though it also has an important function in the transport of carbon dioxide back to the lungs. Each of the 4 subunits of haemoglobin, in the active ferrous (Fe^{2+}) form, can bind to a molecule of oxygen in a physical and not a chemical manner, i.e. becoming oxygenated as opposed to oxidised. Thus 1 mole of deoxygenated haemoglobin (Hb) binds with 4 moles of oxygen to become oxygenated haemoglobin (HbO_2).

The binding of oxygen with haemoglobin is governed by a number of factors. It is normal to talk in terms of the haemoglobin saturation (SO_2), defined as

$$SO_2 = \frac{HbO_2}{HbO_2 + Hb} \times 100 \qquad [Units: \%] \qquad \text{1-1}$$

which expresses the percentage of the total haemoglobin which is oxygenated.

The relationship between haemoglobin saturation and the partial pressure of oxygen in solution is called the oxygen dissociation curve and is shown in Figure 1.1. The sigmoid

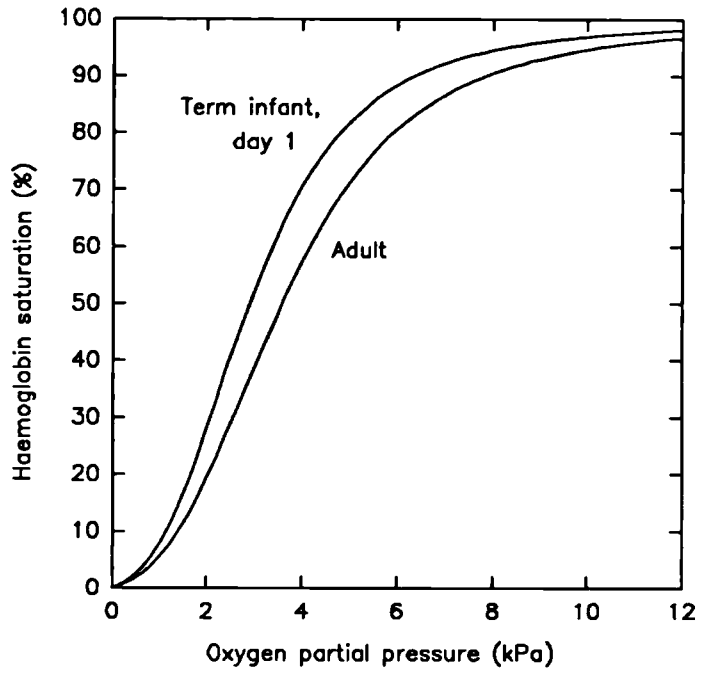

Figure 1.1 Haemoglobin oxygen dissociation curves typical of those for a newborn term infant (day 1) and an adult.

shape is caused by a modification of the subunits affinity for oxygen, dependent upon the number of oxygen molecules already bound. A typical p50 (half saturation point) for adult haemoglobin at a pH 7.4 and a temperature of 37°C, is 3.578 kPa, but this can be modified by other factors. In its deoxygenated form haemoglobin can bind with the metabolite 2,3 diphosphoglycerate (2,3-DPG) resulting in a lowered affinity for oxygen. Increasing levels of 2,3-DPG or carbon dioxide, a lower pH, or a higher temperature all reduce the affinity of haemoglobin for oxygen thus shifting the dissociation curve to the right and vice-versa.

Fetal haemoglobin binds poorly with 2,3 DPG and as a result has a much higher affinity for oxygen, (p50 ≈ 2.5 kPa). In practice the dissociation curve is near that of the adult from 44 weeks post conception. Hence, in theory, preterm infants may keep their fetal haemoglobin for many months[10]. However, in practice, multiple blood transfusions with adult blood are often given for medical reasons.

There have been many equations drawn up to define the relationship between haemoglobin saturation and oxygen partial pressure, such as

$$SO_2 = \frac{e^y}{1+e^y}$$
$$y = 1.875 + x + 3.50 \tanh(0.534x)$$
$$x = \ln\left(\frac{pO_2}{1.955}\right) - 2.303 \lg(p50) \qquad \text{1-2}$$
$$\lg(p50) = \lg\left(p50_{7.4}\right) - 0.48(pH - 7.4)$$

taken from Kokholm[11]. Where $p50_{7.4}$ (at 37°C) is taken as 3.578 kPa and 2.9 kPa for the adult and newborn human infant respectively, pO_2 is the partial pressure of oxygen (kPa).

Normal adult values of in-vivo haemoglobin saturation in the arterial system (S_aO_2) are 94% at an arterial oxygen partial pressure of 12.7 kPa. The saturation in the venous system (S_vO_2) is somewhat variable, being dependent upon blood flow and oxygen utilisation. In adult brain the saturation of the internal jugular vein is reported to be 61.8% (range 55.3% to 70.7%)[12]. The saturation of haemoglobin in the umbilical vessels of the newborn is much lower, with arterial saturation at 56% and venous saturation at 18%[13], hence the requirement for the lower P_{50} of fetal blood.

In addition to the dominant mixture of oxygenated and deoxygenated haemoglobin, there are several other naturally occurring forms of haemoglobin in the blood stream. The most important of these, carboxyhaemoglobin (HbCO), haemiglobin (Hi) and sulfhaemoglobin (SHb) are normally present in fractional concentrations up to a few percent. Haemiglobin can combine with many other groups such as F^-, NO^{2-}, N^{3-}, CN^-, but these compounds rarely occur in the blood stream and can be ignored in-vivo.

Haemoglobin, except in certain pathological conditions, is carried exclusively within the red blood cells of the blood stream. The red blood cells are flexible bi-concave disks 8.5 μm in diameter and 2.4 μm at their thickest section. Their cell membrane is a lipid bilayer made up of 50% protein, 40% lipids and 10% carbohydrates[14]. Red blood cells contain no nucleus, or mitochondria, and make the energy they require for active ion pumps, membrane repair etc. by anaerobic glycolysis. The red blood cell contains an enzyme system to reduce haemiglobin, the inactive (Fe^{3+}) form back to the active haemoglobin (Fe^{2+}) form and other control systems to maintain a fixed internal level of 2,3-DPG. The average useful lifetime of a red blood cell is 120 days.

Table 1.ii Normal red cell values in infancy and childhood. THb is the haemoglobin concentration, PCV the packed cell volume (haematocrit), MCV the mean corpuscular volume and MCHC the mean cell haemoglobin concentration.

Age	RBC Count (10^{12}/l)	PCV (%)	MCV (fl)	Thb (g/dl)	MCHC (g/dl)	RBC content (pg)
Fetus						
10 wk	1.4	31.6	191	9.0	33	60.5
22 wk	3.2	40	141	14.5	33	47
36 wk	3.7	45	122	15	33	40
Term	5.25(3.5-6.7)	53(47-58)	113	16.8(13.7-20)	32.6	36.9
1 day	5.8(3.9-7.0)	60(53-73)	110	18.4(15-23.5)	33	37
1 wk	5.2(4.1-6.3)	55(49-64)	106	17.0(12.5-19)	33.5	36
2 wk	5.1(4.0-6.5)	52(44-60)	102	16.8(12.5-19.5)	34.3	34
3 wk	4.9(4.0-6.1)	50(42-62)	100	15.7(13.0-20)	33.2	30
4 wk	4.35(3.2-5.8)	45(34-64)	101	15.0(12-20)	32.8	30.4
2 mo	3.75(3.0-5.6)	37.7(30-48)	88	11.5(9.5-15.5)	33	30.2
3 mo	3.88(2.8-5.8)	36.7(32-45.7)	82	11.0(9.0-15)	34	28
4 mo	4.3(3.4-5.6)	35.3(32-48)	82	11.5(9.5-15)	33.5	27.7
6 mo	4.21(3.0-5.4)	38.5(33-47)	78	11.5(10.4-14)	33.5	26.1
10 mo	4.35(3.4-5.2)	39(34-48)	73	12.0(10.2-13.8)	33	23.7
12 mo	4.44(3.8-5.6)	39.3(34-48)	73	11.9(10.5-14.5)	32.5	23.5
2 yr	4.77(3.2-5.2)	35.8(34-46)	75	11.7(10.5-13.5)	32.6	24.7
14+						
Male	5.4(4.6-6.2)	47(40-54)	87	16.0(14-18)	34	29
Female	4.8(4.2-5.4)	42(37-47)	87	14.0(12-16)	34	29

Typical characteristics of red blood cells and haemoglobin concentrations are shown in Table 1.ii taken from various references in a Biological Handbook[15]. Values from birth to adulthood indicate variations in development. An anaemic period occurs following normal term birth due to a low level of red cell production, the nadir occurring at 11-12 weeks. This anaemic period is considered a normal physiological response to the much higher arterial oxygen partial pressures experienced after birth compared to those experienced in-utero. The degree of anaemia can be more marked (7 to 8 g/dl) in preterm infants and also occurs at an earlier time compared to term infants.

1.2.3 Biochemistry of cell metabolism

Most of the energy consumed by living cells is derived from stored molecules of adenosine triphosphate (ATP). The brain and some of the other organs also have large stores of phosphocreatine (PCr) another high energy phosphorus compound. As ATP is used up by cells in providing energy, for example to maintain cellular function or in brain cells the release of electrical impulses, the breakdown products adenosine diphosphate (ADP) and inorganic phosphate (P_i) are produced. The store of ATP is replenished in cells by one of two means: either by oxidative aerobic phosphorylation in the mitochondria, or by anaerobic glycolysis in the cytosol. In a normal respiring cell the balance of the kinetics of these reactions keeps the concentration of ADP very low and maintains a steady concentration of ATP. In the event of a short term disturbance in oxidative phosphylation, ATP levels are maintained at the expense of PCr.

The main fuel used in the production of ATP is glucose, one mole of which contains enough energy to convert 46 moles of ADP to ATP. Depending on local circumstances, one mole of glucose only produces 2 moles of ATP via anaerobic glycolysis compared to 25 to 36 moles of ATP by oxidative phosphorylation[16]. Thus oxidative phosphorylation produces 12.5 to 18 times as much ATP per mole of glucose as anaerobic glycolysis.

At rest, the rate of glucose utilisation in the brain is 0.3 to 0.8 μmol/g wet wt/min[17] while oxygen consumption is 1.6 to 5.0 μmol/g wet wt/min. Since six moles of oxygen are required for the combustion of 1 mole of glucose, this indicates that 95% of glucose utilisation in the brain is via oxidative phosphorylation. This is also consistent with lactate production measurements which show, in a normally oxygenated and perfused brain, a percentage glucose utilisation by anaerobic glycolysis of 0 to 4%[18]. The production rate of ATP in the brain is

9.2-32 μmol/g wet wt/min of which only 1% is from anaerobic glycolysis. At rest, it is estimated that up to 40% of the total amount of ATP produced is required merely to maintain the most basic cell function, that is the pumping of sodium across the cell membrane[19]. It is therefore hardly surprising that the brain is extremely sensitive to anoxia, especially with this high metabolic rate compared to that of other tissues. The adult human brain consumes 20% of the body's total oxygen requirement, yet comprises only 2% of total body weight[17].

Oxidative phosphorylation takes place in an organelle within the cells, the mitochondria, the enzymes involved in the process forming part of the inner mitochondrial wall. The two main sources of electrons for the respiratory chain are nicotinamide adenine dinucleotide (NADH) via NADH dehydrogenase (FMN, flavin mononucleotide) and succinate via succinate dehydrogenase (FAD, flavin adenine dinucleotide). The route from the products of digestion to NADH and succinate is through the many different biochemical pathways ending in the tricarboxylic acid (TCA) cycle. A simplified schematic of the electron transport chain is given in Figure 1.2 (a number of non-haem iron-sulphur (FeS) proteins have been omitted from the chain). The electrons from NADH and succinate eventually follow a common path, shown left to right in Figure 1.2, through coenzyme Q (Q) and the cytochrome enzymes b, c_1, c and aa_3[†] finally resulting in the reduction of oxygen to water.

The energy generated at each step as the electrons move down the chain (shown in the figure as the vertical drop) is stored by pumping protons out of the mitochondrion. This results in a proton gradient which creates an electric potential and a pH gradient across the mitochondrial membrane. These electrical and pH gradients drive protons back into the mitochondria, giving up their energy in phosphorylating ADP to ATP[16].

With a supply of electrons from NADH and in the absence of oxygen, all of the respiratory enzymes will become reduced. Alternatively, in the absence of electrons coming down the chain and in the presence of oxygen, all enzymes will become oxidised. Under normal working of electrons moving down the chain, the electron donor will be at a more negative potential compared with the electron acceptor and changes in redox state can be affected by NADH, succinate, oxygen or ATP concentrations. It is obvious that a method of monitoring the concentration of oxygen via the redox state of any of the electron transport

---

[†] The complexity of cytochrome aa_3 is such that it has had numerous names in common usage. For example cytochrome oxidase, cytochrome c oxidase and others. Here cytochrome c oxidase will be used except when it is important to distinguish the separate haem a and haem a_3 sites.

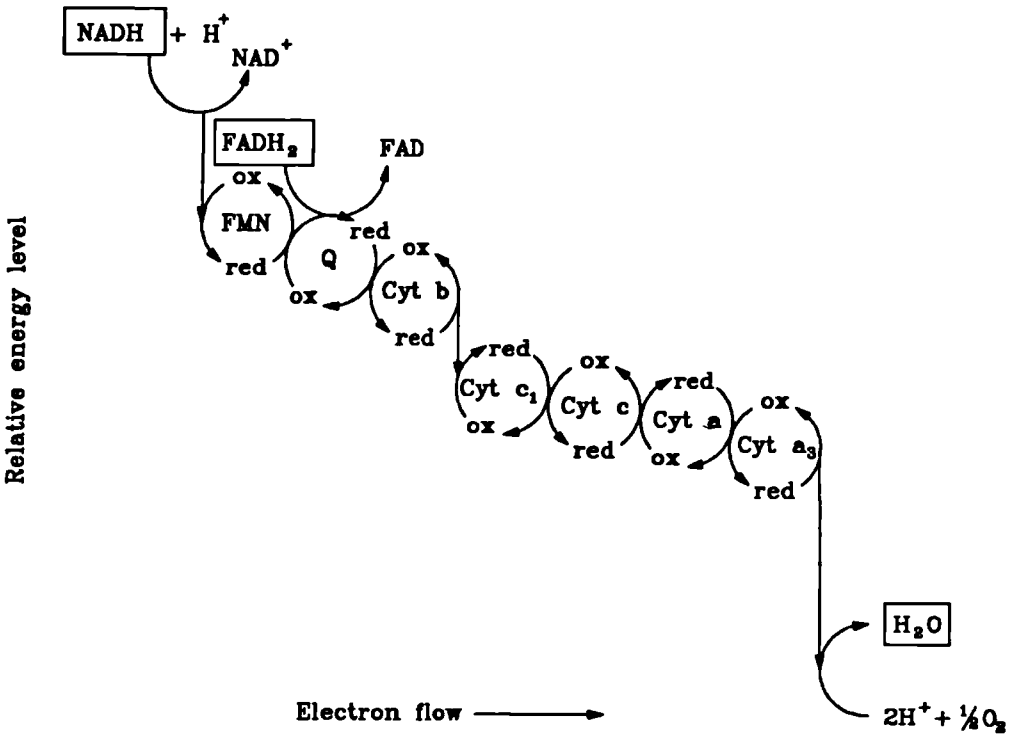

Figure 1.2 Schematic diagram of the electron transport chain. Electrons are transferred from left to right, the energy released at each transfer is indicated by the vertical height.

chain enzymes or monitoring of tissue metabolism via the concentration of the high energy phosphorus metabolites (ATP, PCr) in-vivo would prove interesting. Later it will be shown that cytochrome c oxidase is particularly interesting because of its optical properties.

To detect the respiratory enzymes in tissue they must be present in measurable concentrations. Unfortunately there is no published data on cytochrome enzyme concentrations in newborn infant brain tissue. Obtaining values for these concentrations from the literature involved pooling data from a number of sources and examining consistency. This was slightly hampered by the different methodologies and specific extinction coefficients used by different authors.

The relative concentrations of the components of the respiratory chain have been reported for beef heart mitochondria[20] and are in Table 1.iii. The same cyt $c+c_1$:cyt c oxidase ratio of 1:1 has also been reported in liver mitochondria[21]. Ratios for cyt b:cyt $c+c_1$:cyt c

Table 1.iii Stoichiometry of respiratory enzymes in beef heart mitochondria, data taken from Tzagoloff[20].

Carrier	Concentration relative to cytochrome c_1
NAD	35
FMN	1
FAD	1
FeS	30
Q	19
Cyt b	3.2
Cyt c_1	1
Cyt c	2.1
Cyt a	3.1
Cyt a_3	3.1

oxidase in rat brain mitochondria are reported[22] to be 1.6:1.42:1[†], the cyt c:cyt c oxidase ratio being independent of age with a small age dependence for cyt b.

Most of the studies on the absolute cytochrome concentrations per g wet weight tissue have been made on rats. The cytochrome c oxidase content of adult rat heart is reported at 20.7 μmol/l wet wt[23] and the cytochrome c oxidase content of brain is reported to be 1.5 μmol/l wet wt at birth and 4.8 μmol/l wet wt in the adult[24]. Dallman[25] found that the cytochrome c concentration of adult rat heart was 24 μmol/l wet wt while the cytochrome c content of neonatal rat brain rose from 1 μmol/l wet wt at birth to 3.6 μmol/l wet wt at 30 days. The onset of the increase at 10 days coincided with the onset of myelination. The same paper showed that the guinea pig brain has the same level (3.6 μmol/l wet wt) of cytochrome c from the day it is born, reflecting its maturity at birth.

It is difficult to predict how the above values relate to the human newborn infant. In terms of its development, the human infant brain is part way between the rat and guinea pig and the cytochrome enzyme concentrations in human adults are also not known. The best conclusion that can be reached is that neonatal infant brain cytochrome enzyme levels will be in the range 1-5 μMolar. All other components in the respiratory chain are assumed to be in

---

[†] The cytochrome b value here is twice that of the original publication. The extinction coefficient of cytochrome b used throughout this thesis is 17.8 $mM^{-1}cm^{-1}$ at 556 nm, half the value used by Chepelinsky[22].

the same ratio as indicated earlier.

1.2.4 Cerebral oxygenation and haemodynamics

As previously mentioned, the neurodevelopmental problems observed in some preterm infants are thought to be the result of either a lack of oxygen in the arterial blood or a lack of blood flow to the brain or a combination of the two. The amount of oxygen in the arterial blood depends upon the inspired oxygen concentration into the lungs (F_iO_2) and the pulmonary gas exchange. The arterial blood gas partial pressures are normally written as p_aO_2, p_aCO_2 (units: kPa) for oxygen and carbon dioxide respectively and the term S_aO_2 (units: %) is used to express the arterial haemoglobin saturation. From an arterial blood sample, these parameters together with the blood acidity (pH) and the total haemoglobin concentration THb (units: grams haemoglobin per decilitre of blood, g/dl) can be measured by standard monitoring techniques in an automated blood gas analyser. The oxygen carrying capacity of the blood, can be calculated from the above

$$O_2 = 1.34\,THb\frac{S_aO_2}{100} + 0.022\,p_aO_2 \qquad [Units: ml\,O_2\,dl^{-1}] \qquad \text{1-3}$$

In this equation, the first term on the right represents the quantity of oxygen carried by the haemoglobin whilst the second term represents the amount of dissolved oxygen in the plasma. Putting some typical arterial values into the equation (S_aO_2=95%, p_aO_2=12.7 kPa, THb=15 g/dl) yields a total of 19.4 ml of O_2 per decilitre of blood with 19.1 ml O_2/dl carried by haemoglobin and 0.3 ml O_2/dl dissolved in plasma. This shows that blood plasma carries a negligible amount of oxygen to the tissues and suggests that it is only S_aO_2 that determines the oxygen concentration available to the tissue. It should however be noted that the oxygen delivery to the tissues is by diffusion, and this is driven by the partial pressure difference between the blood in the capillary and the cell cytosol. Haemoglobin acts as a local buffer to maintain plasma pO_2 as oxygen is extracted by the tissue.

Some clinical data is available on cerebral blood flow (CBF). This is normally expressed in terms of the number of millilitres of blood flowing through 100 grams of tissue per minute. The tissue volume is assumed to be uniformly perfused, in other words not containing any large blood vessels, sinuses, bone or ventricles such as are seen in the head. Most of the techniques which provide data on CBF non-invasively cannot measure on such

small volumes of tissue. Usually, measurements are made over a relatively large volume and an average flow for that region is calculated in units of millilitres of blood per 100 ml of tissue per minute. Conversion from units of millilitres to grams is easy as the density of tissues is rather constant, for example brain density[26] is 1060 kg m^{-3}. When comparing data from various sources it should be remembered that some variations will arise from the different techniques of measuring blood flow, because of the partial volume effect. Thus quantified data from invasive studies will tend to be higher than that from non-invasive studies which examine larger volumes of tissue.

A typical averaged value for adult cerebral blood flow is 47.7 ml/100 ml/min[27] which, in conjunction with the previously calculated O_2 content of arterial blood makes the total oxygen delivery 9.25 ml O_2/100 ml/min. For comparison, the typical oxygen consumption of the adult brain is 4.2 ml O_2/100 ml/min[27]. These values are an average of grey and white matter. Cerebral blood flow, cerebral blood volume and cerebral oxygen extraction are significantly greater in grey matter compared to white matter in normal human adults[28].The CBF and CBV of grey matter is approximately 2.5 times that of white matter, while the oxygen extraction ratios (OER, the ratio of oxygen consumed to oxygen delivered) are approximately the same being 0.37 and 0.41 for grey and white matter respectively.

Cerebral blood flow depends upon the perfusion pressure (arterial minus venous blood pressure) and the vascular resistance. In the normal adult, the cardiac output and systemic blood pressure have little effect on the cerebral blood flow. This process of autoregulation works over a large range of mean systemic pressures (60-160 mmHg) but can break down at very low or very high values. In newborn infants, the situation is unclear, and there is no consensus of opinion over whether autoregulation occurs in the very preterm infant, and if it does, whether it may breakdown following a haemorrhage or an hypoxic-ischaemic insult. Techniques which can measure or detect changes in cerebral blood flow are discussed later in Section 1.4.

Although cerebral blood flow is essentially unaffected by systemic blood pressure there are other factors which can affect it greatly. The most potent of these is the cerebral arteriolar response to carbon dioxide, pH and oxygen. The response of these vessels to carbon dioxide is the strongest, with a typical CBF response in the human adult of +31% per kPa change in carbon dioxide partial pressure[29]. The exact mechanism of this action is unknown, but it is thought to be partially mediated via pH. The end result is a dilation of the arterioles with increasing carbon dioxide partial pressure and vice-versa. The effect of oxygen is less

dramatic. Very low p_aO_2 causes much increased cerebral blood flows of up to 500%[30] but p_aO_2 fluctuations in the range 6 - 13 kPa causes insignificant variation in cerebral blood flow[18].

Blood viscosity also influences cerebral blood flow, and this is related to haematocrit. A haematocrit in the region 30% to 40% is normally considered to be optimal for delivering oxygen. At lower values, the loss of haemoglobin lowers oxygen delivery, and conversely much higher haematocrits increase blood viscosity and lower blood flow. The flow of blood in-vivo is normally laminar in nature with the red blood cells being more concentrated in the centre of the vessels. This is thought to give rise to an effect called plasma skimming where the haematocrit in side branches and ultimately the whole capillary bed is lower than that in the larger vessels. This effect has been measured in the brains of adults by Sakai[31]. This paper reports measurements of regional cerebral blood volume made separately on the red blood cells and plasma using radioactive tracers and single photon emission computed tomography (SPECT). The results obtained gave an average for human adult cerebral vessel to large vessel haematocrit ratio of 0.759 ± 0.021 in normoxia decreasing to 0.724 ± 0.22 during hypercapnia. As this is an average value for all the cerebral vessels, the actual capillary haematocrit will be even lower. The cerebral blood volume (CBV) expressed as the blood volume per 100 g of tissue was 4.81 ± 0.37 ml/100 g. This comprises a cerebral red blood cell volume (CRBCV) of 1.50 ± 0.09 ml/100 g and a cerebral plasma volume of 3.34 ± 0.28 ml/100 g. The response of blood volume to hypercapnia revealed that it is the cerebral plasma volume (18.6 ± 6.15 %/kPa CO_2) which increases more significantly than the cerebral red cell volume (11.0 ± 3.60 %/kPa CO_2), indicating that the expected improvement of oxygen delivery to the tissue is not as great as it may first appear. An alternative value for cerebral to large vessel haematocrit ratio (CLVHR) was found in a similar study[32] using positron emission tomography (the technique is described in Section 1.4.2). The global average for CLVHR was 0.69, with regional variations comparable to the accuracy of the measurement, i.e. less than 5%. The mean value of 0.69 is slightly lower than the value of 0.76 reported earlier by Sakai using SPECT. Normally changes in blood flow parallel changes in cerebral blood volume such that this ratio is almost constant (approximately 10 min^{-1})[33]. The CBF/CBV ratio is considered a measure of vascular reserve[34].

A further factor which acts to dilate or constrict cerebral blood vessels is the intracranial pressure. In the adult, the brain tissue, blood vessels and CSF are all contained in a sealed box, comprising the skull and spinal column. As the contents are incompressible, any increase in pressure in the venous or arterial system or increases in tissue volume due to

oedema will cause an increase in the pressure of the whole system, compressing the blood vessels and hence reducing blood flow. The situation in the newborn is more complex as cerebral volume can increase through movement of the fontanelles and expansion of the flexible skull. However, changes in intercranial pressure will still have some effect, although these are likely to be less marked than in the adult.

Data for CBF, CBV and oxygen extraction in newborn infants are less numerous. There are vastly different values reported for neonatal CBF, such as 9-20[35], 14[36] and 12-20 ml/100 g/min[37]. The value for the CO_2 response of cerebral blood flow of 67% /kPa CO_2 (95% confidence limits 13-146% /kPa)[38] is a much higher value than that measured on adult humans. Possible reasons for the variability of the data could be the methods used or the natural variability of the newborns infants studied.

No data appears to be available for CBV in newborn infants, but in newborn piglets[39], the cerebral red cell volume was 1.2 ml/100 g tissue, measured 24 hours after birth with a venous haematocrit of 0.356. These values did drop proportionally with the developing anaemia over the next 14 days. The values agree well with those measured on human adults of 1.5 ml/100 g at a venous haematocrit of 0.45. This study does report a discrepancy in the value of the CLVHR when compared to earlier findings. A value near 1.0, is quoted which may reflect the difference in methodology or the low venous haematocrit of the piglet.

From this data it is possible to calculate a value for the average concentration of haemoglobin in brain tissue. This value is important if an optical system is to be designed to detect its presence. However, before doing this the question of units is to be discussed. Historically, haemoglobin concentration measurements in tissue were always quoted in either **g Hb/100 g wet wt tissue** or **ml blood/100 g tissue**. These are rather inconvenient as spectroscopy measurements naturally produce values in units of **moles per litre** (in this case per litre of tissue). In this thesis, optical measurements will be quoted in the natural units of Molar concentration (M), but at times it will become necessary to compare values derived from near infrared spectroscopy with standard literature data. The conversion of CBV to tissue haemoglobin concentration [Hb_t] (moles/litre tissue) can be expressed in two forms depending upon the data available

$$[Hb_t] = \left(\frac{10\,THb}{MW_{Hb}}\right)\left(\frac{CBV \times CLVHR}{100}\right) D_t \qquad \text{1-4}$$

$$[Hb_t] = \left(\frac{10\,MCHC}{MW_{Hb}}\right)\left(\frac{CRCV}{100}\right) D_t$$

Where the units of all parameters are "clinically recognisable". *THb* (Units: g/dl blood) is the concentration of haemoglobin in the large vessels, MW_{Hb} is the molecular weight of haemoglobin (64450). The cerebral to large vessel haematocrit ratio (CLVHR) is taken from Sakai above at 0.76 and the density of brain tissue (D_t) is 1.06. The second expression is preferred if suitable data (CRCV, the cerebral red cell volume, ml/100 g) is available as the first expression suffers from inaccuracies caused by variations in the CLVHR with large vessel haematocrit. Using the second expression with a MCHC = 34 g/dl and CRCV = 1.5 ml/100 g, then the typical value for haemoglobin concentration in brain tissue is 84 μMolar. Some degree of systematic error must be expected when making these conversions due to inaccuracies and natural variability in the values of CLVHR and tissue density.

The physiology summarised above outlines the range of variations in cerebral blood oxygenation and haemodynamics which any monitoring instrument should aim to detect. Some of the data mentioned is quantitative and can therefore be used for comparison purposes. Unfortunately most of the data relates to adult brain and caution is necessary when comparing this to results obtained in the newborn infant. The discussion in this section is by no means comprehensive, and there are many additional effects which occur in clinical practice such as those caused by the administration of drugs and anaesthetics which have not been mentioned.

1.3 THE HISTORY OF OPTICAL METHODS FOR DETERMINING BLOOD AND TISSUE OXYGENATION.

The fundamental relationship used in almost all optical spectrophotometers is the Beer-Lambert law which is outlined in Section 2.1. In a simple analysis, (ignoring tissue scattering)

the attenuation spectrum of tissue is considered as the summation of the individual spectra of the constituent chromophores multiplied by their individual concentrations

$$A(\lambda)=\lg\left[\frac{I_0(\lambda)}{I(\lambda)}\right]=\sum_{i=1}^{n}\alpha_i(\lambda)C_i l \qquad 1\text{-}5$$

Where $A(\lambda)$ is the tissue attenuation spectrum (the logarithmic ratio of incident $I_0(\lambda)$ to transmitted $I(\lambda)$ light intensity), $\alpha_i(\lambda)$ is the specific extinction coefficient of compound i, C_i is the concentration of the compound i, l the optical pathlength and n the number of chromophores. If the attenuation spectrum is monitored at the same number of wavelengths as there are chromophores in the tissue, then the inverse problem of finding the chromophore concentrations is just a solution of simultaneous equations. In practice, the solution is significantly more complicated than this simple analysis due to the effects of multiple scattering and requires more complex theories, or experimentally determined instrument calibrations.

The following sub-sections look at the historical development of measuring first blood, then tissue oxygenation via the respiratory chain enzymes and finally introduces the technique of near infrared spectroscopy of brain tissue.

1.3.1 Oximetry

An excellent history of oximetry (haemoglobin oxygenation measurement) has been published by Severinghaus[40].

Haemoglobin was one of the first compounds to be studied by optical spectroscopy at the turn of this century, its near infrared absorption bands being reported by Hartridge and Hill in 1914. Spectroscopic measurements of haemoglobin saturation in tissue began in 1932 with Nicolai[41]. The first instruments being made later in 1935 by Matthes[42] and Kramer[43]. The Kramer instrument used only one red wavelength and hence could not compensate for changes in haemoglobin concentration while Matthes overcame this problem by using two wavelengths (one red, one green) the second one being oxygenation independent. Matthes made improved spectral measurements on haemoglobin in-vitro in the red and infrared region in 1939[44], and using this data his previous instrument was modified to use an infrared wavelength which was O_2 independent[45].

Oximetry can be split into in-vitro measurements of blood samples and in-vivo oximetry in tissue. In-vitro work on blood samples built on Kramer and Matthes's early work to techniques requiring smaller volumes of blood for a given accuracy. Kramer had shown[46] that red blood cells suspensions did not in general obey the Beer-Lambert law, but that under certain conditions Beer's law could be applied. In the most accurate oximeters, haemolysis of the red blood cells is first performed allowing not only measurement of Hb and HbO_2 but also HbCO. Commercial oximeters for blood samples are currently made by Radiometer, the OSM2 and OSM3 and Instrument Laboratories, the IL 282. The IL 282 for example aspirates 0.35 ml of blood from a syringe or 0.175 ml from a capillary tube and provides values for THb (total haemoglobin) ±0.3 g/dl and the relative percentages of HbO_2, HbCO and Hi with an absolute accuracy of ±1%[47].

In-vivo oximetry was stimulated during the second World War by military aviation requirements to monitor the oxygenation of pilots in unpressurised aircraft cabins. In 1940, Squire at University College Hospital described an oximeter which was used on the web of the hand. He also described the first method of obtaining absolute oximetric measurements in tissue by first squeezing all the blood from the web, zeroing the instrument and then allowing the blood to return.

The first practical ear oximeter for aviation use was built by Millikan in 1942[48]. Wood and Geraci[49] modified this in 1949 to measure absolute saturation by the compression technique of Squire using an inflatable capsule. Unfortunately due to the poor optoelectronic components available at that time, this ear oximeter was not sufficiently accurate and stable for clinical use, and although taken up by physiologists was never used widely on patients. Further improvements in this area were later made by Shaw, and these resulted in the development of the Hewlett Packard Ear Oximeter. This measures across the pinna of the ear, using a heater to arterialize the vessels of the ear and measuring attenuation at 8 wavelengths to provide an absolute calibration independent of skin pigmentation. This instrument is still regarded as the "gold standard" oximeter. It is however not widely used in routine clinical practice due to its high cost and its bulky "bolt on" ear sensor. A major break through in non-invasive oximetry came relatively recently, with the development of the pulse oximeter[50]. This measures the pulsatile changes in light transmission across a vascular bed such as the fingertip or ear that arise due to an arterial blood volume increase with each heart beat. Absolute arterial haemoglobin saturation is obtained without heating and using only 2 wavelengths. Numerous companies currently make these instruments and they have found

widespread clinical use.

All the oximeters discussed so far have operated by transmission measurement, either in-vitro across cuvettes or in-vivo across the ear, finger or a fold of tissue. Some diffuse reflection oximeters have been built, and these are more flexible in their siting. The precursor of diffuse reflectance oximeters was "Cyclops" developed by Brinkman and Zijlstra[51] which was strapped to the forehead. Diffuse reflectance sensors on the skin and exposed organs have found a place in physiological research but not on hospital wards. The problems of light scattering by tissue means that these instruments cannot measure absolute values. The only exception is the arterial catheter reflectance oximeter, such as the one commercially available from Oximetrix, U.S.A. The reflectance characteristics of whole blood are sufficiently repeatable to permit a pre-calibrated system, to be accurate to a few percent[52].

1.3.2 The respiratory chain enzymes

The potential of optical spectroscopy as a possible method of examining tissue respiration was first considered by physiology research workers. Chance and Williams[53] looked at the optical difference spectra, between 300 nm and 650 nm, of isolated mitochondria suspensions, comparing differing states of oxidation of the various members of the respiratory chain. Some of this data is reproduced in Figure 1.3. Due to the considerable light scattering of the suspension, the spectra are not straight forward to interpret. None the less, the relative heights of the absorption peaks could be measured permitting a great deal of information concerning the respiratory enzymes to be found. The solid line in Figure 1.3 illustrates the difference spectrum of the whole respiratory chain of Figure 1.2, while the broken line is the difference spectrum of all the components with energy levels greater than and including cytochrome b (antimycin blocks electron transfer from cytochrome b to cytochrome c_1).

Recording wide band spectra takes an appreciable amount of time which is a disadvantage when observing kinetic responses of enzyme systems. To overcome this problem, Chance and Williams defined a set of closely spaced wavelength pairs for each of the enzymes of the respiratory chain, whose absorbance differences enabled the kinetics of each one to be examined, with they hoped, minimal interference from other enzymes. Many dual wavelength systems have subsequently been developed, see for example the review by Chance[54].

The dual wavelength spectrometer approach is rather crude for examining

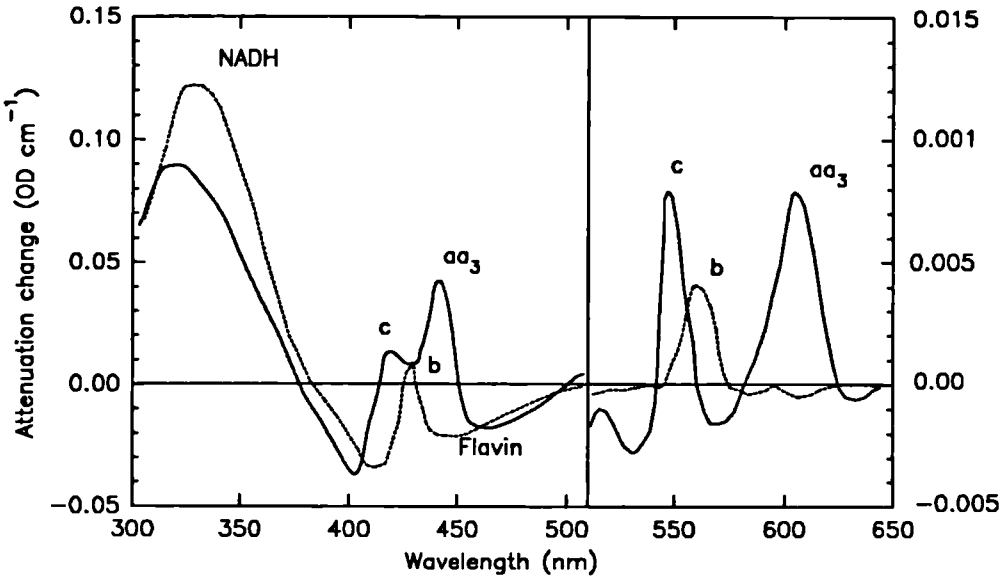

Figure 1.3 Difference spectra between aerobic and anaerobic mitochondria at slow respiration rate (solid line) and between fully oxidised and antimycin A inhibited mitochondria (broken line).

multicompound systems, since as explained earlier, to calculate the exact solution measurements are needed at as many wavelengths as there are compounds. In dual wavelength systems, careful selection of isobestic wavelengths (where absorption by two compounds is equal) or near-isobestic wavelengths are commonly used to minimise but not totally eradicate artifacts due to presence of these extra compounds.

Research workers also started to use diffuse reflectance techniques to examine the respiratory enzymes in-vivo on exposed organs such as the brain, heart, liver and kidney. Jöbsis[55] has published data showing similar difference spectra to the mitochondrial preparations of Chance but on perfused slices of cat brain cortex, together with many dual wavelength investigations on intact living tissue. Problems really arose with these techniques when the oxidation states of the respiratory enzymes were sought in the presence of blood in a normally perfused organ. Absorption by haemoglobin in tissue is almost an order of magnitude stronger than that of the respiratory enzymes.

Lübbers went a long way in improving in-vivo reflectance optical techniques especially where the respiratory chain enzymes were studied in the visible spectral region. He took a more theoretical approach as opposed to the experimental approach of Chance and Jöbsis and developed a rapid scanning spectrophotometer so that wide band diffuse reflectance spectra

could be collected instead of measurements at only a few wavelengths. Initially the problems of scattering were dealt with using a crude form of differential analysis in the vicinity of the visible absorption peaks[56 57]. Later, least-square multicomponent analysis[58 59] was employed based upon the multiple scattering theory of Kubelka and Munk[60 61]. In this way Lübbers was able to obtain more reliable and scientifically rigorous results compared to those available from the dual wavelength methods.

1.3.3 Near infrared spectroscopy (NIRS)

The work described so far does not have an application in measuring brain oxygenation non-invasively because visible and ultraviolet light does not adequately penetrate through the skull and into the brain tissue. The relatively high penetration of near infrared light had however been used to a limited extent in ear oximeters, and the near infrared absorption bands of haemoglobin had been accurately measured[62]. Similar measurements had also been made of the near infrared absorption band of the terminal member of the respiratory chain, cytochrome c oxidase, both as the purified enzyme[63] and in mitochondrial preparations[64]. It was Jöbsis, working at Duke University, North Carolina who put this information together with a sensitive spectrophotometer and showed that it was possible to measure the attenuation spectrum across a cat's head and hence initiated the field of NIRS[65]. Thus it now appeared possible to observe both blood oxygenation in the brain through the haemoglobin absorption and the tissue oxygenation through the absorption of cytochrome c oxidase.

Most of the Jöbsis group's publications on NIRS have been on the application of the technique to basic physiological studies in laboratory animals and are too numerous to mention. The validity of the technique itself and the instrumentation requirements have sadly received minimal attention in the scientific press.

The first clinical publications on NIRS arrived in 1984 from Ferrari and Giannini[66 67 68] and in 1985 from Brazy and Jöbsis[69 70 71]. These clinical data were in the form of traces of changes in the concentrations of oxygenated and deoxygenated haemoglobin together with cytochrome c oxidase redox state, measured on a second to second timescale at the bedside. Comparisons were made between cerebral oxygenation changes, clinical observations and data from other monitored parameters e.g. transcutaneous arterial oxygen and carbon dioxide levels, heart rate, blood pressure etc. The direct effect of clinical

procedures on the oxygenation of the brain could be seen.

The same data also illustrated the major drawbacks of the technique: firstly, the concentration measurements were relative and not absolute (i.e. they are concentration changes from one point in time relative to another); secondly, the measurements of haemoglobin and cytochrome c oxidase redox state were also in arbitrary units. The reason for the chromophore concentrations being quoted in this manner are two fold and relate to the multiple scattering of light within the brain tissue. The first reason is that there is no simple reference cuvette against which brain transmission measurements can be compared and secondly the optical path length (l in Equation 1-5) in the tissue is unknown. The optical path length is necessary in order to calculate concentrations in non-arbitrary units. These points are covered in greater detail in Section 3.4.

The radiation used in NIRS is safe as long as the intensity employed is below that which would cause tissue damage due to thermal heating. The average optical power reported in these early clinical measurements was of the order of 10 mW at the skin surface at an irradiance of approximately 50 $mWcm^{-2}$. This is below the safety levels set by the British Standards Institute for skin exposure to laser radiation[72], and are similar to the intensity of the sun on a sunny day. A discussion of safety aspects is in Section 5.10.

1.4 OTHER TECHNIQUES FOR MONITORING CEREBRAL FUNCTION

In addition to optical spectroscopy, a number of different technologies exist which can be applied to the non-invasive study of the brain. Some of these provide information only on the structure and anatomy of the brain eg. ultrasound, X-ray computerised tomography, nuclear magnetic resonance proton imaging. As these can only give information on structure and not metabolism in the brain they will not be considered here. The techniques discussed below however all provide information on different aspects of cerebral metabolism.

In addition to measuring some parameter of value, the ideal monitoring technique must also be safe and cause minimum inconvenience to both staff and patient. Any clinical measurement that is performed will always involve some degree of risk (if only because of the extra handling) and this risk must be balanced against the value of the information the

study provides.

1.4.1 Nuclear magnetic resonance spectroscopy NMRS

In this monitoring technique the metabolic status of cerebral tissue is determined from the presence of phosphorus (^{31}P) containing high energy metabolites. The patient is placed in a large bore superconducting magnet causing the nuclei of the phosphorus atoms in the tissues to align themselves with the magnetic field. A pulse of radio frequency energy disturbs the nuclei from their alignment, and in returning to their equilibrium position, a radio frequency signal is emitted[73]. For a fixed static magnetic field and nucleus, the frequency of this emitted signal is slightly modified by the molecular environment surrounding the phosphorus nuclei. Hence a frequency analysis of the NMR signal shows several peaks, the position of which is characteristic for each phosphorus containing compound. The integrated signal intensity is proportional to the concentration of the phosphorus compound. Example spectra obtained on a Oxford Research Systems TMR 32-200 spectrometer at 1.89 Tesla are shown in Figure 1.4. The ordinate zero frequency is 32.5 MHz, and deviations from zero are in parts per million.

One spectrum is from a normal infant at 37 weeks gestation, the other from a birth asphyxiated full term infant two days after birth. Characteristic peaks from the phosphorus

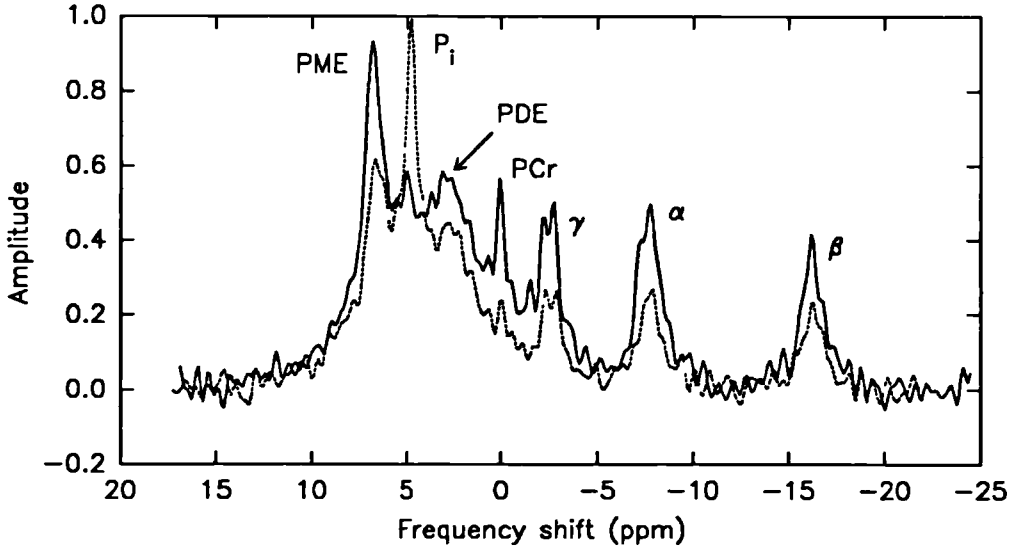

Figure 1.4 ^{31}P NMR spectra from the brain of: (solid line) normal 37 week infant; (broken line) term infant with birth asphyxia, day 2.

atoms in PCr, P_i, phosphodiesters (PDE), phosphomonoesters (PME) and the 3 phosphorus atoms (α, β, γ) of ATP can be seen in both cases. There are no peaks visible for ADP as it is normally present in too low a concentration to be detected by this technique.

Studies of normal newborn infants have shown that the ratio of the concentrations of PCr (the energy store) to P_i (the result of energy release) is near unity[74]. In newborns who have suffered an extended period of anoxia at birth, the ratio of phosphocreatine to inorganic phosphates is low immediately following birth (primary energy failure). The PCr/P_i ratio increases to normal levels in a few hours but then decreases again over the next 24-48 hours (secondary energy failure), recovering back to normal levels approximately 4 days after birth, Figure 1.4 illustrates this point. In nearly 100% of cases, follow up studies have shown that those infants displaying secondary energy failure develop some degree of permanent brain damage[75]. As a result of these findings, phosphorus NMRS is already having an impact on preterm infant care.

Although NMRS provides important data there are a number of practical problems in its routine application. Firstly the instrument is not portable and hence the infant must be transported from the intensive care unit to the machine in a transport incubator, together with monitoring equipment and possibly a ventilator. The infant must then remain in the bore of a magnet for approximately 30 minutes during which time it must not move. Hence although the data obtained is clinically very useful, there are a number of difficulties and risks involved in using it for sick infants. As for the risk from large static magnetic fields and the radio frequency pulses employed, these are at present believed to be harmless.

1.4.2 Positron emission tomography

Positron emission tomography uses a 2 or 3 dimensional array of gamma ray sensitive photomultiplier tubes, arranged to surround the part of the patient under study. From these it is possible to reconstruct images of slices through the patient. Multiple slices allow for the build up of 3 dimensional images. A positron emitting isotope tracer is either injected into the blood stream or inhaled in gaseous form. The isotope then distributes itself around the body, the distribution depending upon the chemistry of the tracer molecule. The emitted positrons travel a negligible distance before annihilating an electron, producing two gamma photons travelling in opposite directions. These gamma photons are detected by pulse coincidence circuits following the photomultipliers. The technique at present produces images of the

distribution of the isotope at about 8-10 mm resolution within a slice with up to 4 slices taken simultaneously.

The isotope used for studies of oxygenation is ^{15}O which can be inhaled as carbon dioxide or as molecular oxygen, or combined with hydrogen and injected as water. The results of PET studies of cerebral oxygenation have provided some unique data on regional cerebral blood flow and oxygen utilization both in adults and newborn infants.

Studies on infants have been performed by one group looking primarily at birth asphyxiated infants and very low birth weight infants diagnosed as having suffered a ventricular haemorrhage assessed by ultrasound examination[35]. Their results show new information particularly regarding regional cerebral blood flow which is much reduced in specific areas of the birth asphyxiated infants brain. In infants with intraventricular haemorrhage that extended into the brain tissue, a 2 to 4 fold decrease in blood flow was observed both posterior and lateral to the haematoma when compared to the unaffected hemisphere, the area of reduced flow extending into white matter and to a lesser degree into the frontal, temporal and parietal cortex.

Difficulties arise in trying to compare these data with those of the normal newborn infant since for ethical reasons the nature of the technique does not allow normal infants to be studied. A second study[76] purely on the birth asphyxiated newborn found that grey matter blood flow was 50% greater than white matter flow though this was considered to be underestimated. This agrees with data measured on adults. Severely birth asphyxiated infants were found to have cerebral blood flows in the parasagittal region that were 15 to 35% lower than the values in "almost normal" term infants. The data suggests a correlation between low parasagittal blood flow observed by PET and the early clinical signs of limb weakness which, if the infant survives, eventually result in spastic quadriparesis or, upon post mortem examination, softening of the brain tissue.

Despite the unique and useful information available with this technique, the use of ionising radiation, particularly as it is circulating in the blood to all areas of the body, makes it an ethically difficult study to perform on newborn infants. The radiation dose is approximately 100 mrem, 10% of that of a X-ray computed tomography scan. Like the nuclear magnetic resonance instrument, the PET scanner is a large, expensive, non-portable machine which additionally requires an on-site cyclotron. The latter is necessary as the half life of the positron emitting isotopes is usually of the order of minutes and hence they must be prepared on site.

1.4.3 Applied potential tomography

The a.c. resistivity of tissue is dependent on tissue type[77]. It is lowest for the body fluids blood, plasma, cerebrospinal fluid (1 Ωm) and highest for bone (166 Ωm). White matter has been measured at 6.82 Ωm and grey matter at 2.84 Ωm. These variations in resistivity can be measured and an image of resistivity variations produced. Tissue resistivity is a function of blood volume and the extracellular water fraction and as such the technique has the potential of detecting hypoxic ischaemic injury. To do this, an array of current supplying and voltage measuring electrodes are applied to the area of the body being studied. Impedance measurements are normally made at frequencies between 20 and 100 kHz, see Brown and Seagar[78]. Converting the surface measurements into a volume distribution of resistivity is a inverse problem that requires much computation but is possible if certain assumptions are made[79 80].

Practical problems of the technique are the positioning and attachment of the electrodes and obtaining reliable low impedance connections. This has been possible on the arm, the chest and the abdomen of adults and some images have been produced. The application of the method to the neonatal head is being attempted, however the problems of electrode attachment to such an irregular and hairy surface are difficult and the differences in tissue resistivity during normal physiological variation of blood flow and volume are small. So far just one image of a head with a very large intraventricular haemorrhage has been produced[81].

The obvious advantages, of the technique are its simplicity, low cost and portability, together with the non invasive and safe nature of applying small electrical currents to the body.

1.5 APPROACHES TO NEAR INFRARED SPECTROSCOPY

From the details of NIRS outlined in the introduction it is clear that the technique has excellent prospects as a non-invasive bedside monitor of cerebral oxygenation in the newborn

infant. The main aim of the work described in this thesis was to develop the technique beyond its existing state, into something more powerful and more clinically acceptable. Using NIRS data to develop theories regarding physiological changes in animal studies requires a lower level of confidence in the data than when it is to be used in making clinical decisions about the treatment of newborn infants.

A certain amount of criticism can be made of the pioneering Jöbsis group regarding their unwillingness to publish exact details of their approach to NIRS data analysis. This has prevented others from verifying their work and has, quite naturally and unnecessarily, led to wide scale scepticism which affects not only this group but the whole field. What the Jöbsis group have published[82] is an example equation for calculating one parameter from data obtained from one instrument

$$\Delta\left[Hb+HbO_2\right]=2.5\Delta A_{765}-1.7\Delta A_{800}-0.4\Delta A_{870}-0.8\Delta A_{904} \qquad \text{1-6}$$

Where $\Delta[Hb + HbO2]$ is the change in total cerebral haemoglobin concentration, and ΔA_{765}, ΔA_{800}, ΔA_{870}, ΔA_{904} are the changes in optical attenuation at the wavelengths employed in the instrument. The units of concentration are arbitrary and called variations of density "v/d". This one equation raised as many questions as it answered. For instance, why was this merely an example and not the real thing, and where were the examples for $\Delta[HbO_2 - Hb]$ and $\Delta[Cyt]$, the changes in cerebral haemoglobin oxygenation and cytochrome c oxidase redox state?†

The form of the equation above is consistent with a calculation of chromophore concentration assuming the Beer-Lambert law to be applicable, i.e. linearity of attenuation with chromophore concentration. However the values for the coefficients in the equation indicate that the spectra used in the calculation are not those published in the literature for purified haemoglobin and cytochrome c oxidase. In another publication[69] it became clear that the Jöbsis group did not trust the spectra obtained when chromophores were isolated in solution. They talked instead of "apparent extinction coefficients" obtained in experiments in which a cat head was perfused with anoxic and oxygenated red blood cell suspensions of differing concentrations. The difference spectrum (i.e. oxidised minus reduced) of

† The author wishes to point out that he was told the coefficients for all of the chromophores in personal communication from F.F. Jöbsis but decided against using them since exact information was not available on how they had been derived.

cytochrome c oxidase was also measured in-vivo using haemoglobin free perfused heads and comparing spectra obtained with the animal live and dead. The main disadvantage of this in-vivo calibration approach is that it automatically leads to chromophore determination in arbitrary units, in Jöbsis's case the "v/d". The use of in-vivo calibrations raises other questions such as: can an in-vivo calibration on one animal be trusted when used on the preterm infant? There is no reason to expect that spectral distortion caused by the preterm infant brain should be the same as that of the cat brain.

Another group working in Rome, have also not published their exact method for calculating chromophore concentration, although two papers [66 67] again point to the use of in-vivo reflection spectra as the calibration spectra.

The approach taken in this thesis has been to try and understand the underlying principles of absorption of light by tissue and to apply these to calculating chromophore concentration from optical attenuation measurements. To do this, an understanding of absorption and scattering in tissue is required. The term which investigators of NIRS have used for the calculation of chromophore concentration from tissue attenuation measurements is the "algorithm", Equation 1-6 is an example of part of an "algorithm" used by the Jöbsis group.

Absorption of light, whether in a clear or a scattering solution, is adequately explained by the Beer-Lambert law. However, in tissue (or any multiple scattering media) light takes a somewhat longer path than it would in a clear solution. If for every wavelength, the photon pathlength is the same, then sequential additions of a chromophore to a scattering medium would produce an undistorted change in the measured attenuation spectrum of the chromophore although the absolute magnitude of the attenuation change would be larger than expected. This situation is plausible if scattering and absorption are wavelength independent. We shall see that this cannot be exactly true, but over a limited wavelength band may be an adequate approximation.

A method of testing out any "algorithm" is also required. If a tissue spectrum contains data at more independent wavelengths than the number of chromophores that are present in the tissue, the data at the extra wavelengths can effectively act as a check upon the accuracy of the proposed algorithm. The development and testing of the "algorithm" used in the work described here is discussed in Chapter 7. The thesis also describes the development of a clinical spectrophotometer, Chapters 4 and 5, and various animal spectrophotometers and spectroscopic measurements of haemoglobin and the respiratory enzymes, Chapter 6.

1.6 CHAPTER SUMMARY

The clinical need for a non-invasive cerebral oxygenation monitoring system has been defined. Near infrared optical monitoring offers the possibility of bedside monitoring which NMR and PET cannot meet while cerebral impedance measurements are still in their infancy and their sensitivity needs much improvement.

Near infrared monitoring can measure blood oxygenation via haemoglobin in the red cell and tissue oxygenation via the enzymes of the respiratory chain. The sensitivity of the near infrared technique depends upon the concentration of these compounds in cerebral tissue. Typical in-vivo concentrations are 84 μM for haemoglobin and 1-5 μM for the cytochrome enzymes.

The rate at which the blood oxygenation changes is related to the transit time of a red blood cell through the head, in the adult this is approximately 6 seconds[34]. An ideal measuring system would therefore need a time resolution of approximately 1 second to observe all transient events, though adverse effects on the brain due to poor oxygenation may take much longer to happen.

CHAPTER 2

ABSORPTION OF LIGHT IN BRAIN TISSUE

The overall aim of this project is to measure quantified concentrations of absorbing compounds in brain tissue. In tissue, multiple scattering of light occurs, making this aim particularly difficult to achieve. However in order to tackle the problem it is important first to understand the factors which can give rise to errors in quantitative optical spectroscopy in non-scattering media. These are dealt with in Section 2.1 of this chapter.

Absorption by the chromophores in tissue is the parameter which we are attempting to measure and there are a number of chromophores which are known to be present in brain tissue. Specific absorption spectra are required for quantitative spectroscopy, and spectra of all of the significant chromophores found in brain tissue are given in this chapter.

2.1 LAWS OF ABSORPTION

Quantitative measurements in spectroscopy are based upon some very early observations and laws, the first of which was derived by Bouguer in 1729 and is often called the Lambert-Bouguer law. It states that successive layers of material of thickness dl absorb the same fraction dI/I of the light I incident upon them ie. $dI/I = \mu dl$ for a constant μ, usually

called the absorption coefficient. Hence

$$I = I_0 e^{-\mu l} \qquad 2\text{-}1$$

for an incident intensity I_0, transmitted intensity I and medium length l. This equation is also expressed in base 10 logarithms as

$$I = I_0 10^{-Kl} \qquad 2\text{-}2$$

The constant K is now known as the extinction coefficient. To introduce some further terms, taking the logarithm of the above equation

$$A = \lg\left(\frac{I_0}{I}\right) = \lg\left(\frac{1}{T}\right) = Kl \qquad [Units: OD] \qquad 2\text{-}3$$

Where T is called the transmittance (what an instrument measures) and A is the absorbance, a dimensionless quantity, normally termed the optical density (OD). There is still another alternative expression for Equation 2-1 above, which arises in situations when Maxwell's equations are used to describe the propagation of light, that is

$$I = I_0 e^{\left[-\frac{4\pi kl}{\lambda}\right]} \qquad 2\text{-}4$$

Here $N = n + ik$ is the complex refractive index, λ the wavelength of the radiation and k (the imaginary part of the refractive index) is called the absorption index.

Some years after Lambert, Beer[83] in 1852, derived a similar absorbance relationship dependent upon the number of absorbing molecules in a solution. It states that for an absorbing substance dissolved in a non-absorbing medium, the optical density, is proportional to the concentration of the solution.

Combing the two laws we arrive at what is commonly known as the Beer-Lambert law

$$A = \lg\left(\frac{I_0}{I}\right) = \alpha Cl \qquad 2\text{-}5$$

Here α is the extinction coefficient for unit absorber concentration and is known variously as the specific extinction coefficient, absorptivity or absorbency index. If the constant α in the

above equation is written as ε then this is normally taken to be the extinction coefficient for a solution of molar concentration and known as the molar extinction coefficient, molar absorptivity or molar absorbency index. In this case, the unit of length in the above equation is centimetres, hence ε has units molar^{-1} cm^{-1}. Despite these definitions it is common practise to use the symbol α for the specific millimolar extinction coefficient (Units: mMolar^{-1} cm^{-1}) and this convention is followed in the rest of this thesis.

Throughout this thesis the term **extinction coefficient** is used for base 10 logarithm units and **absorption coefficient** for natural logarithm units. **Attenuation** is simply the logarithmic ratio (base 10) of two intensities. In line with the common usage, the term absorption will generally be used in preference to the term extinction. It is only important to differentiate between the two when discussing quantified data.

In a solution containing a mixture of compounds, the extinction coefficient of each compound is additive, i.e.

$$\begin{aligned} A &= \left[K_1 + K_2 + \ldots K_n\right] l \\ &= \left[\alpha_1 C_1 + \alpha_2 C_2 + \ldots \alpha_n C_n\right] l \end{aligned} \qquad \text{2-6}$$

hence the attraction of this logarithmic scale of optical density. The typical application of the Beer-Lambert law is that A is experimentally measured (at a number of wavelengths), l is accurately known, $\alpha_1 \ldots \alpha_n$ have been found previously for the pure compounds and the requirement is to find $C_1 \ldots C_n$.

The first experimental verification of the Beer-Lambert law was achieved by Vierordt[84] in 1873. However there are certain situations in which additional effects limit the validity of the law.

2.1.1 Limitations of the Beer-Lambert law

The approach to data analysis in this thesis is to make as much use as possible of the standard and well used Beer-Lambert law and to examine the limitations of this law and thus to estimate the maximum errors such limitations may cause. Where possible, modifications to the Beer-Lambert law are made to enable more accurate quantification of concentration measurements. There are some generally well known problems in quantitative spectroscopy (so well known they can be easily forgotten) and those applicable to this work are covered

in the following sections. For a good introduction to absorption spectroscopy see Lothian[85].

2.1.1.1 *Finite bandwidth effects*

The Beer-Lambert law is valid for monochromatic light sources only. In practise this is impossible to achieve. All light sources for example lasers, spectral line sources and monochromators have a finite bandwidth. The measured transmission is thus given by

$$\tilde{T}=\frac{\int_{\lambda_1}^{\lambda_2} I(\lambda)S(\lambda)10^{-A(\lambda)}d\lambda}{\int_{\lambda_1}^{\lambda_2} I(\lambda)S(\lambda)d\lambda} \qquad 2\text{-}7$$

and the measured absorbance is

$$\tilde{A}=\lg\frac{1}{\tilde{T}} \qquad 2\text{-}8$$

Where $I(\lambda)$ and $S(\lambda)$ are the wavelength dependent light input and detector sensitivity respectively. $A(\lambda)$ is the monochromatic absorbance. The above equation shows that for measurements in a waveband λ_1 to λ_2 under conditions where $A(\lambda)$ is not constant, the source and detector wavelength dependencies will also have an effect. Normally the most important effect is that $A(\lambda)$ is varying over λ_1 to λ_2. For measurements made in a region where $A(\lambda)$ is varying, for example around a spectral peak or on a slope, the resulting effect is the same. The measured attenuation, say $\tilde{A}$, is less than the theoretically expected value for the mean of $A(\lambda)$, say $\bar{A}$, between λ_1 to λ_2. The degree of error very much depends upon the exact nature of $A(\lambda)$ over the region λ_1 to λ_2, but as an example, consider the case of $A(\lambda)$ being a simple linear slope through λ_1, λ_2 resulting from absorption by a single compound, as shown in Figure 2.1. $I(\lambda)$, $S(\lambda)$ are considered flat for this example through λ_1, λ_2.

The magnitude of the error $(\bar{A}-\tilde{A})$ in this case can be expressed in a form independent of both $\bar{A}$ and $\Delta\lambda$. Mathematically it is purely a function of ΔA (where ΔA is the true attenuation difference between $\Delta\lambda=\lambda_2-\lambda_1$):

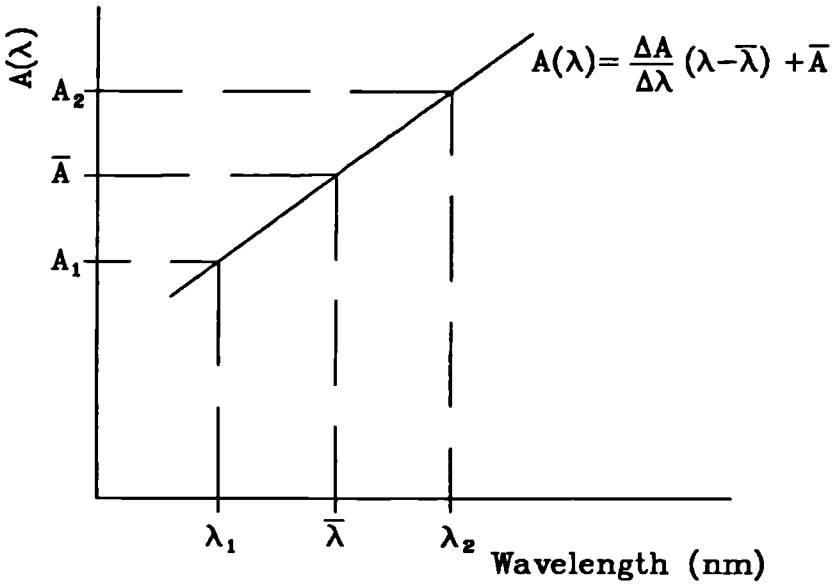

Figure 2.1 An example spectrum used to illustrate the non-linearities which arise in a spectroscopy system of finite bandwidth.

$$(\bar{A}-\tilde{A})=\lg\left\{\frac{\sinh\left[\ln(10)\frac{\Delta A}{2}\right]}{\ln(10)\frac{\Delta A}{2}}\right\} \qquad 2\text{-}9$$

This error can be seen graphically in Figure 2.2, indicating that the attenuation difference between the ends of the measuring bandwidth must be less than 0.1 OD for absolute errors to be less than 0.001 OD.

Similar calculations have been made for special cases such as Gaussian shaped absorption bands and monochromators of finite slit width[86], and correction factors for the errors have been derived. In general though, the experimenter should check his own experimental conditions for $I(\lambda)$, $S(\lambda)$ and $A(\lambda)$ to find the effect of finite bandwidth.

2.1.1.2 *Effect of stray radiation*

This is typically described for a monochromator system where wavelengths other than the band selected by the monochromator slits reach the detector. Qualitatively the effect of stray radiation is to flatten any absorption peak, as do many of the other effects described in this section. Quantitatively, the effective absorbance difference asymptotes to a value equal to the amount of stray radiation e.g. 1% stray radiation will asymptote to a 2 OD absorbance

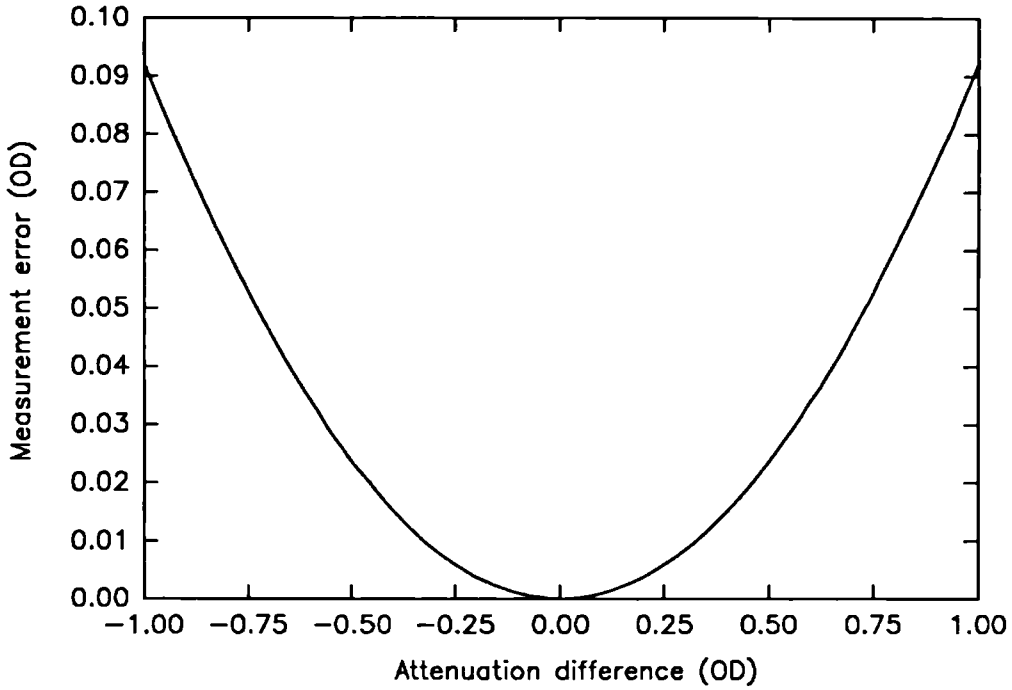

Figure 2.2 Calculated measurement error in a spectroscopy system with a finite bandwidth and a flat spectral response, measuring the optical spectrum in Figure 2.1, see text for details.

difference. The manner in which the measurement approaches the asymptote depends on the individual experimental conditions and particularly the absorption spectrum of the sample being studied. If stray radiation from a monochromator is a particular problem then a double or triple monochromator can be used to eradicate the problem.

Of greater significance is an effect which manifests itself in a similar manner but the cause of which is very different. Any light which manages to get from source to detector without going through the sample under study will produce a similar effect. For example when measuring light attenuation across the head, if some of the light intensity from the input optical fibre "bounces" around the skull and into the detection fibre optic without going through the brain (say I_u, intensity unabsorbed) this will produce an error. The magnitude of this error, will depend on the intensity of light emerging from the brain (say I_e) for an given input intensity I_0.

Presume that the absorbance at time zero ($t = t_0$) is

$$A(0)=\lg\left(\frac{I_0}{I_e(0)+I_s}\right) \qquad \text{2-10}$$

Then some time later at time $t=t_n$ the tissue oxygenation and hence absorbance may have changed to

$$A(n)=\lg\left(\frac{I_0}{I_e(n)+I_s}\right) \qquad \text{2-11}$$

Giving a measured absorbance change from t_0 to t_n of

$$\Delta A(n)=A(n)-A(0)=\lg\left(\frac{1+\frac{I_e(0)}{I_s}}{1+\frac{I_e(n)}{I_s}}\right) \qquad \text{2-12}$$

The true change in attenuation ($\lg[I_e(0)/I_e(n)]$) is plotted against $\Delta A(n)$ in Figure 2.3(a) for three different ratios of $I_e(0)/I_s$ equal to 10000, 1000 and 100. The same data is plotted as a percentage error in Figure 2.3(b). This shows that the acceptable amount of stray light is dependent upon the maximum positive absorbance change observed. For example, stray radiation should be kept to less than approximately 1 part in 500 for attenuation changes up to 1 OD.

The same phenomena also occurs when there is an fixed offset voltage in the measuring equipment due to an incorrect setting of an electronic offset.

2.1.1.3 *Characteristics of the absorbing compound*

Unusual chemical or optical effects in some compounds can make the Beer-Lambert law invalid. There are some compounds which change their composition and hence specific absorption coefficient with concentration but this effect has not been observed for in-vivo compounds.

Potentially greater problems may arise from substances which exhibit dichroism, i.e. substances which have different absorption spectra for the two different polarisations of light.

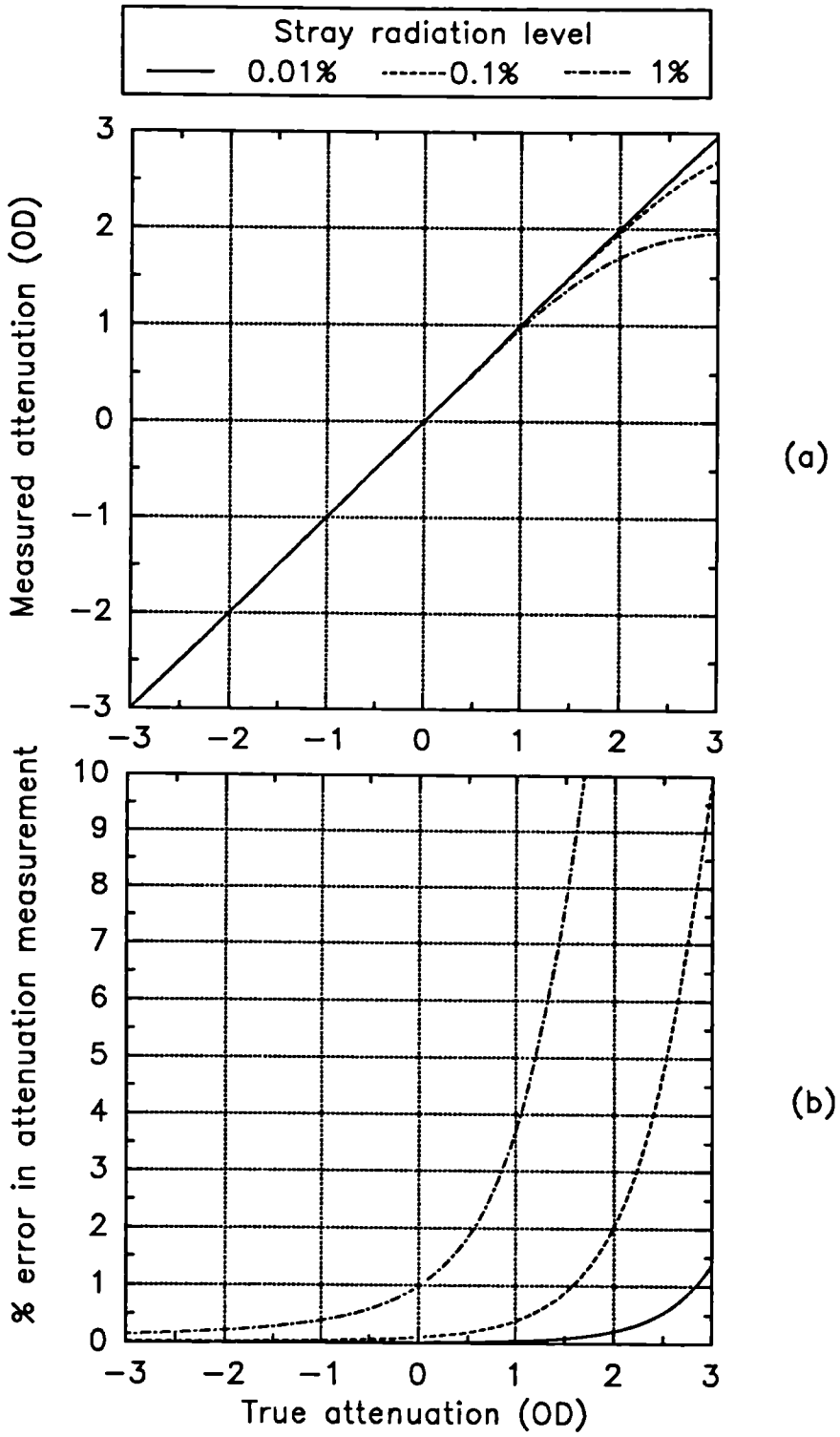

Figure 2.3 Effect of differing amounts of stray radiation upon attenuation measurements: (a) measured attenuation against true attenuation; (b) percentage error in measured attenuation versus the true attenuation.

As a result, dichroic compounds cannot be expected to follow the Beer-Lambert law for unpolarised light and this effect has been observed for the nucleic acids in cells[87]. Their concentration in tissue is however small and does not change rapidly with time, therefore this effect should not be a problem.

2.1.1.4 *Effect of absorbing packets*

Another situation which leads to deviations from the Beer-Lambert law is when the absorbing molecules are concentrated in packets and the packets are sparsely distributed through the solution. This situation occurs for example with chlorophyll in leaves, or visible spectroscopy of suspensions of red blood cells or bacteria. First of all consider the case where the packets are pure absorbers and cause no scattering. Deviation from the Beer-Lambert law arises because of the random distribution of these packets, and non linearities are most significant when the absorption loss per packet is high. Physically, "holes" arise in the suspension when the random distribution predicts few packets along certain lines through the container. Duysens[88] analyzed this situation for rectangular shaped vessels containing suspensions of cubical packets of absorber arranged randomly on a 3 dimensional rectangular grid. Using a simple probability theory for the distribution of the packets in the vessel he obtained the following relationships for the extinction coefficients of the suspension of packets (A_{sus}) and for the equivalent solution (A_{sol})

$$A_{sus}=-\frac{l}{d}\ln\left[1-q\left(1-T_p\right)\right] \qquad 2\text{-}13$$

$$A_{sol}=-\frac{l}{d}\ln T_p \qquad 2\text{-}14$$

Where l is the length of the optical cuvette, d the side length of the cubic packet of absorber, T_p ($0 \le Tp \le 1.0$) the transmission across two opposing faces of a single cubic packet and q ($0 \le q \le 1.0$) the packet density expressed as a fractional volume.

It is interesting to consider the ratio of the above equations and to look for the situation where $A_{sus}/A_{sol} \neq 1$ i.e. the Beer-Lambert law does not hold. It is instructive to introduce the quantity x defined by $T_p = 1 - x$ into the above equations. Then

$$\frac{A_{sus}}{A_{sol}} = \frac{\ln(1-qx)}{q\ln(1-x)} \qquad 2\text{-}15$$

Expanding as a series and dividing by qx gives

$$\frac{A_{sus}}{A_{sol}} = \frac{1+\frac{qx}{2}+\frac{(qx)^2}{3}+\ldots.+\frac{(qx)^n}{(n+1)}+\ldots.}{1+\frac{x}{2}+\frac{x^2}{3}+\ldots.+\frac{x^n}{(n+1)}+\ldots.} \qquad 2\text{-}16$$

So $A_{sus}/A_{sol} = 1$ for the cases where $x = 0$ at any value of q (non-absorbing particles) and for $q = 0$ or 1 for any value of x (none or solid particles). (Note that as $0 \le q \le 1$ then $0 \le A_{sus}/A_{sol} \le 1.0$.) We wish to examine the point where a non-linearity of magnitude ξ has occurred ie. $A_{sus}/A_{sol} = (1 - \xi)$. Simplifying Equation 2-16 above for small x, and neglecting all terms in the expansion greater than o(x), then for an error less than ξ

$$1-\xi < \frac{1+\frac{qx}{2}}{1+\frac{x}{2}} \qquad 2\text{-}17$$

Substituting $x = 1 - T_p$ and rearranging

$$T_p > \frac{1-3\xi-q}{1-\xi-q} \qquad 2\text{-}18$$

Rearranging the above to get the optical density loss per packet we find

$$\lg\left(\frac{1}{T_p}\right) < \lg\left(\frac{1-\xi-q}{1-3\xi-q}\right) \qquad 2\text{-}19$$

and for q, x small,

$$\lg\left(\frac{1}{T_p}\right) < 0.87\xi$$

Taking an example of $\xi = 0.01$, $q < 0.03$, i.e. a non-linearity of 1% and a particle density less than 3%, then the optical density loss per cell must be less than 0.0087.

To estimate the effect for the red blood cell, a bold approximation is made. The red blood cell is taken to be a 4.4 μm sided cube (volume 85 fl) with an internal haemoglobin concentration of 34 g/dl, molecular weight 64450. Using the Beer-Lambert law, then for a single red blood cell to have an absorbance of less than 0.0087, its specific extinction coefficient must be less than 3.75 $mM^{-1}cm^{-1}$. Comparing this with the spectrum of haemoglobin, Figure 2.7, we find that this effect is not a problem in the near infrared region of the spectrum ($\lambda > 650$ nm) for oxy and deoxy-haemoglobin. A problem will however arise in the visible region causing errors of around 5-10% and very large errors will be observed in the Soret bands near 400 nm.

The theoretical analysis used here is based on the assumption of non-scattering packets. Under normal conditions in saline suspensions, red blood cells and bacteria scatter light significantly and this theory no longer strictly applies. By suspending red blood cells in an albumin solution of identical refractive index to that of the internal haemoglobin solution, Barer[89] was able to study red blood cells under non-scattering conditions. He found that for the index matched red blood cell suspension, significant absorption differences were only observed between the clarified suspension of red blood cells and a pure solution in the Soret band. The visible bands were identical but the NIR region was not examined.

From these results we can conclude, that in the near infrared part of the optical spectrum this effect can also be ignored. Also in the real world where red blood cells are not in index matched media, other effects of multiple scattering will greatly dominate over this potential source of non-linearity.

Is it worth adding that Duysen[88] also included a section on a similar derivation for particles of arbitrary shape. Although this may seem more suitable to the red blood cell, the assumptions made are rather broad ranging. The simple cubic model approximation used here shows that extinction coefficients in the near infrared region are much smaller than those which lead to significant non-linearity from this phenomena.

2.2 ABSORBING COMPOUNDS IN BRAIN TISSUE

The purpose of this section is to provide a set of spectra for the chromophores present in brain tissue. Interest lies only in those compounds which are known to exist at reasonable concentrations and which absorb in the near infrared region of the optical spectrum.

Additionally, it is important to differentiate between those chromophores which exist in brain tissue at fixed or at variable concentrations and those whose absorbance is oxygenation dependent. Those chromophores present at fixed concentration (e.g. water) merely add to the overall attenuation of the brain tissue while those which change with tissue oxygenation (e.g. haemoglobin) provide useful information on changes in brain oxygenation.

2.2.1 Water

The average water content of neonatal brain is 90%[90] and 80%[26] for adult brain. This obviously implies that any absorption band of water will have a large optical effect. Data on the extinction coefficient spectrum of water is available[91] over a wide wavelength range from 200 nm to 200 μm which includes the visible/near infrared region of interest. Part of this data is reproduced in Figure 2.4.

The extinction coefficient for water shows a general trend of increasing with increasing wavelength. Due to the many factors involved, it is difficult to set an exact wavelength beyond which transmission through a number of centimetres of tissue is possible. An attenuation due to water, greater than 1 optical density per centimetre would be difficult to cope with, and this suggests a long wavelength cutoff for transmission spectroscopy of tissue at 1.35 μm. At longer wavelengths, the extinction coefficient does not drop below 2 cm^{-1} until the centimetre wavelengths.

At wavelengths shorter than 600 nm, and down to the ultraviolet region, the extinction coefficient of water is less than 0.001 cm^{-1} and is thus negligible. Between 600 nm to 1.35 μm water should have a measurable absorption (depending upon the number of centimetres of brain tissue illuminated and the spectrophotometer signal/noise ratio). At wavelengths between 900 nm and 1.35 μm the losses will be so high that measurements across only a few centimetres of tissue would be possible.

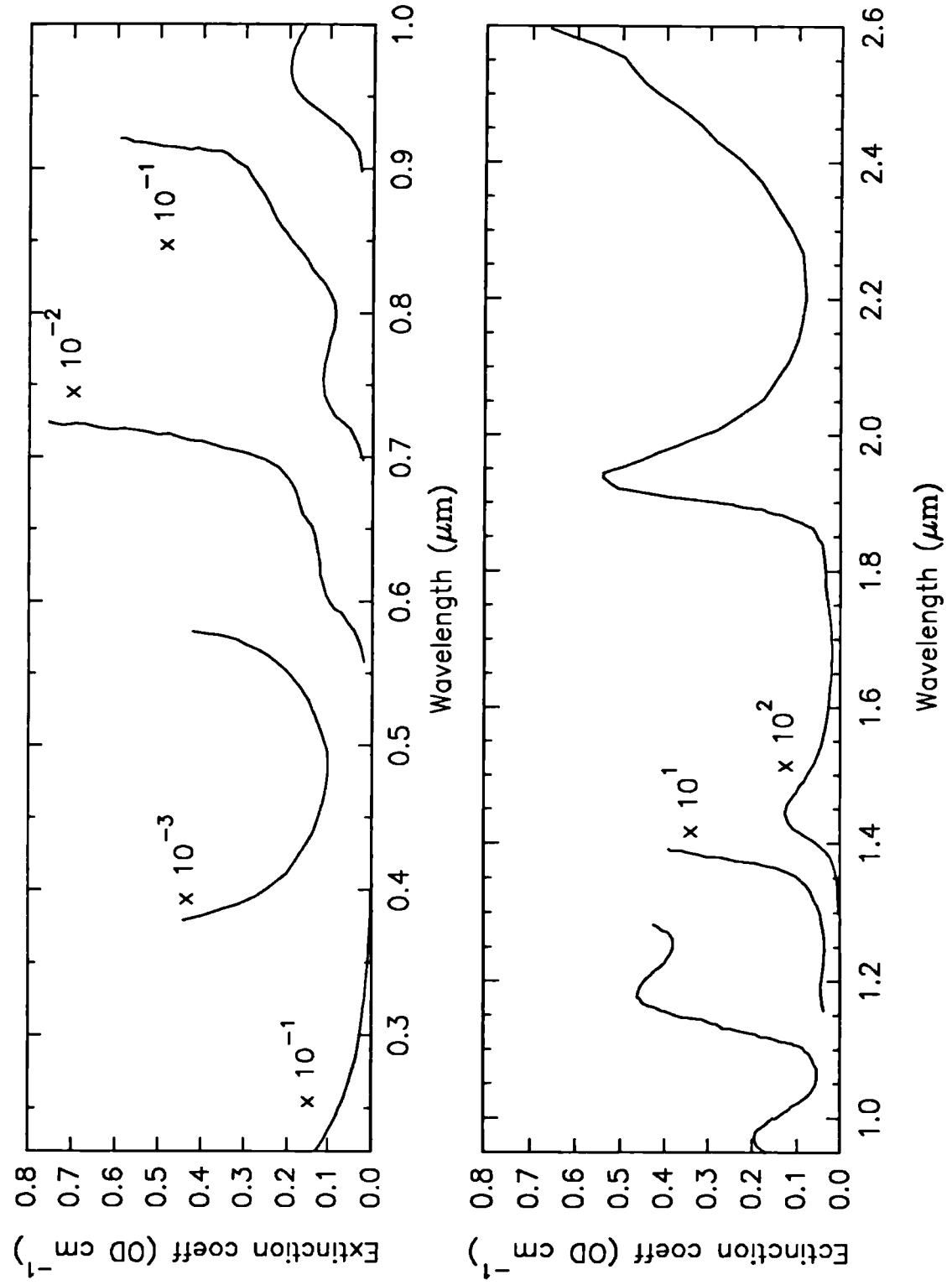

Figure 2.4 Extinction coefficients of distilled water from 0.2 to 2.6 μm (note the use of y-axis multiplying factors). The data is transformed from that of Hale and Querry[91].

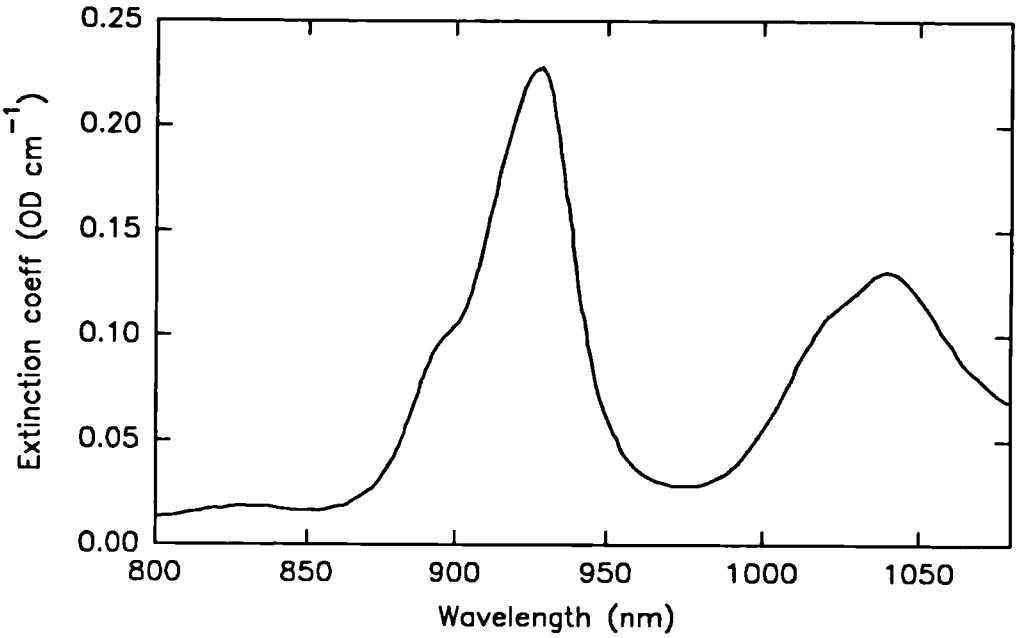

Figure 2.5 Extinction coefficients of pure lipid (pork fat), data taken from Conway et al.[92]

2.2.2 Lipids

Lipids constitute about 5% of the total wet weight of a newborn infant's brain. This percentage increases to 8% of the grey matter and 17% of the white matter in adulthood[90]. Although no one appears to have studied the lipid content of brain tissue optically, near infrared spectroscopy has been used to study the lipid content of muscle in order to determine lean body mass[92]. The extinction coefficient spectrum of lipid in muscle matched the spectra measured for pure pork fat shown in Figure 2.5.

The figure shows that the extinction coefficient for lipid is similar in magnitude to that of water. Lipid will not significantly add to the overall extinction coefficient of brain tissue as it is only present at approximately one tenth the proportion compared to water, although it may still be possible to detect its presence optically in the near infrared.

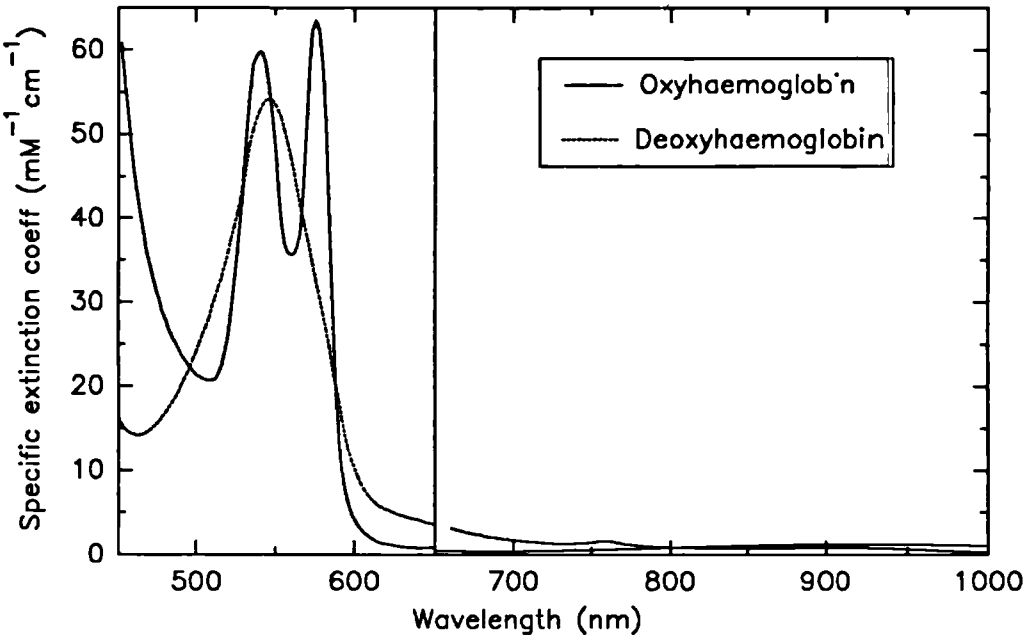

Figure 2.6 Visible and near infrared specific extinction coefficient spectra of haemoglobin (M.W. 64500) in its oxygenated and deoxygenated forms. Data taken from Horecker[62].

2.2.3 Haemoglobin

An introduction to haemoglobin was given in Section 1.2.2. Here, the optical absorption properties of this chromophore are described. In order to look at the absorbing properties of haemoglobin alone, the red cell is ruptured and the cell membranes removed leaving a clear red liquid.

The extinction spectra of haemoglobin solutions, in the two most common forms oxygenated haemoglobin (HbO_2) and deoxygenated haemoglobin (Hb), are shown in Figure 2.6. Note the difference in magnitude between the extinction coefficients in the visible and the near infrared parts of the spectrum. Another feature to note are the isobestic points where the specific extinction coefficients of these two forms of haemoglobin are the same.

Absorption by haemoglobin sets the shortest usable wavelength when transmitting light through centimetres of tissue. In Section 1.2.4 the concentration of haemoglobin in brain tissue

was calculated to be approximately 84 μMolar (MW 64450)†. A practical short wavelength limit must exist beyond which light cannot be detected across many centimetres of tissue at this haemoglobin concentration. A reasonable estimate for this limit is approximately 1.0 optical density per centimetre of tissue which correlates with a short wavelength cutoff of near 600 nm. Hence taking this information together with the water absorption data, the maximum usable wavelength range for optical spectroscopic measurements across many centimetres of tissue is probably 600 nm to 1350 nm††.

Section 1.2.2 also indicated that a number of other naturally occurring forms of haemoglobin can be found in the blood stream, namely carboxyhaemoglobin (HbCO), haemiglobin (Hi) (also called methaemoglobin) and sulfhaemoglobin (SHb). Typical in-vivo concentrations of HbCO are up to 10% of the total haemoglobin content (especially in smokers), Hi are between 0.5 and 2.5%, while normal blood does not contain any SHb. Abnormally high in-vivo levels of Hi can result from some hereditary diseases, and after ingesting certain nitrogen containing compounds, and as the result of taking certain drugs such as the sulphonamides[93].

Near infrared extinction spectra of Hb, HbO_2 and HbCO taken from Horecker[62], Hi taken from van Assendelft[94] and SHb taken from Zwart[95] are shown in Figure 2.7. The near infrared optical effect of HbCO in-vivo is negligible because of its low specific extinction coefficient. Of greater potential importance is the effect of haemiglobin which can be seen to have a significant NIR specific extinction coefficient. Its absorption spectrum is a strong function of pH, having different spectra in its acid and alkaline forms. This could cause numerous problems but fortunately, physiological pH is maintained within a narrow range and Hi concentration is controlled by an enzyme system in the red blood cell at a reasonably low proportion of the total haemoglobin concentration. If its presence is ignored, a small error results which may reach approximately 1% of the total haemoglobin signal. Sulfhaemoglobin is a more difficult compound to characterise. Published spectra only extend to 760 nm in the near infrared where it has a large extinction coefficient. Its effect is ignored here, but could

---

† Note that in this thesis molarities of haemoglobin are calculated per functional unit, in other words for a molecular weight of 64450 and 4 haem groups. This differs from most spectroscopic data for which molarities and specific molar extinction coefficients are quoted per haem group or a molecular weight of 16112.5.

†† As a result of increased attenuation due to the effects of multiple scattering in tissue, the short wavelength limit is in practise reduced to approximately 650 nm.

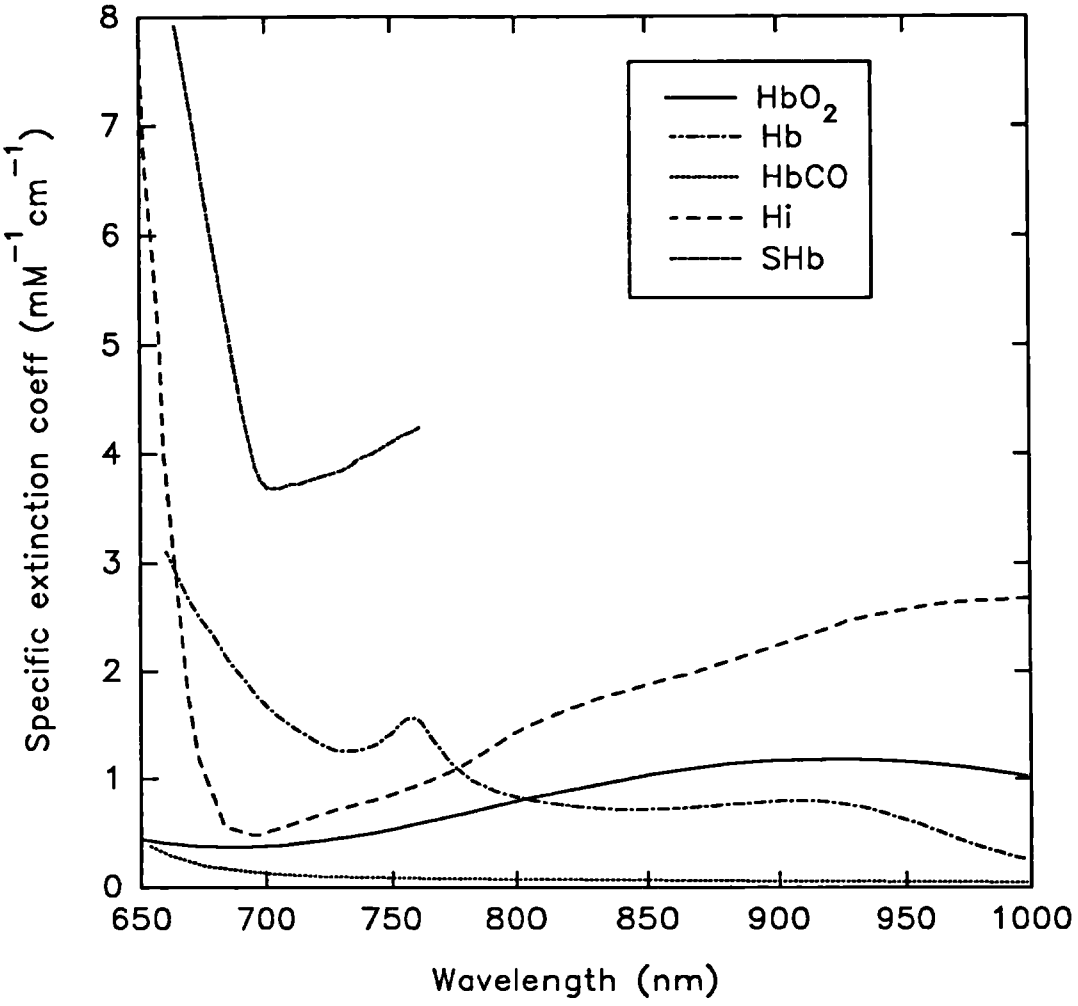

Figure 2.7 Near infrared specific extinction coefficient spectra of haemoglobin derivatives occurring in-vivo (M.W. 64450). Data taken from the literature, (see text for details).

be significant if certain rarely used drugs are given.

The only other haemoglobin compound of interest is the one formed with CN^-, haemiglobincyanide (HiCN). It is the most stable of all the haemoglobin compounds, CN^- will replace all the other ligands of haemoglobin and haemiglobin to produce HiCN (but not SHb). As a result it is most often used as a standard for determination of total haemoglobin concentration by converting any haemoglobin compound to this form and measuring its absorption at 540 nm[96].

Measurements have also been made on the NIR spectra of adult (HbA) and fetal (HbF) haemoglobin[97]. These indicate no perceptible differences in the NIR spectra between 650 nm

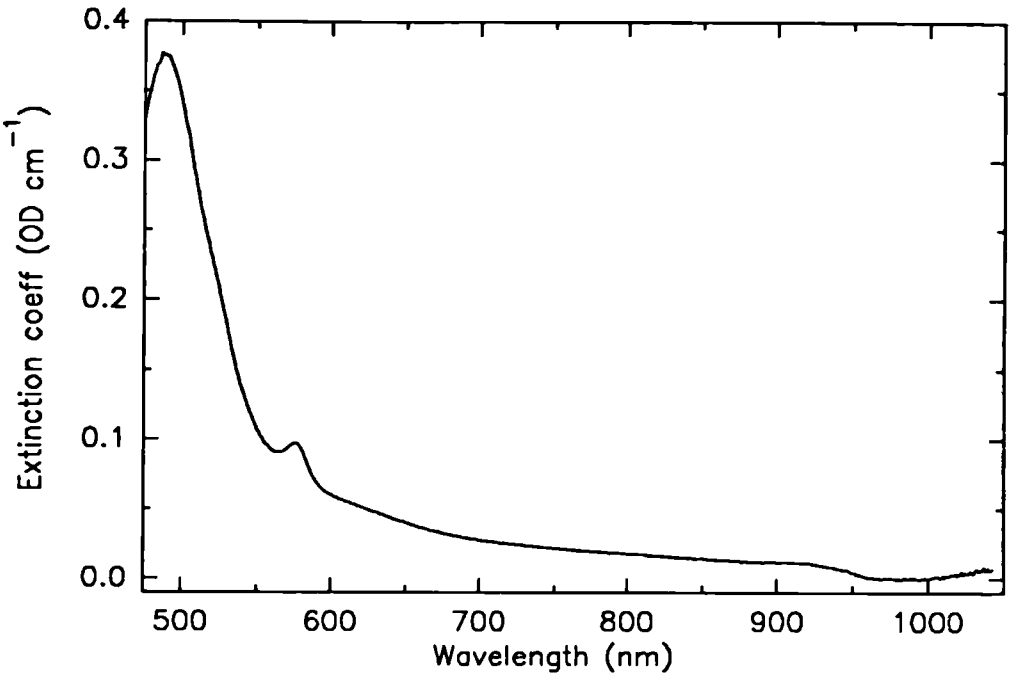

Figure 2.8 Extinction coefficients of undiluted, filtered, freshly extracted plasma from a healthy adult volunteer.

and 1000 nm. Therefore calibration spectra from adult blood are perfectly acceptable for use on newborn infant data.

2.2.4 The absorption spectrum of plasma

Plasma contains a number of absorbing chromophores, appearing as a straw colour to the naked eye. The colouration is mainly due to the presence of bilirubin, present at concentration levels ranging from 2.5 to 19 mg/dl in cases of severe jaundice. The extinction spectrum of bilirubin is well known in the visible region[98], a broad absorption band between 400 and 500 nm. Little information is available on absorption in the near infrared, therefore the extinction coefficient spectrum of plasma, freshly taken from a healthy adult volunteer, was measured and can be seen in Figure 2.8.

The presence of bilirubin dominates the spectrum. The attenuation in the near infrared region is probably caused by molecular scattering (some degree of scattering was still visible despite filtering the plasma with a 0.1 μm filter). The somewhat unusual feature of a "negative absorption peak" at 975 nm is caused by the lower water concentration in the plasma sample

compared to the reference cuvette which contained distilled water. The conclusion that can be reached is that plasma can be treated as a colourless liquid when compared to the absorption of haemoglobin in blood at normal concentrations.

The other fluid in the brain is cerebrospinal fluid (CSF) which fills the ventricles. It also can be treated as a clear fluid, since it contains much lower amounts of protein than plasma.

2.2.5 Cytochrome c oxidase and the other respiratory enzymes

The respiratory enzymes, and cytochrome c oxidase especially, are complex enzymes whose properties are still the subject of much investigation and discussion. Some of the more precise details of their optical characteristics are inconsistent and a detailed discussion on this matter follows later in Section 6.2.1. At this point, simple descriptions of the basic optical spectra of the relevant respiratory chain enzymes are given, see Figure 2.9. Data for the cytochrome c oxidase spectra is from Brunori et al.[99] and cytochrome b and c is from Wilson[100].

The figure shows that cytochrome c oxidase is of special interest, compared to the other members of the respiratory chain. In its oxidised form it has an unusually strong extinction coefficient in the near infrared region (3.5 $mM^{-1}cm^{-1}$ per functional unit), over a broad absorption band centred at 830 nm (FWHM 200 nm). This absorption band disappears when the enzyme is reduced.

Section 1.2.3 also indicated the presence in tissue of NAD, flavoenzymes (FMN, FAD), coenzyme Q and non-haem iron-sulphur proteins, some in much greater concentrations than the cytochrome enzymes. NAD has a strong absorption at 340 nm when hydrogenated, the flavoenzymes have visible absorption peaks in the 400 to 500 nm region, and CoQ has a strong UV absorption at 275 nm when oxidised. None of these substances have known red or infrared absorptions[101]. The non-haem iron-sulphur proteins of NADH dehydrogenase also appear to have a negligible extinction coefficient near 600 nm[102].

The non-haem iron sulphur proteins of succinate dehydrogenase do have a measurable extinction coefficient in the red (600-700 nm) region which may extend further into the near infrared[103], unfortunately near infrared spectra have not been published. The extinction coefficient of the succinate dehydrogenase complex is approximately 1.6 $(mM\ FAD)^{-1}cm^{-1}$ at 700 nm. Cytochrome c oxidase is still likely to dominate over this complex as it is present

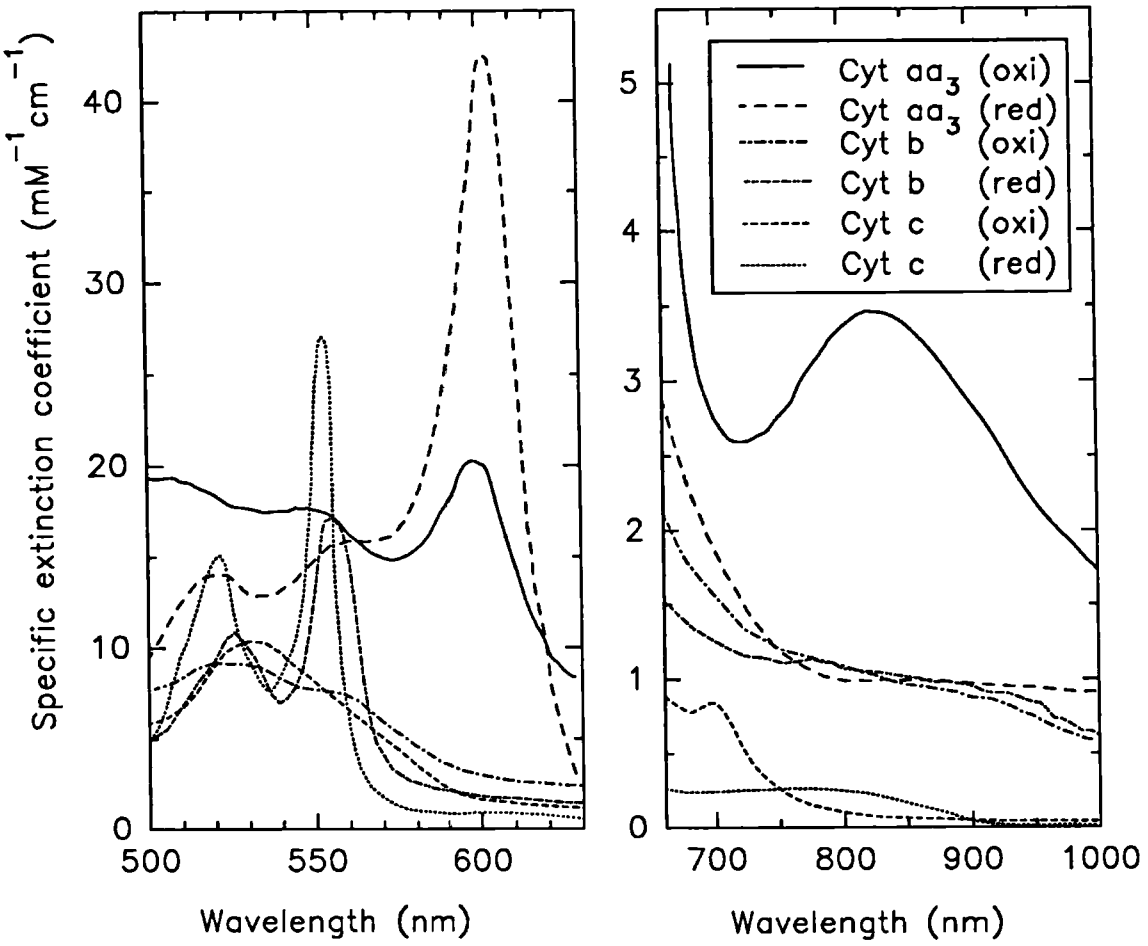

Figure 2.9 Specific extinction coefficient spectra of cytochrome c oxidase, cytochrome b_5 and c (per functional unit). Data taken from the literature, see text for details.

at 3 times the concentration. Additionally, components of the respiratory chain near the electron source are likely to be almost fully reduced under normal working conditions while the components at the oxygen end of the chain will be almost fully oxidised. Thus in anoxia, the largest redox change will arise from the cytochrome c oxidase end of the chain. This means that the non-haem iron-sulphur protein that could have the greatest influence is the one associated with cytochrome c_1. This iron-sulphur protein also has a measurable red but an unknown NIR extinction coefficient[104].

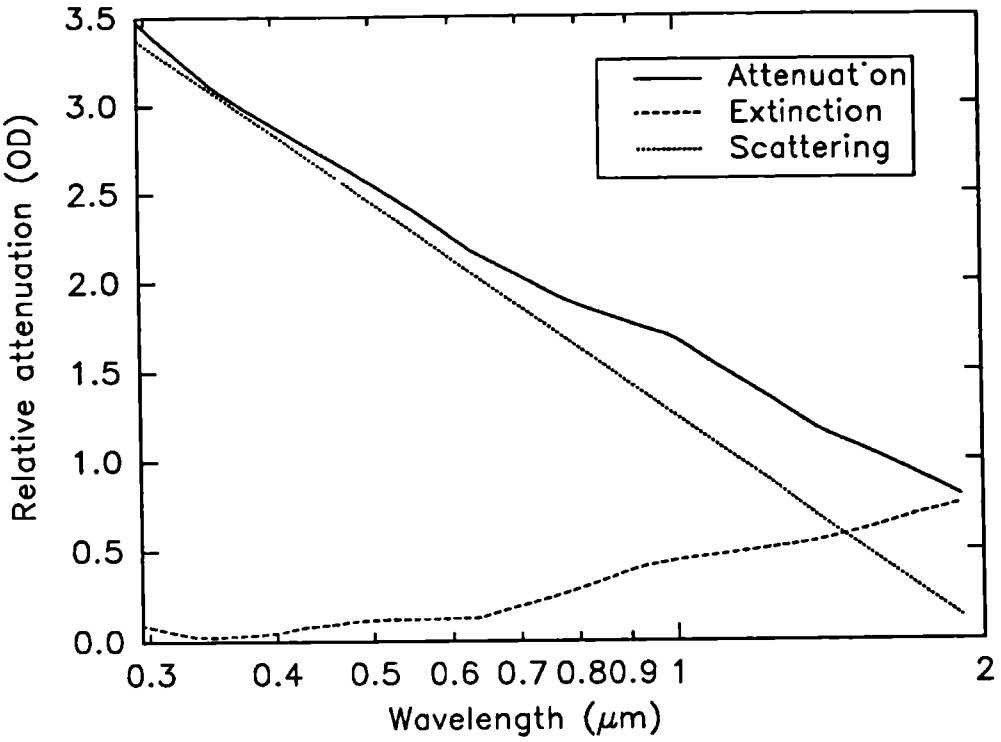

Figure 2.10 Attenuation by melanin is considered to be made up of both Rayleigh scattering ($1/\lambda^4$) and extinction. Data taken from Wolbarsht[105].

2.2.6 Absorption by surface tissues

In a non-invasive monitoring system, before light reaches the brain, it must first pass through the soft tissue and skull. The optics of human skin have been reviewed by Anderson[98]. The stratum corneum (10 μm thick) does not contain any absorbing compounds with a significant visible or NIR extinction coefficient.

The next layer down, the epidermis is 100 μm thick and contains melanin whose attenuation spectrum is shown in Figure 2.10, plotted on a log-log scale reproduced from Wolbarsht[105]. Melanin's attenuation is considered to consist of a component due to Rayleigh scattering at UV/visible wavelengths and a true absorption component at NIR wavelengths, as shown. Melanin has a significant optical effect on skin reflectance. The reflectance of negroid skin is approximately 50% of the reflectance of caucasian skin in the 600-1000 nm region[98]. This suggests that transmission through the skin may also be reduced by the same degree. However, attenuation by melanin only increases the sensitivity required of the instrument. Since its absorption is constant and oxygenation independent, it does not produce

attenuation changes which are time dependent.

The dermis has no additional near infrared absorbers other than those mentioned previously i.e. haemoglobin, cytochrome c oxidase and the respiratory enzymes. In neonatal pigs, the skin has a blood volume comparable to that in brain tissue at 2.5 ml/100 g[39] (density 1.09 $kg\,m^{-3}$)[26]. The skull also contains the same near infrared absorbers found in blood and has a blood volume of 5.5 ml/100 g[39] (density 1.92 kgm^{-1})[26].

Overall the skin and the skull provide a barrier which must be penetrated before light enters the brain tissues. This barrier reduces light intensity by approximately 1.5 OD[106]. The attenuation caused by this region will also change with oxygenation (due to the presence of haemoglobin), the magnitude of this effect being proportional to its thickness and chromophore concentration. It is recommended that the thickness of brain tissue illuminated is therefore much greater than that of the surface tissues.

In the surface layers of the head a small amount of muscle can sometimes be found, the thickness of which is location dependent. Muscle additionally contains the chromophore myoglobin. Fortunately the absorption spectrum of myoglobin in the near infrared is indistinguishable from that of haemoglobin. Further, myoglobin has a very low P_{50} for oxygen (1 kPa). This means that it is not as sensitive to tissue oxygenation until the oxygen delivery from haemoglobin is significantly reduced[107].

CHAPTER 3

LIGHT SCATTERING IN BRAIN TISSUE

The greatest problem in quantitative spectroscopy of tissue is deviation from the Beer-Lambert law as a result of light scattering. The effect of scattering is to increase the observed attenuation over and above the value expected due to the tissue absorption coefficient. It will be shown that this effect is non-linear, and results in the flattening of absorption peaks.

In this chapter the following points regarding the scattering characteristics of brain tissue are addressed:

i) Are they independent of gestational age i.e. brain development?

ii) Are they independent of tissue oxygenation?

iii) Are they independent of wavelength?

An answer of yes to all three points above would enable a far simpler approach to be made to the treatment of scattering effects in quantitative spectroscopy.

The approach of this chapter is to briefly examine the physics of light scattering, followed by a discussion on its origins in tissue and then a survey of some publications on both theoretical and experimental aspects of multiple scattering in tissue. Finally, there is an examination of how the problems of scattering can be handled in spectroscopic measurements.

3.1 THE SCATTERING OF LIGHT BY SINGLE PARTICLES

Light scattering occurs to some degree in all media except for a vacuum and is dependent upon the heterogeneity of the media down to the atomic level. Matter is composed of electrical charges which are set in oscillatory motion by the electromagnetic wave travelling through them. These accelerated charges then re-radiate secondary radiation in all directions forming secondary scattered waves. The final radiation pattern results from the addition of the incident and secondary waves. An alternative to re-radiation of the incident wave is its conversion to thermal energy i.e. absorption.

In optically dense media such as solids, liquids and gases, the intermolecular separation is of the order 0.2 - 0.3 nm for solids and liquids and 3 nm for gases at standard temperature and pressure. In practise, dealing with effects on this scale is an unnecessary complication and the use of refractive index (as a complex number, $N = n + ik$) can describe the bulk properties of a particle with dimensions as small as 10 nm. The value of the refractive index is still a function of the properties of the individual molecules within the particle, dependent upon the power of the oscillation set up in each molecule by the electromagnetic wave (i.e. the polarisability) and upon the number of molecules per unit volume.

Scattering of light also explains effects occurring in optically clear media, such as the reflected and refracted beams which occur at air/glass interfaces. The individual scattered waves add up to produce the reflected beam and the refracted beam travelling at a velocity of c/n, where c is the velocity of light in vacuo. In addition to these main beams, whose directions are given by Snell's law, light is also very weakly scattered in all other directions. The origins of this effect are local density fluctuations within an otherwise statistically homogeneous medium.

The magnitude of scattering and absorption by a medium are dependent upon the real (n) and imaginary parts (k) of the refractive index respectively and are a function of wavelength. n and k are related by integral equations given in Kramers-Kronig analysis[108], but for a more general description of anomalous dispersion refer to Jenkins[109]. Chapter 2 showed that the magnitude of the NIR absorption bands are very small. When absorption coefficients are small the real part of the refractive index (n) varies gently with wavelength

as $1/\lambda^2$, as described by Cauchy's equation[109].

In tissue, the major concern is scattering of light by particles. This differs from the case of scattering by local density fluctuations in that it relies upon the effect of an aggregation of molecules in an otherwise homogeneous medium. In tissue, the particles are complex in shape and can be either homogeneous or heterogeneous. A qualitative feel for the scattering effect of a single particle can be obtained by breaking the particle up into many small dipoles. The resultant scattered wave is then obtained by the addition of the secondary waves from each of the dipoles. If the particle dimensions are small, less than a quarter wavelength, the angular scattering pattern is essentially uniform in direction as the phase differences between the secondary waves are small. For larger and larger particles, there is an increasing possibility of constructive and destructive interference and hence more lobes on the angular scattering pattern. In practise, this simplified approach is only applicable in restricted circumstances where the effect of individual dipoles upon each other can be neglected.

3.1.1 Single particle scattering theory

Single particle scattering theory covers situations where either only a single particle is being considered, or where the number density of multiple particles is so low that the opportunity for a scattered wave from one particle to be re-scattered by another is negligible. This situation does not occur in tissue at optical frequencies, but a knowledge of the individual scattering properties of particles in tissue is an important prerequisite of discussing multiple scattering theories.

The starting point for single scattering theory is the interaction of plane monochromatic electromagnetic waves with particles of differing shapes, sizes and refractive indices as described by Maxwell's equations. More general solutions for mixtures of particles and multiple wavelengths of light can be obtained through the superposition of individual solutions.

The characteristics of scattering by a single spherical particle, depends upon its radius (a) compared to the wavelength of the illuminating light (λ/N) together with the relative refractive index ratio of the particle compared with its surrounding medium (N_1/N). Where N_1 and N are the complex refractive indices of the particle and surrounding medium respectively.

Obtaining the solution for a particle of arbitrary refractive index and arbitrary shape and size is generally only possible numerically[110], but there are a number of areas where

exact and approximate solutions are possible analytically and these provide a useful insight into how the properties of the particle affect its scattering characteristics. An excellent treatise on this subject is available[111] and will be referred to on numerous occasions later. The following three sections summarise theories which can be applied in certain situations and which provide solutions for the scattered far field as a function of angle for a given incoming plane electromagnetic wave.

3.1.1.1 *Mie theory for spherical particles*

This theory, developed in 1908 by Gustav Mie, is an exact solution in spherical coordinates of Maxwell's equations for the interaction of plane electromagnetic waves and spherical particles. It takes into account the complex refractive index ratio (m) (i.e. both absorption and scattering).

$$m=\frac{N_1}{N}=\frac{n_1+ik_1}{n+ik} \qquad 3\text{-}1$$

The solution is not particularly neat and tidy, producing an infinite series expansions of Bessel and modified Bessel functions, in which the speed of convergence depends largely on the particle size parameter (x).

$$x=\frac{2\pi Na}{\lambda} \qquad 3\text{-}2$$

Computer programs are available to generate tables of Mie scattered intensity as a function of azimuthal angle for an arbitrary particle radius and wavelength. One such FORTRAN program is given in Bohren & Huffman[111].

Mie theory is valid for all sizes of spherical particles, and at very small sizes (less than 1/4 wavelength), the Mie theory expansion simplifies to only a few terms and approximates to the equations of Rayleigh for non-absorbing particles (see Section 3.1.1.2).

A typical angular scattering function is shown in Figure 3.1(c) for a particle of refractive index 1.40, radius 2.76 μm in water (refractive index, 1.33), illuminated at 800 nm. Note the forward biased nature of the scattered light at this radius to wavelength ratio. Also their are many peaks and troughs in the side lobe response which would be clearer if plotted on a logarithmic scale. With increasing particle diameter, the mainly forward scattered nature

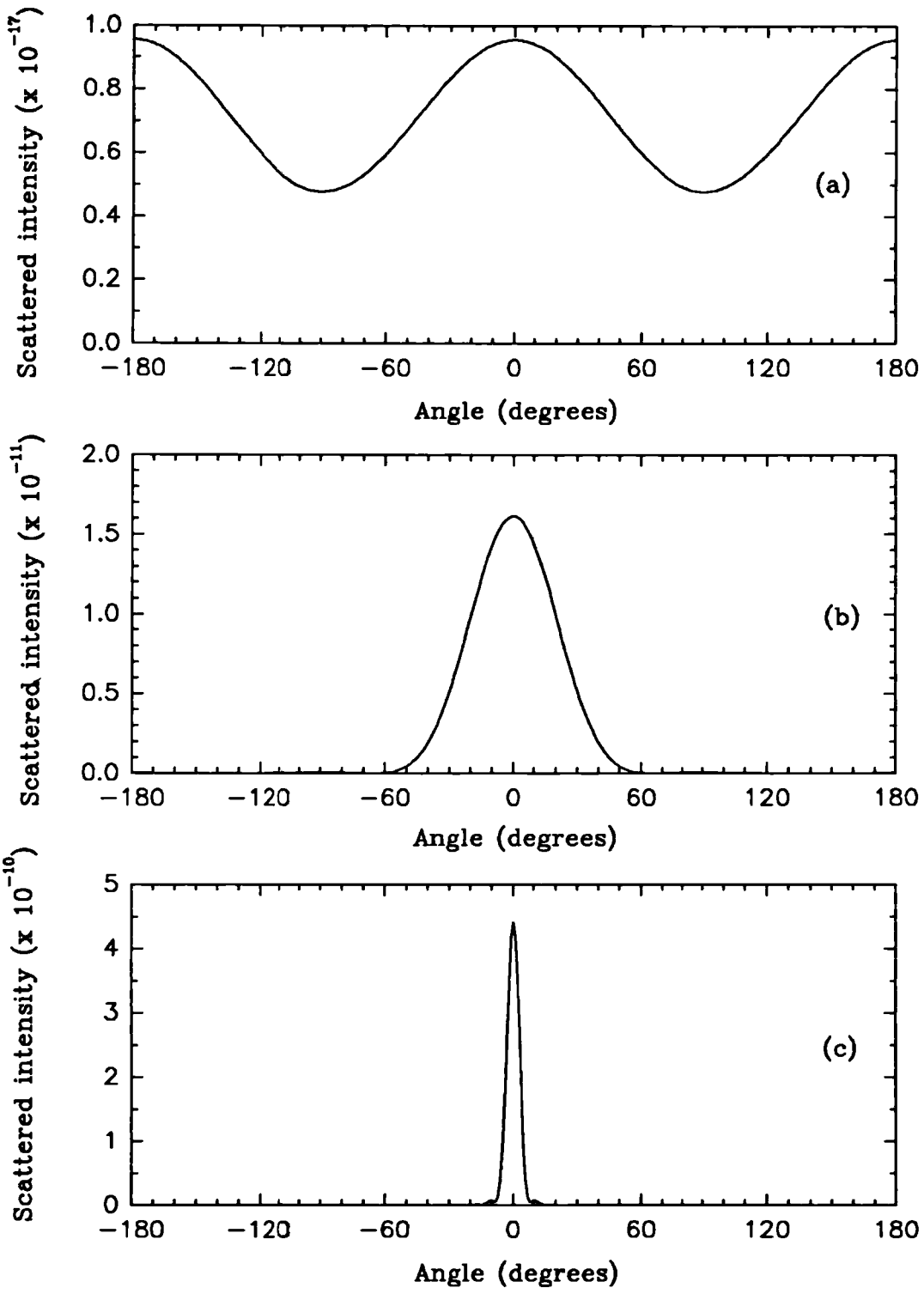

Figure 3.1 Angular scattering functions for single particles: (a) Rayleigh scattering ($a<<\lambda$); (b) RGD scattering (Equation 3-5); (c) Mie scattering ($a>\lambda$).

of the light becomes even more pronounced.

Despite the exact solution (theoretically) possible with this theory, it has several disadvantages. Firstly, as with all numerical solutions, it is very difficult to visualise the interaction effects of the electromagnetic wave and the spherical particle. Additionally, in real life, all particles are not spherical and as a result Mie theory can no longer strictly be applied, although solutions for the cases of scattering by the spheroid, ellipsoid and infinite cylinder have been found.

3.1.1.2 *Rayleigh theory for small particles*

Rayleigh derived his theory of light scattering from a intuitive feeling for the effects of the particle volume V, the distance of the particle from the point of observation r, the wavelength λ, the velocity of light c, and the relative refractive index m. The conclusion he reached was that the scattered intensity I_s is

$$I_s \alpha \frac{V^2}{r^2 \lambda^4} \qquad 3\text{-}3$$

Mie theory can also be used to derive a similar relationship to the above. As the particles are so small only a few terms in the series expansion are necessary to give an accurate result. For unpolarised light with an irradiance I_i, the scattered irradiance I_s is

$$\frac{I_s}{I_i} = \frac{8\pi^4 N a^6}{\lambda^4 r^2} \left[\frac{m^2 - 1}{m^2 + 2}\right]^2 (1 + \cos^2\theta) \qquad 3\text{-}4$$

The term $1 + \cos^2\theta$ represents polarisation effects, the contributions from incident light perpendicular and parallel to the scattering plane. The angular distribution of unpolarised scattered light for such a particle is shown in Figure 3.1(a) to be nearly isotropic. The wavelength dependence of scattering is very pronounced, $1/\lambda^4$, with an additional small effect caused by the wavelength dependence of refractive index.

3.1.1.3 *Rayleigh-Gans-Debye (RGD) theory for tenuous scatterers*

The major advantage of RGD theory is that it can be used to solve the scattering function for arbitrary shaped particles, which in general are not possible to solve. The theory can only be applied in the case of tenuous (soft) scatterers which have a similar refractive index to that of the surrounding medium. Necessary conditions for the RGD theory are the two inequalities

$$\begin{aligned} |m-1| &\ll 1 \\ \frac{2\pi}{\lambda} d\,|m-1| &\ll 1 \end{aligned} \qquad \text{3-5}$$

where d is the largest dimension of the particle. These express the requirement that the relative refractive index of the particle must be near unity and that the phase change across the particle must be very similar to that which would occur in the same distance of the surrounding medium. In practise this means no appreciable reflection at the particle/medium boundary and a field pattern inside the particle that is nearly identical to that in the outside medium.

When the above inequalities are satisfied, the solution is a modified version of the Rayleigh scattering function:

$$\frac{I_s}{I_i} = \frac{4\pi^2 V^2}{\lambda^4 r^2} [\,m-1]^{\,2} f^2(\theta,\phi)\,(1+\cos^2\theta) \qquad \text{3-6}$$

Here V is the particle volume and $f(\theta,\phi)$ is the form factor (θ and ϕ are angles in spherical coordinates) and is given by

$$f(\theta,\phi) = \frac{1}{V}\int_V e^{i\delta} dv \qquad \text{3-7}$$

Where δ, the phase difference, is integrated over the particle volume and is given by $\delta = k\mathbf{R}\cdot(\hat{\mathbf{e}}_s - \hat{\mathbf{e}}_r)$. $\mathbf{R}$ is a vector from an arbitrary origin to the volume dv, $\hat{\mathbf{e}}_s$ is a unit vector in the direction of the incident light, $\hat{\mathbf{e}}_r$ is the unit vector in the direction θ,ϕ.

The equation above is similar to the result of Rayleigh, with a modifying angular function dependent upon the shape of the particle. Calculation of the form factor can be performed by numerical integration in the case of complex shapes or analytically for simple

geometries. In the case of the homogeneous sphere of radius a, refractive index N, the form factor becomes

$$f(\theta)=\frac{3}{u^3}(\sin u - u\cos u) \qquad 3\text{-}8$$

where

$$u=\frac{4\pi Na}{\lambda}\sin\frac{\theta}{2} \qquad 3\text{-}9$$

A plot of the scattering function for a spherical particle of radius 0.4 μm, refractive index 1.40, in water (n=1.33) at 800 nm is shown in Figure 3.1(b). Note that the maximum scattered intensity is less than that of the larger particle in Figure 3.1(c), but scattered light occurs over a much larger spread of angles.

3.1.2 Measurements and terminology in scattering

The practical effect of scattering and absorption by a particle upon a parallel beam of light propagating in the z direction, is that the beam intensity in the z direction is reduced. Light which is absorbed is dissipated as thermal energy, light which is scattered keeps its intensity but travels in another direction. (Processes such as fluorescence, and inelastic scattering are considered insignificant effects at the wavelengths used here).

A method of quantifying these effects is to place the particle between a perfectly collimated light beam and a detector of infinitely narrow acceptance angle. In the single scattering particle literature, the reduction in light intensity caused by a particle is called the "extinction cross section" and has the dimensions of area. The magnitude of this parameter is the equivalent area of a hypothetical, non-scattering, perfectly absorbing disk in the path between source and detector. Extinction cross section C_{ext} is made up of the sum of the absorption and scattering cross sections, C_{abs} and C_{sca} respectively.

$$C_{ext}=C_{abs}+C_{sca} \qquad 3\text{-}10$$

Note that the use of **extinction** in the extinction cross section of single particle scattering (to mean the sum of absorption and scattering) is very different from its usage in spectroscopy

in the rest of this thesis where it represents pure absorption on a log (base 10) scale. A rather unfortunate clash of terminology between the absorption spectroscopists and the atmospheric monitoring community.

The above quantity is expressed for a single particle and can be normalised to produce a number of other useful coefficients. The ratio of the extinction cross section to the particle area produced by projecting the particle onto the detector is called the extinction efficiency Q_{ext}. If the particle is a hypothetical non-scattering black disk Q_{ext} would be unity. In practice it can take on values both larger or smaller than one, depending upon the degree of interference between the scattered and unscattered waves. Although extinction efficiency is commonly used, a more physically meaningful parameter is the extinction cross section divided by the particle volume or mass. These parameters are called the volume extinction coefficient α_{vext} and mass extinction coefficient α_{mext} respectively. Just as before, the extinction parameter is made up of the absorption and scattering parameters.

Figure 3.2(a) shows α_{vext} plotted against particle radius for a wavelength of 0.8 μm and relative refractive index 1.042. The figure illustrates which sizes of particle produce the most effective scattering for a fixed volume of scattering material. Rayleigh ($1/\lambda^4$) type scattering can be seen for particle dimensions less than $\lambda/4$, α_{vext} increasing as a^3. The volume scattering efficiency reaches a peak and then starts to decrease at particle sizes very much larger than the wavelength.

The values of Q_{ext}, C_{ext} and α_{vext} indicate the total amount of light scattered off-axis. We have seen in Figure 3.1, that the distribution of this scattered light is a very different function of angle for different particle sizes. The angular distribution becomes very important when discussing multiple scattering, as particles which scatter light isotropically are effectively much more efficient scatterers than those which scatter light in a forward peaked manner. A convenient mathematical expression to describe the forward biased nature of the angular scattering function, $p(\theta)$, is the so-called asymmetry parameter g

$$g = \int_{4\pi} p \cos\theta \, d\Omega \qquad \text{3-11}$$

where integration is over the full solid angle, and the angular scattering function is normalised such that $\int_0^{2\pi} p(\theta) \sin(\theta) d\theta = 1$.

The effective scattering efficiencies for multiple scattering (as used in diffusion theory,

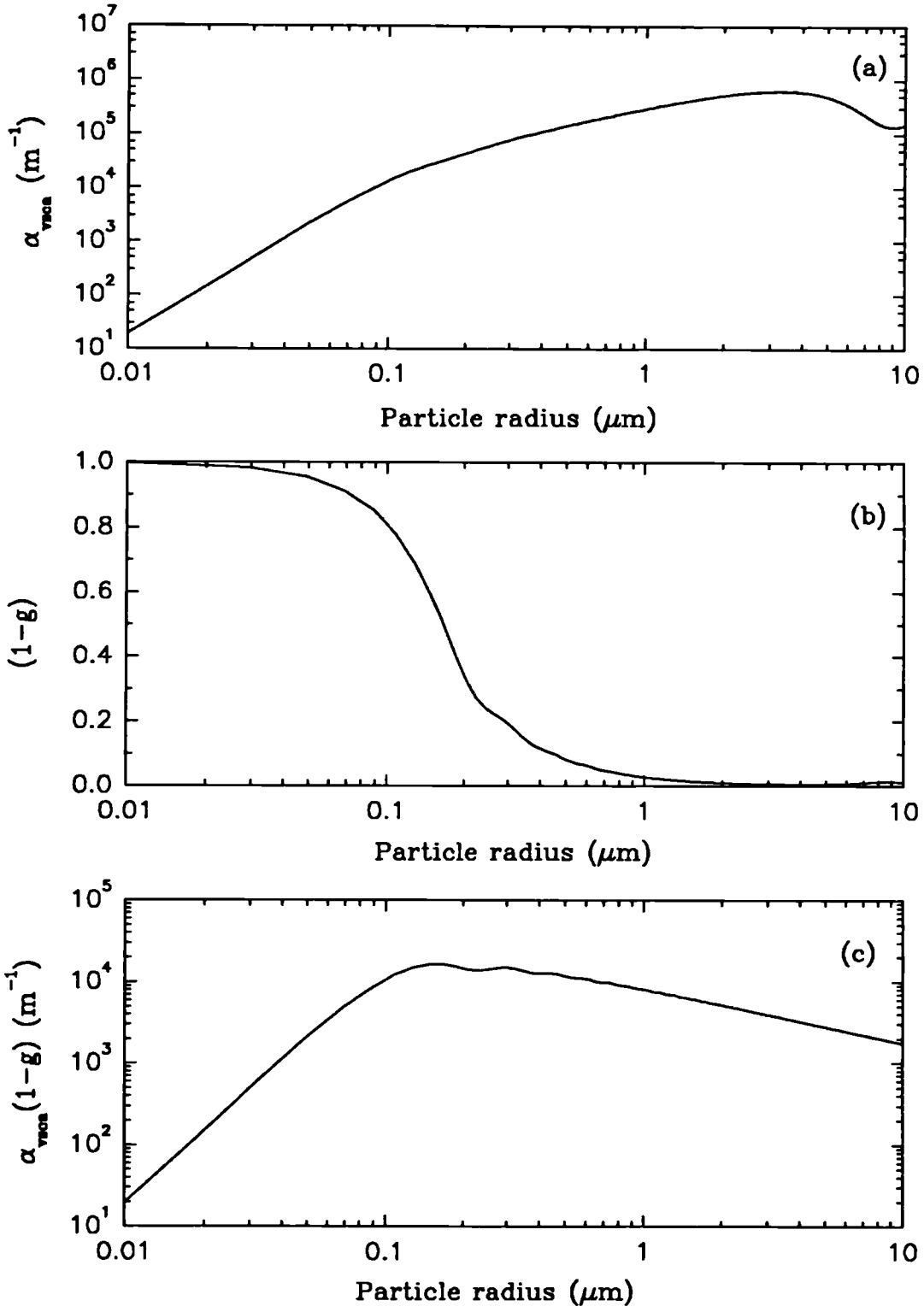

Figure 3.2 Mie theory simulation of particle scattering, N_1/N=1.042, λ=800 nm: (a) volume scattering efficiency; (b) (1−g) and (c) the product of (a) and (b).

see Section 3.3) are then expressed as $Q_{ext}(1-g)$, $C_{ext}(1-g)$ and $\alpha_{vext}(1-g)$. Figure 3.2(b) shows a plot of $(1-g)$ as a function of particle size and Figure 3.2(c) the effective multiple scattering efficiency $\alpha_{vext}(1-g)$. For the above conditions, Figure 3.2(a) shows that the size of particle for the most volume efficient single particle scattering is 3.275 μm (maximum α_{vext}). However, in the case of multiple scattering when $(1-g)$ is taken into account, then Figure 3.2(c) shows that the most volume efficient particle size is 0.166 μm. This indicates the importance of the angular scattering function in determining the overall multiple scattering characteristics.

Practical measurement of these coefficients require the use of collimated light sources and detectors. The degree of collimation is important, as the amount of scattered light which falls within the acceptance cone of the system acts as a source of error and reduces the measured extinction cross section to some degree. This is a particular problem in the measurement of particles with a high degree of forward scatter. Other practical problems exist in obtaining the scattered intensity near 180° i.e. at reflected angles. Note that in the limit as $x \to \infty$, then Mie theory predicts that $Q_{ext} \to 2$ (see Figure 3.3). In other words a very large particle scatters an amount of light equal to twice its projected area, although for practical reasons it may be impossible to see all the scattered light because it will be very close to the forward direction.

3.2 THE ORIGINS OF SCATTERING IN LIVING TISSUE

Variations in refractive index are responsible for the scattering of light in tissue. The previous section on the theory of light scattering describes how particle size and refractive index affect the magnitude and nature of light scattering. The next stage in this discussion is to examine the various cells and cell constituents in brain tissue in terms of their refractive index, their physical dimensions and number density as it is these factors which determine the scattering power of the various "particles" (e.g. nucleus, red blood cell, mitochondrion etc.). This will provide some insight into which tissue components are the dominant scattering centres, and will help to answer the questions raised at the beginning of this chapter.

Scattering by tissue and red blood cells will be examined separately. The red blood

cell is obviously responsible for scattering to some degree, but typically occupies only 1.5% of brain volume. The majority of scattering is far more likely to come from interfaces such as those between cells and the extracellular space or the cellular cytoplasm and cellular organelles.

3.2.1 The relationship between the refractive index of biological material and its density.

Two optical microscope techniques are capable of directly measuring refractive index at cellular and sub-cellular dimensions. These are quantitative phase contrast microscopy and interference microscopy. Both produce microscope images in which contrast is dependent upon the phase shift produced by the object.

Indirect measurements of refractive index are also possible through measurements of the density of various cellular compartments. Most cellular constituents are dissolved or finely dispersed in water and increase the refractive index of the solution by approximately the same incremental amount per unit weight[112]. This relationship applies to proteins, lipoproteins and amino acids which form the greatest part of the cellular solids, see Table 3.i[112]. The refractive index of the tissue fluid n_c is approximately

$$n_c = n_w + 0.0018 C_s \qquad \text{3-12}$$

where n_w is the refractive index of water, C_s is the cell solids concentration expressed as a percentage of weight of solids divided by the volume of solution (% w/v) and 0.0018 is the average refraction increment for dissolved cellular solids. To obtain a more accurate value, the separate effects of the various proteins, amino acids, salts etc should be taken into account using their specific concentration and specific refraction increments. For a pure protein solution, the above can also be calculated from knowledge of the water concentration C_w using

$$C_w = 100 - 0.75 C_s \qquad \text{3-13}$$

One gram of dry protein occupies a volume of 0.75 ml. Care must be taken when using this relationship in situations where protein does not greatly dominate over other cellular solids.

Table 3.i Specific refractive index increments for biological materials used in the calculation of refractive index, Equation 3-12. The data is from Ross[112].

Substance	Wavelength (nm)	Specific refraction increment
Bovine plasma albumin		0.001820
Human serum albumin		0.001862
Bovine serum albumin	578	0.001870
Human serum globulin	white light	0.001830
Human fibrinogen	589	0.001880
Human haemoglobin	white light	0.001942
Beta-lipoprotein (containing more than 75% lipid by weight)		0.001700
Amino acids		
Glycine		0.001790
Alanine		0.001710
Valine		0.001750
Trytophane		0.002500
Nucleic acids		
DNA	436	0.001810
RNA	436	0.001940
Carbohydrates		
Sucrose		0.001410
Glucose		0.001430
Starch		0.001330
Inorganic salts (in dilute solution)		
NaCl		0.001630
KCl		0.001150
CaCl2		0.002100

3.2.2 Scattering by red blood cells

The technique of refractive index matching using phase contrast microscopy has been extensively applied to red blood cells. Their internal structure is not observable under an optical microscope as they contain no organelles, and only have a very fine fibrous composition. They are by far the easiest of the body constituents to examine as they are only

slightly polydisperse (in normal pathological situations) and are regular in shape.

The major problem is to find an immersion medium whose refractive index can be varied, which does penetrate the cells and with a tonicity that does not make the cells shrink or swell. Bovine plasma albumin, fraction V is a suitable protein, dissolving readily in water up to 50% w/v to produce a maximum refractive index of 1.424. It does not appear to enter the cell but in practise, balancing tonicity is a difficult problem and measurement errors do arise.

Results have been reported by Ross[112] who quoted a mean red blood cell refractive index of 1.385 giving a haemoglobin concentration of 27% ± 1.5% as opposed to 34% ± 2% when measured by standard haemoglobinometry. The standard deviation of 2% appears to be a natural variation between red blood cells. The underestimation of the true haemoglobin concentration using this method was later shown to be caused by water movements due to incorrect tonicity of the immersion fluid[113]. Correcting haemodilution in the red cell gives the in-vivo refractive index of the red blood cell as 1.40 ± 0.01.

The refractive index of plasma can be calculated from its protein concentration which is 5.5 g/100 ml[114], this gives a value of 1.343. The haemoglobin solution inside the red cell is separated from the plasma by cell membranes, approximately 8 nm thick. As the dry weight of the cell membrane is only 3% of the total dry weight of a red cell, its effect on red cell scattering can be ignored in any approximate calculation.

Having obtained a value for the refractive index, the next parameters required are the dimensions of the red blood cell. The cell is a biconcave disk of equatorial diameter 8.5 μm, minimum thickness 1 μm at its centre, and a maximum thickness of 2.4 μm having a volume of 88 fl[115]. None of the three theories already described for single particle scattering are really capable of solving the scattered light distribution of the red blood cell because of its irregular shape. It is theoretically too large for Rayleigh-Gans theory to apply. However, Chadwick and Chang[116] have examined the red blood cell using Rayleigh-Gans theory and found an adequate fit between experimental and calculated data for the scattering phase function. This is a very interesting result which confirms the highly forward peaked nature of light scattered from large low refractile particles and provides a surprisingly good agreement between experiment and theory considering that the Rayleigh-Gans criteria, Equation 3-5, are not met. It may be that the criteria are not too important when calculating the scattering phase function, that is the **relative** scattering intensity as a function of angle, but large errors may occur when calculating the **absolute** scattered intensity.

It would be useful to assess the scattering characteristics of a red cell as a function of wavelength. Rayleigh-Gans theory does not appear to be suitable, as it predicts a variation of $1/\lambda^4$, which is highly unlikely for such large particles. Instead the red cells are treated as volume equivalent spheres, Steinke and Shepherd[117] have shown that this approximation is valid for determining the total scattering cross section C_{sca} of red blood cells. Mie theory did however underestimate $(1-g)$ by a factor of 2-3 compared to experimental measurements†. This makes relative plots of $(1-g)$ against red blood size or wavelength somewhat approximate.

The Mie theory simulation is performed for an internal refractive index of 1.40, an external refractive index of 1.343, and a red cell volume 88 fl (a sphere of radius 2.76 μm), ignoring absorption by the red cell. The plots in Figure 3.3 were produced for this equivalent "red blood cell sphere" using Mie theory and the FORTRAN program in Bohren and Huffman[111]. The plot of $Q_{sca}(1-g)$ shows the wavelength dependence on scattering is much less ($1/\lambda^{0.32}$) than Rayleigh scattering in the region 500 to 1000 nm. In fact, $Q_{sca}(1-g)$ decreases by only 13% in changing wavelength from 650 to 1000 nm.

3.2.3 Scattering by brain tissue

In transmitting light through several centimetres of brain tissue in vivo, the number, type and size of neurones will vary dramatically, especially between white and grey matter. It is therefore an enormous task to examine the scattering properties of each type of neurone and to average all the effects.

A simple motor neurone with a myelinated nerve fibre is shown in Figure 3.4[118]. It shows the general features to be found in most nerve cells although the size and position of the cell body; the length, diameter and number of nerve fibres (axon and dendrites) can vary considerably. In general, the grey matter is almost exclusively cell bodies whereas the white matter is almost exclusively nerve fibres. Neurones however are not the largest population of cells in the brain, they are outnumbered 10 to 1 by the smaller glial cells: microglia which are scavenger cells; oligodendroglia involved in myelin formation (Schwann cells); and astrocytes that mechanically bond neurons to blood vessels and constitute part of the blood brain barrier.

---

† The reason for the overestimation of g by Mie theory is that randomly orientated non-spherical particles have a less forward peaked angular scattering function than their volume equivalent spheres.

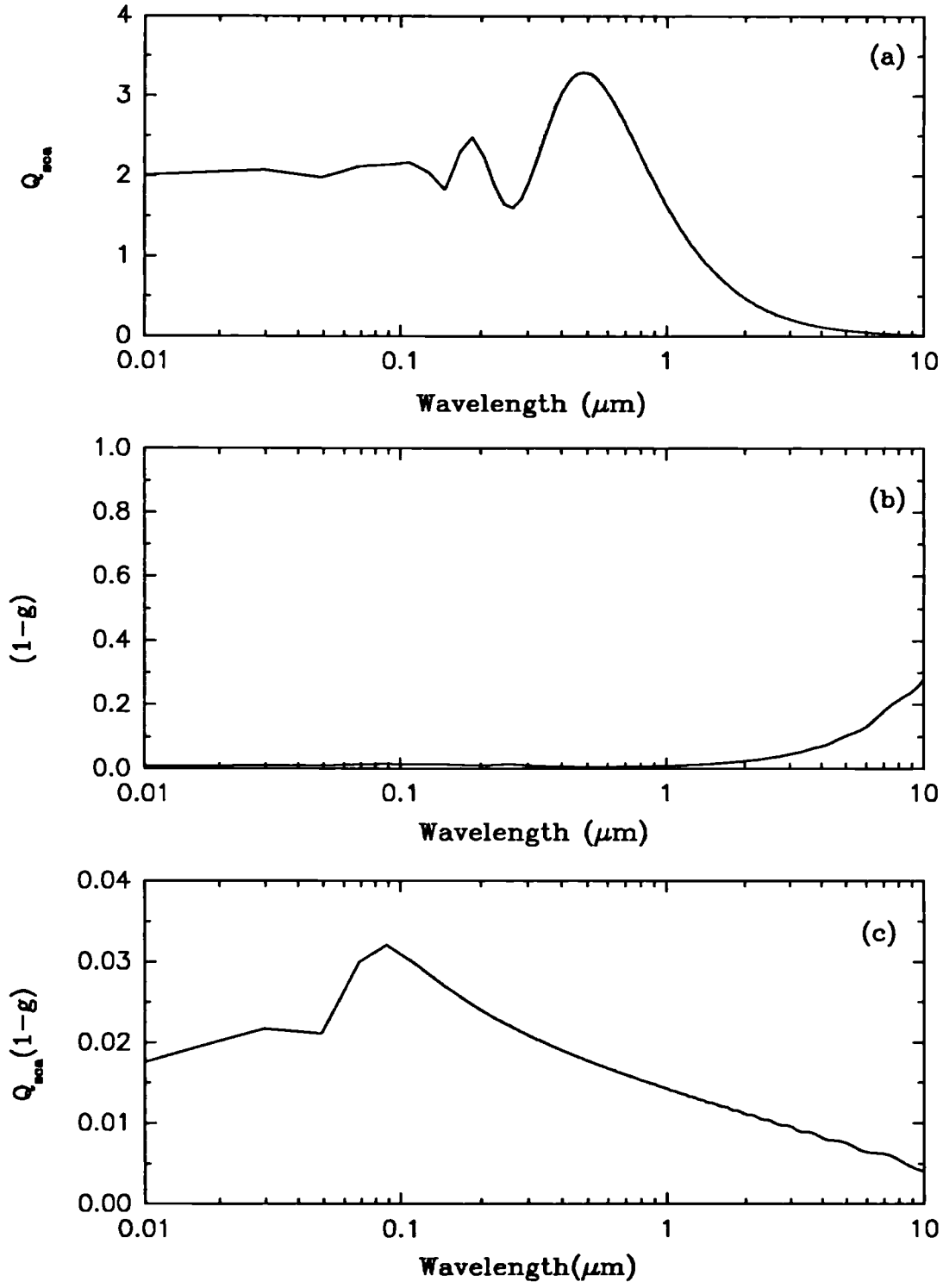

Figure 3.3 Mie theory simulation of scattering by a red blood cell as a function of wavelength: (a) scattering efficiency; (b) (1-*g*) and (c) the product of (a) and (b).

Table 3.ii The water, lipid and protein content of the human brain at various stages of development, data is taken from Brant[120].

	Water (mg/g)	Lipid (mg/g)	Protein (mg/g)
Fetus, 20 weeks			
Cortex	900	16.9	83
White Matter	900	24.0	76
Newborn			
Cortex	900	27.3	73
White Matter	900	36.6	63
Adult			
Cortex	850	45.3	105
White Matter	710	166.0	124

Scattering by brain tissue is also highly age related. In Section 3.2.1 it was shown that the refracting power of a cell inclusion was proportional to its solid contents, expressed as %w/v. The total protein and lipid fraction of the developing rat brain has been shown to increase from birth to adulthood by a factor of two[119], suggesting a comparable increase in scattering. Similar changes take place in the lipid and protein content of human brain, values for white matter and cortex are given in Table 3.ii, the data is taken from Brant[120]. The largest growth dependent changes are in lipid concentration, particularly in the white matter, where lipid increases its concentration nearly 7 fold. In the pre-term and newborn human infant, the protein content is larger than the lipid content, this changes with the onset of myelination when the rate of growth in lipid concentration exceeds that of protein.

3.2.3.1 *Static scattering effects*

Within any cell, see Figure 3.4, there is a standard collection of organelles and inclusions[121], all of which have the possibility of being scattering sites:

i) There is one **Nucleus** per cell, consisting of three distinct areas. Chromatin, which is rich in DNA, but is not present in significant quantities in the nucleus of neurons. The

nucleolus, a highly refractile body, which is a honeycomb structure formed by thread like nucleolonema (made up of ≈15 nm granules) and the dense structureless pars amorpha. Chromatin and the nucleolus are suspended in nuclear sap within a nuclear envelope, two 7.5 nm thick lipoprotein membranes separated by 40-70 nm.

ii) There are 2 **Centrioles** per cell. These are hollow cylinders 300-500 nm long by 150 nm in diameter forming a tubular structure within a dense wall.

iii) **Mitochondria** are cellular organelles forming long slender structures 2-3 μm long with a volume of ≈1 μm^3. They are enclosed by a bilayer membrane (each 7 nm thick with 8 nm gap), the inner membrane being folded into cristae. The number density of mitochondria per cell depend upon the energy turnover of the tissue and hence they are particularly plentiful in brain, heart muscle and brown adipose tissue. They are refractile bodies which contain variable numbers of coarse dense granules between 30 and 50 nm in diameter.

iv) The **Golgi Apparatus** was discovered by phase contrast microscopy are hence must have a different refractive index to the cytosol. It has a rather variable structure of membrane bound flat saccules 15 nm thick laid in parallel layers with ≈20-30 nm gaps between them. Their function is a secretory and excretory one.

v) The **Endoplasmic Reticulum** is a structure of anastomosing tubules 40-70 nm in diameter which also has a secretory function. It is differentiated into the rough and smooth endoplasmic reticulum, the rough containing dense granular particles (ribosomes). **Nissl bodies**, are a typical feature surrounding the nuclei of neuronal cells, consisting of stacks of endoplasmic reticulum and ribosomes.

vi) **Lysosomes** were discovered and defined as a mitochondrial subfraction of cell suspensions containing acid phosphatase but no cytochrome enzymes. They are highly heterogeneous and very variable from cell type to cell type and perform a digestive function.

vii) **Microtubules** and **Filaments** are both long thin structures, being hollow and solid respectively. They can range from 5-25 nm in diameter and of unknown length. They are found in numerous quantities in neurons and as processes of neuroglial cells, the axons for example have large numbers of neurofibrils (probably the dense protein keratin) and microtubules.

viii) **Cell inclusions** include a number of granules and pigments. In neurons there are a number of neurosecretory granules ≈100 nm in diameter which travel along axons.

Tissue also contains the pigment melanin and glycogen for energy storage.

ix) The **Cell Membrane** is a lipid protein bilayer which encloses all the above in the cytosolic fluid. It has a total thickness of 8-10 nm, made up of two layers with a small gap. The protein content of the membrane is variable with cell type.

x) The **Myelin Sheath** of the **Schwann Cell** deserves a special mention in neuronal tissue. Schwann cells surround either single or multiple axons (nerve fibres) and perform an electrical insulating role. They do this by wrapping a sheath of myelin (lipid/protein) around the fibre many times, each layer being about 12 nm thick. So called "unmyelinated fibres" have very thin sheaths, whereas large nerve fibres have thick (up to 500 nm) sheaths. In infants, the process of myelination of the nerve fibres is a process which starts before birth but is not near completion until 12 months after birth.

The magnitude and nature of scattering for each of the organelles and cell inclusions listed above is presented in Table 3.iii. This table is semi-quantitative and incomplete due to the difficulties in obtaining all the necessary data from the literature. The first three columns relate to the refracting power of each constituent and the next two columns to the scattering characteristics of an individual particle. The column headed "% of total brain contents" suggests the significance of that organelle/inclusion's contribution to the total brain scattering coefficient (the total solids content of the neonatal brain being 100 mg/g wet wt). Many sources of information were used to construct the table:

i) **Red blood cells**: see Section 3.2.2.

ii) **Mitochondria**: the refractive index and total solids content is from Zglinicki et al.[122]; the lipid content (approximately 25% of the total dry weight) is from Darley-Usmar et al[123]; the percentage of the total solid contents in neonatal brain is calculated from Dahl and Sampson[124] and Clouet and Gaitonde[119]. Additional data which is disputed, are the number of mitochondria per gram wet weight of neonatal brain and their individual dry weight, 12×10^{10} g^{-1} and 0.37 pg respectively, (Samson et al.[125]) or 36×10^{10} g^{-1} and 0.1 pg (Gregson et al.[126]). However, both these sets of values suggest that mitochondria make up approximately 8% of the total brain volume.

Table 3.iii The characteristics of cellular constituents, that effect the scattering of light by brain tissue.

	Internal lipid content	Internal protein content	Refractive index	Individual size or volume	Scattering properties	% solids content neonatal brain	Other comments
Red blood cell	1 g/dl	34 g/dl	1.40	88 fl	Mie	5%	$\alpha_{vest}=6.2\times10^{5}\ m^{-1}$, (1-g)=0.0147
Mitochondria	13 g/dl	39 g/dl	1.428	≈ 0.2 fl	Mie	20%	$\alpha_{vest}=1.8\times10^{5}\ m^{-1}$, (1-g)=0.132
Lysosomes					Mie	small	
Nucleolus	Lip+pro ≈	37-47 g/dl	1.40-1.42	≈ 0.2 fl	Mie	negligible	One per cell
Centrioles				≈ 0.03 fl	Mie+Rayleigh	negligible	Two per cell
Golgi apparatus			> cytosol		Mie+Rayleigh		
Endoplasmic reticulum (Smooth and Rough)			Nissl bodies ≈ 1.5		Mie+Rayleigh		
Microtubules & filaments			≈ 1.5		Rayleigh		
Cell granules			≈ 1.5		Rayleigh		
Lipoprotein membranes			≈ 1.46		See text	50%, including	
Myelin sheath	330-470 mg/g	130-270 mg/g	≈ 1.46	< 1 µm	Mie	myelin sheath	Insignificant in brain
Triglyceride			1.491				
Dried protein			1.53-1.54				
Cytosol		10 mg/ml	1.354			≈ 6%	
Cerebrospinal fluid		0.28 mg/ml	1.335				
Extracellular fluid		≈ 0.25 mg/g	1.334				
Nuclear sap	Lip+pro ≈	8.5-12 g/dl	1.350-1.356				
Blood plasma		5.5 g/dl	1.343				

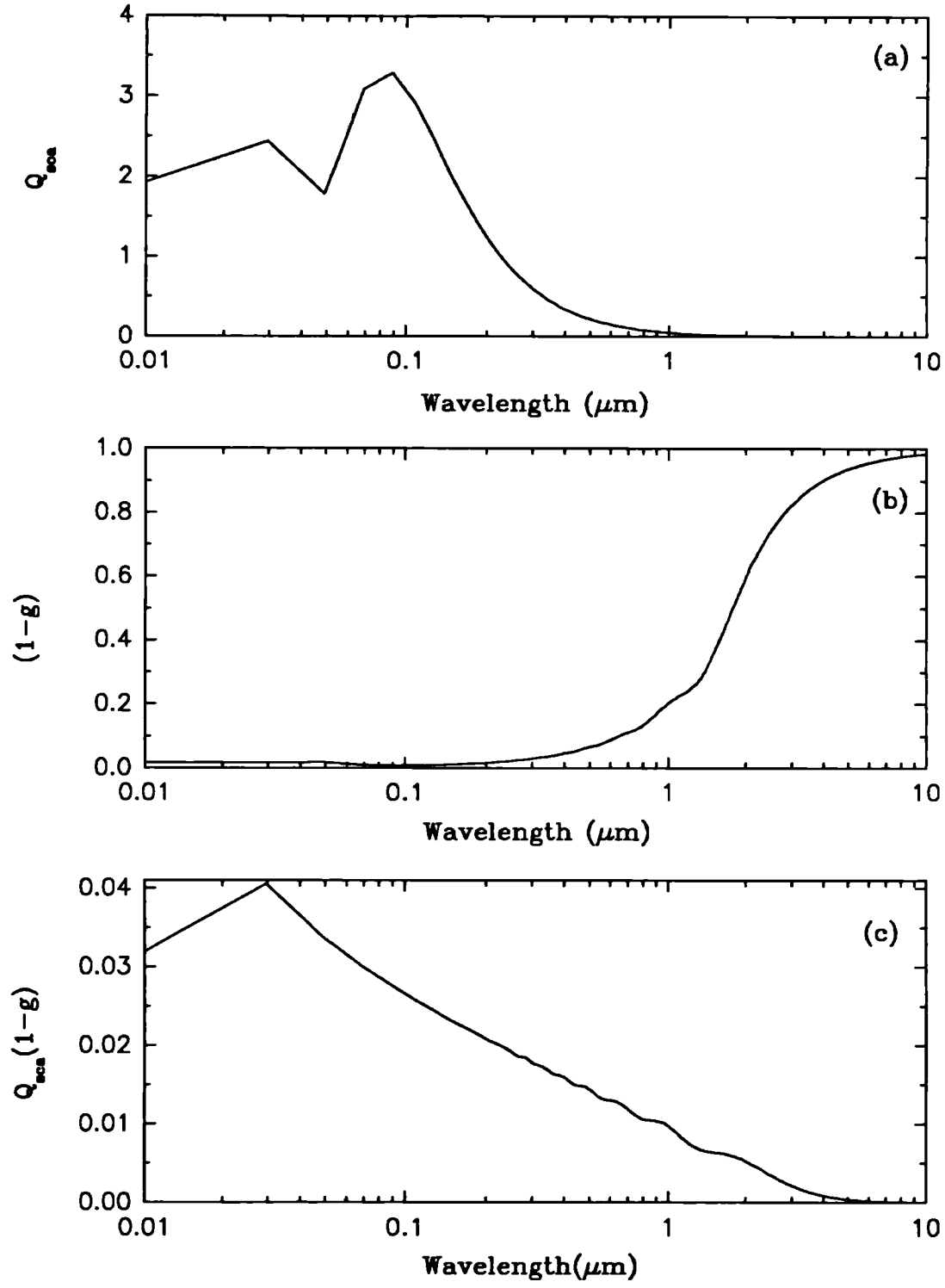

Figure 3.5 Mie theory simulation of scattering by a mitochondrion as a function of wavelength: (a) scattering efficiency; (b) (1-*g*) and (c) the product of (a) and (b).

iii) **Lipoprotein membranes**: the percentage of total brain solids in cell membranes† includes all other membranes after excluding mitochondria and red blood cells. It is an approximate calculation and assumes all brain lipids constitute cell/organelle membranes with an average protein:lipid ratio of 50:50 in the newborn infant. This represents an informed estimate based on a 60:40 protein:lipid ratio for plasma membranes[127] and a 25:75 protein:lipid ratio for myelin sheaths[128].

iv) The refractive indices of the nucleus, triglyceride, dried protein, cytosol and nuclear sap are taken from Ross[112].

v) The remaining refractive indices values, marked as approximate in Table 3.iii, are estimated from their predicted %w/v using Equation 3-12.

vi) The %solids content which is still unaccounted for in the table (19%), is protein which must make up the microtubules, filaments, endoplasmic reticulum and golgi apparatus.

The single scattering properties of mitochondria can be simulated in the same (approximate) manner as for the red blood cell, i.e. they can be treated as volume equivalent spheres. The Mie theory simulation assumes a radius of 0.36 μm, an internal refractive index of 1.428 and an external refractive index of 1.354 and predicts a wavelength dependence of scattering shown in Figure 3.5. In the 600 to 1000 nm region the dependence of $C_{sca}(1-g)$ is $1/\lambda^{0.6}$, which is a larger wavelength dependence (27% variation over the 600-1000 nm region) than the red blood cell but still much less than for Rayleigh scattering.

Scattering by cell membranes cannot be modelled as spherical particles with Mie theory, instead it is best to consider them to be thin (10 nm), flat, dielectric reflecting films. The reflection coefficient of such a film can be derived from Maxwell's equations where n_0, n_1 and n_2 are the refractive indices in the layer 1, layer 2 (the cell membrane) and layer 3 respectively, see Figure 3.6. Reflectance from thin films is a common problem in electromagnetic theory, and can be easily derived from standard textbooks, for example see Kong[129]. The reflectance of a simulated flat cell membrane, for unpolarised light at 800 nm as a function of the angle of incidence, can be seen in Figure 3.7(a). The reflectance is very low for angles of incidence less than 50° (0.00017).

It is of more interest to consider the "scattering response" of a distribution of randomly

---

† Here lipoprotein membranes mean the plasma membrane surrounding the cell, the organelle membranes of the endoplasmic reticulum, Golgi apparatus as well as the myelin sheaths surrounding axons.

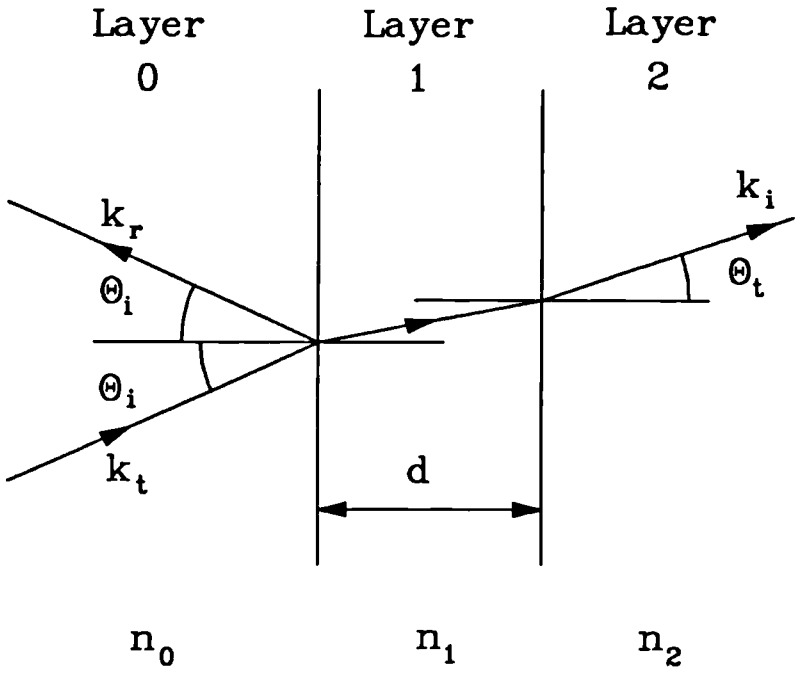

Figure 3.6 Schematic diagram of reflection and transmission of an incident plane wave by a thin, flat membrane of thickness *d*.

orientated thin films which is a crude approximation to the situation in tissue. In this case the response in Figure 3.7(a) is multiplied by the cosine of the angle of incidence to take into account the effective area of the membrane intersecting the input beam. This response is shown in Figure 3.7(b). In order to make a comparison with the scattering efficiencies of mitochondria and the red blood cell, the data in Figure 3.7(b) is integrated over all angles to give a value of 0.0019, which is equivalent to Q_{sca} (the scattered intensity normalised for area). α_{vesi} is obtained by dividing by the membrane thickness (10 nm) giving a value of 1.9×10^5. The asymmetry factor g is approximately zero (in fact slightly negative) as the "scattered" light peaks near 90° with respect to the transmitted beam. The integrated reflectance is virtually wavelength independent, decreasing by only 6% between 600 and 1000 nm. The one weakness of all the wavelength dependence simulations discussed so far is that the variation of refractive index with wavelength has not been taken into account, but apart from data for water, this information is simply not known.

Treatment of the single scattering properties of cell membranes described above is very approximate and is really only applicable to the plasma membranes of large cells. Scattering by large cylindrical myelinated axons, the endoplasmic reticulum, the Golgi apparatus etc. are not suitable for the simple models used so far and are not attempted here. Microtubules and

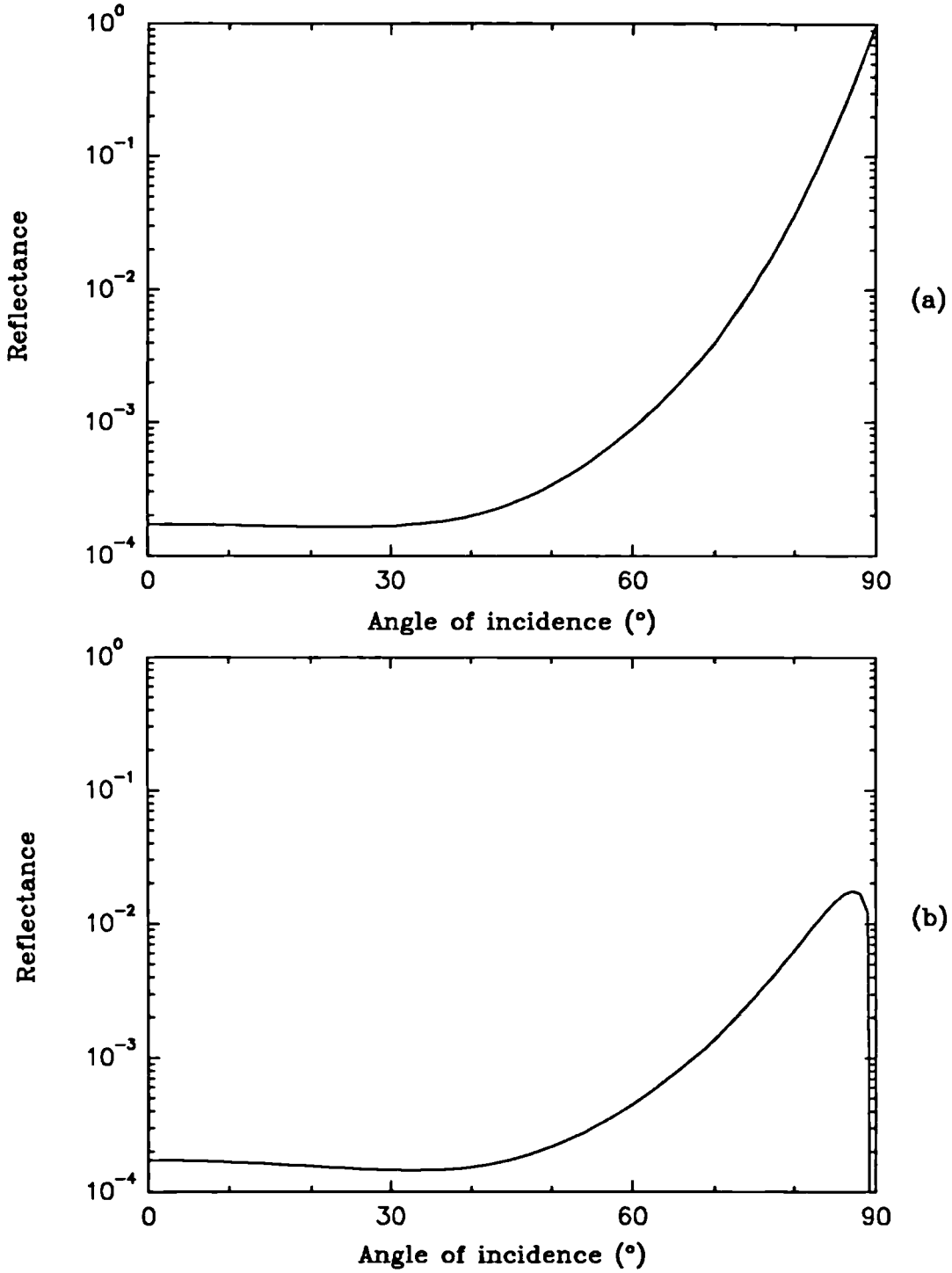

Figure 3.7 Reflection of 800 nm unpolarised light by a 10 nm thick film versus Θ. n_0=1.33, n_1=1.46, n_2=1.354: (a) uncorrected; (b) corrected by the cosine of the angle of incidence.

filaments are very small and will have Rayleigh scattering characteristics. A serious attempt at finding the scattering properties of brain tissue/cell components is the work of a Ph.D. thesis in its own right and would require many experimental measurements.

The above analysis suggests that lipoprotein membranes (excluding mitochondria, red blood cells) account for approximately 50% of the total solids in newborn infant brain. This information coupled with the estimate of the volume extinction coefficient ($\alpha_{vext}(1-g)$) for membranes suggests that cell membranes are the most important source of scattering in brain tissue. Mitochondria are also a very important source of scattering, composing 20% of the total solids content and with a large $\alpha_{vext}(1-g)$. The remaining cell contents (endoplasmic reticulum, Golgi, tubules, filaments) must constitute the next largest scattering component. Red blood cells only constitute 5% of the total solids contents and, being very large, have a low $\alpha_{vext}(1-g)$ and hence will not be a significant contributor to the overall scattering coefficient in tissue.

3.2.3.2 *Dynamic scattering effects*

The previous section discussed the possible origins of the background scattered light intensity. Also of interest are changes in the scattered light intensity which may occur in brain tissue. Isolated perfused cortical brain slices show changes in reflectance when stimulated and when the osmolarity or refractive index of the perfusate is modified[130]. These observations were made at 700 nm in order to minimise any interference which may have arisen due to absorption. A decrease in reflectance (back scattering) was observed for:

i) a decrease in the osmolarity of the perfusate,

ii) membrane depolarisation caused by high extracellular potassium, ouabain, veratridine, electrical stimulation or anoxia.

In general, reflectance changes were reversible except following periods of anoxia lasting longer than 4 minutes (removal of chemicals or drugs was not tested). All reflectance changes could be blocked by exchanging chloride ions in the perfusate for the larger, less permeant, glucuronate ion, thus greatly inhibiting ion movements. Tissue respiration increased during depolarisation by up to 60% and the addition of glucuronate did not affect this increased tissue respiration. The magnitude of the reflectance changes at a stimulation frequency of 60 Hz was −7% while high potassium concentrations (60 mM) and the application of other drugs produced affects up to −30%.

Differences in response were found between brain cortex and kidney cortex. Brain cells appeared to swell significantly more than kidney cortex cells for a given osmotic pressure and also were more sensitive to anoxia than kidney cortex. Whereas brain could only survive 4 minutes of anoxia and return to its pre-anoxic reflectance value, kidney cortex recovered even after 20 minutes of anoxia. Depolarisation of kidney cortex by electrical stimulation and high potassium concentrations did not affect its reflectance.

The conclusions drawn in this study were that tissue reflectance decreases occur as the cell volumes increase, and that membrane depolarisation results in an increase in cell volume in excitable tissues, which is reversible except after prolonged anoxia. The author put forward further evidence to suggest that the origin of the observed scattering changes was at the intra/extra-cellular barrier. This is a possibility, but there are additional effects such as mitochondrial shrinkage which are also likely to be important. Note that these measurements were made on thin (less than 100 μm) tissue slices in reflectance only. The angular scattering function of brain tissue is highly forward peaked, see Figure 3.8 from van der Zee[131], and forward scattered light may respond differently to back scattered light, making it difficult to predict the overall scattering change which would be observed with multiple scattering in thick

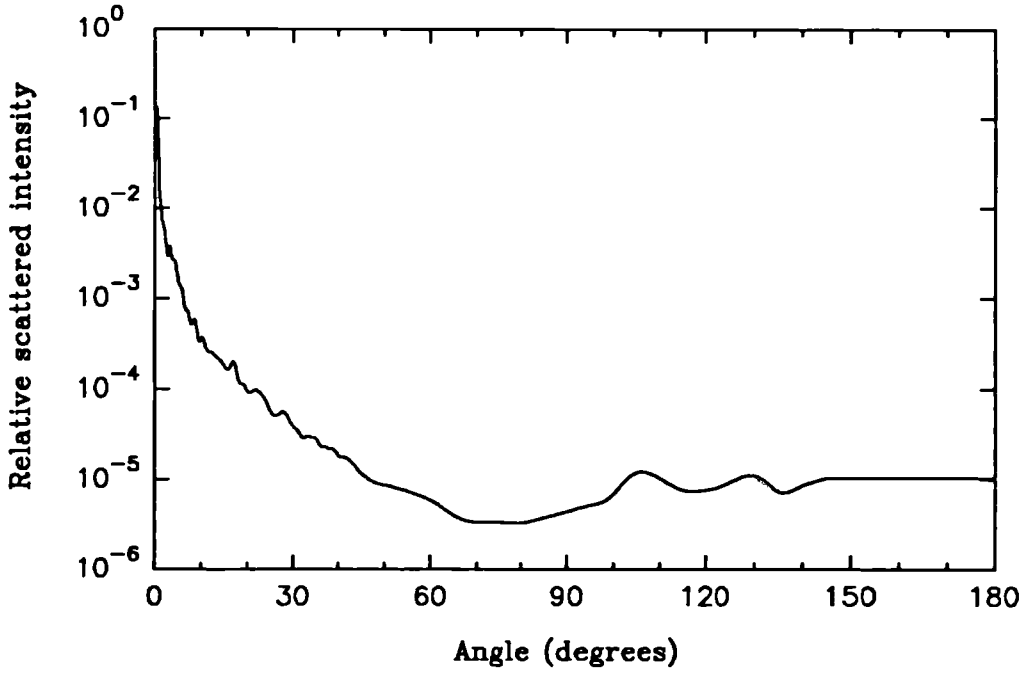

Figure 3.8 Angular scattering function of post mortem adult rat brain tissue, taken from van der Zee[131].

(e.g. 1 cm) sections of tissue.

The magnitude of cellular water movements have been published. Typically 15% of brain volume is occupied by the extracellular space, and this shrinks to 4% in cases of asphyxia[132]. Extracellular space in the newborn may be even larger[133] and greater water movements may therefore occur. This topic is returned to later in Section 7.5.3.2.

3.3 MULTIPLE SCATTERING IN BRAIN TISSUE

The previous sections on single scattering by particles used solutions of Maxwell's equations to predict the scattered field in situations where the single particles could be considered far enough apart not to interact with each other. This is clearly not the situation in tissue of any type. Attempts to solve Maxwell's equations for multiple scattering have been performed[134] for example using a spatially varying, random perturbation of refractive index[135]. The applicability of this approach to light transport in tissue is not favoured however because of the complexity of the solutions and the difficulties of expressing a realistic spatial distribution of refractive index. Solutions have been found by Twersky[136] for the simpler situation of a suspension of red blood cells and this theory, combined with experimental results, is used later to illustrate some of the spectroscopic effects observed in scattering media.

For the calculation of light transport in tissue, where red blood cells contribute only a small part to the total scattering coefficient, the two techniques which have found most favour are solutions of radiative transfer theory[137] and Monte Carlo analysis.

Monte Carlo analysis is an exact analysis, performing simulations of particle paths within the media which can easily have spatially varying absorption and scattering parameters. The main disadvantage of the technique is the extensive computing time required to generate solutions with a good signal to noise ratio. Its main advantage is its ability to cope with complex boundary conditions and areas of differing optical characteristics. For a concise description of Monte Carlo techniques see the review paper by Patterson et al[138]. This review paper also includes a description of the many techniques used to model light transport in tissue, including the radiation transfer theory.

Both the Monte Carlo and radiative transfer approaches to multiple scattering of light in tissue are "billiard ball" methods which ignore the wave nature of light. Typically, polarisation effects are also ignored. This latter assumption has been demonstrated to be valid[139], coherence being rapidly lost with the high number of multiple scatters.

In the application of radiative transfer theory, the most popular approaches have been the so-called two flux approximation of Kubelka-Munk[140] and the P_n approximations (where the *n* refers to the number of Legendre polynomials which approximate the angular scattering function). The Kubelka-Munk approximation assumes that the light field is isotropic at all times, which as previously shown, is generally not true. The P_1 approximation (or diffusion equation) is more realistic in that it allows for linearly anisotropic radiation. Star[141] has shown that the P_1 approximation is inadequate when applied to light transport in thin tissue sections such as skin at 633 nm. Significant improvements resulted when a P_3 approximation was coupled with a delta function to approximate the tissue phase function. The P_3 approximation does however lead to a substantial increase in complexity so we will continue to use results from the more widely used P_1 (diffusion approximation) to model light transport in thick tissue sections.

The limitations of the P_1 approximation become most noticeable when the scattering term does not greatly dominate over the absorption term, but this is not such a problem at wavelengths between 650 nm and 1100 nm, especially in brain tissue. General difficulties of the P_n approximations are the application of boundary conditions for realistic objects and light sources and also dealing with collimated light sources and detectors, where linear anisotropy cannot be assumed[142]. This has led to solutions which apply the P_1 approximation to simple geometries, for example the infinite slab, illuminated by collimated, point or cylindrical sources[143].

3.3.1 Optical attenuation in red blood cell suspensions

Although analysis of absorption and scattering of red blood cell suspensions is not strictly relevant to effects observed in tissue, it has been investigated thoroughly and is useful in illustrating some of the salient features of spectroscopy in scattering solutions.

The optical effects observed in whole blood suspensions are not effectively predicted by diffusion theory even at near infrared wavelengths[144], as scattering does not greatly dominate over absorption. The theory of Twersky[136 145 146] and variations thereof have

proved much more successful in matching experimental data. This multiple scattering theory is a solution of electromagnetic wave theory, and is able to take into account the separate absorption and scattering parameters of the single red blood cell, the number density of red blood cells per unit volume and the acceptance angle of the detector. The theory assumes that the red blood cells can be treated as large absorbing tenuous scatterers, i.e. the Rayleigh-Gans approximation, with a forward peaked scattering phase function. Twersky's equation for the attenuation of a whole blood suspensions is†

$$\lg\left(\frac{I_0}{I}\right) = \alpha C d - \lg\left[10^{-adH(1-H)} + q\left(1-10^{-adH(1-H)}\right)\right] \qquad 3\text{-}14$$

where the first term on the right is the standard Beer-Lambert extinction term, α the specific extinction coefficient ($mM^{-1}cm^{-1}$), C the haemoglobin concentration (mM) and d the cuvette thickness (cm). The second term on the right is the scattering term, H is the haematocrit, a and q are constants that depend upon the wavelength, particle size, refractive index and the geometry of the photodetector.

There are numerous published experimental data concerning light transport in blood, comparing the results to predictions from different theories[46 144 147 148]. This area is of practical importance to whole blood oximetry and pulse oximetry.

One paper by Steinke and Shepherd[144], describing optical attenuation by whole blood suspensions, will be discussed in the remainder of this section. Figure 3.9, taken from this paper shows that the relationship between the attenuation of light by whole blood and its haematocrit is non-linear. This data was obtained using light from a 940 nm light emitting diode which illuminated a flowing stream of deoxygenated blood, 1.6 mm thick. Transmitted light was collected by a silicon photodiode. The data, as replotted here, is the **attenuation** of the whole blood plotted against its equivalent **extinction coefficient** when lysed at the same overall concentration in the same optical cell, each data point being a different haematocrit (shown on the second x-axis). If red blood cells were non-scattering the result would be a straight line of unity slope and zero intercept as predicted by the Beer-Lambert law. In practise this is found not to be the case. The effect of increased scattering by the red blood cell is most marked at low and high haematocrits, since at low haematocrits, equal increases

† Note that at near infrared wavelengths, Twersky suggests a modification to his earlier theory to account for the lower NIR extinction coefficients[144].

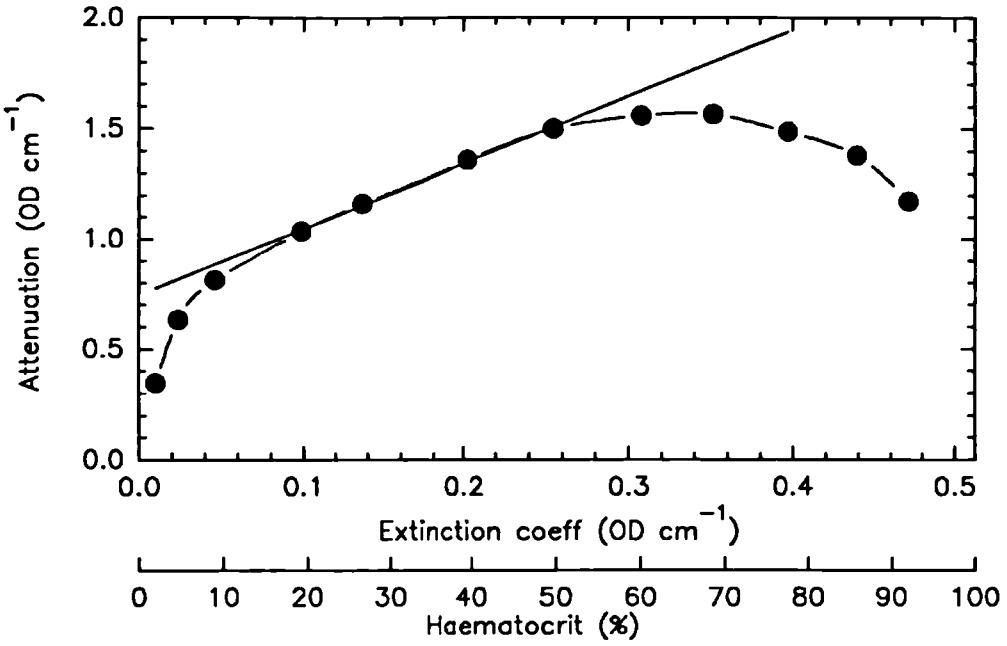

Figure 3.9 Attenuation versus extinction coefficient for a deoxygenated red blood cell suspension in a cell 1.61mm thick, λ=940 nm. Haematocrit varied from 0 to 100%. Data of Steinke[144].

in haematocrit produce proportionally more scattering than at intermediate haematocrits, whereas at high haematocrits, the red cells start to abut each other and less scattering occurs. Between 20% and 50% haematocrit (normal physiological range 43% to 46%), the relationship does become approximately linear but with a slope of 3.0 instead of unity.

A slope greater than unity in the "linear" region can be explained by two theories. Firstly, that increased scattering leads to increased attenuation directly, or secondly, that scattering increases the effective pathlength of the light which travels through the cuvette. An increased pathlength means greater overall absorption. Both of these effects are known to occur, the question is, what is the contribution of each one.

In this same paper Steinke and Shepherd[144] performed an experiment which helps to resolve this question, but does not resolve it completely as it was performed at a different wavelength, namely 660 nm. In this experiment scattering was kept constant (haematocrit 37%) and extinction coefficient changed by varying the haemoglobin saturation. This data is replotted in Figure 3.10, in a form identical to Figure 3.9. The authors claim that this data has a linear relationship (R^2=0.99), although a closer examination reveals a slight quadratic relationship (improved R^2), see the fitted curve of Figure 3.10. The local gradient of the curve

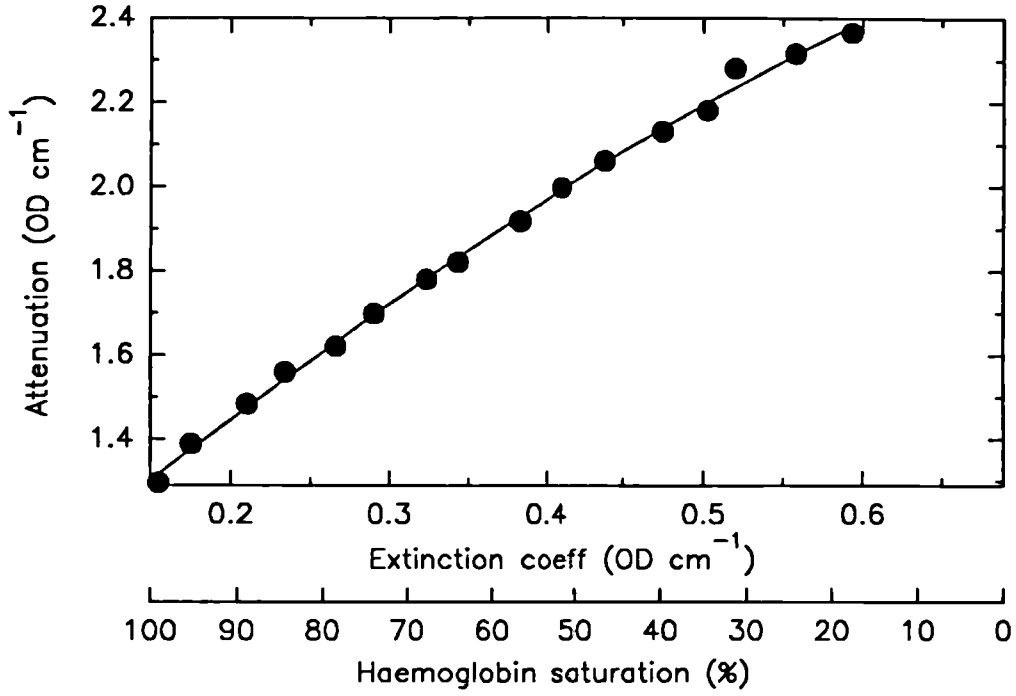

Figure 3.10 Attenuation versus extinction coefficient in a red blood cell suspension, 37% haematocrit, cell 1.61mm thick, λ=660 nm, oxygen saturation varied 0 to 100%. Data of Steinke[144].

varies over the whole range but at similar extinction coefficients to the linear region of Figure 3.9 it is 2.9-3.0. This suggests that effective optical pathlength considerations and not increased scattering explains almost all the observed slope of 3.0 in the linear region of Figure 3.9. In summary, the experimental data of Steinke and Shepherd[144] shows that the effective optical pathlength decreases with increased absorption coefficient, other experiments in this paper also show that effective optical pathlength increases with increased scattering coefficient.

Steinke and Shepherd[144] also compared their experimental results with the predictions of a number of theories, and a modification of Twersky's theory was found to provide the best fit (the theoretical fit is not shown in the figures here). In terms of the broad shape and mean square error, the fit is reasonable, but by no means flawless. The problem with Twersky's theory is that the absorption term does not take into account the increased optical pathlength due to multiple scattering. The increased slope in the linear region of Figure 3.9 is accounted for by the scattering term alone, see Equation 3-14. Loewinger[149] proposed a semi-empirical modification of Twersky's theory to take increased pathlength due to multiple scattering into

account, but Steinke and Shepherd found that this theory did not improve upon the fit of the original theory of Twersky. The authors concluded that they had separated the effects of scattering and absorption upon attenuation in whole blood as illustrated in Twersky's equation. This appears to be very doubtful due to the inadequacies of Twersky's equation itself.

3.3.2 Optical attenuation in tissue

The majority of the published work on light absorption in tissue has been performed in order to predict the effects of laser irradiation of tissue. Here, the parameter most frequently calculated is the radiation dosage per unit volume of tissue, the "space irradiance". Some practical measurements of the rate of decrease in intensity with distance within different organs and tissues have been performed on post mortem tissue. Figure 3.11, taken from Svaasand[150], shows the forward, backward and sideways irradiance into an optical fibre in post mortem neonatal brain tissue, 32 weeks gestation, for a 660 nm laser input beam. These experimental results show a two stage fall in intensity, which matches diffusion theory predictions. The initial rate of fall is very rapid as the collimated input beam is scattered into a diffuse beam within the first 8 millimetres. Once this has occurred, the attenuation drops less rapidly at a rate which is more dependent upon absorption by tissue chromophores.

The linear fall which occurs after the first few millimetres is quantified as the penetration depth, normally defined on a $\log_e$ scale as the length over which the space irradiance drops by 1/e. The penetration depth is a function of the tissue type and the wavelength of the light, the more highly pigmented organs having shorter optical penetration depths. In addition to penetration depth being dependent upon absorption, it has also been shown to be dependent on scattering. This is most clearly seen in the case of the developing human brain. Table 3.iv, also taken from Svaasand[150], gives data on penetration depth as a function of wavelength and maturity, and shows a decrease of penetration both with increasing maturity (increased scattering coefficient) and decreasing wavelength (increased absorption coefficient). As explained earlier in Section 3.2.3, the major increase in scattering is due to the process of myelination. The practical result of these changes is that the brain of the premature infant is much more transparent than that of the adult.

A simple expression for the time independent diffusion equation is

$$\nabla^2\phi - \frac{\phi}{\delta^2} = S \qquad \text{3-15}$$

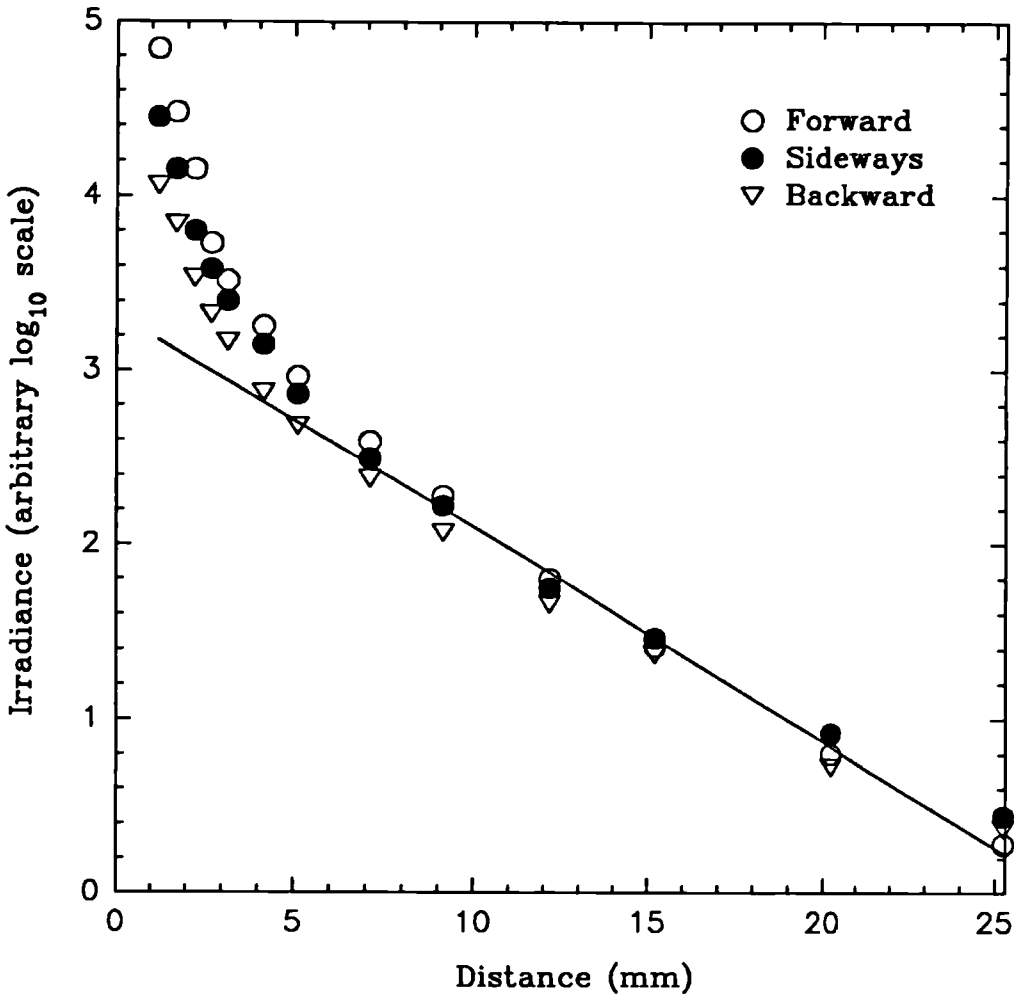

Figure 3.11 Irradiance in three directions as a function of depth within post mortem neonatal brain, wavelength 660 nm. Data taken from Svaasand[150].

where ϕ is the space irradiance, Γ is the penetration depth and S represents light source terms. The solution for a spherically symmetric geometry is

$$\phi = \phi_{OS} \left(\frac{\Gamma}{r}\right) e^{-\frac{(r-\Gamma)}{\Gamma}} \qquad \textbf{3-16}$$

where r is the distance from the source and ϕ_{OS} is the space irradiance at one penetration depth. The penetration depth Γ is given by

$$\Gamma = \frac{1}{\sqrt{3\mu_a\left(\mu_a + (1-g)\,\mu_s\right)}} \qquad \textbf{3-17}$$

Table 3.iv Penetration depth (mm) of light in post mortem human brain tissue. The penetration depth is the depth at which the intensity has fallen by 1/e, data from Svaasand[150].

WAVELENGTH (NM)	AGE					
	2 months premature	Term infant	67 years	81 years		84 years
				Grey matter	White matter	
488	1.7	1.3	0.4	0.5	0.5	0.7
514	1.7	1.1	0.4	—	—	0.6
660	5.4	3.7	1.2	1.7	1.6	1.6
1060	8.8	7.1	3.2	3.5	2.9	4.3

where μ_a (Units: mm^{-1}) is the transport absorption coefficient in the tissue (base *e*), μ_s (Units: mm^{-1}) is the transport scattering coefficient and g is the anisotropy factor, previously described in Equation 3-11. The term $(1-g)\mu_s$, abbreviated μ_s' is known as the *reduced* scattering coefficient. Note that the absorption coefficient μ_a is related to the extinction coefficient α ($OD\,cm^{-1}$) by $\alpha = 10\,\mu_a/\ln(10)$ and μ_s is related to the single particle scattering cross-section C_{scs} by $\mu_s = N C_{scs}$ where N (m^{-3}) is the particle number per unit volume.

Values for μ_a, μ_s and g are notoriously difficult to measure and a concurrent project within this department is examining this problem with the aim of characterising tissue by its optical properties. Sterenborg[151] has published graphs of μ_a and μ_s' for post mortem adult human brain as a function of wavelength. This data is very noisy and also exhibits large variations between individuals. This is currently the best data which has been published (though it probably still contains some errors). The reduced scattering coefficient appears to lie in the range 1.5-4 mm^{-1} with a small wavelength dependence, an approximate 25% decrease from 650 to 1000 nm. The data is not sufficiently accurate to indicate a difference in the scattering coefficient between white and grey matter. The absorption coefficient falls in the range 0-0.25 mm^{-1} for the same wavelength region, the absorption coefficient of grey matter being larger than that of white matter. A similar relationship between these coefficients and wavelength has also been found by Wilson et al[152].

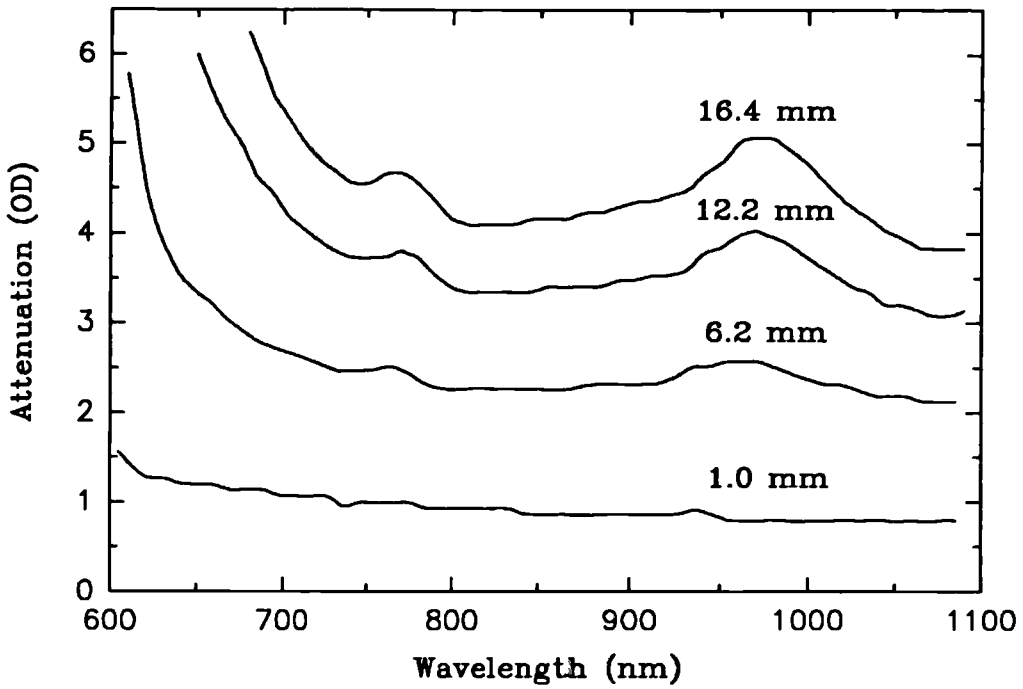

Figure 3.12 Attenuation of lean striated muscle as a function of wavelength for various tissue thicknesses, data taken from Preuss[153].

Typical tissue attenuation spectra for lean muscle are shown in Figure 3.12 (data taken from Preuss[153]) and indicate the major features of tissue transmission as a function of wavelength. Firstly, at wavelengths shorter than 650 nm, tissue attenuation becomes too large to measure across many centimetres of tissue. The absorption peak of water at 975 nm and of deoxy-haemoglobin at 760 nm are clearly visible. Note that in the wavelength range 750 - 930 nm, the dynamic range of the measuring instrument does not need to be large, the difference in attenuation over this wavelength range being less than 0.5 OD through 16.4 mm of lean muscle.

3.4 CLASSIFICATION OF SPECTROSCOPIC MEASUREMENTS

It is important to classify the various types of chromophore concentration measurements that can be made. To do this, an introduction to some of the terminology is

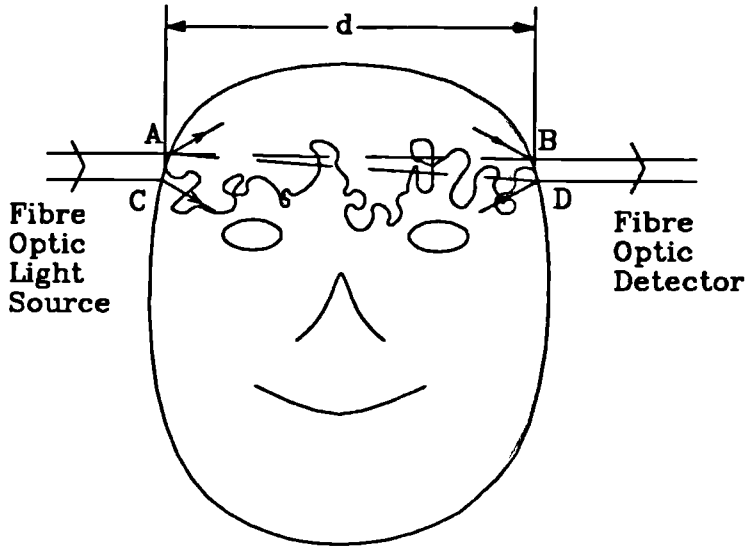

Figure 3.13 Schematic diagram of OPTODE positioning showing example photon paths for non-scattering and scattering solutions.

useful. The terminology is introduced by considering a hypothetical example involving a head shaped container, as shown in Figure 3.13, and which in the beginning contains a clear liquid. A non-collimated optical fibre coupled light source (called an OPTODE, c.f. electrode) is placed on one side of this "head" and a non-collimated optical fibre coupled detector (another OPTODE) on the opposite side, separated by the width of the "head" (the OPTODE spacing) d cm. This description may appear trivial but spells out in detail a classification which becomes important when spectroscopy is performed in highly scattering media.

3.4.1 Non-scattering solutions

When the "head" contains only water the detector measures the transmitted intensity I_0 as a function of wavelength. Consider the addition of an unknown concentration of absorbing dye C_1 which has a known specific extinction coefficient, α $mM^{-1}cm^{-1}$ to the water. The detector now measures an intensity I_1 and the concentration of the compound is given by simply rearranging the Beer-Lambert law, Equation 2-5

$$C=\frac{A}{\alpha l} \qquad \text{3-18}$$

In this case, $C = C_1$ (units: millimolar), $A = \lg(I_0/I_1)$ and $l = d$. The intensities can be measured

at any wavelength (though there may be an optimum under a given set of conditions to maximise the accuracy of C (see Section 4.1). In the terminology introduced here, this is an example of a measurement of dye concentration which is **absolute and quantified in non-arbitrary units.** A measurement of this type requires prior knowledge of the optical path l, the specific extinction coefficient α and a reference intensity when the "cell" (head) contains only solute. Consider now a second measurement on the same "head" some time later, made by a second observer who does not know the value of C_1, the concentration of dye already present and I_0, the transmitted intensity for solute only. If a second amount of dye ΔC is now added to the "head", ΔC can still be found from the equation above with $A = \lg(I_1/I_2)$ where I_1 and I_2 are the intensities before and after adding ΔC respectively. What cannot be found is the absolute dye concentration in the "head" as I_0, the correct reference intensity, is unknown. This is an example of a measurement which is **relative and quantified in non-arbitrary units.** This type of measurement only requires a prior knowledge of the optical path l and the specific extinction coefficient α. Knowledge of the existing concentration of dye before adding ΔC or of I_0 would have allowed an absolute measurement to be made.

These examples illustrate the situations when **absolute** or **relative** measurements are made. The important point to note is that attenuation A is always given by a logarithmic ratio of a reference intensity and a sample intensity and the concentration measurement derived from A is always relative to the point at which the reference intensity was measured. The only difference between the two cases above is the dye concentration, which was known in the absolute example and unknown in the relative example at the time the reference measurement was made.

The second pair of terms describing the determination of chromophore concentration are **quantified** and **trend** measurements. Simply put, quantified concentration measurements are possible when the optical path l itself is quantified, and trend measurements are made when the optical path is not quantified. (Note that the use of the word quantified allows optical path to be in arbitrary units). The importance of this differentiation can again be shown by the following example.

Consider a situation in which a set of different "heads" of different sizes exist, each containing a given concentration of dye. **Identical changes in dye concentration** are introduced to each "head", by adding a bleaching material. The resulting (differing) changes in attenuation ΔA are measured for each "head", i.e. the logarithmic ratio of transmitted intensities before and after addition of the bleach. In quantified measurements, the attenuation

change is divided by the quantified length (any unit) giving $\Delta A/l$ which, in this example, should be identical for each "head" (to within the experimental error). In these circumstances the conclusion would be drawn that the "stimulus" (in this case an injection of bleach to produce an identical change in dye concentration) caused identical responses in all "heads". However, in trend measurements, l is not quantified and hence only ΔA is known and this will be different for each "head". When l is not quantified the only conclusion that could be drawn from the trend measurements is that dye concentration decreases in response to identical stimuli. This conclusion contains less information than the quantified measurements.

A comparable but more realistic example would be where we wish to know the response of the cerebral blood volume (haemoglobin concentration) to administration of a drug, in a population of newborn infants with different head sizes. In order to examine the significance of the response in clinically different groups of infants, quantified measurements would be required.

The last pair of terms to be defined are **non-arbitrary** and **arbitrary** units of concentration. For concentration measurements in non-arbitrary units, the units of the specific extinction coefficient and the optical path must be consistent, resulting in values traceable to Molar units. It is difficult to make such spectroscopic measurements in tissue, and until recently this has meant that all measurements of concentrations of chromophores have been in arbitrary units. As an example, one could define the arbitrary optical pathlength unit of 1 Cope as being equivalent to an OPTODE spacing of 1 cm of brain tissue and hence measure optical paths in brain in "Copes". If the specific extinction coefficient of haemoglobin, etc was also available in $Molar^{-1}Cope^{-1}$ then no problem would arise since the resulting measured concentrations would be in Molar units. Normally, however, the units of specific extinction coefficient are $Molar^{-1}cm^{-1}$ (where cm refers to effective optical pathlength and not OPTODE spacing). Hence, the concentration measurements would have units of Molar Cope cm^{-1}. Arbitrary units of this type are adequate until comparisons need to be made with other methods of measuring the same quantity. For example, comparing cerebral blood volume with the isotopic techniques described in the opening chapter. Ideally data in non-arbitrary units are required to allow optical spectroscopy methods to be compared with established methods of measuring the same parameters. An example of an arbitrary unit is the "v/d" or variation in density which can be found in the publications of Brazy and Jöbsis[69].

Summarising this section, three pairs of terms have been defined above; absolute/relative, quantified/trend and arbitrary/non-arbitrary. The classification which contains

the maximum amount of information is absolute and quantified in non-arbitrary units while the classification with the minimum amount of information is trend monitoring where, by definition, the units are also always arbitrary.

3.4.2 Scattering Solutions

The above classifications of spectroscopic measurements have been introduced with examples of measurements in non-scattering solutions. The need to introduce the idea of an unknown optical pathlength in this case may appear unnecessary. This is however not always the case, see for example Figure 3.13. With uncollimated detectors of finite size, the optical path is a sum of the multiple differing paths from AB to AD. In the figure as drawn, the variation is a small percentage of the total path†. Variations of optical path are of much greater importance in scattering solutions.

Continuing with the example of Section 3.4.1, starting with pure water in the "head", a large quantity of scattering material is now added to ensure multiple scattering. The transmitted intensity after adding the scatterer is I_s (compared to I_0 prior to the addition), so the attenuation due to the scattering material is $A_s = \lg(I_0/I_s)$. The value of A_s is however not very meaningful as it is not only a function of the scattering properties of the "head" but also the size and geometry of the "head", and the light source and the detector. The light emerging from the "head" will now be diffuse due to the multiple scattering. Increasing the acceptance angle of the detector would increase I_s and hence decrease A_s. Thus attenuation measurements of this type can only be quantified for certain predefined geometries and it is not possible to place infant heads of different sizes (non-invasively) into one of these preferred geometries.

If a dye is now added to the scattering solution in the "head", there is little point in comparing the new intensity I to I_0. What is more useful is to use I_s as the reference intensity. The attenuation change which will now be observed, $\lg(I_s/I)$, is much larger than the attenuation change observed for the same dye concentration in a clear solution. This effect was illustrated in Figure 3.10 where red blood cells were the scatterer and the extinction coefficient was changed by altering the blood saturation. As a result of multiple scattering the pathlength of the optical rays was much larger than d the physical thickness of the cell. Observations of the intensification of absorption bands caused by increased pathlength have been observed by

---

† Normally in precision spectrophotometers both the light source and the detector are highly collimated to overcome this problem.

Keilin and Hartree[154] in frozen samples and by Butler and Norris[155] in calcium carbonate solutions.

What does not appear to have been previously attempted is to use these intensified bands in quantitative tissue spectroscopy. The methodology proposed in this thesis is to modify the Beer-Lambert law to take account of the additional optical pathlength. There must be a number β, such that any measured attenuation change δA observed across the scattering medium is related to the change in the extinction coefficient ($\delta K = \Sigma\alpha_i\delta C_i$, units: cm^{-1}) of that medium, such that

$$\beta = Bd = \frac{\delta A}{\delta K} \qquad \text{3-19}$$

β has been named the "differential pathlength" (DP, or effective optical pathlength) and has units of length (cm). B has been named the "differential pathlength factor" (DPF) and is dimensionless. The DPF is of great practical use because when it is multiplied by the thickness of the "head" d it gives the effective optical path ($\beta = Bd$). In general, the DP is likely to be a function of extinction coefficient, otherwise the data points in Figure 3.10 would all have fallen on a straight line of slope β (it is also obvious that β is a function of the scattering coefficient). However, Figure 3.10 does suggest that over limited ranges β may be considered a constant within some systematic error margin.

An experiment was designed to examine how the DP might behave in a neonatal head. A rectangular cuvette of dimensions 6 cm wide by 8 cm high by 1 cm path was filled with a scattering suspension of polystyrene latex spheres (diameters 1.003 μm, 1.89 μm, 0.0049 μm) selected such that the angular scattering function matched that of brain tissue[131 156]. The concentration of polystyrene spheres (≈2.5% v/v) was chosen so that the total attenuation of the cuvette was approximately equivalent to that of 1 cm of neonatal brain when, in addition to the scatterer, the cell contained an absorber producing an extinction coefficient of 0.1 OD cm^{-1} (ICI dye, S109564). The attenuation of light across the cuvette, at 800 nm, was monitored as known concentrations of absorber were added to the cuvette, starting from a pure scattering solution. The results are shown in Figure 3.14(a), the abscissa is the known extinction coefficient of the dye in the cuvette, while the ordinate is $\lg(I_s/I)$ (the attenuation). β, the DP, is the local gradient of the curve and can be seen in Figure 3.14(b) expressed as the DPF ($d = 1$ cm). The figure shows that the DPF is a function of extinction coefficient in the range of extinction and scattering coefficients expected for neonatal brain

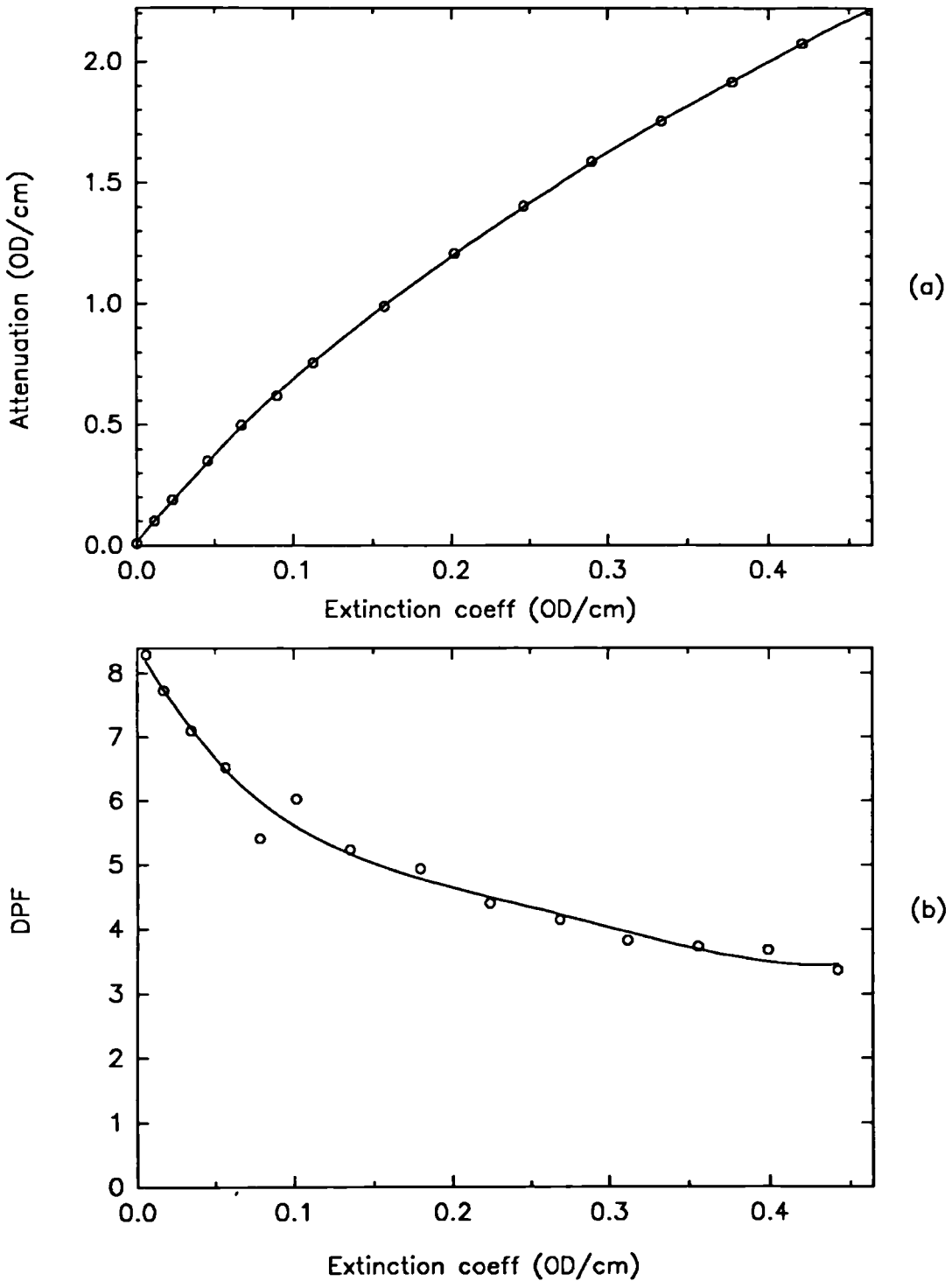

Figure 3.14 (a) Attenuation coefficient versus extinction coefficient. (b) DPF verses extinction coefficient; for a neonatal brain phantom, see text for details.

tissue. The DPF varies rapidly at very low extinction coefficients (< 0.007 OD cm^{-1}) becoming a more gentle function of extinction coefficient at larger extinction coefficient values. The absolute value of brain tissue extinction coefficient is needed in order to use this graph to predict the non-linearity due to scattering. A minimum value of 0.12 OD cm^{-1} can be estimated based on data presented in Chapters 1 and 2 which covers the specific extinction coefficient spectra and concentrations of the major compounds. This suggests a DPF in the range of 5.0 which decreases by approximately 15% for a 0.1 OD cm^{-1} increase in the extinction coefficient (likely to be the maximum possible change in extinction coefficient in the near infrared).

In general, the DPF will increase with increasing scattering coefficient and decrease with increasing extinction coefficient (approaching unity as the extinction coefficient approaches infinity). Once the DPF is known, it is possible however to quantify **changes** in chromophore concentration in non-arbitrary units just as in non-scattering solutions. Section 7.2 will look at techniques of determining the DPF in-vivo.

An important question which arises here is what type of measurements are possible when attempting to determine chromophore concentrations in the heads of newborn infants? A light source and detector can obviously be placed against the head and a reference spectrum taken. At this time, the concentrations of the chromophores in the head are not known, and hence all measurements of chromophore concentrations are **relative**. Attenuation changes which occur from this point onwards can however be related to changes in chromophore concentration. We have seen that a typical concentration of haemoglobin in brain tissue is 84 μM, with a maximal range of physiological variation of 30 to 150 μM. Over this range, the phantom experiment of Figure 3.14 suggests that to a first approximation we can assume a constant DPF (±15%). Whether the absolute value of the DPF measured in this brain phantom is accurate remains to be validated.

Without an accurate value of the DPF for the neonatal head, Equation 3-19 above can be used either with the brain phantom DPF value of 5.0, or without any value for the DPF, to produce measurements in **arbitrary** units. Trend measurements can be avoided if the optical path is measured in units of the number of centimetres of brain tissue. Measuring in transillumination mode across the head would appear to be a sensible starting point as the number of centimetres of brain tissue is easily measured (path AB of Figure 3.13). If measuring at angles of less than 180° between source and detector, then the number of centimetres of brain tissue is taken as the shortest distance between light source and detector,

(the physical OPTODE spacing). This latter assumption is based on the knowledge that light inside the brain becomes essentially diffuse within a few millimetres of entering the tissue[150], at which point it becomes a unidirectional source. Hence the straight line approximation between source and detector is justifiable based on experimental observations.

The first clinical measurements of chromophore concentration in newborn infants were made in **relative, quantified and arbitrary units**[157]. It was not until a number of years later that the value of the DPF for neonatal human brain was found[158] and then chromophore measurements could be made in non-arbitrary units.

The ultimate goal of performing absolute measurements in a straight forward manner is still awaiting development, although as we shall see, some absolute measurements are currently available by resorting to additional physiological manipulations and assumptions.

3.5 CHAPTER SUMMARY

At the beginning of this chapter three questions were asked. What has been illustrated is the complex nature of multiple scattering by brain tissue and this has led to these questions being answered in part. One important concept has been introduced, that of the differential pathlength (DP) and the differential pathlength factor (DPF), which permit the quantification of chromophores in non-arbitrary units in brain tissue (and in other scattering solutions).

From the literature it appears that the scattering coefficient of brain tissue increases with gestation. This is a gradual change, which in human infants takes place over many months, and thus it can be considered to be constant over a single monitoring period of many hours. However it does suggest that the DPF will increase with gestation, but it is difficult to predict by how much.

Changes in the reflectance of thin tissue slices with electrical activity and cell depolarisation indicate a back scatter decrease with an increase in cell size and the concomitant decrease in the extracellular volume. Thus, particularly with anoxia, there may be a scattering change in brain tissue. Other work has been performed on light scattering by single axons and this is covered in Section 7.5.3.2. Section 3.2.3 on the origins of light scattering may help in suggesting the origin of this scattering change. Changes in blood

volume (i.e. red blood cell concentration) also have the potential to change scattering coefficient. However it has been shown that red blood cells constitute only a small part of the total solids content of the neonatal brain, and also have a small volume *reduced* scattering efficiency due to their large size.

All evidence (both theoretical and experimental) points to a decrease of scattering coefficient with wavelength of up to 25% from 650 to 1000 nm, making the DPF a function of wavelength in the near infrared. In addition it has been shown that the DPF is also a function of extinction coefficient. For ease of data processing it is initially convenient to treat the DPF as a constant (then attenuation is linear with extinction coefficient). Narrowing down the wavelength band of observation from 650-1000 nm to a smaller one is helpful in reducing changes of the DPF which occur with both scattering and extinction coefficient variations. Although this does not eradicate non-linearities it does minimise them, and for first attempts at quantification it is proposed to assume a constant DPF within a smaller wavelength band.

CHAPTER 4

DESIGN CONSIDERATIONS FOR A CLINICAL NEAR INFRARED SPECTROPHOTOMETER

The starting point of any design involves the setting of specifications for the system. This can be done now that the magnitude of "oxygenation changes" in tissue have been estimated, and the absorption and scattering properties of tissue discussed. As a result of multiple scattering, the classification of chromophore concentration measurements that are possible in tissue are **relative, quantified and (initially) in arbitrary units.**

The final specification of the instrument requires an optimum selection of many optical and electronic components. In this chapter the characteristics of the various options are discussed.

4.1 SYSTEM DESIGN PARAMETERS

Any design is a compromise between the available optical technology and the practical and safety requirements necessary for a clinically usable instrument which ideally can be operated by a non-technically qualified doctor or nurse.

The major design considerations of the spectrophotometer are set out below:

(i) The attenuation by brain tissue affects the sensitivity required of the system. The equation below is an approximation of the optical loss involved in penetrating the surface tissues (skin and skull)[106] and the brain tissue, see Table 3.iv and Figure 3.11,

$$attenuation\,(A) = 3 + 0.8\,d \qquad [Units: OD] \tag{4-1}$$

Where d (Units: cm) is the OPTODE spacing across the head. Thus, to transilluminate a babies head of up to 8 cm diameter requires an instrument capable of operating at **optical losses of 10 OD.**

(ii) The major part of tissue attenuation is caused by light scattering, which is largely dependent upon cell density and hence is expected to remain constant at least on a daily time scale. What is detectable in the short term are rapid changes in attenuation caused by blood (haemoglobin) and cytochrome c oxidase. The magnitude of these changes will depend upon the molar concentrations of these compounds in tissue. The molar concentration of haemoglobin in brain tissue was calculated in Section 1.2.4. Hence attenuation by haemoglobin at 800 nm is predicted to be

$$\begin{aligned} attenuation/cm &= \alpha C B \\ &= 0.88 \left(\frac{340}{64.5} \times 1.5\% \right) 5.0 \\ &= 0.35 \qquad [Units: OD/cm\,brain] \end{aligned} \tag{4-2}$$

The value taken for the DPF (B) is that found from the simulation of neonatal brain tissue using polystyrene spheres and its accuracy is difficult to assess†.

The value for cytochrome c oxidase concentration is established on rather scarce data, see Section 1.2.3. Based upon measurements on neonatal rat brain, attenuation by cytochrome c oxidase in tissue at 800 nm is estimated to be

$$\begin{aligned} attenuation/cm &= 2.0 \times 0.005 \times 5.0 \\ &= 0.05 \qquad [Units: OD/cm\,brain\,tissue] \end{aligned} \tag{4-3}$$

---

† In fact it turned out to be 3.85 when measured on the heads of preterm infants, post mortem, see Figure 7.11.

Thus it is the precise detection of cytochrome c oxidase which sets the accuracy required in the measurement of attenuation changes. In order to detect a 10% change in the redox state of cytochrome c oxidase, a measurement accuracy of 0.005 OD cm^{-1} is needed. At this same accuracy, an absolute blood volume change of 1.4% can be detected.

(iii) Multiple scattering in tissue also determines the characteristics of the optics used to launch light into the tissues and to receive the light emerging at some distance away. Emerging light is diffuse and distributed over a large area. Hence, no optical system can increase its radiance. Thus a detector directly in contact with the skin surface is the most efficient method of collecting this light. The collection efficiency of the detector is proportional to the product of its active area and the square of its numerical aperture (NA)[†].

Similarly the degree of collimation of the input light has little effect on the amount of detected light, as multiple scattering in the first few millimetres of tissue will rapidly make any beam diffuse. It is more important to get as much light as possible onto the tissue surface, collimation being very much a secondary factor.

(iv) Other limitations are enforced by the requirement to monitor the newborn infant at the bedside. A safe, flexible method of sending light into the head and collecting the light transmitted is required. The very preterm infant's head can be small, down to 6 cm in diameter, and hence the attachments must be small and lightweight leaving the infant free to move its head. The equipment itself must be capable of being used at the bedside, reliably and safely, both from the view point of electrical and optical hazards. Practical considerations thus limit the active area of the light source and detector at the skin surface to approximately 1 cm^2.

(v) Only three compounds are known to cause wavelength dependent attenuation changes in tissue; the attenuation changes at three different wavelengths are given by

---

[†] The laws of optics for incoherent light state that étendue, the product of the area of a detector aperture and the solid angle it subtends is a constant, regardless of the optical system used to image the aperture. In other words, the radiance of a light source emitting incoherent light cannot be increased.

$$\Delta A_1 = \left\{ \alpha_1(Hb)\,\Delta C(Hb) + \alpha_2(HbO_2)\,\Delta C(HbO_2) + \alpha_1(Cyt)\,\Delta C(Cyt) \right\} Bd$$
$$\Delta A_2 = \left\{ \alpha_2(Hb)\,\Delta C(Hb) + \alpha_2(HbO_2)\,\Delta C(HbO_2) + \alpha_2(Cyt)\,\Delta C(Cyt) \right\} Bd \qquad \text{4-4}$$
$$\Delta A_3 = \left\{ \alpha_3(Hb)\,\Delta C(Hb) + \alpha_3(HbO_2)\,\Delta C(HbO_2) + \alpha_3(Cyt)\,\Delta C(Cyt) \right\} Bd$$

where ΔA_j is the attenuation change, and $\alpha_j(Hb)$, $\alpha_j(HbO_2)$, $\alpha_j(Cyt)$ are the specific extinction coefficients at the wavelength j, $j = 1$ to 3. d is the OPTODE spacing in centimetres. B is the DPF which if known allows non-arbitrary units to be used in determining $\Delta C(Hb)$, $\Delta C(HbO_2)$, $\Delta C(Cyt)$, the changes in chromophore concentrations. The concentrations are found by the solution of simultaneous equations if three wavelengths are used (and assuming B is constant). If more than three wavelengths are used, the extra wavelengths are also useful. For instance they can be used to observe attenuation changes caused by dyes injected into the blood stream (e.g. cardiogreen). Alternatively they can be used as a check on the accuracy of the calculation in a multilinear regression analysis, see Section 7.1. The prototype proposed here will use four wavelengths to allow for such possibilities.

The choice of wavelengths is important. If the absorption coefficients at all wavelengths are nearly identical the solution of the simultaneous equation becomes very unstable (collinear) and noise in the attenuation measurements will be amplified greatly. At the other end of the scale, the wavelength separation should not be too large as this increases the effects of wavelength dependent scattering and hence spectral distortion. The wavelength band 750 to 900 nm: minimises the effects of the absorption bands of cytochromes b and c; oxy- and deoxy-haemoglobin have very different spectra; and the 150 nm wide band cuts down the degree of wavelength dependent scattering effects compared to larger wavelength bands.

The important parameter to maximise in the instrument design is the accuracy of the chromophore concentration measurements. The important equation which governs this is the modified Beer-Lambert law, Equation 3-19, which rearranged and expressed for a single chromophore is

$$\Delta C = \frac{\Delta A}{\alpha B d} \qquad 4\text{-}5$$

Minimising errors in ΔC not only involves mathematical considerations but anatomical and mechanical considerations as well. There are two sources of error in determining ΔC. Firstly, there are the random **statistical** errors which result in ΔC having a mean value μ_C and a standard deviation σ_C. Secondly there are the **systematic** errors $\varepsilon(\mu_C)$ which can result from a variety of sources such as system non-linearity, system drift, mechanical instabilities etc. All of these sources of error need to be taken into account in choosing an instrument design.

Initially, consider the problem of noise in optical measurements. From purely mathematical considerations, for a given set of conditions, there is a trade off involved in increasing the optical pathlength. Consider an optical cell of length d containing a scattering solution which simulates brain tissue. If the number of photons entering the medium in each measurement interval is n_0, the number of exiting photons can be calculated using Equation 4-1. If the optical detector has a quantum efficiency η, the number of **detected** photoelectrons (N) is given by

$$\lg\left(\frac{\eta n_0}{N}\right) = a + bd \qquad 4\text{-}6$$

where a is the fixed optical loss in the first few millimetres resulting from the diffusing of the input beam and b is the brain tissue attenuation (units: OD cm^{-1}) and both are a function of wavelength. d is the tissue thickness and must be greater than 0.3 cm for the equation to be valid. The number of detected photons per measurement interval, N is a source of noise due to the discrete nature of light (photon noise, see Section 4.2.2 which follows)†. This number has a Poisson distribution ($N = f(n;\mu_p)$, see Equation 4-10) when measured over multiple sample intervals. N has a mean value is μ_p and the standard deviation $\sigma_p = \sqrt{\mu_p}$. Thus, the measured optical density has noise superimposed on its mean value $\mu_A = \lg(n_0/\mu_p)$ and a standard deviation σ_A such that††

† n_0 is also a source of noise as the number of emitted photons per measurement interval also has a normal distribution. It can be neglected here as $n_0 >> n$.

†† Other noise sources are neglected here i.e. the system is photon noise limited.

$$\sigma_A = \lg\left(\frac{\mu_p + \sigma_p}{\mu_p}\right) \approx \frac{\lg(e)}{\sqrt{\mu_p}} \qquad 4\text{-}7$$

where the approximation $\ln(1+x) \approx x$ is made for small x, which is valid for $\sigma_p/\mu_p < 0.05$.

In the presence of only one absorbing compound, the noise on the calculated concentration measurement (σ_C) is linked to the optical density noise (σ_A) by the modified Beer-Lambert law

$$\sigma_C = \frac{\sigma_A}{\alpha B d} \qquad 4\text{-}8$$

Here, d is the thickness of tissue and B the differential pathlength factor. Eliminating μ_p from the Equations 4-6, 4-7 and 4-8 gives

$$\sigma_C = \lg(e)\left[\frac{10^{\left(\frac{a+b}{2}\right)}}{\alpha B d\sqrt{\eta n_0}}\right] \qquad 4\text{-}9$$

A plot of σ_C and σ_A against tissue thickness is shown in Figure 4.1 for $a = 3$, $b = 0.8$ OD cm^{-1}, $\alpha = 1$ mM^{-1}cm^{-1}, $B = 5.0$, $\eta = 0.1$ and $n_0 = 1 \times 10^{14}$. This shows that increasing the tissue thickness from near zero (starting at 3 mm to ensure the validity of Equation 4-1) has the beneficial effect of decreasing σ_C. The minimum value is obtained at $d = 2/[b \ln(10)]$ after which it increases logarithmically. Note that the minimum is only a function of b (the optical attenuation per centimetre of tissue). At near infrared wavelengths the minimum standard deviation in concentration occurs for tissue thicknesses of 1 cm where $\sigma_C = 2.2$ nM. Additionally note that σ_C improves as the square root of the intensity of the light source and the quantum efficiency of the detector (though it may improve more rapidly than this in the case of a non-photon noise limited detector).

The simple mathematical analysis above indicates that the optimum tissue thickness for a minimum noise on the calculated chromophore concentration is 1.08 cm, corresponding to an attenuation noise of 0.000012 OD (or 0.003%). Obtaining a noise level of 3 parts in 10^5

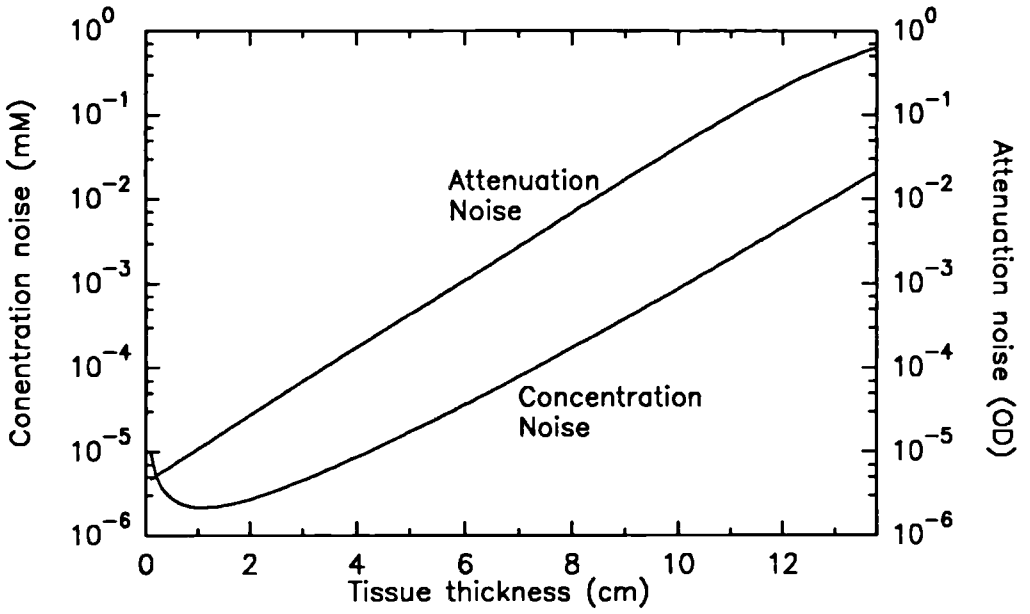

Figure 4.1 Noise level expressed in terms of chromophore concentration and attenuation (optical density) as a function of the thickness of neonatal brain tissue, see text for further details.

may be just possible in a real system, but there are a number of practical reasons why this may not be the overall optimum and these relate to the other sources of uncertainty in the mean value of the concentration, in other words the systematic errors $\varepsilon(\mu_c)$.

Anatomical considerations must be taken into account here, arising from the non-invasive nature of the measurement of oxygenation we wish to perform which requires transillumination through the skull and surface tissues. In any such measuring system, some light has the opportunity of taking a path from source to detector without entering the brain and this acts as a background light intensity which will make attenuation measurements non-linear (this effect has been described in Section 2.1.1.2). It is intuitively obvious that there must be a minimum required separation between the OPTODES before the detected signal will contain an adequate component arising from the brain tissue. However, estimating this value is difficult. As a matter of personal judgement the author would estimate a minimum separation of 3 cm is required for an infant's head of 7 cm (BPD) and the greater the separation the better. On larger heads (adults) where the skull is thicker, this minimum separation should be greater and on smaller (small animal) heads it can be less. Thus for the neonate the author will impose a minimum OPTODE separation of 3 cm which is a much larger

separation than the optimum derived from purely statistical noise considerations. Jöbsis[159] suggested a minimum separation of 4 cm on the adult head based upon experimental measurements.

Mechanical considerations provide another limiting factor, that of maintaining a fixed OPTODE separation (d) on the head. This is a particular problem when studying newborn infants as their skull is not a rigid box, but is quite flexible allowing it to change shape. Any method of attaching optodes must exert minimal pressure and leave the infant free to move its head. Clinical experience with masked ventilation has shown that long term excessive pressure on the head can permanently deform the shape of the skull[8]. If the OPTODE attachment is made to the skin surface, which can move over the skull, this gives rise to a potential change in OPTODE spacing with movement (ε_d). Operation with OPTODES on opposite sides of the head (i.e. transillumination mode), can minimise the effect of side to side movement on OPTODE spacing as these movements are then perpendicular to the line of separation. When optodes are attached at angles of less than 180° and perhaps only a few centimetres apart (i.e. reflectance mode), it may then be necessary to fix their separation mechanically.

The maximum acceptable fractional mechanical change in OPTODE spacing (ε_d/d) is related, via Equation 4-1, to the required accuracy of the attenuation measurements in optical density per centimetre of brain tissue (0.005 OD cm^{-1} to detect a 10% change in cytochrome c oxidase redox state). Thus ε_d/d must be less than 0.006, which means ε_d is of the order of 0.3 mm.

The above points illustrate the complexity involved in selecting the optode separation required to achieve the best possible accuracy for concentration measurements. This decision is made even more difficult by the semi-quantitative description of some of the problems. The following points are however apparent:

i) Increasing the separation of the optodes increases the probability of looking at oxygenation deep within the brain and minimises errors due to the skull and surface tissues.

ii) Stable fixation of optodes to the head is a major limitation on accuracy however errors are reduced by measuring in transillumination.

iii) Having statistical errors due to photon noise very much less than the systematic errors is only advantageous if these systematic errors can be detected and eliminated. Otherwise it is better to operate at optode separations where the magnitude of the

photon noise is similar to that of the systematic errors.

Based upon the above considerations, the final decision was to design the instrument to operate at as large an OPTODE separation as possible and to achieve a level of photon noise that resulted in an attenuation noise σ_A of approximately 0.005 OD per measurement interval. This is a lower level of attenuation noise than the 0.005 OD cm^{-1} brain tissue which has been discussed so far to detect an 10% change in cytochrome c oxidase redox state. However this value assumed a single wavelength measurement of a single compound. As Hb, HbO_2 and Cyt are to be measured at four wavelengths, a lower attenuation noise will in practice be required at each of the wavelengths to achieve the same chromophore concentration noise. The mathematical analysis of the variance of the three chromophore concentrations measured at multiple wavelengths is described later in Section 7.1.1.2.

Figure 4.1 shows that this level of attenuation noise should be possible at optode separations up to 8.0 cm at reasonable values for the optical input power (≈0.1 mW), detector quantum efficiency (10%) and measurement interval (1 second).

4.2 CHARACTERISTICS OF OPTICAL COMPONENTS

The design specification in Section 4.1 outlined a number of the important points to be considered in the design of a cerebral oxygenation measuring system. Any spectroscopy system requires some form of monochromatic light source and a light detection system. The possible optical components suitable for this system are given in Table 4.i and these can be employed in a rather large number of possible combinations. The characteristics of the individual components are discussed in the sub-sections that follow.

4.2.1 Fibre optics

For maximum efficiency, a direct attachment of the light source and detector to the head is preferred, but this may not be possible for reasons of safety or convenience. Should fibre optics be required, then there is an efficiency penalty in their use.

Table 4.i A table of optical components suitable for incorporating into a clinical near infrared spectrophotometer.

Light Source		
Type	**Filtering**	**Delivery**
"White light"	Monochromator/ Interference filter	Fibre optics
Quartz-halogen lamp		
C.W. arc lamp		
Pulsed arc lamp		
Monochromatic		
LED		Direct/ Fibre optics
Semiconductor laser	None	

Detector		
Type	**Signal conditioning**	**Delivery**
Photomultiplier tube	Lock-in amplifier Boxcar integrator Photon counting	Fibre optics
S20 extended		
GaAs		
S1		
Photodiode	Lock-in amplifier Boxcar integrator	Direct/ Fibre optics
Silicon p-i-n		
Silicon avalanche		

The first requirement of a practical system is that the fibres must be made of glass, as plastic fibres absorb near infrared light too strongly, even over a distance of a few metres. This immediately sets an upper limit on the size of the individual fibres since a flexible connection is required. The maximum usable single glass fibre diameter which provides adequate flexibility is 250 μm.

Incoherent large area light sources, e.g. quartz-halogen or arc lamps, require larger diameter fibres than 250 μm to collect their output efficiently. To accomplish this, fibre optic bundles with diameters up to 10 mm diameter containing many thousands of small glass fibres

Table 4.ii Characteristics of typical optical fibre bundles, data supplied by Eurotec Optical Fibres (Doncaster, U.K.).

Individual fibre characteristics	
Nominal diameter	50 μm
Numerical aperture	0.54
Attenuation	0.1 dB/m
Bundle characteristics	
Packing fraction	> 80%
Broken fibres	< 3%
Overall transmission 700-900 nm, 1 metres	> 50%
Overall transmission 700-900 nm, 2 metres	> 40%

are required. The end area of such a bundle has gaps between the fibre cores, so it only collects a fraction of the light which is incident upon it. Characteristics of a typical glass fibre optical bundle (Eurotec Optical Fibres Ltd, U.K.) can be seen in Table 4.ii and indicates coupling efficiencies up to 50%.

Another important parameter of the optical fibres is their numerical aperture, which defines the input angle of the incident light which can be coupled into the fibre. This varies a great deal between different types of fibre and for the type of glass fibres normally used in bundles, the numerical aperture typically lies in the range 0.5 to 0.64. This corresponds to an acceptance (half) angle of 30° to 40°. The effective numerical aperture of the same glass fibre in long fibre bundles (greater than a few metres) may however be smaller than this.

In silica optical fibres, fibre attenuation can be negligible over kilometre lengths, but this is achieved at the expense of low numerical apertures, near 0.21. The glass optical fibres designed for use in bundles typically have an attenuation of 0.1 dB/m as opposed to the attenuation of silica fibres which is of the order of 0.1 dB/km. The final source of loss to be taken into account is that of reflection from the end faces (Fresnel reflection). The magnitude of the reflection loss for unpolarised light at an air/glass interface is 4% for angles of incidence from 0 to 45°.

4.2.2 Detectors

The type of optical detector and the method of detector conditioning used offer a wide scope of both possibilities and sensitivities. An adept description of the characteristics of optical detectors is available in the literature[160].

The light that emerges after travelling through many centimetres of highly scattering tissue is no longer coherent to any degree. Therefore any detection method which relies on the coherent properties at optical frequencies cannot be used. Section 4.1 specifies that the maximum size of a detector which can be considered for direct attachment to a newborn infants head is 1 cm^2. If fibre optics are used, then the maximum detector area is somewhat reduced to 20 mm^2 (diameter 5 mm) as large glass fibre optic bundles are impractical due to their excessive weight and poor flexibility.

The ultimate noise determining factor is that of light itself, i.e. photon noise. Under circumstances of the random arrival of photons at the detector, the probability that n photons will arrive in the measurement interval τ is given by the Poisson distribution

$$P(n,\tau)=\frac{(\eta N_p\tau)^n}{n!}e^{-\eta N_p\tau} \qquad \text{4-10}$$

where N_p is the average photon arrival rate and η is the quantum efficiency of the detection process i.e. the probability of a conversion of a photon to a photoelectron. The mean (μ_p) and the variance (σ_p^2) are then

$$\mu_p=\eta N_p\tau \qquad \text{4-11}$$

$$\sigma_p^2=\mu_p \qquad \text{4-12}$$

Hence the signal to noise ratio (SNR) for purely Poissonian noise S'_r is μ_p/σ_p, which is given by

$$S'_r=\sqrt{\eta N_p\tau} \qquad \text{4-13}$$

There is an additional noise contribution from detected dark emission μ_d (shot noise)

in the measurement interval τ, arising either from unwanted background light sources or thermal emission from the detector. The variance of this effect is of the same form as above $\sigma_d^2 = N_d\tau$. Hence the overall signal to noise ratio S_r including the effect of shot noise is

$$S_r = \frac{\eta N_p \tau}{\sqrt{\eta N_p \tau + N_d \tau}} \qquad 4\text{-}14$$

This equation illustrates factors which affect the SNR of the detection system. To obtain a high SNR in a fixed detection interval τ, the dark emission should be much less than the optical signal, the quantum efficiency near unity and the photon arrival rate high. Note that in situations where the dark emission noise term is negligible in comparison with the photon noise term, the detector is then operating photon noise limited i.e. its SNR is only dependent upon the intensity of the light striking it. An improved signal to noise ratio is always available at the expense of increasing the measurement interval.

Equation 4-14 is written in terms of photon arrival rates and is best used in systems where it is convenient to talk in terms of individual photons such as in photon counting photomultiplier and photodiode systems. A similar equation can be written when the arriving photons are considered to generate a continuous photocurrent. For an unilluminated, biased photodiode, the shot noise I_n is given by

$$I_n = \sqrt{\left(2qI + 4qI_0\right) B} \qquad 4\text{-}15$$

where q is the electronic charge, B the bandwidth, I the diode current and I_0 is the reverse bias saturation current. I and I_0 are related by the standard diode equation

$$I = I_0 \left[e^{\left[\frac{qV}{kT}\right]} - 1 \right] \qquad 4\text{-}16$$

Here V is the diode bias voltage, k Boltzman's constant and T is the absolute temperature.

A photodiode is typically used in one of two modes of operation. Firstly consider the diode with a zero bias voltage applied across it. As the photodiode is unbiased, it behaves like a Johnson noise source with a shunt resistance R_{sh} calculated from the gradient (dV/dI) of Equation 4-16, evaluated at zero voltage

$$R_{sh} = \frac{kT}{qI_0} \qquad 4\text{-}17$$

The zero bias noise current is then

$$I_n = \sqrt{\frac{4kTB}{R_{sh}}} \qquad 4\text{-}18$$

Which can be seen to be identical to Equation 4-15 evaluated with $I = 0$.

However, in most situations, the photodiode is used reverse biased to obtain a lower shunt capacitance and hence greater speed, then $I = -I_0$ and the shot noise current is given by

$$I_n = \sqrt{2qI_0B} \qquad 4\text{-}19$$

When the diode is illuminated, the current resulting from incident photons is i_p, related to the photon arrival rate by $i_p = \eta q N_p$. The overall signal to noise ratio is then given by

$$S_r = \frac{i_p}{\sqrt{2qi_pB + 2qi_0B}} \qquad 4\text{-}20$$

Comparison of this with Equation 4-14 shows that they are identical when the observation time τ and bandwidth B are linked by $\tau = 1/2B$, a standard result of the sampling theorem. Note however that in photon counting systems the equivalence is not identical as low energy noise events can be selectively removed (see Section 4.2.3.3), thus improving the signal to noise ratio in these circumstances.

The above Equations 4-14 and 4-20 allow a comparison to be made between the various types of detectors that are available by using a standard figure of merit known as D^* (D-star). At a given wavelength D^* is defined as the root mean square (rms) signal to noise ratio (V_s/V_n) in a 1 Hz bandwidth (B), per rms incident radiant power (P_s) per square root of detector area (A_D), measured over a full 2π steradian of input solid angle[†].

[†] On occasions where the full 2π steradian are not illuminated, an alternative definition $D^{**} = D^* \sin\theta$ (units: cm $Hz^{1/2} ster^{1/2} W^{-1}$) can be used for a limited acceptance angle θ.

$$D^* = \frac{\sqrt{A_D B}}{P_s}\left(\frac{V_s}{V_n}\right) \qquad [Units: cm\,Hz^{\frac{1}{2}}W^{-1}] \tag{4-21}$$

If comparisons are required between detectors without taking their area into account then the A_D term is dropped and detectivity (D) is defined as

$$D = \frac{D^*}{\sqrt{A_D}} \tag{4-22}$$

Alternatively the quality of a device can be expressed as the noise equivalent power (P_N), the signal power required for a signal to noise ratio of unity at 1 Hz bandwidth

$$P_N = \frac{1}{D} \tag{4-23}$$

A comparison of detectivity values of various detectors has been published[161] and is reproduced in Figure 4.2 together with their detector areas to allow the calculation of D^* †. Examination of Figure 4.2 at wavelengths near 900 nm show that the photomultiplier tube is an order of magnitude better in detectivity than the silicon photodiodes. The difference becomes more marked when D^* is considered as the silicon detectors are much smaller in area compared to the photomultiplier tubes.

The definitions of the figures of merit used in the comparison above are calculated for a signal to noise ratio of unity. The system specification for this instrument requires signal to noise ratios of approximately 100 and this alters the situation somewhat. Rearranging Equation 4-14 and solving for the photon rate N_p gives

$$N_p = \frac{S_R^2}{\eta\tau}\left[\frac{1+\sqrt{1+\frac{4\tau N_d}{S_R^2}}}{2}\right] \tag{4-24}$$

† In the case of photomultipliers the relation between D and D^* may not simply be related to area because of leakage currents.

Hence, in situations where the signal to noise ratio is large and the measurement interval is short then the dark count N_d plays a less significant role than it does at a signal to noise ratio of unity. When the square root term is very much less than the dark count, it can be ignored and

$$N_p \approx \frac{S_r^2}{\eta\tau} \qquad 4\text{-}25$$

In this situation, the primary requirement is for a large value of quantum efficiency to reduce the incident photon rate for a given signal to noise ratio in a given period of time.

An additional consideration to be added at this point is the effect of using pulsed light sources and gated detectors. If a gated detector is used with a duty cycle ($\gamma = t_{on}/\{t_{on} + t_{off}\}$) then for a real measurement interval τ, the effective measurement interval of the detector is $\tau' = \gamma\tau$ and hence the effective dark count of the detector is reduced to $N_d' = \gamma N_d$. To achieve the same average photon rate during τ, the peak photon rate must be increased to N_p/γ. This modifies Equation 4-24 to

$$N_p = \frac{S_R^2}{\eta\tau}\left[\frac{1+\sqrt{1+\frac{4\gamma\tau N_d}{S_R^2}}}{2}\right] \qquad 4\text{-}26$$

How does this equation predict how real detectors will perform? From Figure 4.2, the detectors which are possible candidates for this system (i.e. those that have a high detectivity in the NIR) are the photomultiplier tubes with gallium arsenide, multialkali or S1 photocathodes and silicon photodiodes either normal or avalanche types. A list of typical devices with detector areas of near 1 cm^2 are given in Table 4.iii. All these particular devices are manufactured by Hamamatsu Photonics K.K., Japan. Other companies supply similar devices, for example RCA (U.S.A.), EMI (U.K.), Centronics (U.K.).

To compare the various detectors, some typical measurement conditions must be specified. The required signal to noise ratio (100:1) has already been discussed. A clinically acceptable measurement interval is likely to be in the range of 1 to 20 seconds, a value of 5 seconds is taken for this comparison. The one parameter which is thus available for manipulation is the duty cycle. This can be varied depending on the type of light source and

Table 4.iii Detailed characteristics of optical detectors which have a high D^* in the near infrared spectral region.

Type	Hamamatsu Part No.	Q.E. [900 nm]	Dark Current (e^-/s)	Area (mm^2)	D^* [900 nm] (cm $\sqrt{Hz}$ W^{-1})
PMT					
S20 Ext	R936	0.1%	3×10^3	192	8×10^{13}
GaAs	R636	3%	3×10^4	36	3×10^{14}
S1	R406	0.1%	9×10^5	192	4×10^{12}
Photodiode					
Avalanche	S2385	70%	5×10^8	20	2×10^{13}
PIN	S1723-06	83%	6×10^9	100	5×10^{12}

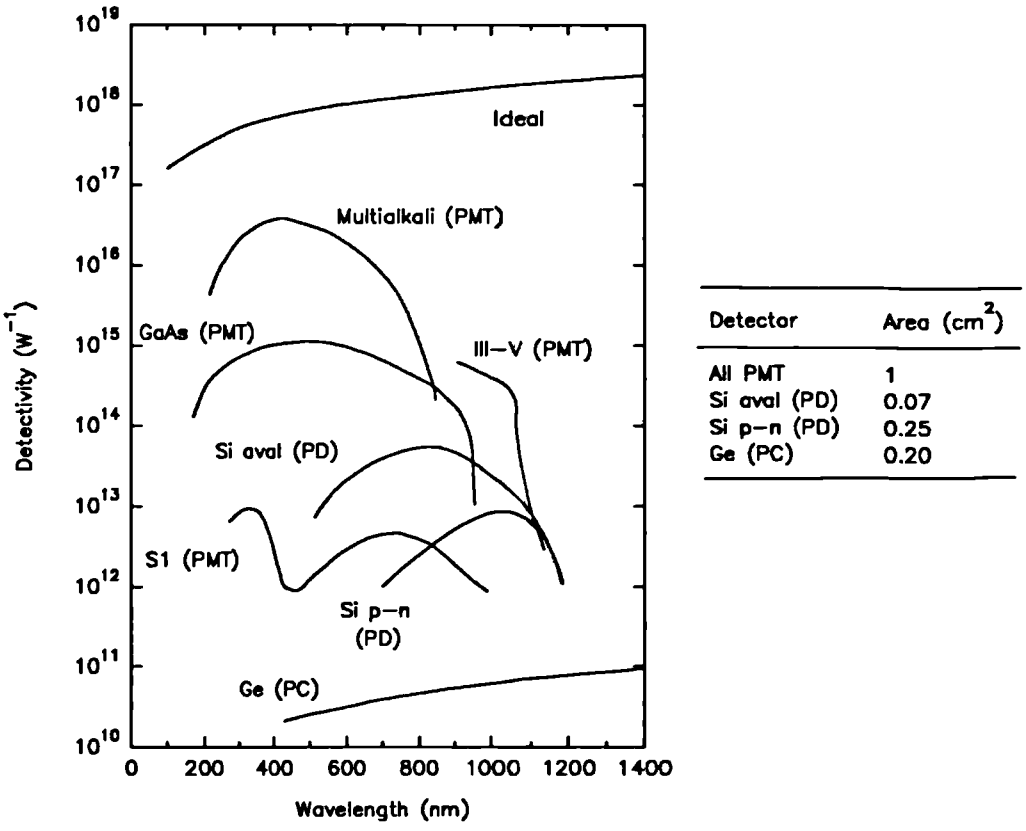

Figure 4.2 Detectivity of various detectors with near infrared sensitivity.

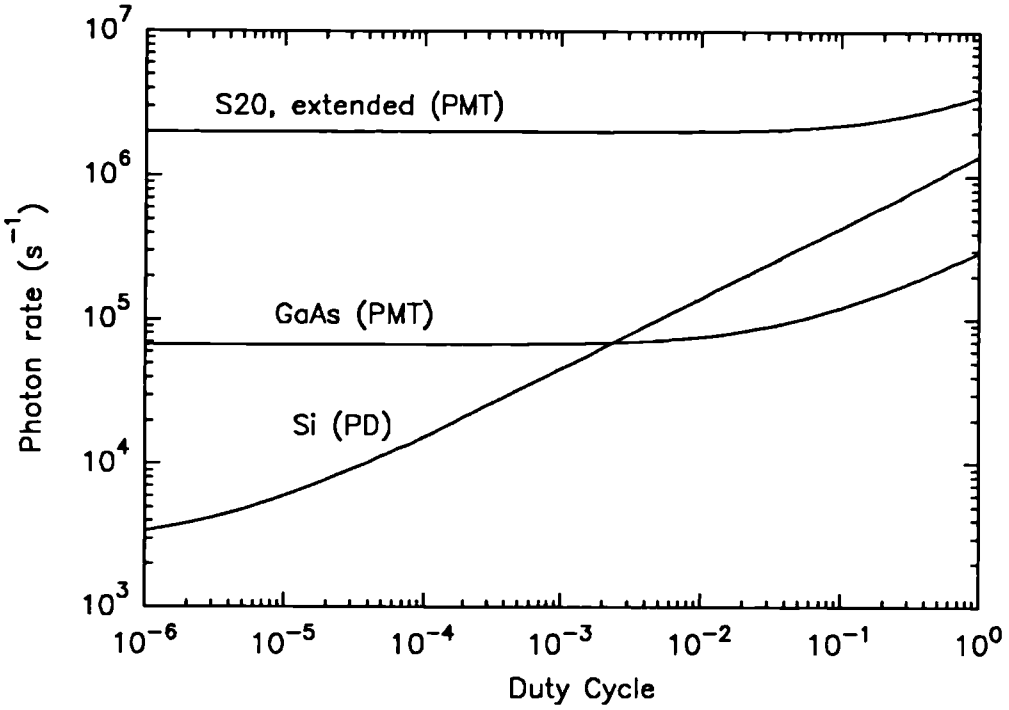

Figure 4.3 Required photon rate for a signal to noise ratio of 100, measured in 5 seconds at a fixed average input power. The effects of the 3 different detectors from Table 4.iii at different duty cycles.

the detector circuit employed. Figure 4.3 shows the effect on the required average light intensity (photon rate) at the detector, for the conditions specified above, and for duty cycles between 0.000001 and 1.0 for three detectors in Table 4.iii (the S1 PMT omitted, since it is inferior to the S20 at 900 nm).

At very low duty cycles, the dark noise of the detector becomes insignificant and it is the quantum efficiency of the detector which determines the light level necessary under these conditions. In this situation, silicon diodes are clearly the best detectors requiring less light by a factor of 23 over the best photomultiplier tube. At the opposite end of the duty cycle scale, near unity (continuous measurement) the required photon rate depends upon a combination of shot noise and quantum efficiency effects. Clearly here the gallium arsenide photomultiplier tube is the best detector. At intermediate values, the graph shows the way in which duty cycle affects the photon rate. For detectors with high dark counts such as the silicon photodiode, photon rate decreases as the square root of duty cycle until very low duty cycles are reached. For low noise detectors such as the gallium arsenide photomultiplier tube,

photon rate decreases at a much lower rate than the square root of duty cycle and eventually crosses the silicon photodiode curve at a some value of duty cycle.

In summary, based on this criterion, the gallium arsenide photomultiplier tube is the best detector at long duty cycles whereas the silicon photodiode is best at very short duty cycles. The crossover point occurring at a duty cycle of about 0.004. Short duty cycles are inherently favourable, improving the performance of the gallium arsenide photomultiplier tube by a possible factor of 6 and the silicon photodiode by a possible factor of 1000[†].

As well as these theoretical problems, there are the practical ones which need to be noted. Photomultiplier tubes require protecting from excessive current to prevent them from damage, and their quantum efficiency is temperature dependent, especially near the long wavelength cut-off region. Photodiodes are less susceptible to damage from excessive light but also have temperature dependent quantum efficiencies, although these are not normally as severe as in PMTs.

4.2.3 Detector signal conditioning

Photomultiplier tubes and photodiodes all produce a photocurrent proportional to optical intensity. Therefore the simplest detector would be one that directly measured current in some way, either as an average value, a peak value or an integrated value measured over a specific time interval. However, there are a number of other measurement regimes which can be beneficially used at low light levels.

4.2.3.1 *Phase sensitive detectors*

In this technique, the light source is modulated (most efficiently at a 50:50 duty cycle) at a convenient fixed frequency and the modulation frequency is additionally fed, as a reference frequency, to the detector circuitry. The signal from the detector and the reference are mixed (multiplied) so that only signals (and noise) in phase with the reference frequency are amplified. The noise bandwidth of the detector circuit can easily be less than 1 Hz centred on the reference frequency.

[†] Note that in practice the duty cycle cannot continue to be made smaller and smaller whilst maintaining the same average power. A limit is reached when the peak optical power exceeds the maximum allowed for a given detector.

The reference frequency is best selected in the kilohertz range where amplifier noise is significantly less than near zero frequency. Interference from ambient room lighting and detector dark current is largely rejected but does act as a noise source.

4.2.3.2 *Boxcar integration*

This is a form of signal averaging for pulsed light sources. The signal from each light pulse is integrated to form a voltage which is then itself averaged in some manner with similar voltages from a number of other pulses. The most suitable choice of the averaging method depends on the duty cycle and the total averaging time. Averaging can be performed in an analogue or digital fashion.

4.2.3.3 *Photon counting*

Photon counting is only applicable when the arrival of single photons can be detected as individual events and is traditionally used with photomultiplier tubes at high gain (approximately 10^7). More recently, avalanche silicon photodiodes biased above breakdown potential[162] have also been used, but their small physical area, 0.1 mm diameter, makes them too small to be of use in this project.

When a photomultiplier tube is operated in photon counting mode, individual photons or thermal emission produce an electron at the photocathode which is subsequently amplified by accelerating the electron to hit "dynodes" where the single electron produces a number of secondary electrons. After colliding with typically 10 dynodes the electron pulse will consist of typically 10^7 electrons spread over a 3 to 20 ns wide pulse, representing a peak current of approximately 0.16 mA. This current when passed through a 50 Ω resistive load produces a voltage of adequate size to be detected electronically by a voltage comparator and hence converted into a digital pulse.

The main advantage of photon counting is that it reduces dark current when compared to standard detection methods using the same PMT, thus achieving a higher signal to noise ratio. The way that this is achieved is illustrated with reference to Figure 4.4. Electrons resulting from thermal emission from the dynodes have a low pulse height energy distribution, shown in Figure 4.4 by the broken line. Electrons emitted from the photocathode as a result of incoming photons or photocathode thermal events, produce a distribution of pulse heights

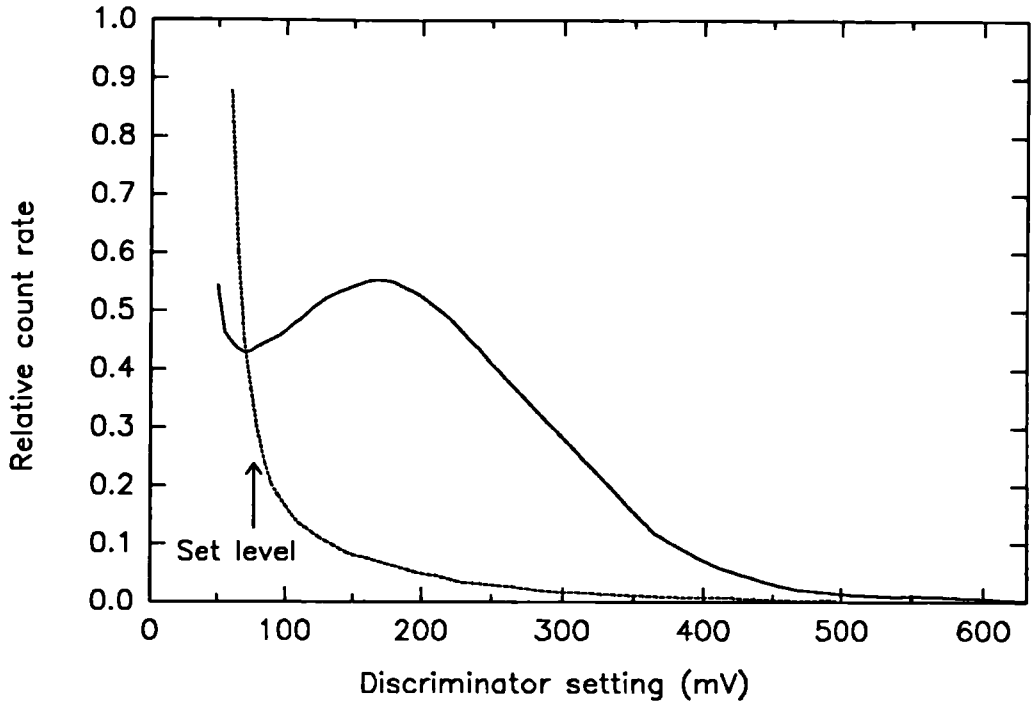

Figure 4.4 Pulse height distribution of both photon and dark photoelectrons (solid line) and just dark electrons (broken line) for the Hamamatsu R636 photomultiplier tube.

of higher energies, as shown in by the solid line in Figure 4.4. This energy spread is due to the statistical nature of the electron emission from the dynodes. By selecting a voltage comparator level at the position shown, virtually all the thermal emission from the dynodes is rejected with minimal effect on photon detection. Note that thermal emission from the photocathode cannot be reduced by this method.

The major disadvantage of photon counting concerns linearity at high photon arrival rates. If two photons arrive within the time resolution limit of the system, then only one of them is recorded, hence the detector under reads. This is known as "pulse pile-up error".

The "state of the art" in commercially available photon counting system is a maximum of 100 MHz count rate. For pulse pile up errors of less than a few percent however, the maximum average count rate must be kept below about tenth of the maximum instantaneous rate, in this case nearer 10 MHz. The statistics of pulse pile-up errors is well known, and in some cases can be corrected for, see Section 5.11.3.

4.2.4 Light sources

For convenience this section is split into two: one describing the characteristics of broadband white light sources, such as quartz-halogen and arc lamps; the other describing monochromatic sources such as semiconductor laser diodes.

4.2.4.1 *"White light" sources*

"White light" sources include quartz-halogen lamps and pulsed or continuous arc lamps. Their major advantage is the range of wavelengths they produce, any of which can be selected by means of a monochromator or interference filter. The amount of power which can be collected from various continuous wave lamps is shown in Figure 4.5, reproduced from the sales literature of Oriel Ltd. (Stratford, CT, USA). This data indicates the lamp irradiance at 50 cm from the bulb of a quartz-halogen and Xenon arc lamp. The amount of power into a collimated aperture of f/1.0 (numerical aperture 0.5) is obtained by multiplying the y-axis values by 1.15 (for all wavelengths longer than 500 nm), the new y-axis units being mW. It is apparent that apart from at the spectral peaks of the xenon lamp, the collected power is similar for both type of lamps. It should be noted that krypton filled lamps have more favourable NIR peaks.

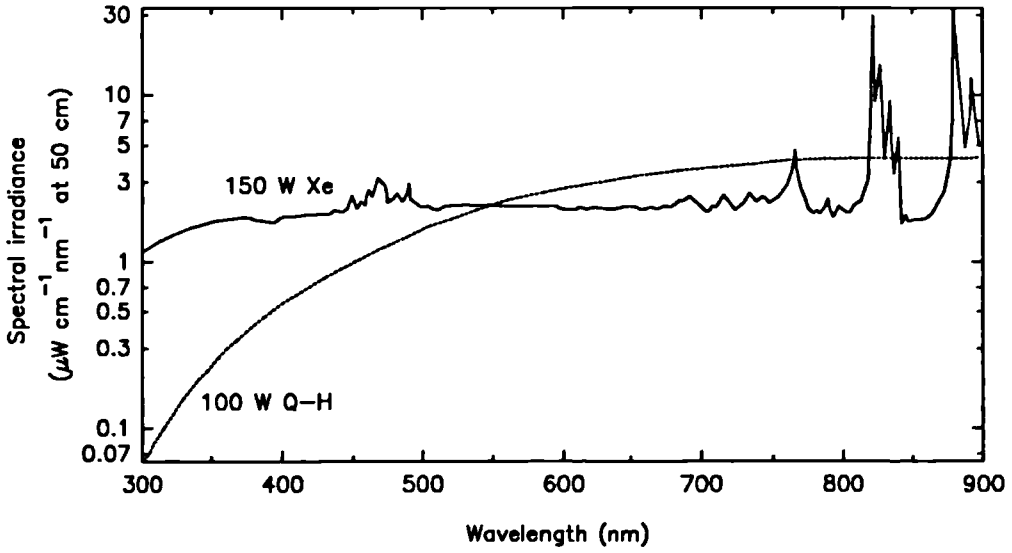

Figure 4.5 Spectral irradiance of a 150 W Xenon arc lamp and a 100 W quartz halogen lamp at a distance of 50 cm from the source.

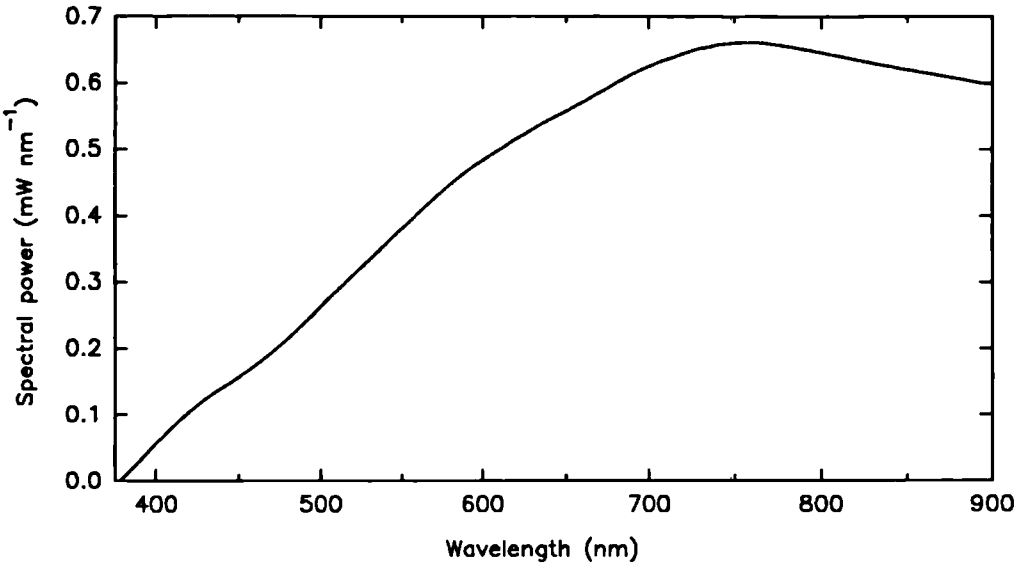

Figure 4.6 Spectral power at the output of a 3.2 mm diameter glass fibre bundle coupled to a 100 W quartz halogen lamp.

Also of importance is the size of the emitting area, which if a similar f/1.0 lens is used to refocus the light onto a fibre, will define the fibre size required to catch all this optical power. For the halogen lamp, the filament size is 9.7 mm^2, while the arc size of the 150 W Xenon lamp is 1.1 mm^2. On this basis, an arc lamp, with a similar arc size to the filament size of a 100 W quartz halogen bulb would be one of 1000 W. Such a system is unfortunately not practical for a bedside monitor due to the large size of the power supplies and the fans or water cooling necessary for the removal of unwanted heat.

The small arc size could be useful for coupling into smaller optical fibre bundles more efficiently. However, as the proposed fibre optic bundle has a maximum area of 20 mm^2 and a NA of 0.5, the smaller arc lamp source size represents only a minor benefit.

A further data sheet from Oriel reveals the power available from an optical fibre bundle coupled to a 100 Watt quartz-halogen lamp (Oriel USA, 77501). This is shown in Figure 4.6 for the case of a 3.2 mm (NA 0.56) diameter glass fibre optic bundle 0.9 m long and provides a practical figure for a fibre coupled 100 W quartz-halogen lamp of 0.6 mW/nm in the NIR (with no more than a factor of two improvement expected for similar wattage arc lamp).

Pulsed arc lamps generally offer less average power (up to 50 Watt electrical) at efficiencies similar to arc lamps. The disadvantage of a slightly lower average power can be

offset by the very high peak powers available at low duty cycles (of the order 0.05%). A large practical disadvantage of these lamps is the high acoustic noise and electrical interference which results from the large current pulses, up to 1000 amps, at pulse widths of a few microseconds.

The production of monochromatic radiation from white light sources requires the use of either a grating monochromator or an interference filter. Interference filters offer the highest optical throughput, typically 50% transmission at bandwidths of 5 nm, when placed in the parallel part of the optical beam within a collimator. Use of collimators up to f/1.0 optics does not cause problems. Grating monochromators offered tunability but at the expense of physical size and throughput. The speed of monochromator optics is typically f/4 with an input aperture of 1 mm wide by between 5-15 mm high, to obtain a 5 nm bandwidth. Thus, monochromators are approximately a factor of 20 to 100 less efficient than interference filters in producing monochromatic light.

4.2.4.2 *Monochromatic light sources*

Monochromatic light sources emit light which is coherent to some degree. This description covers a multitude of devices from the purest single frequency laser to light emitting diodes (LEDs).

There are two types of coherence, temporal and spatial. Temporal coherence describes the frequency (or wavelength) pureness and is commonly measured by a coherence length. This length describes the distance over which the phase of the light wave can be predicted and is important when considering interference between two light waves with different path lengths. A rough estimate of the coherence length of a laser is that it is the same as the cavity length, which for gas lasers is of the order of one metre and semiconductor lasers a few millimetres. Spatial coherence describes the spatial predictability of phase along a propagating wavefront.

The use of large lasers is not practical in the design of a bedside instrument, being too bulky, fragile and expensive. Semiconductor lasers are much more convenient and emit in the NIR. The degree of temporal coherence is not of great importance in this application, any bandwidth less than 5 nm is adequate, but the spatial coherence is important as it affects the ability to couple the light output into optical fibres. The modal structure of semiconductor lasers varies with the manufacturing technique and is largely dependent upon the dimensions

of the emitting area and the method by which lasing is confined to this region. The number of lateral modes for all types of semiconductor laser diodes is normally one as the junction thickness is typically a few microns thick. The width of the emitting area is more variable and defines the number of transverse modes which can exist (i.e. that satisfy Maxwell's equations). Ideally this would be a single mode, since for a single gaussian mode, the laser beam can be focused to a diffraction limited spot with approximately the dimensions of its wavelength. This facilitates coupling into a single small optical fibre. Single optical fibres offer much better coupling efficiencies over the bundles described earlier and fibre to fibre connectors are readily available.

As the number of transverse modes increase then the light beam behaves more like incoherent light, obeying the law of étendue. This would appear to be leading to the same problems that apply to coupling "white light" sources into optical fibres. However, the radiance of the emitting area of a semiconductor laser diode ($\approx$1 W $nm^{-1}ster^{-1}mm^{-2}$) is much higher than that of the white light source (quartz-halogen $\approx$0.22 mW $nm^{-1}ster^{-1}mm^{-2}$ or of a Xenon arc $\approx$8.4 mW $nm^{-1}ster^{-1}mm^{-2}$). The high radiance coupled with the greater accessability of the emitting area of a laser diode compared to a white light source does lead to significant benefits in using laser diodes.

A maximum emitting irradiance exists for semiconductor lasers, just as with black body radiators. The limit is set by the optical damage threshold at the facet of the cleaved semiconductor face. Impurities at the surface of the facet and surface imperfections absorb some of the radiation, resulting in heating and facet damage at high optical powers. Improvements in processing technology may increase the radiance available from semiconductor lasers in the future. The time constant of this type of damage is very fast (a few nanoseconds), therefore this limitation applies to the peak optical irradiance from the facet, rather than average facet irradiance. The limitation on average power is set by the ability to remove unwanted heat from the junction area.

To obtain very large powers from laser diodes, a large emitting area is therefore required. Typically high power devices have an overall emitting width of 400 μm with a height of 2 μm. The 400 μm may represent a single device or it may be split into many small, largely independent, devices dependent upon the manufacturer. As there is no spatial coherence with these high power devices across their width, étendue applies and therefore the emission angles are very important in determining the efficiency with which output light can be collected into a fibre optic of finite size. The output beam is elliptical, as the emitting

angles are different in the two planes. The emitting angle in the plane perpendicular to the narrow (approximately 2 μm) width is larger than the emitting angle in the parallel direction. These angles are very much device dependent.

Coupling efficiencies greater than 20% can normally be achieved into single optical fibres with core diameters of the same size as the largest dimension of the emitting area. The highest efficiency is obtained (up to 50%) if the fibre is "pig-tailed" close to the laser diode facet during packaging by the manufacturer. As the electrical efficiency can also be of the order of 25%, overall efficiencies of optical power into a fibre compared to electrical power can be better than 5%. This should be compared to the white light source efficiency of nearer 0.2%. However, note that laser diodes also have some disadvantages such as a temperature dependence of both wavelength and output power.

Table 4.iv and Table 4.v shows the features of a number of commonly available laser diodes for pulsed and continuous wave semiconductor laser diodes respectively. The tables have been compiled to include the highest power devices. They are not comprehensive of all manufacturers, and due to the speed of developments in this field they are probably already out of date.

The tables are very different to similar ones which were drawn up at the beginning of this project. At that time c.w. laser diodes were only available in sample quantities and at power of a few milliwatts, since then the available c.w. powers have gone up by more than a hundred fold, and the shortest available wavelength moved from 820 nm to 670 nm. Developments in pulsed laser diodes have not been very dramatic, that is until recently with the announcement of MOCVD devices such as the C86083E from RCA Inc Electro Optics, Canada. These devices promise to replace the older style pulsed laser diodes.

Table 4.iv Characteristics of commercially available PULSED high power semiconductor laser diodes.

Manufacturer	Model No.	Wavelengths	Linewidth	Emitting size	Peak Power	Pulse Length	Duty cycle	Average Power
Laser Diode Labs	LA-68	775-875 nm	3.5 nm	2 x 400 µm	12 W	100 ns	0.05%	6 mW
Laser Diode Labs	LD-67	904 nm	3.5 nm	2 x 400 µm	16 W	200 ns	0.1%	16 mW
Laser Diode Labs	CVD-97*	820-870 nm	3 nm	2 x 381 µm	25 W	100 ns	0.1%	25 mW
RCA	C86040	800-900 nm	5 nm	2 x 150 µm	3 W	100 ns	0.05%	1.5 mW
RCA	C86083E*	850 nm		1 x 300 µm	10 W	100 ns	0.1%	10 mW
Spectra Diode Labs	SDL-2100	810-870 nm	2 nm	1 x 100 µm	1 W	100 ns	1%	10 mW
Spectra Diode Labs	SDL-3200	810 nm	5 nm	0.9 x 10 mm	<160 W	150 µs	1.5%	1.6 W
STC	LA10-2	904 nm	5 nm	2 x 230 µm	12 W	200 ns	0.2%	24 mW
STC	LB1	800-900 nm	5 nm	0.5 x 100 µm	0.5 W	350 ns	15%	75 mW

* MOCVD devices, recently introduced, with improved temperature characteristics.

Table 4.v Characteristics of commercially available CONTINUOUS WAVE high power semiconductor laser diodes.

Manufacturer	Model No.	Wavelengths	Linewidth	Emitting size*	Average Power
Hitachi	HLP5400	1200 nm		STM	5 mW
Hitachi	HLP1322	1310 nm		STM	10 mW
Hitachi	HLP1541	1500 nm		STM	5 mW
Toshiba	TOLD9211	670 nm	0.5 nm	3 x 13 μm	5 mW
Technoexan		780-860 nm	3 nm	1 x 100 μm	500 mW
Sharp	LT031	750 nm	0.2 nm	STM	10 mW
Sharp	LT024	780 nm	0.2 nm	STM	30 mW
Sharp	LT017	810 nm	0.3 nm	STM	50 mW
Sharp	LT015	830 nm	0.3 nm	STM	40 mW
Sharp	LT011	840 nm	2 nm	STM	5 mW
Sony	SLD100 and SLD200 series, similar devices to Sharp				
Sony	SLD3xx	770-840 nm		Broad area	up to 1 W
SDL+	SDL5400	820-860 nm	2 nm	1 x 3 μm	100 mW
SDL+	SDL2400	790-830 nm	3 nm	1 x 200 μm	up to 1 W
SDL+	SDL3400	790-830 nm	3 nm	1 x 1000 μm	10 W

* STM- Single Transverse Mode, a small emitting area of approximately 1 x 3 μm.

+ SDL- Spectra Diode Laboratories.

CHAPTER 5

DESIGN AND TESTING OF THE CLINICAL NEAR INFRARED SPECTROPHOTOMETER

A considerable amount of information has been presented on both the system design specification and the characteristics of optical components available for the instrument design. A decision had now to be made regarding which optical components would best match the specification of the instrument.

White light sources were too bulky to place directly against the infant's head, and would have therefore required coupling with fibre optics. It had been shown that fibre optic coupled white light sources using interference filters produced about 0.3 $mW\,nm^{-1}$. The data in Table 4.iv and Table 4.v also showed that fibre optic coupled semiconductor laser diodes could match or better this value and were in addition more efficient and compact. The only reason for preferring a white light source (pulsed or c.w.) was the greater choice of wavelengths. However the wavelengths available from semiconductor laser diodes appeared to be adequate for this instrument. Semiconductor laser diodes were therefore the preferred choice for the light source.

The theoretical analysis of optical detectors, in Section 4.2.2, lead to a preference for a pulsed light source with a short duty cycle and high average power. At the beginning of this project the choice was easy, as average powers from pulsed and c.w. diodes were identical, near 4 mW. The pulsed diodes LA-68 and LD-68 (Laser Diode Labs., USA) provided the largest range of wavelengths available for a single style of laser diode. However, the LA8-02

from ITT Components Group, U.K. was used as a cheaper equivalent to the LD-68 at 904 nm. Thus the LA-68 and LA8-02 laser diodes were the most obvious devices for the light source†. The use of pulsed sources also meant that the different wavelength diodes could be pulsed sequentially and hence multiplexed onto a single detector.

The selection of a detector was more difficult. The theoretical analysis of Section 4.2.2 indicated that with the LA-68 pulsed laser diodes, the instrument would operate in the region where the choice between the silicon photodiode and the GaAs PMT was not clear cut. A major advantage of the silicon photodiode was its small size, which would have allowed it to be placed directly on the infant's head. A point in favour of the PMT was its built in "valve amplifier", which provided gains up to 10^7 at bandwidths in excess of 100 MHz and with an excellent noise figure. Also PMT noise could be further reduced by the use of photon counting. Matching the overall performance of a PMT with a silicon photodiode and electronic amplifier would not be a trivial matter, and the benefits which could have resulted were questionable when they were compared with the simplicity of the PMT option. After weighing up these factors, the GaAs photomultiplier was selected for the detector, the specific device chosen was the R636 tube (Hamamatsu Photonics K.K., Japan). However, the silicon photodiode may be an avenue worth pursuing at a future date.

Boxcar integration and photon counting were the two possibilities for the detector signal conditioning with a very low duty cycle pulsed light source. Photon counting reduces the inherent noise of the PMT and also makes gating the PMT against ambient light easier (gate widths of approximately 200 - 300 ns are possible), but this gain is realised at the expense of limiting the maximum photon detection rate in order to avoid pulse pile-up error. Once again the choice was not an easy one and at the start of this project a decision was made to select photon counting because of its low inherent noise. This was because transillumination of infant's head up to 8.5 cm was a major priority of the design, see Section 4.1.

---

† The currently available range of c.w. laser diodes with much higher mean powers (up to 1 Watt) makes the choice more difficult. However the older pulsed devices still maintain a large price advantage, and pulsed light sources are in general preferable in reducing the effective thermal noise of the optical detector.

5.1 SYSTEM OVERVIEW

Figure 5.1, shows a schematic diagram of the system, a brief description of which has been published[163]. The four semiconductor laser diodes and the GaAs PMT discussed above are shown, together with the rest of the system. Many of the additional optical components and electronic circuits have been added to overcome some of the practical problems encountered in the use of laser diodes and a GaAs PMT in a clinical situation.

Each part of the system is described in turn in the following sections. The light source consists of four laser diodes and their associated power supplies. The laser diodes operate at 778 nm, 813 nm, 867 nm and 904 nm and are coupled via fibre optic connections to the skin surface. Direct optical connections also exist between the laser diodes and a silicon photodiode which monitors the intensity of the laser diodes for stabilisation purposes. To check the reliability and continuity of the optical contact at the skin surface, there is a separate reflectance monitoring optical connection to a second photodiode.

Light transmitted through the patient is collected by a separate fibre optic bundle and taken via suitable optics to the photomultiplier tube and into a multichannel photon counter. The whole system is controlled by a microcomputer. However both the multichannel photon counter and the data logger are stand alone microprocessor controlled instruments.

A large degree of flexibility was included in the system design. Particularly to allow for examination of the effects of varying the pulse width of the laser diodes and the timing delays between the laser triggering and the optical detection. The use of digital as opposed to analog data processing gives the maximum amount of flexibility in terms of data analysis.

5.2 LASER DIODE DRIVER

The choice of a high power pulsed laser diode light source put great demands on the laser diode driver. A current pulse of 60 A was required for a duration of 100 ns at a repetition rate of 4 kHz. At the start of this project, commercially available laser diode drivers used thyristor switches, and in addition to being expensive, were known to have technical

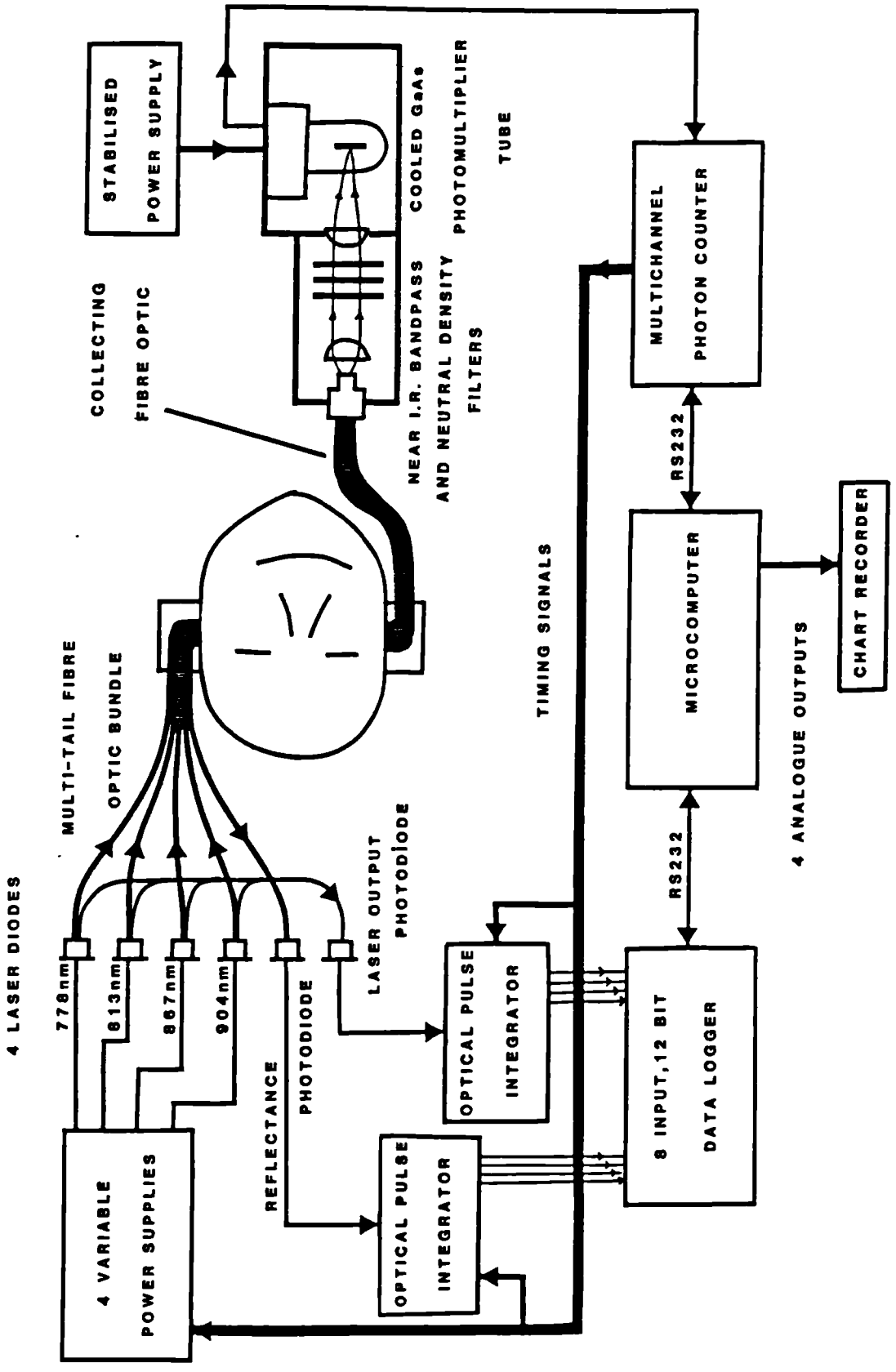

Figure 5.1 Schematic diagram of the clinical near infrared spectroscopy system.

problems. In situations where several closely spaced laser diodes were being fired sequentially, incorrect triggering had been reported by many users, with the firing of one laser inducing incorrect triggering of its neighbours. This was probably due to the large induced voltages caused by the 60 A pulses affecting the gate of the neighbouring thyristor switches.

In the design of the driver for this equipment, an alternative to the thyristor switch was sought for a number of reasons:

(i) The problems of incorrect triggering reported with multiple laser diode circuits using commercially made drivers.

(ii) For reasons of efficiency and flexibility a switch that could be actively turned both on and off was preferred. Thyristors can only be passively turned off by lowering their anode current to less than a specified value. In the simplest thyristor circuit, a single capacitor would be discharged through the laser diode to produce a current pulse which decayed exponentially. Pulse forming networks could be used to produce a more rectangular pulse but only at a fixed pulse width.

(iii) The cost of a correctly specified thyristor for this application is approximately £150, (available from Motorola, 2N2403JAN). Cheaper devices could have been used with insufficiently specified di/dt rating (1500 A/μs is required), but these thyristors would be prone to failure by secondary breakdown.

It was therefore decided to design and build a new style of laser diode driver. The design of the driver is shown in Figure 5.2. The laser diode driver is effectively a pulse transformer, it converts an incoming logic pulse, typically at Transistor Transistor Logic (TTL) levels, up to a 60 amp pulse at a higher voltage, approximately 100 volts. Recent developments in the production of high power Metal Oxide Semiconductor Field Effect Transistors (MOSFET) have enabled their use at pulse currents in excess of 60 amperes. The major question regarding their use in this application was their switching time. The limitation on switching time is the energy required to charge the various capacitances associated with the device. The input, output and reverse (Miller) capacitances all have an effect on the switching characteristics of the device. The input and Miller capacitances must be charged from the finite impedance of the power source driving the gate of the MOSFET. Careful circuit design is therefore necessary to switch the MOSFETs as quickly as possible. The MOSFET chosen in this design is the IRF 640 (International Rectifier) rated at 72 A maximum pulse current and a drain source breakdown voltage of 200 V. The effective gate capacitance has

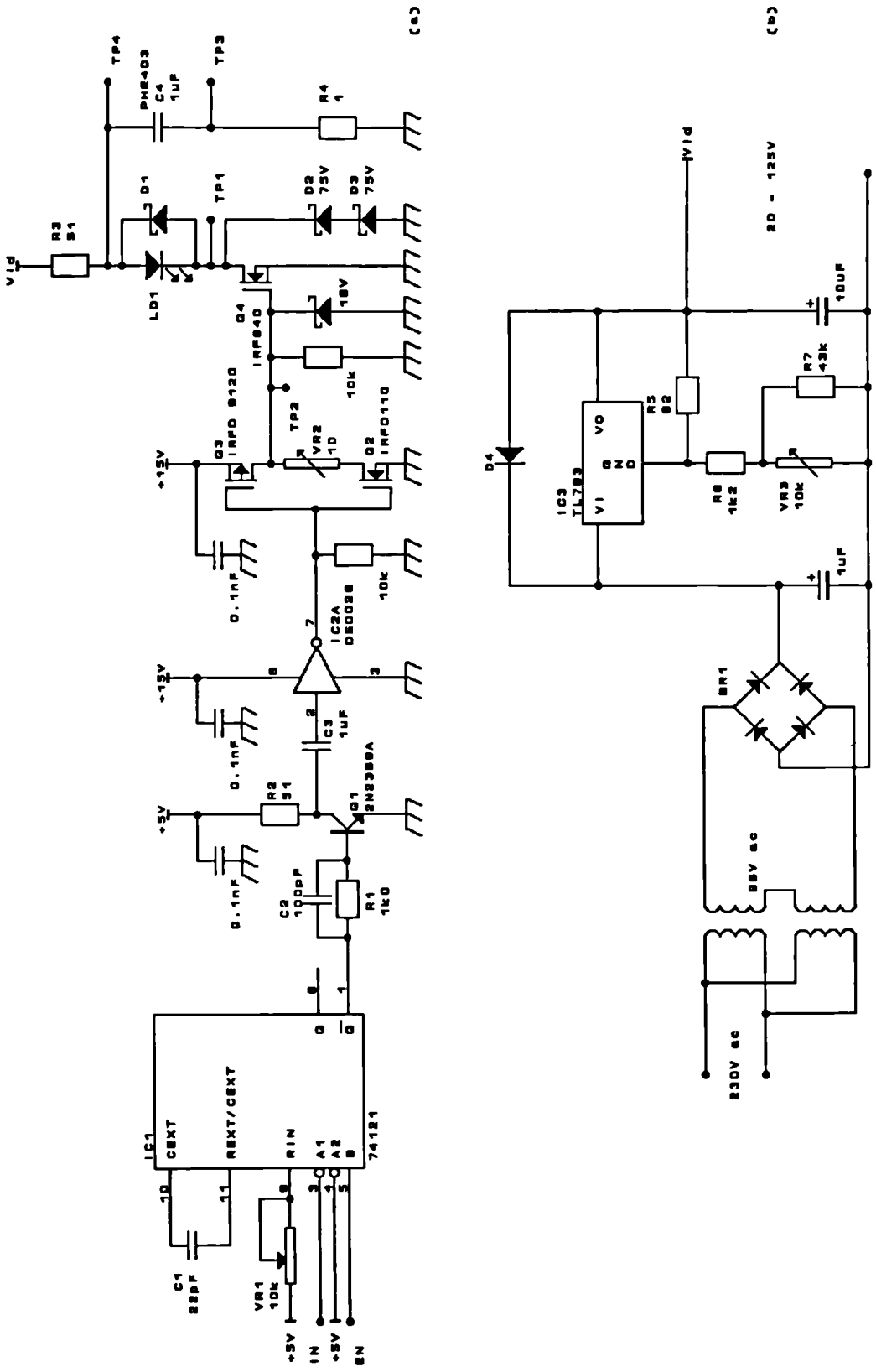

Figure 5.2 Circuit diagram of the semiconductor laser diode driver.

been well documented by this manufacturer (other manufacturers are not always as informative). A plot of stored gate charge against gate voltage is shown in Figure 5.3. It is obvious that gate capacitance is a non-linear function of gate voltage, but an estimate of charging time can be made from the total of 60 nC of charge which is required for the device to conduct.

Optimum performance of the IRF 640 with fast switching speeds and low on resistance are only obtained if the gate of the MOSFET is driven from a 15 V low resistance source. To achieve this, the first few stages of the pulse amplifier both magnify the driving voltage and also lower the source resistance. The driver input pulse is at 5 V and sources approximately 1 mA while the output drive pulse to the IRF 640 MOSFET is 15 V at 5 A.

The laser diode driver is edge triggered to provide a preset TTL pulse of nominally 100 ns duration (variable 50-500 ns using C1, VR1, Figure 5.2). This pulse is boosted to a 50 Ω source impedance at 5 V via the speed up network R1, C2 to transistor Q1. This output is capacitively coupled to a DS0026 (N.S.C., USA) clock driver, IC2A, where it is level shifted to 15 V. This device can provide a peak current of 2 A. Finally, two discrete MOSFETs Q2, Q3 produce an even lower source impedance providing, up to 5 A at 15 V. In practice the sink resistance for Q4 is increased using VR2 to prevent Q4 switching off too quickly and

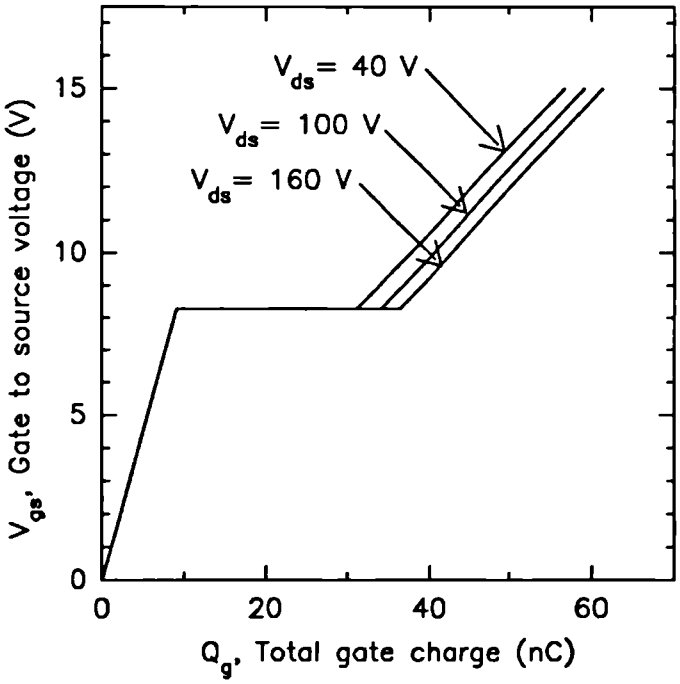

Figure 5.3 Voltage-Charge characteristic of the gate-source "capacitor" of the IRF 640 MOSFET.

causing voltage spikes at its drain from the load inductance. Large decoupling capacitors are also necessary near to each switching device in the chain to maintain fast switching speeds. To first check that the gate drive to Q4 was adequate, Q4 was removed and replaced at its gate/source by an equivalent capacitive load of 4.7 nF. Rise and fall times of 27 ns were achieved as shown in Figure 5.4.

It is important to get the best possible performance out of the final MOSFET switch, Q4 both in terms of gate drive and the layout of the components in the drain circuit. The total resistance of the circuit elements in the drain lead is in the range of 1-2 Ω, hence inductances of the order of a few nanohenries will adversely affect risetime. Also, since the current rises at around 10 A/μs, the manufacturers specified 5-10 nH inductance for the laser diode will alone produce voltage spikes of approximately 100 V. Therefore, all lead lengths must be kept to a minimum and the choice of all the drain circuit components and their specifications must be closely examined.

In particular, the choice of decoupling capacitors at this position is very demanding. They must have a low series resistance and inductance and be capable of supplying 60 A

Figure 5.4 Response of the laser diode driver at TP2, Figure 5.2, to an ideal 4.7 nF capacitor load in place of the MOSFET load Q4. The voltage pulse height is 15 V.

pulses with fast risetimes repetitively for thousands of hours without damage. Manufacturers data on these characteristics is not always possible to obtain. It was easier to obtain sample quantities and to at least test their pulse response. The capacitor eventually selected was the PHE403 (RIFA, Sweden) because of its good pulse response and its large contact area. The effect of drawing a 60 A, 150 ns pulse from the device is shown in Figure 5.5, where the capacitors ability to hold the supply voltage constant can be seen. The onset of the 60 A pulse leads to a dramatic decrease in the voltage across the capacitor. The voltage drop appears to be dominated by the differential of capacitor current (the capacitor current is the bottom trace of Figure 5.5) suggesting that the reason for the voltage drop is capacitor inductance. Any effect of capacitor series resistance is not evident. The capac tor is not significantly recharged during the pulse discharge period and as a result the voltage across it will drop due to the charge lost. Estimating this voltage drop is difficult due to circuit oscillations but appears to be 8 V. This is close to the expected value of 9 V for a 1 μF capacitor losing 9 μC of charge. The capacitor is then slowly recharged over 5 time constants by R3 in time for the next pulse. The ballast resistor R4 was used as a current monitoring resistor, the voltage across it being

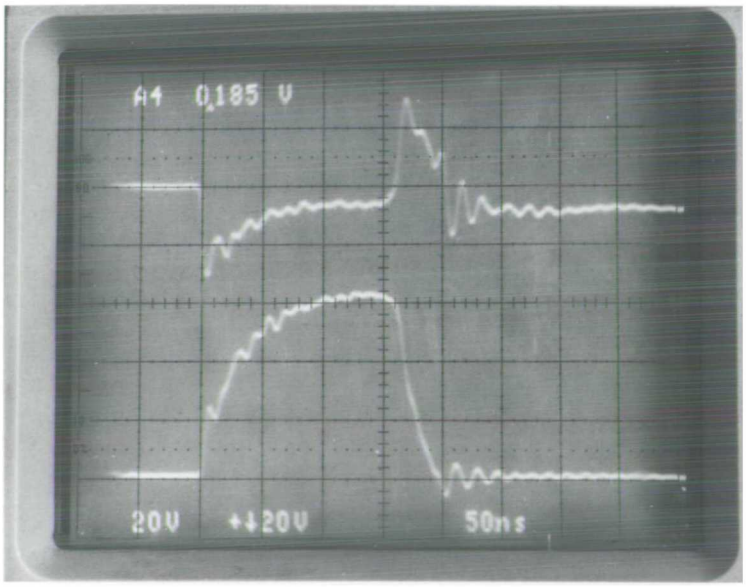

Figure 5.5 Change in the voltage across the storage capacitor C4 (top trace) when a 60 A, 150 ns current pulse (bottom trace) is drawn from it.

monitored via a 10:1 probe connected to an oscilloscope of bandwidth 100 MHz or greater.

All components which carry the 60 amp pulse are mounted as close together as physically possible. In addition the "tab" of the MOSFET Q4 is used as the drain contact in place of the more conventional pin since it has a lower stray inductance. The laser diode itself is protected against reverse voltage spikes by the Schottky barrier diode D1, while the MOSFET is protected by zener diodes D2, D3, which attempt to clamp the maximum drain source voltage, but are not completely effective.

The circuit response was initially tested by using a low inductance 0.5 Ω resistor as a dummy load in place of the laser diode. Voltages at test points TP1, TP2, and TP3 can be seen in Figure 5.6(a),(b). The initial response of the drain voltage is rapid, falling to 90% of its final value in 10 ns, the current pulse (bottom trace, Figure 5.6(a)) does not change as quickly, indicative of an inductive load.

A similar picture is seen when the laser diode is the load (Figure 5.7). The drain voltage again falls within 10 ns but the current pulse rises even more slowly than was the case with the 0.5 Ω dummy load. The difference in the current pulse with the two loads can be seen more clearly in Figure 5.8 where the current pulses for both loads are shown side by side. The rise time for a 0.5 Ω load is 42.7 ns, significantly less than the value for the laser diode load (71.8 ns) under otherwise identical conditions. The conclusion to be drawn is that the laser diode adds a significant amount of inductance to the drain load, making drain inductance an inherent problem when using this type of laser diode package.

Improvement in the current risetime in an inductive circuit can be achieved by increasing the ballast resistance of the load (R4) thereby decreasing the time constant (L/R). This leads to the need for increased power supply voltages to achieve the same load current and therefore higher power switching devices. Higher power MOSFETs are now becoming available but there still exists the problems of large inductive spikes at faster switching speeds, hence this is probably not the best approach. It may be better to look for improvements from the laser diode manufacturers in the form of lower inductive packaging, or packages incorporating in built switching devices.

Under identical driving conditions, both the laser diode and 0.5 Ω dummy load have the same fall time, probably due to voltage clamping of the load voltage by the Schottky diode D1. This switch off time is not the maximum obtainable but is limited by the variable resistor VR2 to keep gate and drain voltage transients within the maximum allowed for Q4.

The optical output power from the laser diode is related to its drive current by the

(a)

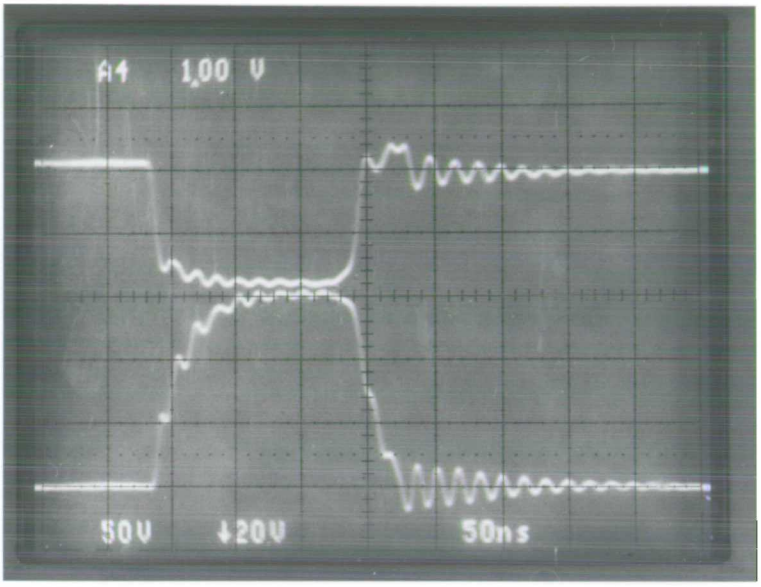

(b)

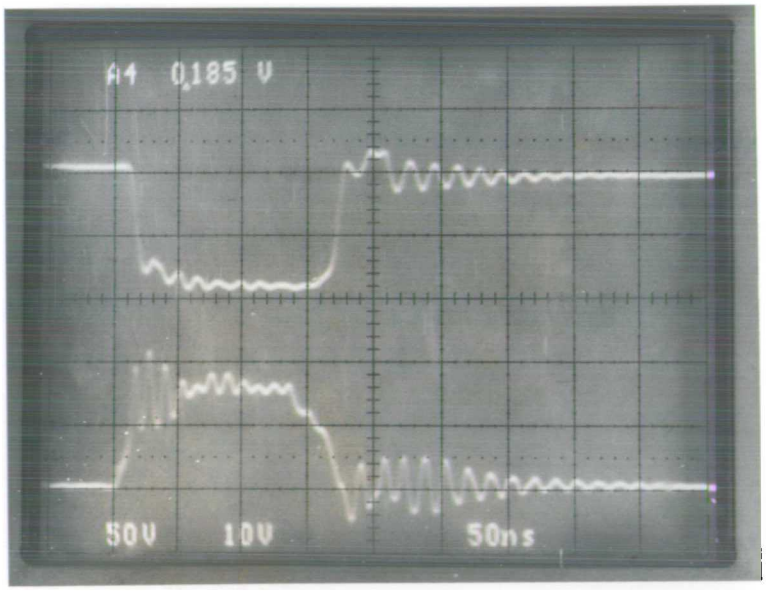

Figure 5.6 Response of the laser diode driver circuit, Figure 5.2, when the laser diode is replaced with a 0.5 Ω resistor. (a) top trace is TP1, bottom trace TP2· (b): top trace is TP1, bottom trace TP3.

(a)

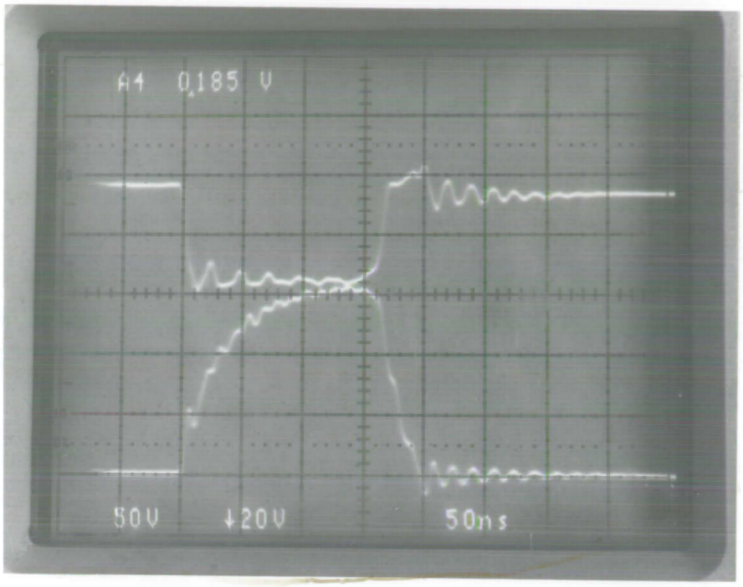

(b)

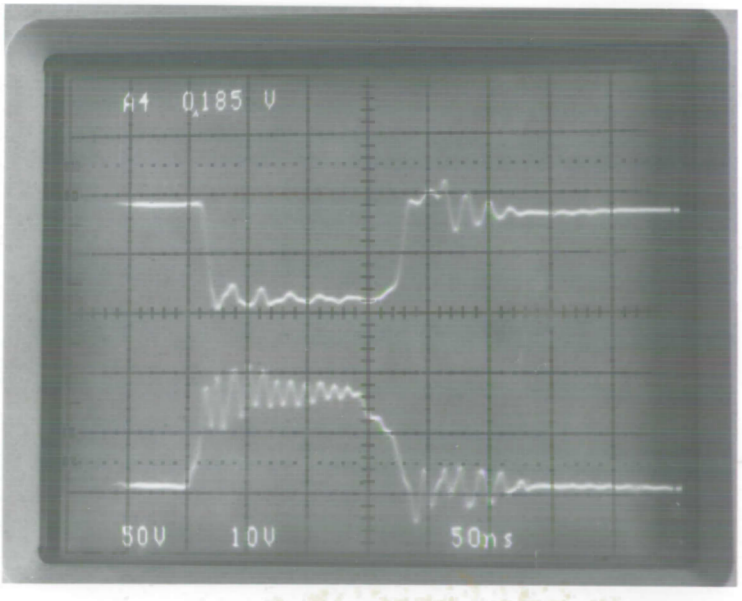

Figure 5.7 Response of the laser diode driver circuit, Figure 5.2, with the laser diode in place. (a) top trace is TP1, bottom trace TP2; (b): top trace is TP1, bottom trace TP3.

(a)

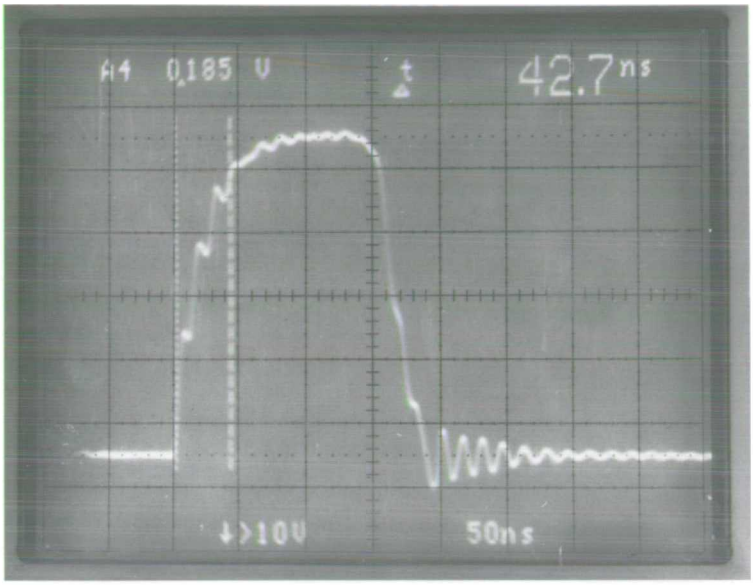

(b)

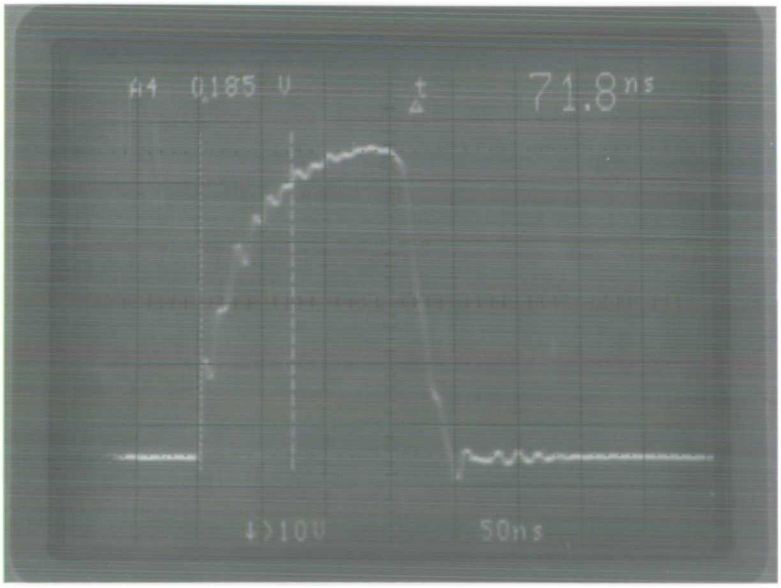

Figure 5.8 Comparison of the 60 A peak current pulse through the load (voltage at TP3) for both (a) a 0.5 Ω load and (b) the laser diode

ideal characteristic of Figure 5.9. In practice, this is obviously not the case as Figure 5.10 shows. The light output does not turn on until 30 A is flowing (I_{th} for this device is specified at 10 A) and turns off when the diode current drops below 10 A. This looks like the result of a time delay (approximately 5 ns) which may be the result of transient heating in the junction area (increased junction temperature increases I_{th}) or other non-ideal characteristics. On the whole, the time response of the optical power and the current pulse of individual laser diodes was very variable.

The amount of optical power from each laser diode can be controlled by means of its own variable d.c. supply (V_{ld}) set by the potentiometer VR3 in Figure 5.2(b). This is a standard application of the TL783 (Texas Instruments, U.S.A.) power supply I.C. The optical output power is also affected by temperature and typical data for single heterostructure and multiheterostructure diodes are shown in Figure 5.11 taken from a RCA Electro Optics data sheet. The temperature of the laser diode junction T_j is given by

$$T_j = T_a + (\Theta_{ca} + 50) V_{ld} I_{ld} \eta \qquad \text{5-1}$$

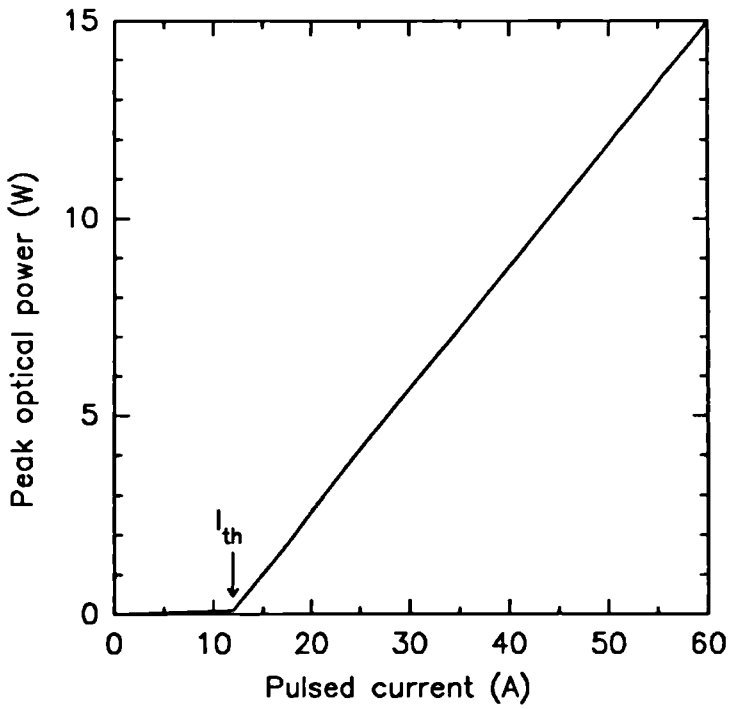

Figure 5.9 The ideal response between emitted optical power and drive current for the semiconductor laser diode.

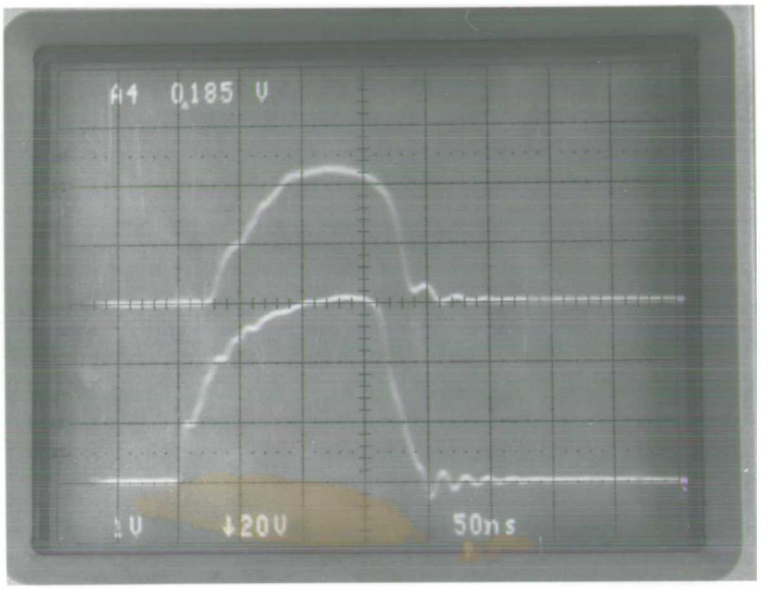

Figure 5.10 The relationship between the optical output power (top trace) and drive current (bottom trace) for an LA-68 laser diode, threshold current 12 A.

where T_a is the ambient temperature Θ_{ca} is the thermal resistance from the case to ambient, (the thermal resistance of the laser diode junction to the case is 50 $°CW^{-1}$), I_{ld} is the laser diode current, $V_{ld} = (1.4 + 0.14I_{ld})$ is the laser diode voltage, and γ is the current pulse duty cycle. Thus at the maximum peak current of 60 A and a duty cycle of 0 0005, the average dissipated power is 0.3 W. Therefore the junction will be between 15 and 30°C higher than ambient temperature assuming a reasonable heatsink. The heatsinking used here is one of low thermal mass but with efficient forced air cooling to give a low thermal resistance, low thermal mass and therefore a short time constant. The laser diode's centre wavelength is also a function of temperature, the coefficient is +0.25 nm°C⁻, which with the expected temperature rise will typically amount to a shift of about 5 nm.

An attempt was made to drive the laser diodes at longer pulse lengths and lower drive currents than those specified by the manufacturer, longer pulse lengths being advantageous to the photon counting detector. The responses of individual laser diodes were very variable. In general it was possible to extend the optical pulse to 150 ns at a lower peak power. However this was only a minor improvement and the manufacturer would not specify how this

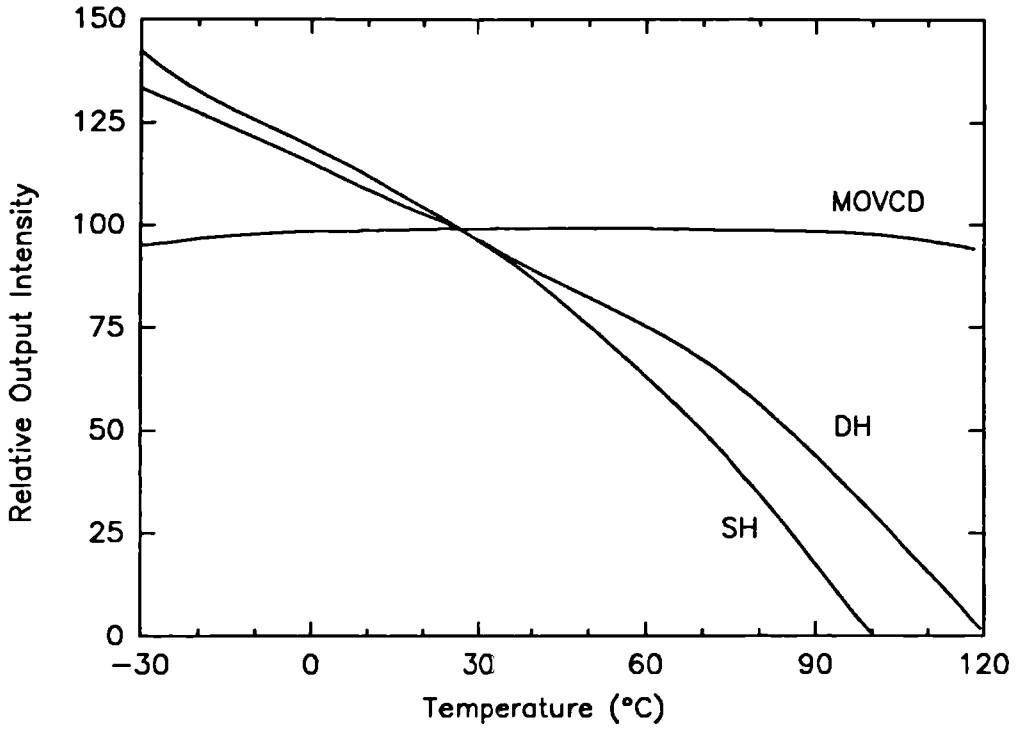

Figure 5.11 Relative optical power output of pulsed single heterostructure (SH), double heterostructure (DH) and MOVCD laser diodes as a function of junction temperature.

might affect laser diode lifetime. The LA-68 laser diodes were therefore set to the manufacturers specifications of a 60 A peak current pulse, 100 ns pulse length (FWHM) and 4 kHz repetition rate. The LA-8 laser diode was also set to its manufacturers suggested drive conditions of 40 A peak, 200 ns pulse length (FWHM) and 4 kHz repetition rate.

5.3 THE LASER DIODE BEAM AND ITS COUPLING TO OPTICAL FIBRES

Earlier it was stated that ideally the laser diodes should be mounted on the skin surface. However, the nature of this type of laser diode and its drive electronics do not make this feasible. An efficient method of coupling the output light into some sort of fibre optic was thus required.

There are two types of laser diode in the system, the 904 nm, LA8-02 diode (ITT component group, U.K.) is substantially different in structure from all the other LA-68 laser diodes (Laser Diode Labs, U.S.A.). The LA8-02 is a single heterostructure junction device whereas the LA-68 is a multi-heterostructure device. This difference results in dissimilar beam characteristics. A schematic diagram of a typical multi-heterostructure laser diode is given in Figure 5.12.

The light emitted by the 904 nm diode was well specified by the manufacturer while the specification for the other (LA-68) diodes was minimal. As a result, this information had to be obtained by experimental measurements. (It is possible that the lack of specifications implies that the optical characteristics are not well controlled). The angular emission characteristics of both types of laser diodes are shown in Figure 5.13(a). Note that the LA-68 diodes will be less efficient to couple into fibre optics. These diodes have a substantial amount of power at angles greater than 30° (numerical aperture 0.5) as is particularly evident from Figure 5.13(b) where the proportion of the total emitted power within a given numerical aperture is shown. Thus it is impractical to collect "The Total Assessable Radiation" (i.e. the integrated optical power over all angles) which is the optical power output quoted by the laser diode manufacturers.

The specified emission area of the laser diodes is 400 μm by 2 μm. One might expect this area to be evenly emitting, but in some 775 nm devices local "hotspots" and "deadspots"

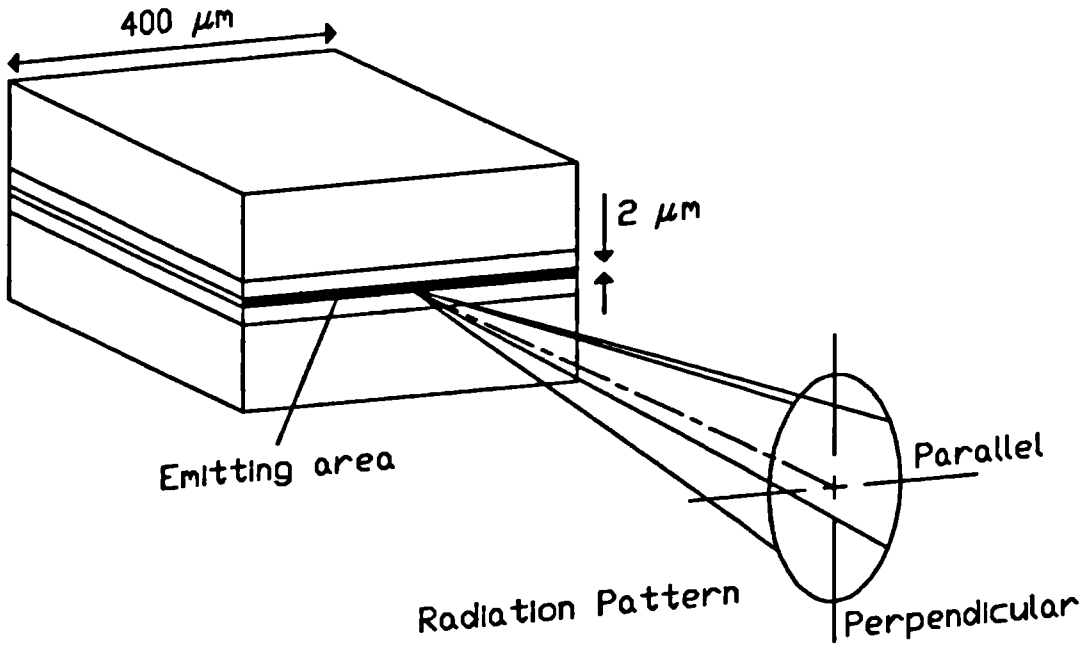

Figure 5.12 Schematic diagram of a multi-heterostructure laser diode.

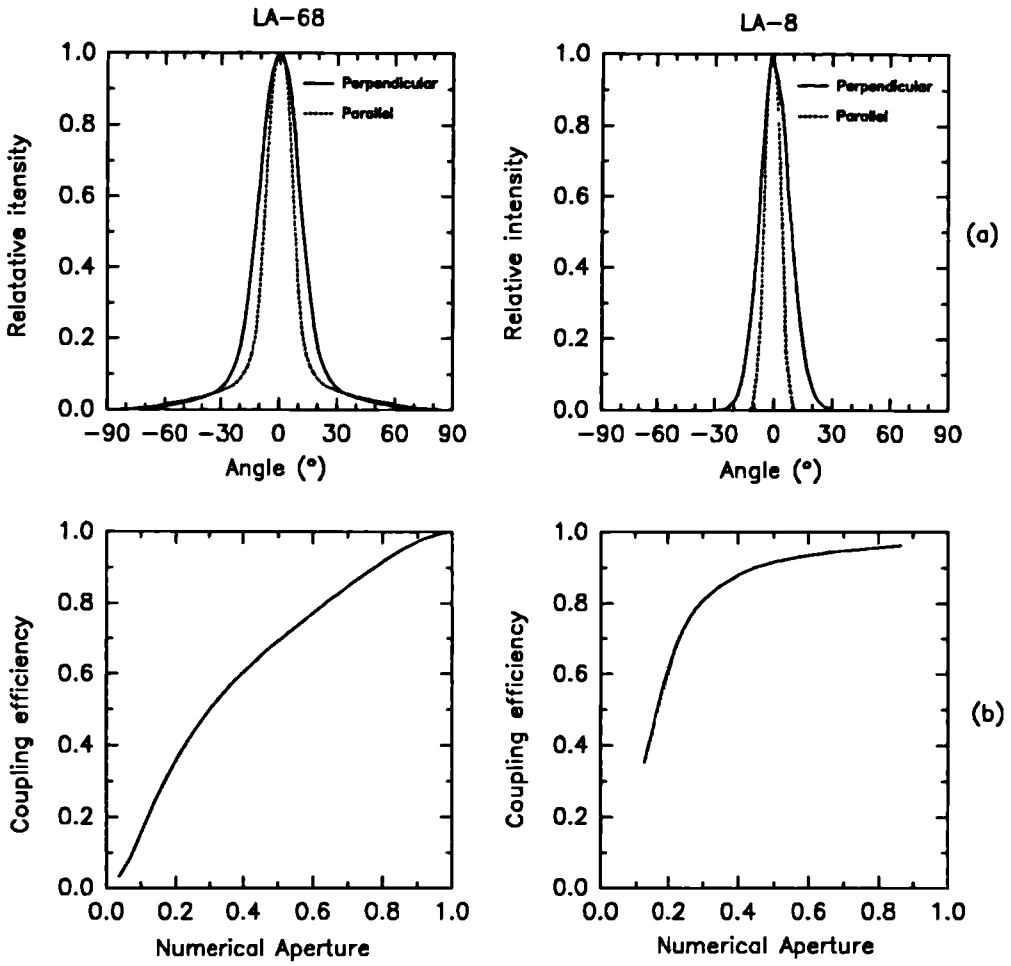

Figure 5.13 Optical characteristics of the LA-68 (column 1) and LA-8 (column 2) laser diodes. (a) relative intensity as a function of observation angle, (b) coupling efficiency versus fibre numerical aperture.

have been observed along the 400 μm facet. Non ideal behaviour of this kind alters the angular emission characteristics and is difficult to take into account in the design of an optical collection system. Its existence indicates the obvious difficulty in manufacturing the 775 nm devices.

Given these laser diode output beam characteristics, what is the best way of coupling this power into an optical fibre? Pigtailing of the diode by the manufacturer is probably the best method, but results in a high initial cost (an additional £150 per diode) which, if the laser diode fails, is lost for ever. Alternatively, specialist optics are available (e.g. Melles Griot, U.S.A.) but again the cost is prohibitive at four laser diodes per system. Instead, a simple, cheap and robust coupling method was sought.

The two main choices lie in the types of fibre optic to be used, either single large core (250 μm) silica fibres, or a fibre optic bundle. In the latter case, the bundle area would be limited to 4 mm^2 (2.25 mm diameter) per laser diode†.

A suitable optical system for the single fibre approach would need to focus the 400 μm by 2 μm emitting area of the laser diode onto a single optical fibre of 250 μm core diameter. For high efficiency, at least two high numerical aperture, accurately positioned, cylindrical lenses would be required. This approach was not considered in the instrument described in this thesis. It was unlikely that it would lead to coupling efficiencies greater than 50% and the mechanical problems of building a robust yet precise coupling optics were large.

The alternative approach of a fibre optic bundle, 2.25 mm in diameter, promised to be simpler, its larger size relieving many alignment problems. The simplest possible arrangement was for the end of the fibre optic bundle to be placed in direct contact with the glass window of the laser diode package, approximately 1.65 mm away from the emitting area, see Figure 5.14. A calculation of the coupling efficiency of this approach required knowledge of the size of the optical beam at the outside of the laser diode window. An accurate calculation of the beam characteristics at this point would not be trivial as it would be a near field problem. An "engineering approximation" was therefore used which simply defined the beam extent in two orthogonal directions, one parallel and the other perpendicular to the diode junction.

The engineering approach first looked at the location of the beam at the package window as a function of the angle of emission. As the height of the emitting area was only 2 μm this meant that the radiation emitted perpendicular to the junction could be calculated based on the far field angular characteristics of Figure 5.13(a). In the parallel direction, the problem was a near field one but the extent of the beam could also be estimated from the far field angular characteristics but adding an additional 400 μm due to the width of the junction. The extent of the beam as a function of emitting angle has been plotted in Figure 5.15 for both orthogonal directions. This figure indicated that a fibre optic bundle of radius 1.125 mm, would cover all of the light emitted from the diode at angles of less than 37°. Light collection systems with larger numerical apertures than this are rarely seen. The coupling efficiency was therefore governed largely by the fibre bundle efficiency (between 40 and 50% depending upon the fibre length, see Table 4.ii). Thus for a 2 metre fibre optic bundle, numerical

† This value is derived from the maximum area of 20 mm^2 of total fibre optic already specified, divided by 5, for the 4 laser diodes and the reflectance optical fibre.

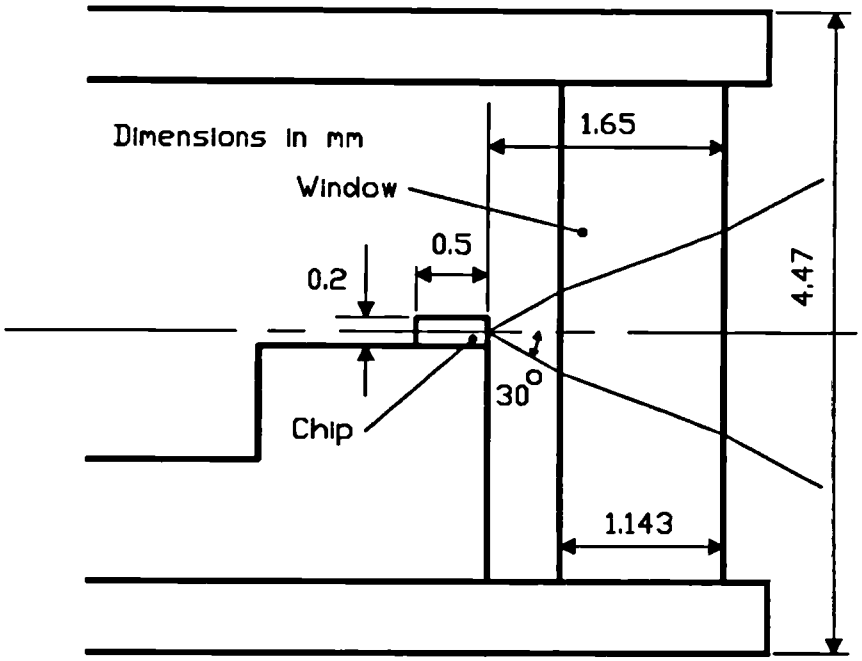

Figure 5.14 Cross section through a laser diode package illustrating the position of the laser diode chip and the package window.

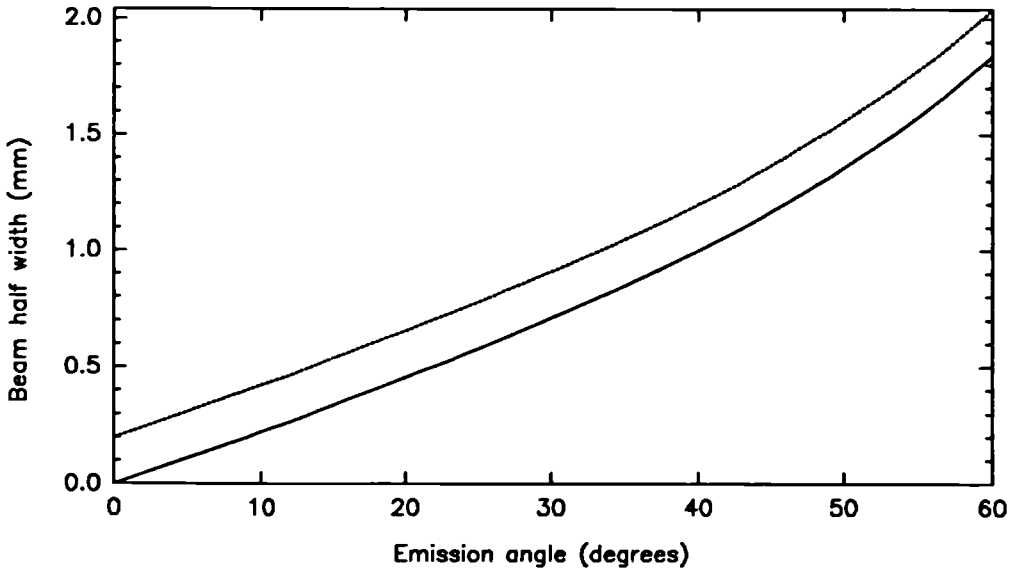

Figure 5.15 The maximum extent of the laser beam plotted as a function of the angle of emission, both for light emitted parallel (broken line) and perpendicular (solid line) to the junction.

Table 5.i Coupling efficiencies of light emitted from a 813 nm semiconductor laser diode (LA-68) into various type of optical fibre placed directly against the package window.

Manufacturer	Material	Diameter (mm)	Length (m)	Efficiency (%)
Verre & Quartz	Silica (single)	1	0.2	17
Eurotec Optical	Glass (bundle)	2.25	1	25
Eurotec Optical	Glass (bundle)	2.25	4	20
Radio Spares	Plastic (single)	1	0.7	13
Radio Spares	Plastic (single)	1	2.3	6

aperture 0.54, the predicted overall coupling efficiency for the LA-68 diodes was 30% and for the LA-8 diode 37%. Obtaining a significant improvement over this simple approach by any other method would be difficult to achieve.

These calculations were tested experimentally. A table of coupling efficiencies for a number of different large single optical fibres and fibre bundles placed against the laser diode package window is shown in Table 5.i. The coupling efficiencies correspond to the amount of light detected down the fibre compared to the total amount of light emitted from the laser diode package window over all angles from an 813 nm LA-68 diode. Note that the 2.25 mm diameter glass fibre bundle is only fractionally below its predicted performance and that both the plastic and glass 1 mm diameter single fibres have a significantly lower performance compared to the fibre bundle.

5.4 THE LASER DIODE TO PATIENT OPTICAL CONNECTION

The previous section has shown that fibre optic bundles of 2.25 mm diameter are an efficient way of collecting the light from the four laser diodes. In this instrument however, this function needs to be combined with the additional requirement of monitoring the output light intensity of each diode and of measuring the skin reflectance. A multitail fibre bundle

approach can easily cater for these additional requirements.

Describing the light intensity at each point in such a multitail fibre optic bundle can prove confusing so first let some terms be defined. With reference to Figure 5.16 the optical power at point LP_j is the "laser optical power" provided by laser diode j. IP_j is the "incident optical power" from laser diode j, PP_j is the "patient optical power" and RP_j is the "reflectance optical power".

The incident optical power IP_j for each laser diode is used as a monitor of the optical power delivered to the patient PP_j, and hence needs to respond linearly with the patient optical power (independent of the reflectance optical power RP_j). Only if this is true will it be possible to compensate effectively for any fluctuations which may occur in the laser optical power due to temperature or other variations. The reflectance optical power must similarly respond linearly with the incident optical power.

The initial design of the multitail fibre aimed at achieving this function at each laser diode ferrule by fully randomising the position of the optical fibres carrying IP_j with those

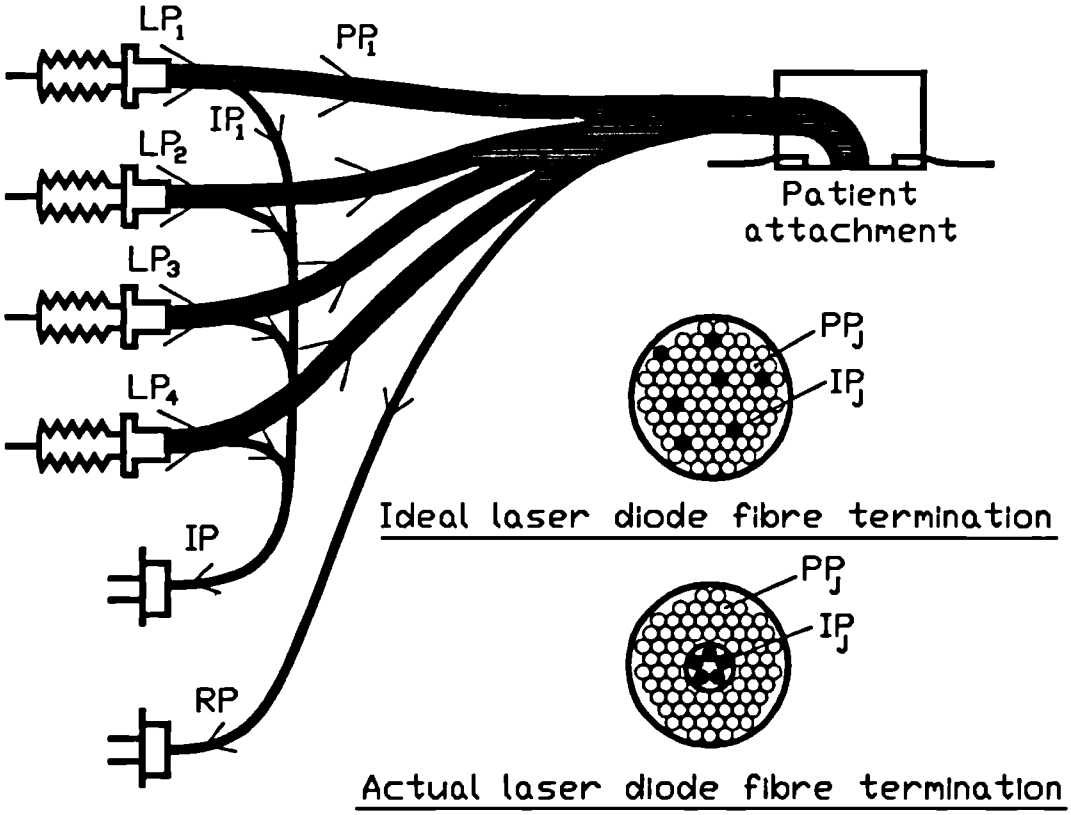

Figure 5.16 Schematic diagram of the multitail fibre optic bundle to couple light from the laser diodes to the patient and to the "incident" and "reflectance" photodiodes.

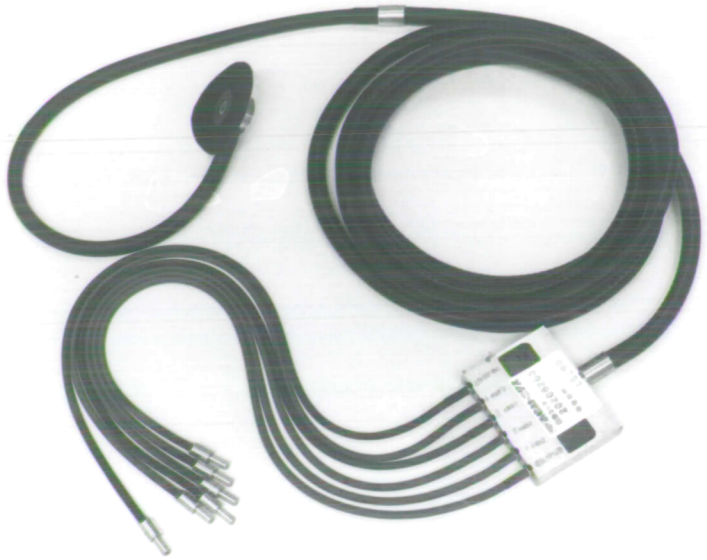

Figure 5.17 Photograph of the actual multitail fibre optic bundle.

fibres carrying PP_j. The "ideal case" in Figure 5.16. It was estimated that 10% of the total fibres would provide enough light for the monitoring silicon photodiode to measure IP_j. A similar randomisation is ideally required at the patient end of the multitail fibre bundle for both the fibres from the four laser diodes and those carrying the reflectance signal, Thus providing a reflectance signal which is unbiased with respect to the four laser diodes. Despite the helpful collaboration of the fibre manufacturer (Eurotec Optical Fibres Ltd, Doncaster, U.K.), randomisation of the fibres at all these positions proved impossible to achieve during manufacture. As a compromise the patient end of the bundle was fully randomised, but the incident power was derived from a small bundle of fibres set into the laser diode ferrule as shown in Figure 5.16. This ferrule end is held in contact with the laser diode window, and can be translated and rotated to optimise the amount of power going down to the patient and into the "incident" groups of fibres.

At the patient end, the fibres in the OPTODE are turned through 90° for convenient mounting onto the skin surface (see the photograph in Figure 5.17). An annulus of thin flexible black plastic sheet is trapped by the plastic ring to provide additional light shielding. The plastic ring is first stuck to the skin with a double sided adhesive ring. The plastic sheet

is also attached to the skin surface with adhesive tape, and in addition to acting as a light shield improves the strength of the attachment.

A protective armoured sheath covers the length of the bundle from the "junction box" to within 30 cm of the patient OPTODE, the last 30 cm being sheathed in thick black silicon rubber which is more flexible.

5.5 DETECTION OF TRANSMITTED LIGHT

5.5.1 The optical system

As previously stated, the GaAs PMT has to be mounted remotely at the end of an optical fibre bundle. This has the same fibre bundle characteristics as that given in Table 4.ii and shares many of the features of the previously described laser diode bundle such as the attachment to the patient and the material of the fibre sheath. The only differences are that this bundle has no bifurications, and although it is 5 mm in diameter at the patient it changes to a slit configuration at the photomultiplier tube end. The size of the rectangular slit is 8.9 mm by 2.24 mm and is designed for optimum coupling to the PMT photocathode. This fibre bundle was also made by Eurotec Optical Fibres Ltd., U.K.

The photocathode of the PMT is set back 14.3 mm from the external glass envelope and hence requires optical coupling to the high numerical aperture optical fibre bundle. The optical system used is shown as part of Figure 5.1. Two high numerical aperture aspheric lenses (diameter 65 mm, focal length 53 mm, Melles Griot USA, 01 LAG 019) are used as a collimator to focus the end of the optical fibre bundle onto the photocathode at 1:1 magnification. The spherical aberration of these lenses is very low, and the numerical aperture theoretically matches that of the fibre bundle. However, the overall coupling efficiency of this arrangement was found to be quite low at around 40%. This is thought to be due to high reflection losses at the large angles of incidence and the large fibre bundle size. Between the two lenses is a filter holder for 50 mm square filters. This houses a near infrared bandpass

filter, (RG9, Schott Glass, F.R.G.) which reduces interference from ambient light. Inconel coated neutral density filters (Corian, U.S.A) can also be added when required. The lens in front of the PMT also acts as the input window of the peltier cooled photomultiplier housing (Products for Research, U.S.A.).

Photomultiplier tubes are sensitive detectors and must not be exposed to high levels of ambient lighting. In practical use in a hospital environment accidental exposure may be difficult to prevent and the instrument must incorporate some measure of protection. To achieve this, a solenoid operated shutter was built into the housing and this sits in front of the rectangular fibre optic. This shutter is sprung loaded in the closed position and is operated remotely.

5.5.2 Peltier cooler temperature controller

The temperature coefficient of sensitivity for GaAs PMTs at near infrared wavelengths is high as can be seen in Figure 5.18. A typical value at 900 nm is $+5\%°C^{-1}$. It is therefore necessary for the tube to be held at a given temperature plus or minus 0.1°C. A temperature controlled PMT housing is therefore required, such a housing can hold the PMT either above or below ambient temperature. Heating would have a beneficial effect of increasing the red response of the tube, but at the expense of an increased dark current. The maximum allowed anode current for GaAs PMTs is however very small and is close to its dark current at room temperature. For this reason heating the PMT is not a possibility, and the tube must be cooled. In selecting the operating temperature to use, there is a trade off between red response and dark count so an optimum temperature exists.

The temperature controller was built by modifying an **uncontrolled** peltier power supply manufactured by Products for Research, U.S.A., see Figure 5.19. An uncontrolled d.c. voltage of 9 volts (no load) is pulse width modulated by the power MOSFET Q1, the degree of modulation being set by the controller. The modulation frequency is approximately 2 seconds (triangle wave generator IC3A, IC3B), much faster than the time constant of the peltier housing. The temperature of the housing is detected by a built in positive temperature coefficient thermistor (VT1). The relationship between the thermistor resistance (R_T in kΩ) and its temperature (T in °C) is approximately logarithmic over the temperature range –30°C to 20°C.

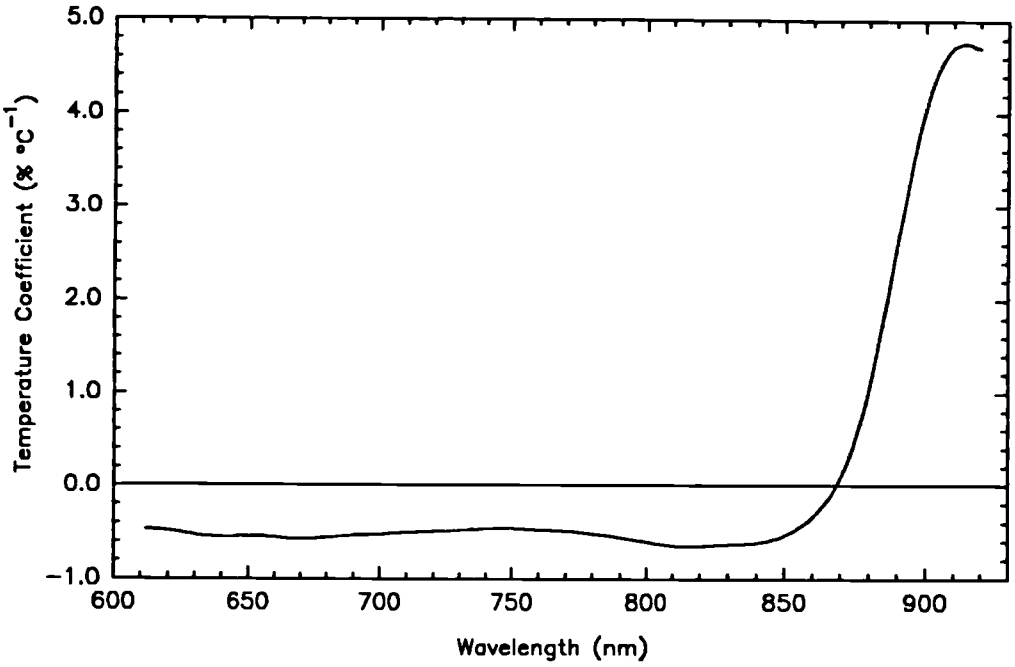

Figure 5.18 Temperature coefficient of sensitivity as a function of wavelength for a GaAs photomultiplier tube.

$$R_T = 4.34\, e^{0.0538\,T} \qquad (in\,k\Omega) \tag{5-2}$$

Ideally the characteristics of the thermistor should be linearised to produce a voltage which is proportional to resistance over its usable range, but a slightly non-linear response can still be accommodated within the feedback loop. The thermistor voltage (v_T) as a function of temperature (see bridge circuit in Figure 5.19) is therefore

$$v_T = \frac{10}{1+\frac{100}{R_T}} \qquad (R_T\, in\,k\Omega) \tag{5-3}$$

This voltage together with a "set temperature voltage" (v_R), set by VR1, are fed into a difference amplifier IC1A, IC1B which has a gain of G, so that the voltage v_E is

$$v_E = G\left(v_R - v_T\right) \tag{5-4}$$

Hence the differential gain between the error voltage and the temperature of the thermistor

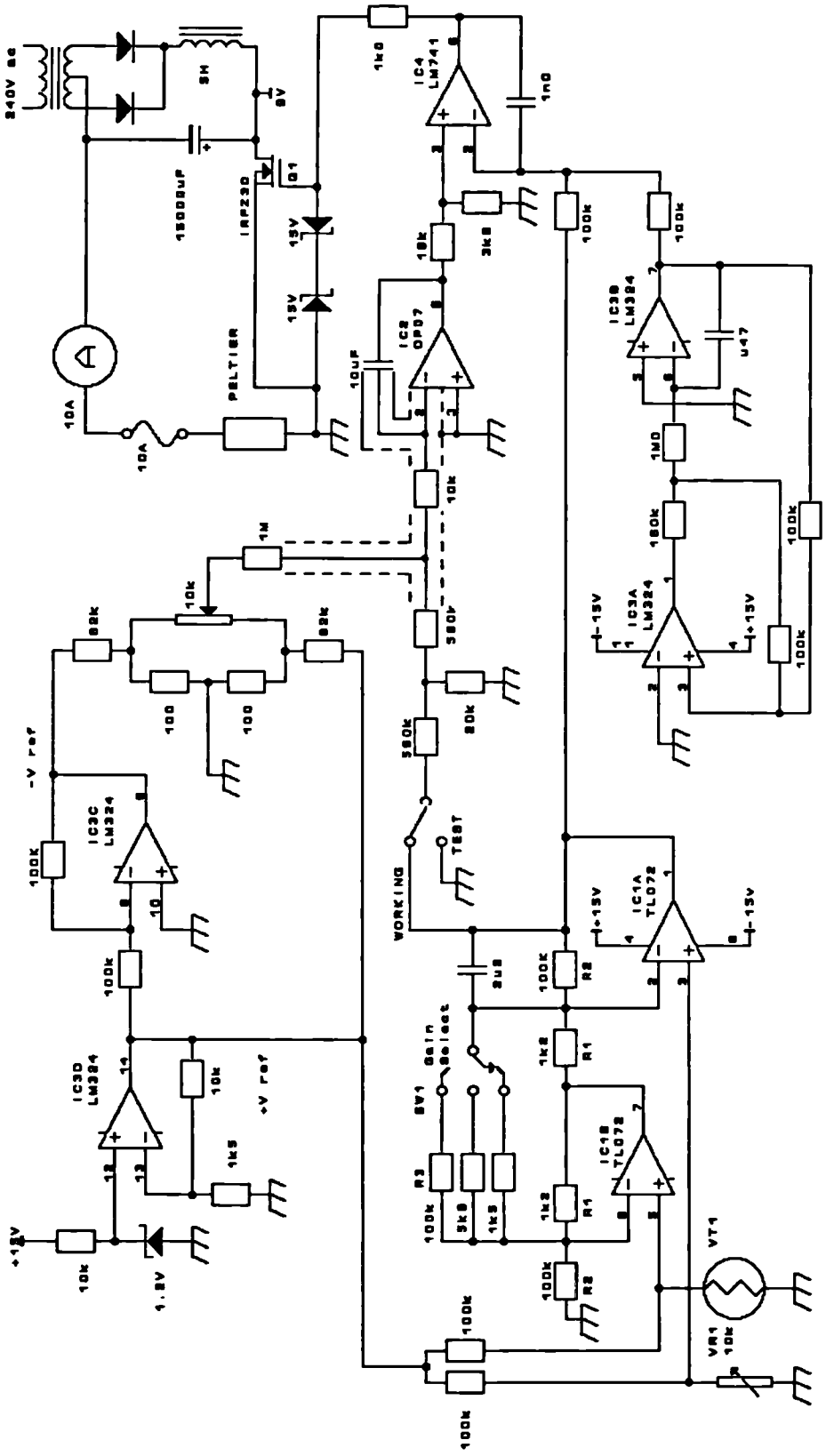

Figure 5.19 Circuit diagram of the peltier controller used to control the temperature of the photomultiplier tube housing.

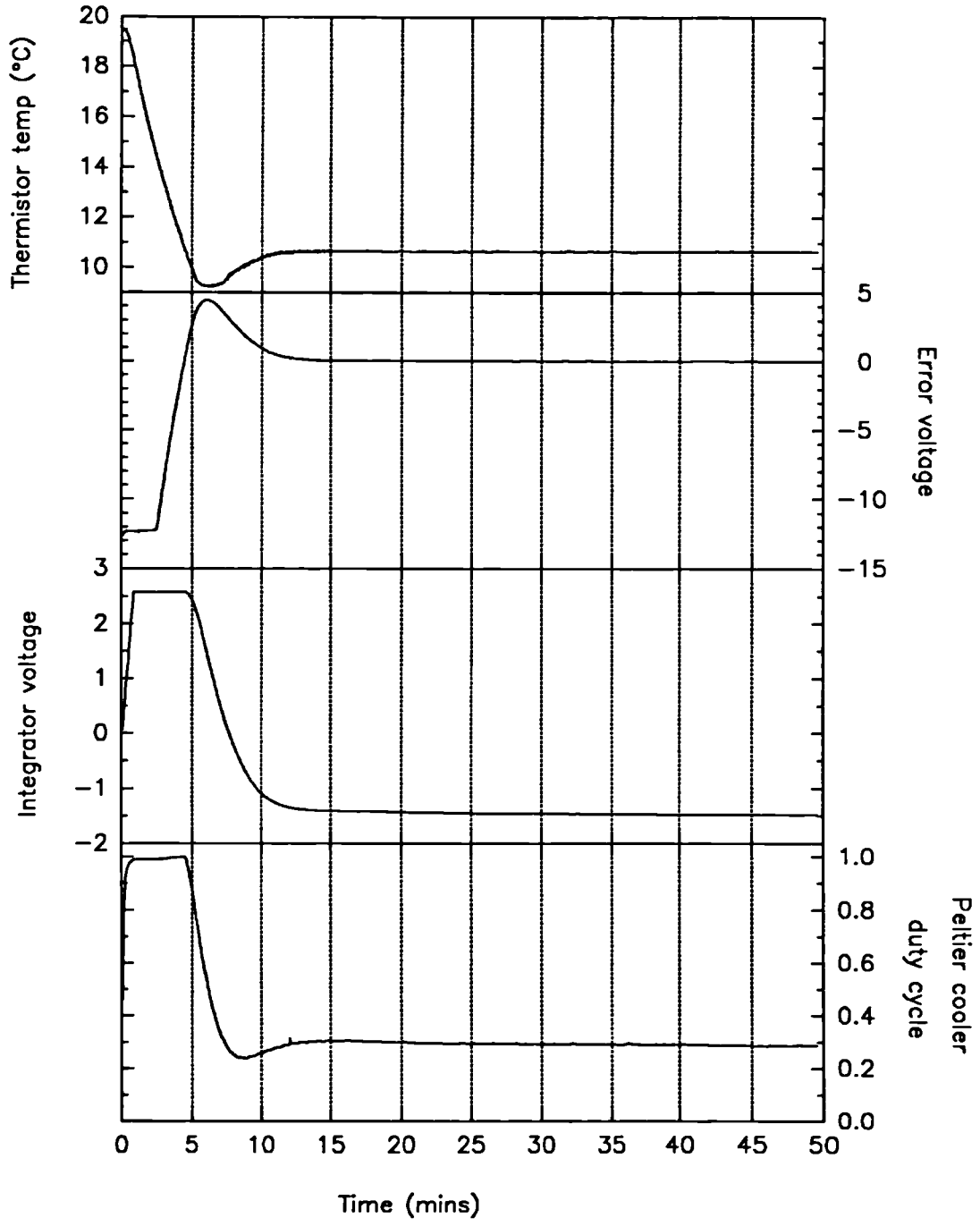

Figure 5.20 Time response of the peltier controller in cooling down from room temperature to 10°C.

($\Delta v_E/\Delta T$) is

$$\frac{\Delta v_E}{\Delta T} \approx -0.00877\, G e^{0.0538\, T} \qquad 5\text{-}5$$

The value of G can be set to 86, 120 or 218 by switch SW1. These three ranges are needed to maintain $\Delta v_E/\Delta T$ at roughly the same value throughout the range of "set temperatures" of -20°C to 15°C.

The values of proportional gain (G) were selected experimentally, with VR1 set to approximately 7 kΩ (approximately 10°C). The integrator (IC3) was first disabled, and G was increased until the controller error voltage showed a slight oscillatory response in settling to its final value. At the largest proportional gain possible without instability, the steady state error voltage was high, $v_{ess} = 0.7$ V (≈ 0.14°C). The significance of a large steady state error voltage is that changes in ambient temperature will change the temperature of the photomultiplier tube housing, and this is unacceptable.

Addition of an integral term to the feedback loop effectively gave infinite gain to any steady state error, and therefore reduced v_{ess} to zero. The time constant of the integrator, was chosen to be marginally less than the response time of the system itself (10 minutes). The final controller response with both proportional and integral terms can be seen in Figure 5.20, when the PMT housing was cooled from 20°C to 10°C. The steady state error voltage was 20 mV ± 5 mV (S.D.) equivalent to approximately 0.004 ± 0.001°C.

Ideally a differential term should be added to the feedback loop to produce a full Proportional Integral Differential (PID) controller. This would speed up the settling time but would also add additional errors due to the long time constants required. A digital as opposed to an analogue controller would be the ideal solution.

5.5.3 Single photon detection electronics

Commercially available instruments were used to perform the photon counting function. The maximum instantaneous count rate was specified at 10 MHz. This is not as fast as would have been liked, but was adequate for the initial system. The cost of faster (100 MHz systems) is significantly higher. The photon counting system consists of two separate instruments, a single channel counter with amplifier and discriminator (Hamamatsu Photonics, Japan, C1230) and a multichannel counter (Malvern Instruments, U.K., K7025).

The single channel photon counter is described in this section.

A block diagram of the C1230 circuit is illustrated in Figure 5.21. A single photo-electron generated at the R636 PMT photocathode is amplified by the PMT dynode chain into a charge pulse (approximately 2×10^{6} electrons, 3.2×10^{-13} C). This is fed into a charge amplifier (Hamamatsu Photonics, Japan, C716-07) with a transfer coefficient of 30 mV/10^{-13}C. This output is fed to a further amplifier of variable gain (4 to 34 dB). The resulting voltage pulse has a rise and fall time of 15 ns and a pulse width of 30 ns. Finally, this pulse is compared to a preset d.c. voltage at a voltage comparator, where if the incoming voltage pulse is high enough, a TTL pulse of width 37 ns wide is generated.

The important parameters in a photon counting circuit are the "deadtime", both of the PMT/amplifier network and the discriminator/counter. The "deadtime" is the time which occurs after the detection of one photon and during which time the detector will not respond to the arrival of a second photon. The "deadtime" for the PMT/amplifier (τ_p) was measured at 30 ns and the overall "deadtime" of the discriminator/counter (τ_d) was dominated by the K7025 multichannel counter, measured at 109 ns. These two deadtimes affect the pulse pile-up error, the details of which are discussed in an assessment of the operation of the complete system in Section 5.5.2. The manufacturer specified a maximum synchronous count rate of 10 MHz and a maximum random count rate of 1 MHz, the experimentally determined values above equate to a maximum synchronous count rate of 9 MHz.

The C1230 single channel photon counter can display the average count rates of up

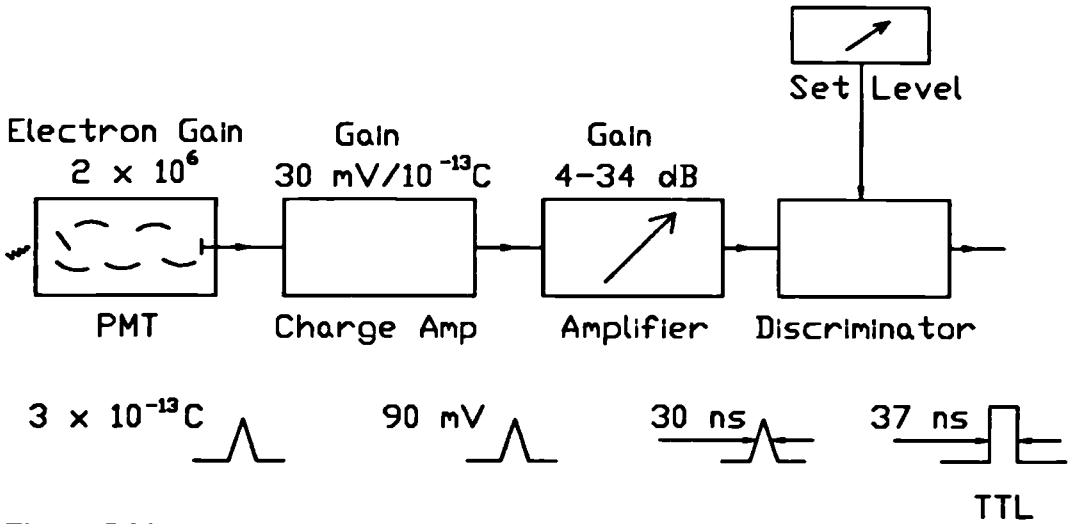

Figure 5.21 Schematic diagram of the Hamamatsu Photonics K.K. C1230 single channel photon counter.

to 10 MHz, measured over a time of 0.1, 1 , 10, or 100 seconds, and also incorporates a high voltage power supply, adjustable from −500 V to −1500 V, stability 0.2% (at maximum voltage).

5.5.4 Multichannel photon counter

This instrument is fed from the single channel photon counter (C1230) which has a buffered TTL output directly from the discriminator. The photon count displayed by the single photon counter is the sum of the light detected from all the laser diodes, the PMT dark count and the stray ambient light. To measure the detected photons from each laser diode, a separate photon counter is required for each laser plus an additional counter to measure the sum of dark current and stray ambient light, i.e. a total of five separate counters. This function is performed by the K7025 multibit correlator, which in one of its modes of operation acts as a multichannel photon counter. The K7025 is a programable instrument consisting of 64, separate 24 bit counters, each with a maximum synchronous count rate of 9 MHz (experimentally tested). The 64 counting channels are cycled sequentially with a preset time (T_{chan}) spent on each counter before moving onto the next. The number of complete 64 channel cycles per measurement period is another preset value (N_{cycles}). At the end of N_{cycles} the instrument stops and the accumulated count in each channel can be read out via an RS232C port. This RS232C port also acts as a means of presetting N_{cycles}, T_{chan} and other parameters and of starting an accumulation of length N_{cycles}.

A schematic diagram of the operation and timing of the system is shown in Figure 5.22. The instrument was modified by its manufacturer to also perform the operation of triggering the laser diodes. The manner in which this was done may not appear to be elegant, but was necessary to allow the instrument to continue to operate in all its other possible modes of operation.

Figure 5.22 shows that each counting channel (CC_l) is associated with either one of the laser diodes or with the dark count. It is convenient to consider the dark count as laser diode 0 (LD_0) where laser diode zero does not exist, the real laser diodes being LD_1 to LD_4. Then counting channel l, $l=0$ to 63, (CC_l) is associated with its laser diode by $CC_l = LD_{[l-5*MODULUS(l,5)]}$.

In operation the counter channels are first cleared, then with CC_0 connected the photon counter gate is opened and LD_0 is triggered (LD_0 does not of course exist, therefore only dark

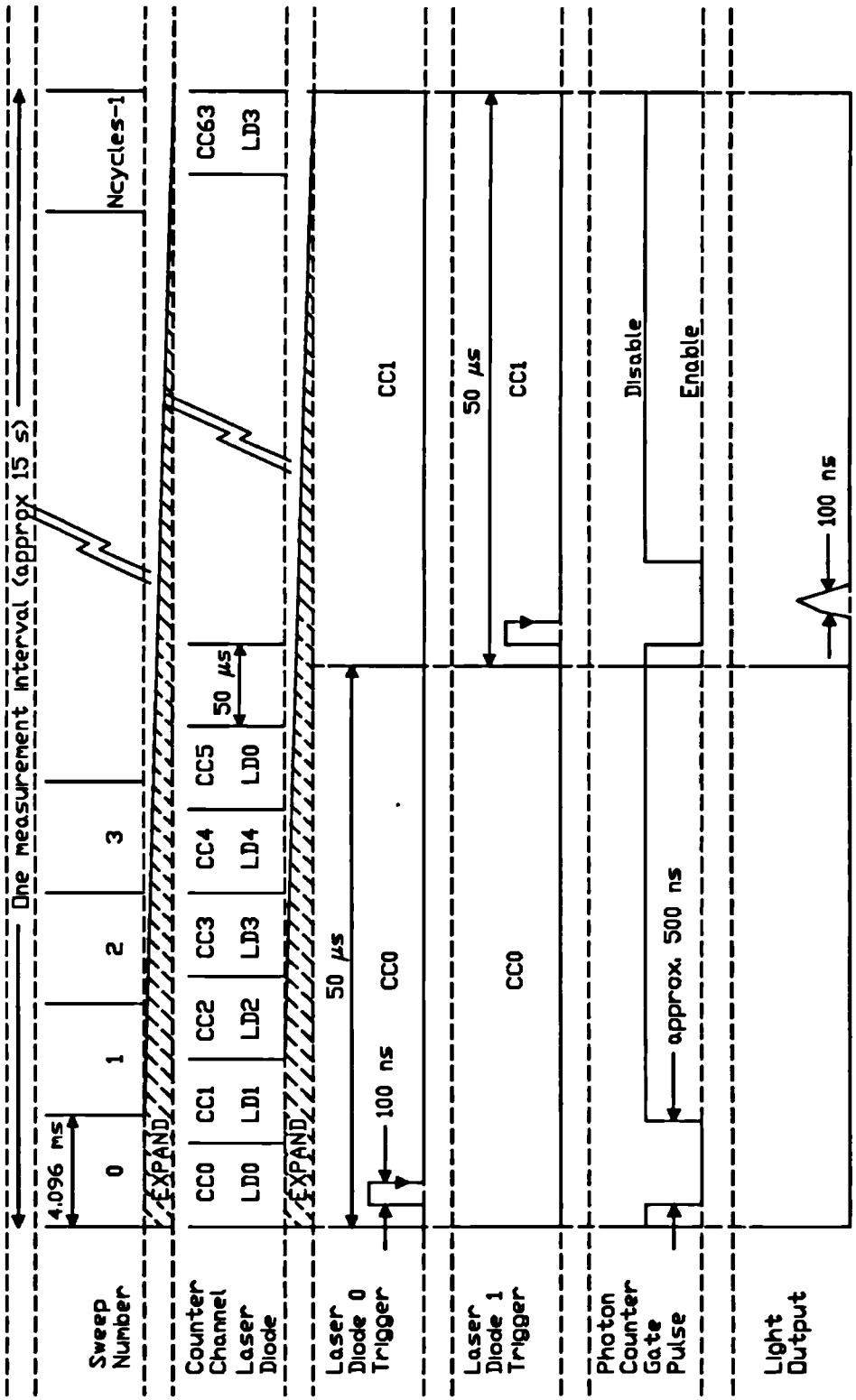

Figure 5.22 Timing diagram showing the relationship between the multibit photon counter timing, the laser diode pulses and the photon counter gate signal.

count is accumulated until the gate closes some 500 ns later). After a total time T_{chan} has elapsed (50 μs in this figure), then channel 1 becomes active, the gate opens and LD_1 fires. The detected photons from it (and the dark current) are accumulated for the same period as before. This sequence repeats for all the 64 channels. At this point, the whole process repeats until a total of N_{cycles} have occurred. The accumulation then stops and a record of the contents of the 64 channels and the instrument status are sent in ASCII format via the RS232C interface to the controlling computer†. The whole accumulation cycle can then be started again, after first resetting all channels back to zero††.

5.6 ELECTRONIC CIRCUITRY FOR THE STABILISATION OF THE LASER DIODE OPTICAL POWER

The laser diodes are not controlled for constant optical output. They typically exhibit a pulse to pulse intensity jitter of some 10% and a slower drift in intensity caused by temperature variations. Instead of attempting to stabilise the laser diode optical power directly, a signal proportional to the average optical power reaching the patient is fed to the system controller via the data logger of Figure 5.1. The computer then mathematically corrects for any change in laser output power. Exactly how this small fraction of the optical laser beam is split off from the main beam to the patient has already been described in Section 5.4.

The transmitted light intensity, at each wavelength, is measured by the GaAs PMT and photon counting circuit as the total number of photons detected over an accumulation interval which is approximately 20 seconds. The accumulated count is therefore proportional to the sum of all the laser diode pulse energies. Therefore, this laser diode monitoring circuit should look at a signal which is also proportional to the summed total laser pulse energy over the same interval. Measurement of the optical peak power is not a good idea, as both peak power

---

† The least significant bit of each counter is not transmitted in the data record, this leads to a small error, therefore to obtain the real photon count (±1), multiply by 2.

†† Note that laser diodes 0 to 3 are fired 13 times in each 64 channel cycle while laser diode 4 is fired 12 times. This is not ideal but can be taken into account later in software.

and pulse shape may vary. An integrated energy measurement takes into account drifts in both the peak optical power and optical pulse width. The circuit designed to achieve this is shown in Figure 5.23 and in the future it will be referred to as the INCIDENT light measuring circuit.

The optical pulse from the INCIDENT optical fibre bundle is converted into a current pulse by a biased p-i-n Si photodiode, PD1 (Hamamatsu Photonics, Japan, S1722). The area of this device (13.2 mm^2) is adequate to collect all the light exiting the fibre bundle. Before the arrival of the optical pulse, the integrating capacitor C_{int}, is reset to zero volts by the small signal MOSFET Q1. The current pulse from the photodiode integrates onto this capacitor, and the resulting voltage is amplified by IC1 and then held on a sample and hold amplifier IC2 until the arrival of the next current pulse for LD_1. As the light from all the laser diodes are multiplexed to the same photodiode down the same fibre bundle, they are demultiplexed by using separate sample and hold amplifiers, one for each laser diode. The individual voltages now represent the pulse energies from each laser diode stretched into the next pulse producing a stepwise continuous signal. Each of these voltages also passes through a variable gain amplifier and filter network. The filter is a 2^{nd} order active filter network (IC3B) with a 1 second time constant and a gain of 2. The time constant removes glitches resulting from the switching of the sample and hold amplifiers and also 50 Hz line pickup from the photodiode. The variable gain amplifier IC3A allows each of the 4 voltages to be preset to an output value of approximately 2 V for maximum laser power. This permits maximum use to be made of the 12 bit resolution of the data logger that follows. The final output voltages are labelled INC_1 to INC_4 (INCIDENT light measurement) for convenience and later use.

The peak photocurrent from each laser pulse is arranged (by means of optical filters in front of the photodiode) to be around 0.5 mA, which when multiplied by the 100 ns pulse width, results in a total charge generation of 50 pC per laser pulse. There is normally sufficient light available to permit a peak photocurrent of more than 0.5 mA, but values of this order are the maximum permissible before the photodiode becomes saturated and non-linear (larger photocurrents are possible for larger area photodiodes when evenly illuminated). An integrating capacitor value of 470 pF was selected which develops approximately 0.1 V from the 50 pC photocharge and this is followed by an amplifier IC1 with a gain of 10. The value of integrating capacitor is 2 orders of magnitude greater than the inherent capacitance of the photodiode and the input capacitance of the amplifier, making the effects of stray capacitance insignificant. Offset voltages from IC1 and IC2 are trimmed by VR1 and VR4 respectively.

In addition to the normal d.c. offset of the operational amplifier itself, there is a

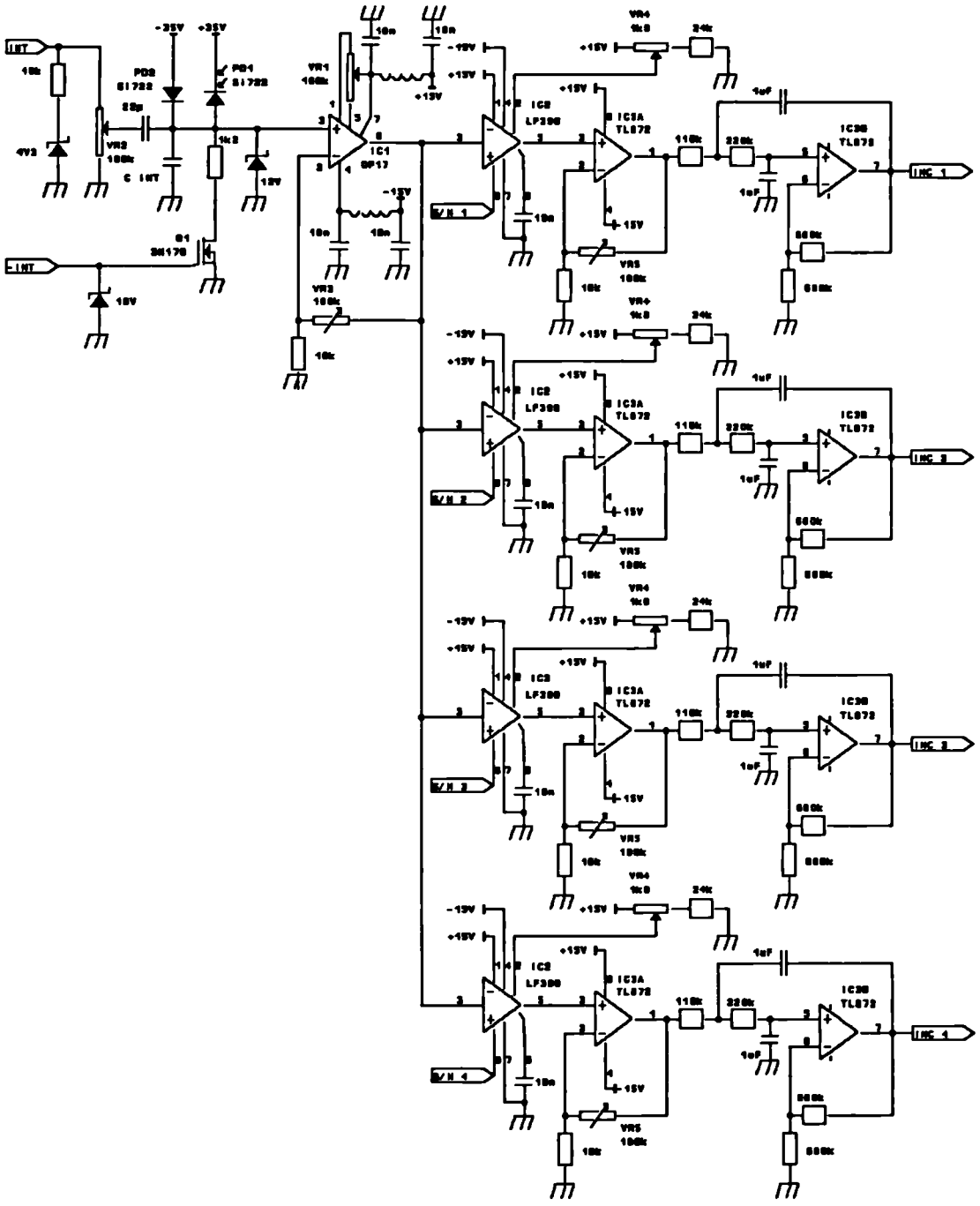

Figure 5.23 Circuit diagram of the optical integrator circuit used to measure the INCIDENT and REFLECTED optical pulse energies.

second "a.c. offset" caused by feedthrough from the logic signal which controls the integrator reset. This results from the parasitic capacitances around the reset MOSFET, Q1. The magnitude of this signal depends upon the voltage step at the gate of the MOSFET and the ratio of the reverse transfer capacitance (C_{rss}) of the MOSFET to that of the integrating capacitor. This feedthrough voltage step injects charge into the integrating capacitor whose magnitude is equal to the product of V_{step} and C_{rss}. In this circuit, the injected charge is equal to 15 pC and is therefore a significant part of the photodiode charge. Thus, the MOSFET must be carefully selected to minimise the charge injected, provided that its on resistance is low enough to discharge the integrating capacitor within a few microseconds. This particular MOSFET was selected for its low C_{rss} of 1.3 pF. To null the injected charge, the same logic pulse but of opposite sign is capacitively fed into the integrating capacitor. The magnitude of this current pulse is controlled by VR2.

Drifts in the d.c. offset of this circuit can also occur due to temperature. The most temperature sensitive device is the photodiode itself with a leakage current of 10 nA at room temperature and a temperature coefficient of 15% $°C^{-1}$. In this circuit, this temperature drift is compensated by the dark current of an optically shrouded identical photodiode connected with the opposite polarity and biased with an equal and opposite voltage.

Other possible factors to consider are the drift in sensitivity caused by the temperature coefficient of sensitivity of the photodiode or the temperature coefficient of the integrating capacitor. In this case these are small. The temperature coefficient of sensitivity of the photodiode is only +0.1%$°C^{-1}$ at 900 nm, and that of the integrating capacitor 125 ppm$°C^{-1}$.

5.6.1 Reflectance measuring circuit

The circuit which measures skin reflectance is identical to that used for the "incident power" (Section 5.6). Its 4 outputs, one per laser diode can also be fed into the 8 channel data logger and are labelled REF_1 to REF_4 for later use.

5.7 SAFETY CIRCUITS

There are two safety circuits, one of which automatically controls the laser diodes, the other protecting the photomultiplier tube against accidental light exposure.

The laser diode safety circuit is shown in Figure 5.24(a). It is designed to provide a safe mode of instrument operation such that the lasers will be switched off in the event of the skin reflectance from the patient (REF_4) dropping below a preset voltage (V_{safe}). The lasers then stay off until manually switched back on.

For the laser diodes to be enabled, the TTL voltage V_{LDE} must be HIGH. When the equipment is first powered up, V_{LDE} is always LOW, independent of the position of switch SW1 (i.e. the laser diodes must be deliberately switched on). SW1 has three positions OFF, TEST and SAFE. Pressing the momentary push-to-break switch SW2 will always switch on

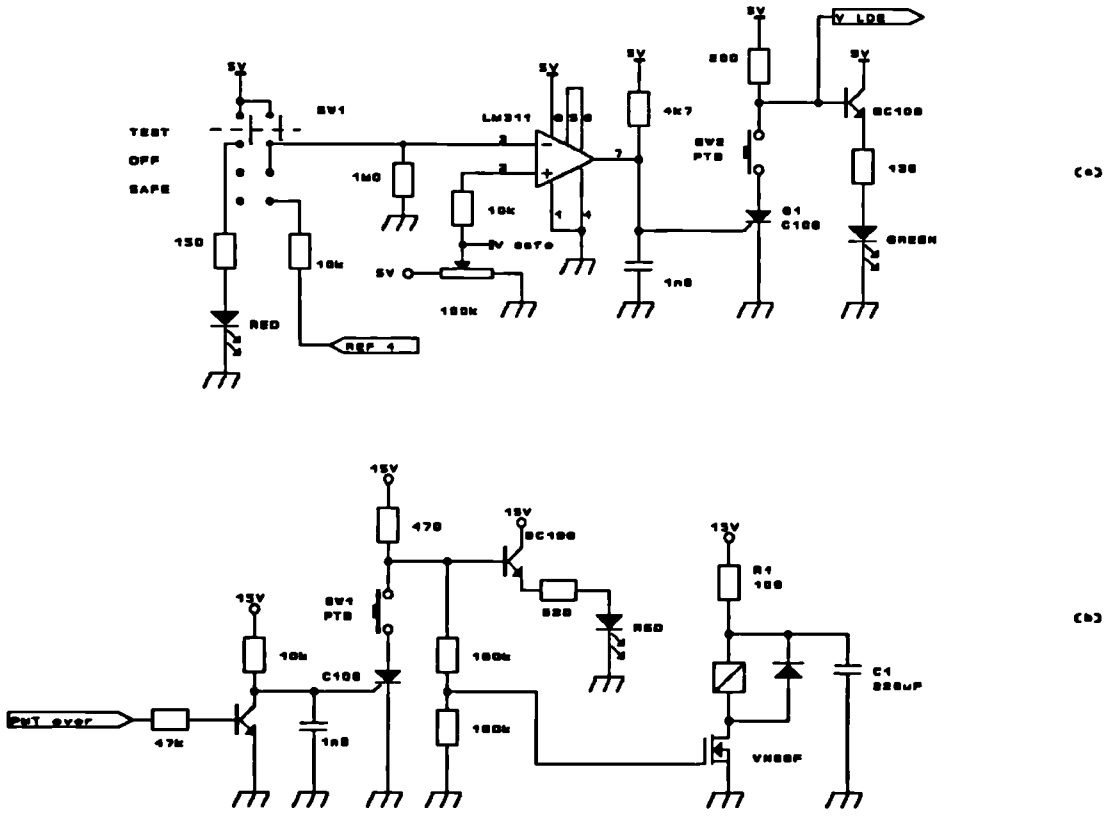

Figure 5.24 Circuit diagrams of (a) the laser diode safety circuit; (b) the photomultiplier protection circuit.

the lasers while the switch is held down. Upon releasing SW2 the system response depends upon the position of SW1. In the OFF position, the lasers will immediately switch off, in the TEST position the lasers will always stay on. This unsafe TEST status is indicated by the red light emitting diode. In the SAFE position, the lasers diodes will remain on as long the voltage REF_4 is higher than the voltage V_{safe}. Should the reflectance signal from the patient change dramatically (normally set for REF_4 to drop by 50%), then thyristor Q1 will conduct, switching off the laser diodes. Q1 latches in the conducting state until SW2 is pressed again. Manually switching off of the laser diodes is achieved by returning the switch SW1 to the OFF position.

The safety circuit for the photomultiplier tube works by powering a solenoid activated shutter previously described in Section 5.5.1. This shutter is sprung closed when not powered. Excessive light levels to the photomultiplier tube are possible if the receive OPTODE accidentally becomes detached, or the operator forgets to switch off the high voltage PMT power supply before removing the OPTODE from the patient.

The shutter is opened by pushing the momentary push-to-break switch SW1 in Figure 5.24(b) which then latches open. A PMT overload is detected by the single photon counter C1230, the C1230 logic signal PMT_{over} going HIGH in an overload condition switching off power to the solenoid. The shutter stays closed until the operator has cured the overload condition and presses SW1 again. The red status LED indicates that the shutter is open. The capacitor and resistor network R1, C1 produces the high initial current pulse which is required to open the shutter. It can then be held open with a lower d.c. current. Ideally the protection circuit would operate faster than this simple mechanical shutter but this circuit suffices for the majority of situations.

5.8 SYSTEM INTEGRATION

The main components of the system have been described in previous sections. They are collectively driven from a controlling computer, an Olivetti M24 (M24) which is IBM-PC® compatible. The M24 is configured with a 10 Mbyte Winchester disk, 360 kbyte diskette and 640 kbyte RAM running the MS-DOS® operating systems. System software is written in the

'C' language and compiled by the Lattice Inc. (USA) 'C' compiler, running under the MS-DOS® operating system.

Figure 5.1 shows that the computer is interfaced to three devices, the multichannel photon counter K7025, a data logger and to 4 digital to analogue convertors. The multichannel photon counter and data logger are both microprocessor controlled themselves, and this allows the system tasks of data acquisition, analysis and display to be shared between the M24 and its external devices. Data transfer between the M24, multichannel photon counter and data logger is by RS232C serial interfaces at 9600 baud using ASCII data. This is not the ideal method for speed and reliability, but was cheap, convenient and readily available. The digital to analogue convertors are directly connected to the M24 expansion bus.

The basic flowchart of the control software is shown in Figure 5.25. Firstly, a disk file is opened to save the results of the session and the user is asked to enter information such as patient identification, etc. All devices are then reset to a known state by copying the contents of stored set up files to both the multichannel photon counter and the data logger. These files specify the accumulation time of the photon counter and the sampling time of the data logger which is normally set to 2 seconds on all 8 channels.

After initialisation, the laser diode trigger pulses (described in Section 5.5.4) are continually sent from the multichannel photon counter to the laser diode drivers. Before the lasers start to emit light they must first be enabled from front panel switches of the safety circuits. Once enabled the lasers run continuously and the voltages (INC_1 to INC_4 and REF_1 to REF_4) from the incident and reflected light detector boards are available to the data logger. Running the lasers continuously is recommended for maximum stability of the light sources.

The START routine first clears the data logger of all data, and zeros all channels of the multichannel photon counter before instructing both machines to start accumulating data. The M24 then waits for the multichannel photon counter to complete a collection (normally 15 seconds), and without being polled transfer an ASCII table of its counter contents to the M24. The M24 now stops the data logger and polls it for an ASCII table of its digitised analogue inputs, INC_1 to INC_4 and REF_1 to REF_4. These will consist of a number of readings, taken every 2 seconds, for all 8 channels. After data transfer, the START routine begins again immediately. During this accumulation the M24 is free to analyse, display and then store the previously transferred data set. It is also free to interact with the user. The user can attach a comment to the data to be saved on disk, NORMALISE the current data set (see later) or exit from the monitoring session. Performing these functions during the accumulation of the next

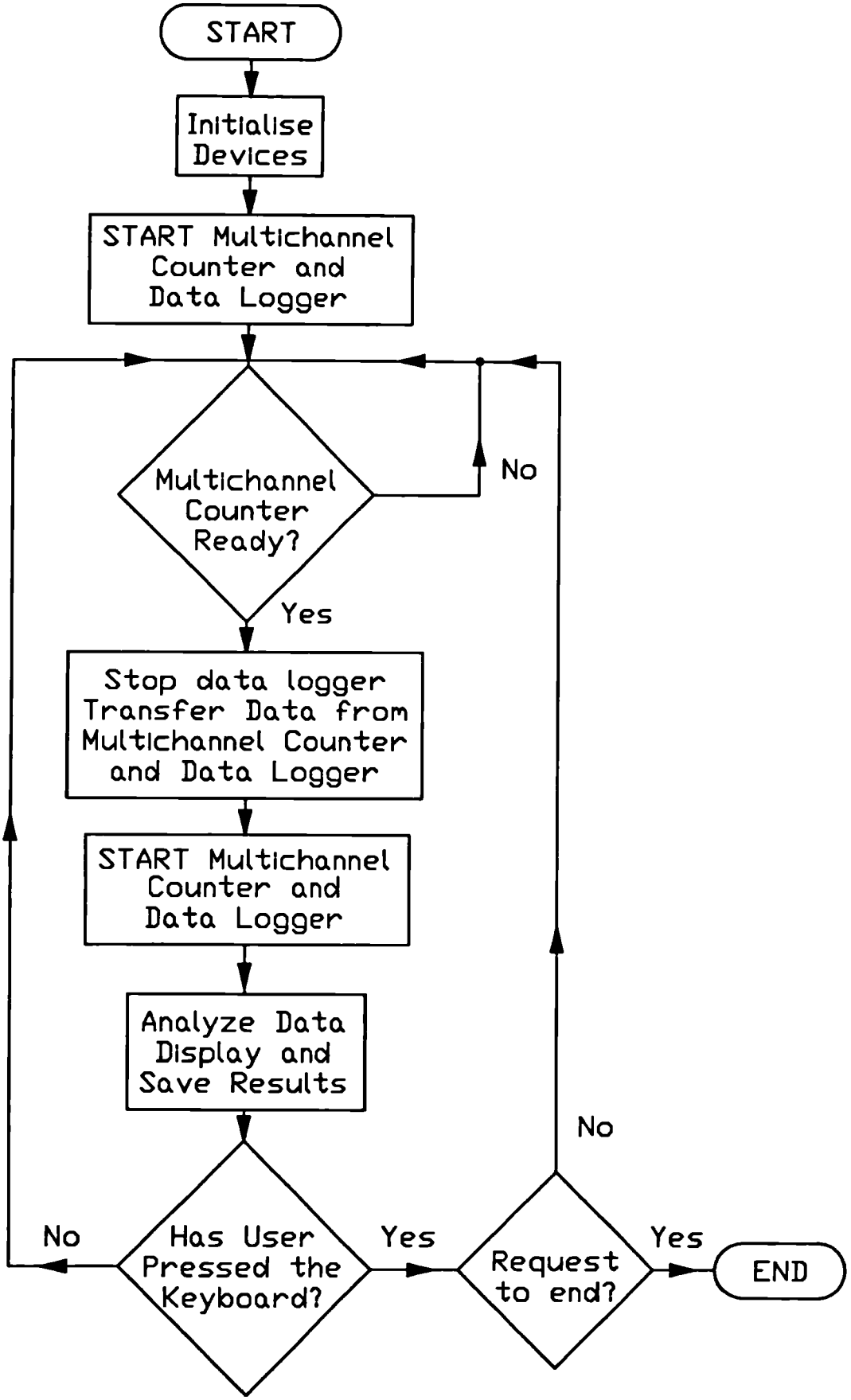

Figure 5.25 Flowchart of the computer program which controls the near infrared spectrophotometer system.

data set ensures the time delay between accumulations is as small as possible. Data transfer over the RS232C interfaces is performed by interrupt driven software for maximum reliability and minimum delay.

Real time analysis has been kept simple, not because of the problems in handling the analysis in real time but because the rapid development of ideas would have lead to the rapid production of redundant software. The analysis routine itself, must first convert the ASCII data records into program variables. The multichannel photon counter data has 64 channels of information concerning the 4 laser diodes and the dark count. The relevant channels need to be added together to obtain the total received photon count for each laser and the dark count. The total dark count is then subtracted from the total count for each laser to remove the effect of both thermal detector noise and ambient light leakage into the system. The photon counts for each laser are then normalised to the number of laser pulses i.e. photoelectrons per laser pulse. The number of laser pulses can easily be calculated as the multichannel photon counter also transfers the number of sweeps of its 64 counters (N_{cycles}) with each data transfer. This now means that the transmitted light data variables (called PC_0 to PC_4 where PC_0 is the count in the dark channel) are independent of accumulation time and hence accumulation time can be easily changed during a session without affecting comparisons with previously stored data. The other advantage of this approach is that it enables "pulse pile-up" error to be easily checked and corrected. To avoid large pulse pile-up errors, maximum photon count rates during a laser pulse are kept below 5 MHz, (i.e. PC is less than 0.5 photoelectron per laser pulse for a 100 ns pulse duration). The incident and reflected light signals (already defined as INC_j, REF_j for $j = 1$ to 4, Units: Volts) are also easily converted into a "per reading" form from the multiple reading taken by the data logger in an accumulation time.

The parameters of interest are changes in the attenuation of the object at the four wavelengths. The system calculates these attenuation changes with reference to the values at some previous point in time, this is called the NORMALISATION time (t_0). (Setting this time is a user option in real time as described earlier.) The attenuation change ΔA_{jk} at wavelength j and time t_k compared to the NORMALISATION time, t_0 is

$$\Delta A_{jk} = \lg\left[\frac{\left(PC_{j0} - PC_{00}\right) INC_{jk}}{\left(PC_{jk} - PC_{0k}\right) INC_{j0}}\right] \qquad \text{5-6}$$

where INC_{j0}, REF_{j0}, PC_{j0} are the values recorded for laser diodes $j = 1$ to 4 at the NORMALISATION time. The attenuation changes are corrected for changes in laser output by the use of the incident light signals and compensated against changes in dark count by first subtracting the dark count PC_{0k}. Note that these values are relative changes in tissue attenuation at one point in time compared to another, and the data set ΔA_j for $j = 1$ to 4 is the basic information which this instrument provides and which is subsequently used to calculate the chromophore concentrations, as outlined in Section 4.1. The instrument is therefore only capable of directly measuring relative concentration changes in chromophore concentration.

Methods for converting this attenuation data into chromophore concentration data are covered in some detail in Chapter 7 and were performed by subsequent off line analysis of the data. A simple three wavelength, three unknowns solution of the Beer-Lambert law was however performed in real time to act as a visual indication of the relative changes in cerebral oxygenation at the bedside.

A printout of the data stored on disk in shown in Figure 5.26. The data contains information on both the incident, reflected and transmitted light together with the dark count and comments entered by the user, recorded next to the accumulation period to which it applies. The data storage is in an ASCII format which can be read by post-analysis programs or commercially available spreadsheet programs such as Lotus-123® or Smart®. Numerical values and text are differentiated by the use of inverted commas. The use of ASCII makes data storage rather inefficient, but this disadvantage is outweighed by flexibility in handling compared to binary data. The storage of the incident and transmitted data instead of the calculated change in attenuation adds to the amount of data stored. This may eventually prove unnecessary but is useful when debugging problems such as possible instrument drift or non-linearity in the system.

5.9 SYSTEM OPERATION

The system components are mounted in a 19" instrument rack on wheels which is first positioned at the bedside. Initially, the laser diode power supplies are all set to give maximum power and a total of 4 optical densities of neutral density filter added to the PMT housing.

```
"ired9" "   775nm." "   813nm." "   847nm." "   904nm."
"Patient's Name: xxxxxx"
"Patient's No.: 127"
"Patient's Run No.: 01"
"Date: 26/ 5/1987"
"paralysed, diaphragmatic hernia"
" mins ""x"  "inc 1"  "inc 2"  "inc 3"  "inc 4"  "ref 1"  "ref 2"  "ref 3"  "ref 4"  "tmt 1"  "tmt 2"  "tmt  3"  "tmt 4"    "nse""comment"
      0.00 "     -1.00     -7.25     -1.63     -0.38   -107.87   1733.62   -109.00   -106.88    0.00000    0.00000    0.00000    0.00000    0.00000 "
      0.33 "     -1.89     -6.78     -1.33     -0.44   -107.44   1743.44   -109.44   -107.33   -0.00007   -0.00010   -0.00017   -0.00010    0.00193 "
      0.67 "     -2.00     -5.89     -1.00     -0.56   -105.11   1744.00   -106.67   -104.44    0.00070   -0.00043   -0.00073    0.00003    0.02037 "
      1.00 "    340.44   1273.00    394.11    179.67   -106.11   1753.89    -99.22   -104.89    0.30160    0.32233    0.09323    0.01327    0.02393 "
     29.62 "    271.78   1005.89   1061.22   2338.67   -102.11    435.00   1863.67   -101.00    0.35327    0.32490    0.34547    0.24883    0.00560 "
     29.95 "    275.11   1005.00   1061.11   2338.44   -101.00    435.00   1874.33   -100.33    0.35147    0.32090    0.34620    0.24497    0.00530 "
     30.28 "    272.22   1005.11   1061.67   2339.00   -103.56    435.11   1880.00    906.56    0.33993    0.31140    0.33240    0.24017    0.00623 "
     30.67 "    270.00   1007.90   1062.10   2337.80   -103.60    435.30   1875.10    902.80    0.33657    0.30743    0.32970    0.23537    0.00577 "lasers stable now"
     31.00 "    272.22   1007.33   1062.56   2338.33   -100.67    435.33   1847.67    884.33    0.32583    0.30557    0.32570    0.23113    0.00557 "chan5 co2"
     31.48 "    262.77   1008.92   1063.31   2334.38    -99.46    438.85   1747.15    826.62    0.30087    0.27103    0.29073    0.20720    0.00583 "chan6 tcpo2 upper body"
     31.83 "    264.50   1010.20   1063.70   2334.20   -102.20    445.10   1670.20    799.60    0.29350    0.27020    0.28613    0.20383    0.00577 "chan7 searle po2 1 body"
     32.17 "    267.00   1011.56   1064.11   2332.89   -101.44    445.11   1636.78    799.56    0.29240    0.26820    0.29013    0.20483    0.00603 " gas co2 - 4.6"
     32.50 "    272.33   1012.78   1064.67   2332.67    -99.44    445.00   1626.67    788.89    0.27573    0.25017    0.26360    0.18880    0.00547 "
     32.83 "    274.00   1011.44   1063.89   2332.56   -106.33    447.22   1610.89    805.11    0.30063    0.27980    0.29370    0.20883    0.00573 "
     33.17 "    273.44   1012.44   1064.89   2335.00   -104.44    455.11   1602.11    812.78    0.31777    0.29073    0.30857    0.21840    0.00580 "
     33.50 "    272.22   1011.44   1065.00   2336.22   -104.44    452.00   1609.00    810.11    0.28903    0.25620    0.27010    0.19423    0.00600 "
     33.83 "    272.11   1012.00   1065.78   2336.67   -102.44    445.33   1611.00    823.11    0.30890    0.28140    0.29747    0.21300    0.00500 "
     34.17 "    273.22   1010.89   1065.22   2337.78   -108.33    445.33   1610.00    790.56    0.30993    0.28190    0.30113    0.21617    0.00597 "
     34.50 "    274.67   1010.67   1065.22   2336.22   -104.89    445.22   1611.11    765.44    0.30467    0.27200    0.29067    0.20953    0.00567 "
     34.83 "    276.22   1011.33   1064.67   2336.22   -101.44    445.33   1605.78    807.22    0.31553    0.28413    0.30127    0.22043    0.00560 "
     35.17 "    274.67   1009.22   1064.22   2333.56   -100.33    445.33   1611.33    794.22    0.30610    0.27660    0.29330    0.21063    0.00570 "
     35.50 "    274.67   1007.33   1063.11   2334.11   -105.44    446.56   1593.67    775.67    0.28463    0.25580    0.27067    0.19723    0.00523 "
     35.83 "    274.11   1007.33   1062.56   2334.00   -104.44    446.78   1591.67    793.67    0.29660    0.26793    0.28790    0.21007    0.00543 "
     36.17 "    275.11   1007.44   1063.33   2334.11   -100.89    453.89   1587.89    771.56    0.29030    0.25873    0.27510    0.20490    0.00537 "
     36.50 "    272.67   1008.56   1063.11   2334.11   -101.00    455.22   1571.33    747.78    0.29173    0.26490    0.28037    0.20847    0.00530 "
     36.83 "    273.11   1009.67   1063.67   2335.44   -104.89    455.11   1566.78    749.11    0.29820    0.27433    0.29160    0.21543    0.00510 "
     37.17 "    274.00   1009.25   1063.63   2334.38   -103.75    455.00   1573.50    733.00    0.28543    0.26680    0.28083    0.20723    0.00557 "
     37.50 "    271.22   1009.22   1063.00   2335.33   -100.11    447.56   1561.00    722.00    0.27430    0.24713    0.26000    0.18990    0.00543 "swing o2"
     37.83 "    270.56   1010.44   1063.56   2336.00    -99.89    451.11   1481.78    691.89    0.29113    0.27387    0.29517    0.21563    0.00520 "
```

Figure 5.26 Part of a printout of the data stored on disk for a near infrared monitoring session.

After powering the system up, the peltier cooler must be left on for a minimum of 30 minutes for the PMT temperature to stabilise (60 minutes for the best performance, see Section 5.11.2.2). While this is taking place, the OPTODES are positioned on the patient and then shielded against excessive ambient light using a light tight black cloth. The patient information is entered via the keyboard, the system initialised, and with the lasers still off the incident and reflected light signals are zeroed, if necessary, by means of the offset controls. After checking the OPTODE attachments the lasers are switched on in SAFE mode and the PMT high voltage supply switched on.

The next task is to optimise the photon per pulse values (*PC*) for each laser to the optimum value of 0.125. This is achieved by first of all lowering the neutral density filter value in the PMT housing, so that the lowest *PC* value for any diode is 0.125. The *PC* values for the other laser diodes are brought down to 0.125 by lowering their emitted power via the laser diode power controls. The process is slightly iterative because the output power from the laser is temperature dependent and they take about 10 minutes to settle down after their power setting has been changed.

By this time the PMT temperature has usually stabilised and the system is ready for NORMALISATION and the recording of attenuation changes.

5.10 SAFETY REQUIREMENTS

Instruments manufactured for use in a patient environment (defined as being within 2.5 m of a patient) must comply with a number of British (BS5724)[164] and International safety standards (IEC 601-1)[165] on electrical and mechanical safety. A medical instrument must not pose a danger to the patient or operator either from an electrical or mechanical viewpoint. Equipment which incorporates the use of a laser (not specifically medical equipment) must additionally comply with a British laser safety standard, BS4803[72].

5.10.1 Electrical safety

BS5724 involves testing medical equipment at high voltages and is aimed at checking mass manufactured equipment, where the item tested is sacrificed to show the integrity of other identical instruments. These high voltage tests are not recommended for "one off" instruments such as this clinical near infrared spectrophotometer[166], the reason being that the instrument may be weakened.

This spectrophotometer was still designed to comply with the mechanical and electrical isolation requirements of BS5724. Electrical isolation of the patient (greater than 50 MΩ) was easy to achieve as optical fibres are the only connection between the instrument and the patient. The earth leakage currents of the items built in the laboratory were all less than the specified value, but this was not true of the computer (Olivetti M24) which uses standard mains filters. This problem can be overcome by running equipment in the instrument through a mains isolating transformer. All exposed metal parts were connected to protective earth through a mains connector with a resistance of less than 0.2 Ω.

5.10.2 Laser safety

Laser safety in this country is covered in the British Standard, BS 4803. Part I covers possible damage to both eyes and skin for a variety of laser wavelengths and exposure regimes using both pulsed and continuous wave (c.w.) laser sources. Part II covers aspects of the general design of laser products and is not specific to medical equipment.

Tissue damage is dependent upon the optical irradiance, exposure duration and the characteristics of the laser source, e.g. wavelength, beam divergence, pulse and c.w. characteristics. Eye damage occurs at a much lower radiation level than skin damage. The pathological effects of excessive laser radiation at near infrared wavelengths (Infrared A) are retinal burns or cataracts, while much higher radiation levels can burn the skin.

The type of damage caused by single pulses differs depending upon pulse duration. Nanosecond or shorter pulses cause acoustic transients and possibly cell disruption. Longer pulses from 100 μs to many seconds cause damage to the cellular protein as a result of generalised heating. Any damage resulting only after exposures greater than 100 seconds is due to photochemical effects.

5.10.3 Maximum permissible exposure (MPE) levels for laser exposure

The charts supplied in BS 4803, Part I allows for the separate calculation of the maximum permissible skin and eye exposure levels. The pulsed laser sources used in this instrument must satisfy these MPE levels. The standard specifies that a pulsed light source (as used here) must satisfy the MPE value for a single pulse, a train of pulses and for the average irradiance.

As a number of wavelengths are used, the laser hazard should be calculated as the average effect of each laser wavelength. In practice the "worst case" approach has been taken, based on each laser having the same wavelength, the one which gives the lowest MPE values. Table 5.ii summarises the characteristics of the laser light source in this instrument, treated as a single pulse, a pulse train and a continuous source as specified in BS4803.

Table 5.iii shows the MPE values for skin and eye exposure calculated from BS4803, together with the values calculated for the worst case (100% coupling efficiency) for the clinical near infrared spectrophotometer. The values for skin exposure are calculated at the surface of the emitting OPTODE (patient end). The calculated skin values are less than the specified MPE.

The MPE values for eye exposure are more complicated. A decision must be made as to whether the observer is viewing the laser "intrabeam" or as an "extended source". Intrabeam is when the laser beam subtends an angle less than 0.024 radians at the eye and extended source is for subtended angles greater than 0.024 radians. For these OPTODES this limit occurs at a viewing distance of 0.21 metres.

The data in Table 5.iii shows that all the instrument values are less than the MPE

Table 5.ii Characteristics of the semiconductor laser diode light source used in the clinical near infrared spectrophotometer, calculated for comparison with BS4803.

	Power (W)	On-axis irradiance (W $ster^{-1}$)	Pulse width (ns)	Pulse repetition frequency	Area (mm^2)	Numerical aperture
Single pulse	10 (pk)	70 (pk)	100	—	20	0.54
Pulse train	10 (pk)	70 (pk)	400	4 kHz	20	0.54
Continuous	0.016 (av)	0.112 (av)	∞	—	20	0.54

Table 5.iii Comparison of the maximum permissible exposure values (MPE) in BS4803 with values calculated for the clinical near infrared spectrophotometer.

Exposure conditions	MPE value, BS4803	Laser system output	
For skin exposure			
Single pulse radiant exposure	200	0.05	$J\ m^{-2}$
Pulse train radiant exposure	12	0.20	$J\ m^{-2}$
Average irradiance	2000	800	$W\ m^{-2}$
Eye exposure, Extended source closer than 0.21 metres			
Single pulse integrated radiance	690	0.35	$J\ m^{-2}\ ster^{-1}$
Pulse train integrated radiance	41.3	1.40	$J\ m^{-2}\ ster^{-1}$
Average radiance	9000	5600	$W\ m^{-2}\ ster^{-1}$
Eye exposure, Intrabeam greater than 0.21 metres			
Single pulse integrated irradiance	7.05	≤ 0.16	$mJ\ m^{-2}$
Pulse train integrated irradiance	0.42	≤ 0.64	$mJ\ m^{-2}$
Average irradiance	4.5	≤ 2.54	$W\ m^{-2}$

except for one, the intrabeam eye exposure. A number of other values are within a factor of two of their MPE. However, the calculation made here used the manufacturers data for the maximum amount of light available from the semiconductor laser diodes together with a 100% coupling efficiency from laser diode to fibre optic bundle. In reality the optical powers are a factor of 5 to 10 less than these worst case calculations due to optical coupling efficiency and the very generous specification of the laser diode manufactures. This leaves a safety margin of at least a factor of two making the instrument safe for both eye and skin exposure. Note that in any case a safety circuit is installed to prevent accidental eye exposure.

5.11 SYSTEM PERFORMANCE

A number of checks were made on the system performance. The first was to determine the independence of the signals from the four laser diodes. This was easily checked by switching on each one in turn, observing all incident, reflected and photon count data. No interference between channels was observed. Similarly, the average values of the photon count minus dark count were independent of dark count level.

More importantly, the system is subject to a number of possible sources of drift which could affect a measured attenuation value at one or more wavelengths.

5.11.1 Sources of system drift

Drift can be measured when a stable phantom absorber is placed in the light path such as a large number of neutral density filters. Sources of drift can occur anywhere from the light source to the detector, and the system design included many features to reduce each source of drift to an acceptable level. An acceptable level of systematic error was defined, Section 4.1, as being 0.005 OD cm^{-1} tissue transmitted (typically 0.03-0.04 OD across an infant's head), for each diode, over a measurement session of up to four hours.

5.11.1.1 *The photomultiplier tube detector*

A problem common to all photomultiplier tubes is that of maintaining a stable high voltage bias. The gain/voltage relationship of a R636 PMT is a straight line relationship on a log log scale, described mathematically as

$$\lg G = a \lg V + b \qquad \text{5-7}$$

To estimate the stability in bias voltage required to maintain the anode gain to within an error say ξ, consider two points on the straight line at G_1, V_1 and at $(1+\xi)G_1, V_2$. Eliminating G_1 from the equations and solving for the ratio V_2/V_1 gives

$$\frac{V_2}{V_1} = \sqrt[a]{1+\xi} \qquad \text{5-8}$$

The high voltage power supply in the C1230 was specified at 0.2% drift so that V_2/V_1 was less than 1.002. For the R636 PMT, $a = 7.5$, $b = -16.3$, which entered into Equation 5-8 above gave $\xi = 0.015$ so the maximum possible drift due to PMT bias voltage was 1.5% (or 0.0065 OD). This was within the 0.02 OD specified over a 4 hour period. A drift caused by PMT high voltage bias variations would be observed equally at all wavelengths. A drift in the gain of the pre-amplifier or the voltage of the discriminator would also show up in a similar manner.

Drifts which are wavelength dependent are also possible. These are caused by the wavelength dependent characteristics of the photocathode material and are particularly important for GaAs photocathodes, operated near the cut off wavelength of 900 nm. However, Section 5.11.3 illustrated that the GaAs PMT can be considered drift free as long as an adequate amount of time was allowed for the temperature controller to reach its control band.

In the long term, this type of photocathode suffers significantly from aging, resulting in a decrease of quantum efficiency. The rate of aging is essentially proportional to the integral of the photocathode current. This should not prove to be a problem at the low light levels expected here, but aging is likely to be noticeable on a 1000 hour timescale.

5.11.2 The laser diodes

The effectiveness of the INCIDENT light measuring circuit (Section 5.6) in correcting for laser diode optical power variations was investigated using a commercial power meter (Coherent, USA, Model 212) fitted with a 1000:1 attenuator. The Coherent power meter was placed at the patient end of the multitail fibre optic bundle of Figure 5.16 measuring the average light intensity delivered to the patient. Its output should correlate linearly with that of the "incident" measuring optical pulse integrator because the pulse repetition frequency of the laser pulses is constant (quartz crystal controlled).

This test was set up using one of the laser diodes (at 847 nm) as the light source. The optical pulse width was set to 100 ns (FWHM) and the pulse repetition rate to 4 kHz. Changes in laser diode output power were achieved by varying the peak diode current through the laser diode power supply voltage control.

The result of the test is shown in Figure 5.27(a). The result was highly non-linear and unpredictable with an unacceptable deviation from the linear regression line. This degree of non-linearity was not acceptable in this application. The rather unpredictable nature of the

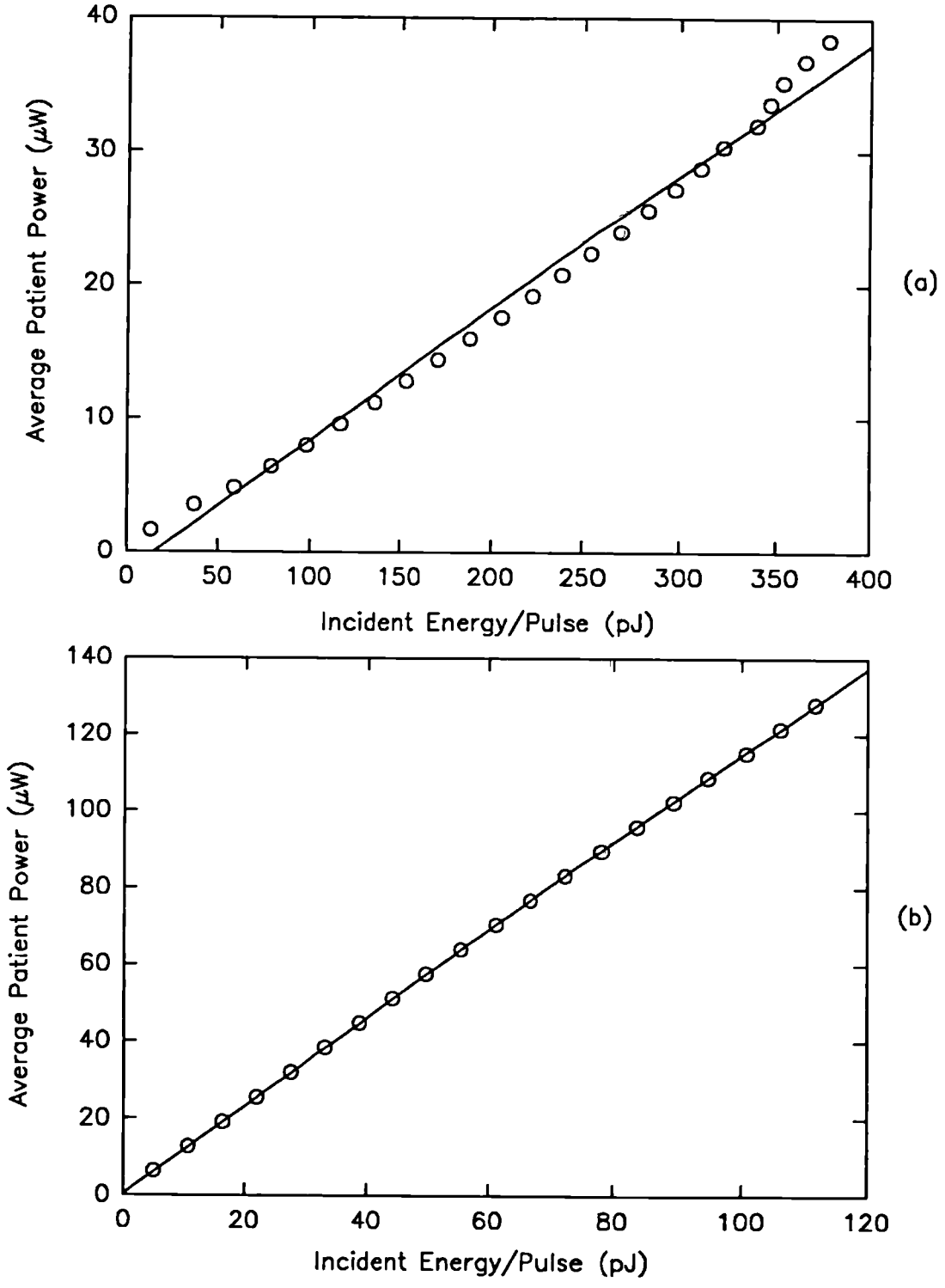

Figure 5.27 Linearity of the "incident" measuring technique: (a) no fibre optic rod mode scrambler; (b) with fibre optic rod mode scrambler.

deviation from linearity suggested it was not due to the INCIDENT optical pulse integrator circuit itself. A more likely cause was a variable division of the laser diode output beam entering into the INCIDENT and PATIENT optical fibre bundles. The method by which the beam was split into these two fibre bundles (Figure 5.16) was such that any change of the laser diode beam shape would affect the percentage of the signal going into each bundle of fibres. It has been shown that laser diodes produce highly elliptical output beams, and there are several reasons why the output beam shape may change with drive current. For example thermal expansion of the emitting region width and changes in the emitting pattern along the emitting length, such as the "hotspots" and "deadspots" already reported. It was obvious that some optical arrangement was needed to overcome these problems due to the deviations of the laser diodes from the ideal light source.

There were a number of possible solutions to this problem. Firstly, the fibre optic bundle bifurcation could be made (as originally suggested) totally randomly. In practice this may be impossible to achieve. Secondly, an optical system consisting of lenses and a beam splitter could provide an exact but expensive solution requiring precise alignment. The solution adopted in this instrument was to remove the elliptical nature of the emitted light by using a large diameter rigid glass fibre optic rod, core diameter 2.25 mm, placed against the laser diode window.

The rod scrambles the elliptical beam over many internal reflections into a near circular beam (the longer the rod the greater the effect). In practice a 6 cm length rod was placed between the window of the laser diode package and the ferrule of the fibre optic bundle. With this rod in place, the previous experiment was repeated to produce the results shown in Figure 5.27(b). A large improvement can be noted, the R^2 value for a linear regression was 0.99998. This result shows that once the optical reference sampling method was satisfactory, then the output of the optical pulse integrator circuit varied linearly with respect to the optical power delivered to the patient. Hence, drift in laser diode output power could be accurately corrected for by the addition of a fibre optic rod placed against the laser diode window. These rods were therefore incorporated into the system.

The use of a fibre optic rod to improve the performance of a beamsplitting system in this manner is the subject of a Patent[167].

5.11.2.1 *The combination of the PMT and laser diodes*

The previous two sections have shown that the inherent sources of drift in the photomultiplier tube and laser diodes can be overcome by careful attention to detail. There is however one source of drift which is inherent and not easily overcome. This is the result of a combined effect of the laser diodes and the photomultiplier tube. This problem was overlooked during the system design and turned out to be the most significant source of long term drift.

All the laser diodes have a temperature dependence with wavelength of +0.25 nm°C^{-1}. The PMT has a wavelength dependence of sensitivity as shown in Figure 5.28 (solid line). Multiply the two effects together and "effectively" the quantum efficiency of the PMT for each laser diode is dependent upon the temperature of that laser diode. The fractional change in quantum efficiency per unit wavelength for the R636 PMT is also shown in Figure 5.28 and indicates that the only laser diode which is sensitive to this effect is the 904 nm one. It has a temperature sensitivity of −1.25% °C^{-1} (or +0.005 OD °C^{-1}).

During the warm up from cold, after first switching on the laser diodes, the laser diode junction temperature rises by about 15°C. The instrument obviously cannot be used during this period. However this period is kept to a minimum by using a laser diode heatsink

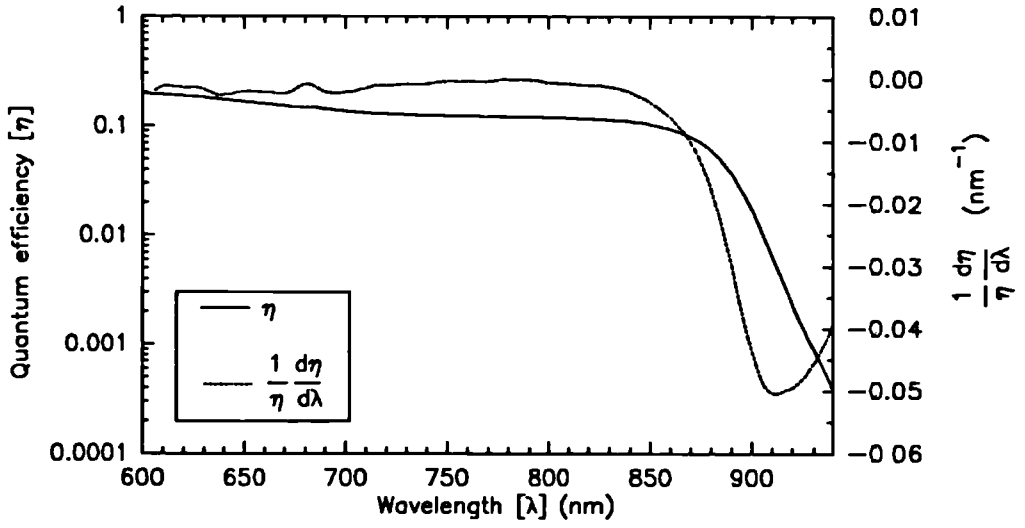

Figure 5.28 Quantum efficiency of the R636 (GaAs) photomultiplier tube and the fractional change of quantum efficiency per unit wavelength as a function of wavelength.

of low thermal mass.

Variations in room temperature will also have an effect but this is less dramatic. The room temperature variations could be overcome by controlling the temperature of the laser diode heatsink, most sensibly with a peltier cooler. However the problems during the warm up period would always exist, due to the high junction to case thermal resistance of the laser diode package.

5.11.2.2 *Overall drift performance*

The overall drift of the system was tested experimentally. After allowing the PMT temperature controller 30 minutes to stabilise, filters totalling 10 OD were placed in the neutral density filter holder of the PMT housing. The optical fibres were placed 5 cm apart and the photon/pulse settings of each laser channel set to 0.125 after a warm-up period. The whole system was then switched off and allowed to reach ambient temperature over a period of many hours. All settings were kept the same. The whole system was then switched on and after an initial 2 minute warm-up period, the system response to this stable attenuator was monitored for a period of 6 hours.

The result of this experiment can be seen in Figure 5.29, the data was NORMALISED at 60 minutes. At three different times during this run, additional 0.1, 0.3 and 0.5 OD filters were placed between the fibres, and the results can be clearly seen at each wavelength. The drift of the system over the period from 1 to 6 hours was less than 0.02 OD at all wavelengths. The worst drift occurred at 778 nm and 904 nm.

The drift in attenuation of +0.02 OD (from 1-6 hours) by the 904 nm diode was probably caused by an increase in the ambient temperature causing a increase in wavelength and hence a decrease in the effective quantum efficiency of the PMT for this laser diode. The drift at 778 nm was more difficult to explain. It coincided with a drift down in the 778 nm laser diode output power. This did not occur with the 813 nm, 867 nm and 904 nm laser diodes which were relatively stable after the initial 10 minutes. It may be that the "fibre optic rod" in front of this laser diode together with the bifurcated optical fibre bundle was still not acting as an ideal beamsplitter for this laser diode.

The one hour stabilisation period, before the instrument can be used, is somewhat longer than expected and appears to be a time lag before the PMT photocathode reaches a constant temperature (see the PMT dark noise graph in Figure 5.29). The thermistor in the

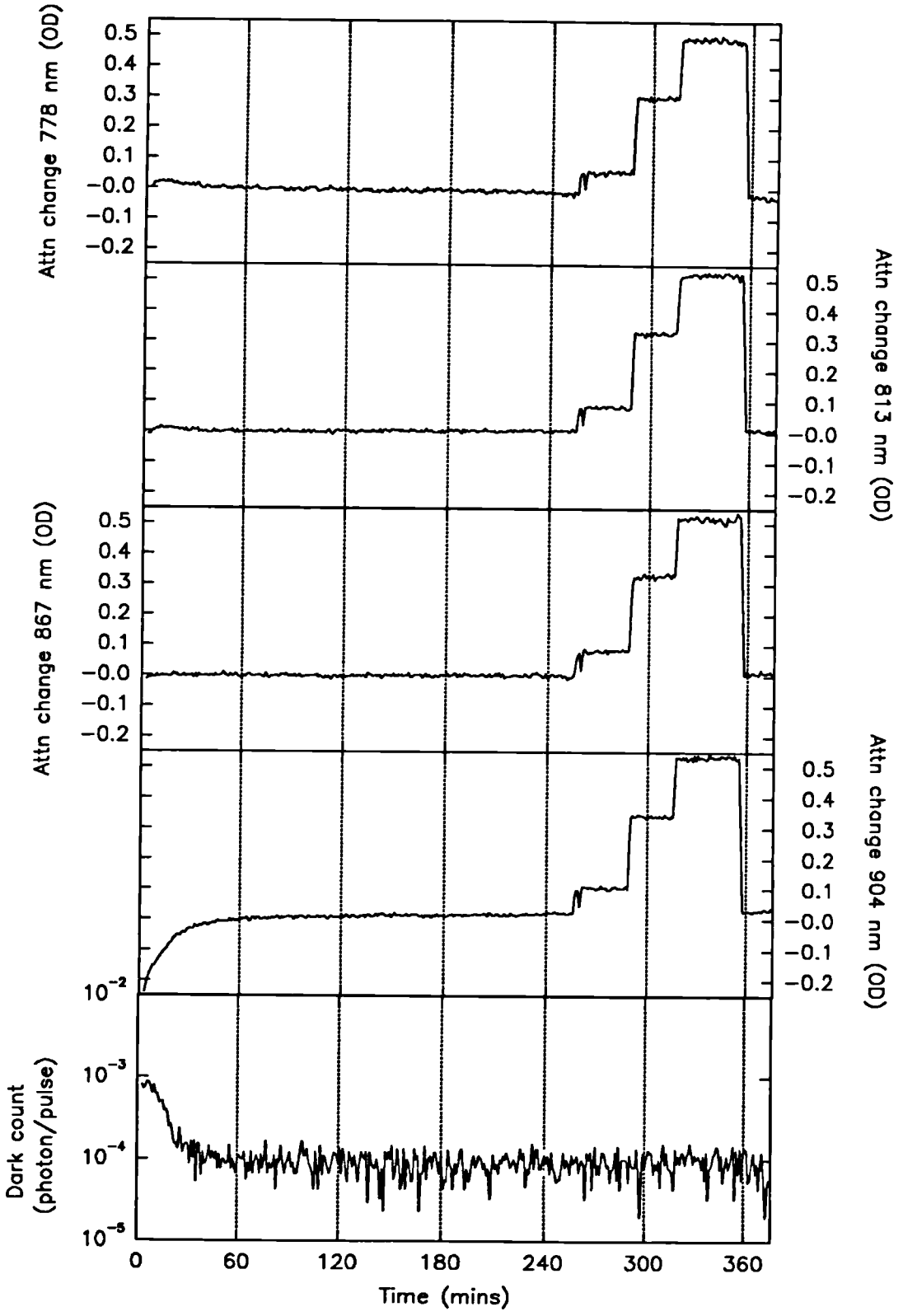

Figure 5.29 Drift of the complete near infrared spectrophotometer system over a 6 hour period from switch on.

peltier cooled housing reached a constant temperature within 20 minutes. Thus for optimal drift performance was it best to wait 1 hour after switching on the peltier cooler and 8 minutes after switching on the laser diodes before taking any readings. However an adequate performance would have been available after 30 minutes.

5.11.3 System non-linearities

Previous sections have discussed the system performance in terms of its drift characteristics. Drift performance has been shown to be adequate and was limited mainly by the 904 nm attenuation measurement. In this section, performance is examined with respect to non-linearities of the measured attenuation changes. A known source of non-linearity is the use of photon counting at high count rates. The ideal clinical spectrophotometer would make measurements both with a high signal to noise ratio and perfect linearity, but photon counting puts restrictions on obtaining both these characteristics simultaneously. Low noise measurements obtained in a short time period requires a high photon rate (see Equation 4-13) whereas a high count rate also means greater non-linearity.

5.11.3.1 *Pulse pile-up error theory*

The total deadtime of the R636 PMT and the C1230 amplifier has been measured at 30 ns (τ_p) and the deadtime of the C1230 discriminator/K7025 multichannel counter at 109 ns (τ_d). The statistics of photon arrival at a PMT are Poissonian (see Equation 4-10). It is assumed that the light transmitted through the head can be treated as an unpolarised thermal source. A simple description of pulse pile-up error for a continuous light source is available in the manufacturers literature[168].

A detection error will arise when two photoelectrons are emitted from the PMT photocathode within the PMT/amplifier deadtime. The probability of the second photoelectron being detected is given by the probability of zero photoelectrons arriving in the PMT deadtime which (from Equation 4-10) is given by $P(0,\tau_p) = \exp(-N_p\tau_p)$. Thus the input photoelectron arrival rate (N_p) and detected photoelectron output rate from the PMT/amplifier (N_{op}) are related by

$$N_{op} = N_p e^{-N_p \tau_p} \qquad 5\text{-}9$$

The discriminator is somewhat different in its response. Unlike the PMT, a second pulse arriving in its deadtime will not paralyse the discriminator for a further deadtime. In an accumulation time t, the number of incoming pulses from the PMT is $N_{op}t$ and during this accumulation time the detector is "dead" for a total time of $N_{od}t\tau_d$, where N_{od} is the output count rate from the discriminator. The number of output pulses is given by the incoming pulse rate multiplied by the time during which the discriminator is able to count pulses, which is $N_{od}t = N_{op}(t - N_{od}t\tau_d)$, rearranging this equation gives

$$N_{od} = \frac{N_{op}}{1 + N_{op}\tau_d} \qquad \text{5-10}$$

The derivation above assumes a continuous light source. The same equations were applied to the repetitively pulsed laser diode system, assuming a repetitive train of rectangular optical pulses, duration t_p. During the pulse ($0 < t \leq t_p$) the photoelectron arrival rate is N_p (as in the above equations), but it is zero for ($t_p < t \leq t_n$), where t_n is the time between pulses. Thus the number of photoelectrons per light pulse (n_p) is $n_p = N_p t_p$. Similarly, the detected counts from the PMT/amplifier per light pulse is $n_{op} = N_{op} t_p$, and from the discriminator output $n_{od} = N_{od} t_p$.

The analysis described above was tested in an experiment using a single laser diode at 847 nm, pulse width 100 ns. In this test, the whole system was tested using the photon counting detector combination of the R636 PMT, C1230 counter and K7025 multichannel counter. The delivering and receiving fibre optic probes were placed 5 cm apart and filters totalling 8 OD placed between them, The fibre optic mode scrambler was used to linearise the INCIDENT measuring circuit. Changes in reference and transmitted optical power were made using the 847 nm laser diode output control, any changes in the laser diode pulse width were ignored. This method of adjustment can only achieve a dynamic range of one order of magnitude in optical power. To obtain a larger dynamic range, three overlapping sets of results were taken with additional 1.0 and 2.0 OD filters. The three sets of experimental data, matched by eye to provide the best overlap, are shown as three different types of symbols in Figure 5.30(a). The ordinate is in units of the average number of detected photoelectrons per light pulse (n_{od}), while the abscissa is arbitrary, measured experimentally as the voltage from the INCIDENT light measuring circuit. To facilitate a comparison with the theory above, the ordinate has been scaled to match the axis for the theoretical results i.e. the average number of photoelectrons per light pulse emitted from the photocathode (n_p). The matching was

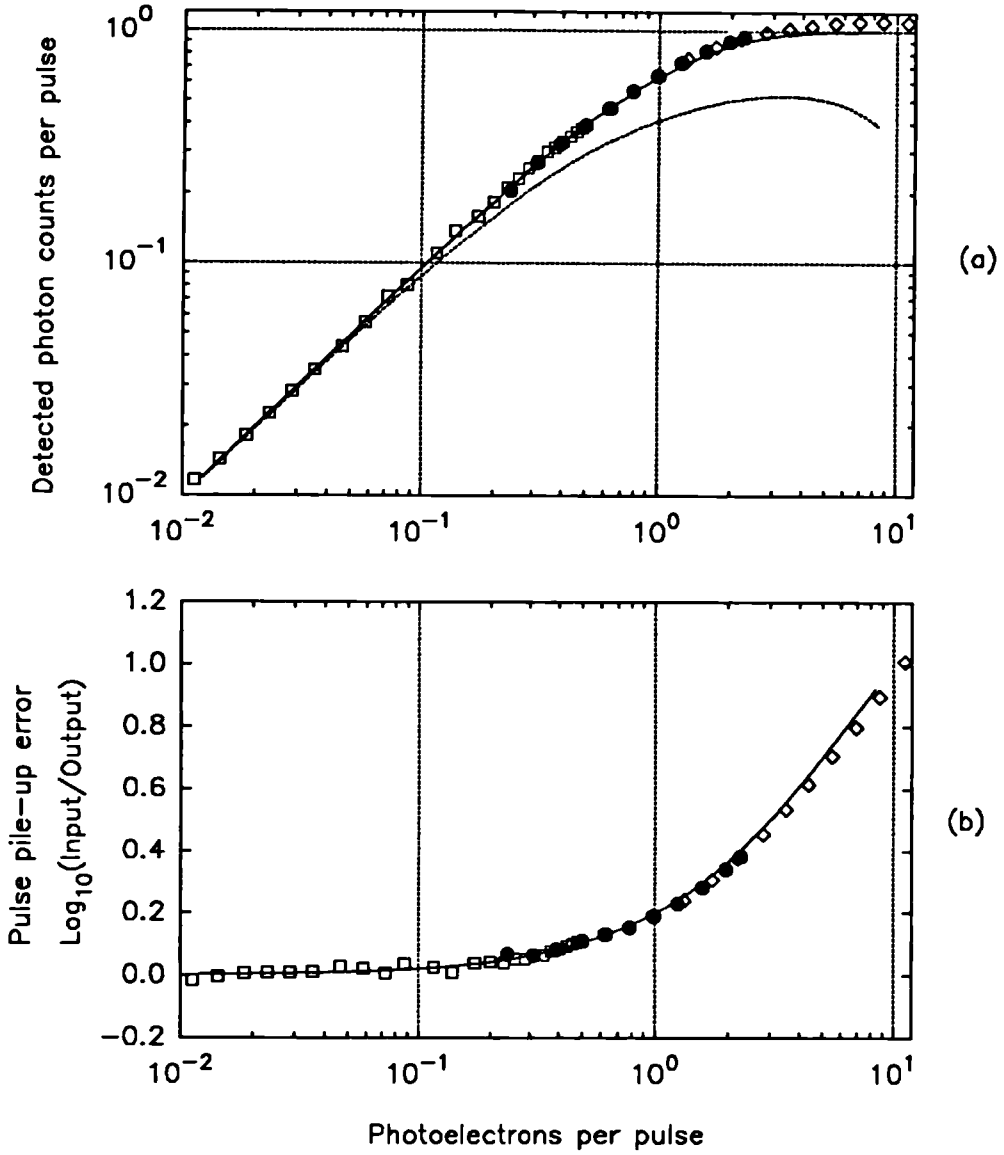

Figure 5.30 (a) Non linearity due to pulse pile-up error, symbols=experimental data points; broken line="continuous light source" theory; solid line="pulsed light source" theory. (b) The pulse pile-up error.

achieved at lowest photon count rates where the pulse pile-up error is insignificant. The theoretical curve, the dashed line in Figure 5.30(a), was calculated using the deadtimes measured experimentally and Equations 5-9 and 5-10.

The results showed the characteristic fall off in sensitivity of a photon counting detector as the mean time between photoelectrons approached the deadtime of the photon counting system. The match between theory and experiment was poor, especially at the

highest count rates. Experimentally the system was more linear than was predicted by the theory. For this reason the theory was re-examined for the case of a pulsed light source, where the optical pulse width (t_p) was approximately equal to the deadtime τ_p, τ_d.

A more thorough examination of the effect of the pmt/amplifier deadtime has been published[169], but it was difficult to add the effect of the discriminator/counter deadtime to this theory. However, the theory was considerably simplified in the case when the discriminator deadtime was longer than the individual light pulse duration. Then, for any individual light pulse which generated one or more photoelectrons the detected count would always be unity. Thus the probability of detecting one count per light pulse was given by $1 - P(0,t_p)$ and therefore the mean discriminator output count per light pulse was given by

$$n_{od} = 1 - e^{-n_p} \qquad 5\text{-}11$$

Hence when the light pulse width was shorter than the deadtime of the photon counting system, the relationship between the detected counts per light pulse and the input photoelectrons per light pulse was independent of the system deadtime and the pulse duration. The solid line of Figure 5.30(a) showed that Equation 5-11 and the experimental data matched very well. Figure 5.30(b) showed the pulse pile up error (plotted as $\lg[n_p/n_{od}]$). The accuracy of this theory was more clearly here, the deviation between experiment and theory probably being due to the non rectangular pulse in the experiment which was wider than τ_d (109 ns) at its base.

Equation 5-11 has been used in this thesis to correct for the pulse pile-up error in the data from all the LA-68 laser diodes, as they were all used with pulse lengths of 100 ns. The LA-8 diode was however used with a pulse length of 200 ns and hence Equation 5-11 cannot be used. An analytical solution for this case was very difficult to derive, therefore a Monte Carlo simulation of the pulse pile-up problem was performed, the program description is in Appendix A.

The LA-8 diode was normally used with a 200 ns current pulse and typically produced a 185 ns optical pulse (full width half maximum). The experimentally measured pulse pile-up error of the LA-8 diode provided a good match for the Monte-Carlo simulation of a 170 ns laser pulse (see the results and discussion in Appendix A). Hence the Monte-Carlo simulation data of the 170 ns pulse in Appendix A was used, as a look-up table, to correct for pulse pile-up error of the LA-8 laser diode data presented in this thesis.

5.11.3.2 *Noise and dynamic range considerations*

To achieve a signal to noise ratio of 1% (0.0043 OD) as set down in the system specifications required 10000 detected counts per laser per measurement interval. For example, 10000 counts would be detected in a 20 second measurement interval given that $n_{od}=0.125$. In this situation the pulse pile-up error would be significant (≈7%) were it not corrected for.

In use, the system was first set to operate at some initial value of n_{od} (typically 0.125) but then this value would change as the oxygenation of the brain changed. The maximum dynamic range of the instrument was approximately +1 OD to –0.7 OD before either the noise became very large or the detector saturated. The possible dynamic range of the signal due to extinction coefficient changes in an infant's brain could be estimated from the data in Section 1.2.4. Based on possible p_aCO_2 variations of ±3 kPa, the blood volume in the brain was predicted to vary from 56 μM to 112 μM, therefore the maximum optical density change per centimetre of brain tissue (at 800 nm) would be approximately ±0.23 OD cm^{-1} (Equation 4-2). Likewise if we imagine all the blood in the brain going from its oxygenated to deoxygenated form, then the tissue attenuation would change in the range +0.22 to –0.15 OD cm^{-1} over the wavelength region 775 nm to 910 nm.

These are the maximal magnitudes of changes possible, and if they ever occurred would be outside the maximum dynamic range of this instrument when measuring across 6-8 cm of brain tissue. However in clinical practice, intervention in the care of the infant would mean that these maximal changes in cerebral haemodynamics would be unlikely to occur.

Thus, it was possible to meet all the required specifications, both for signal to noise ratio and system linearity, albeit over a limited dynamic range. In practice this meant optimising the system with added neutral density filters for each patient studied in order to obtain an optimum initial photon count of 0.125 photon/pulse.

In future systems, problems of achieving good signal to noise, linearity and faster data acquisition simultaneously could be alleviated by using faster photon counting systems or by replacing photon counting with boxcar integration of the PMT photocurrent.

5.11.4 Attenuations changes across an adult forearm

The system was first tested out on the forearm of a healthy adult human volunteer. The fibres being placed in contact with and on opposite sides of the forearm. The OPTODES were 6 cm apart, and held rigidly to maintain this spacing. The site was then covered in a black cloth. The system was set up as outlined in Section 5.9.

After an initial steady state period of 4 minutes, a blood pressure cuff on the upper arm was rapidly inflated to above systolic pressure, achieving both arterial and venous occlusion. The cuff was released some 12 minutes later (at 16 minutes). Later, after a total elapsed time of 29 minutes the cuff was again inflated but this time to 60 mm Hg, thereby impairing venous return while still allowing arterial blood to enter the limb.

The results are shown in Figure 5.31, corrected for pulse pile-up error. The system was NORMALISED at time zero (normoxia) and tissue attenuation changes were measured from that point onwards. During the first cuff inflation period (12-16 minutes), little blood entered or left the limb, therefore the main process that occurred was the conversion of oxy- (HbO_2) to deoxy-haemoglobin (Hb) caused by tissue oxygen consumption. This interpretation agreed with the increase in attenuation observed at 778 nm and the decrease in attenuation at all other wavelengths, (see Figure 2.7). At 9 minutes, deoxygenation of haemoglobin (and myoglobin) appeared to be complete, and the subsequent decrease in attenuation which occurred at all wavelengths could have been due either to redistribution of blood within the vasculature of the arm or a reduction in the cytochrome c oxidase redox state. Redistribution of blood was an unlikely explanation as the haemoglobin should have been completely deoxygenated by this time and because deoxyhaemoglobin would have produced the largest attenuation changes at 778 nm. It was therefore more likely that this represented a change in cytochrome c oxidase redox state.

At 16 minutes, the cuff was released and reactive hyperaemia occurred, and an excess of arterial blood, was pumped into the arm as natural compensation for the oxygen deficit. The step jump in attenuation at 16 minutes was largest at 904 nm being of progressively lower amplitude at shorter wavelengths. This matched the absorption characteristics of HbO_2. The arm returned to normoxia over the next 12 minutes at which point the cuff was inflated to 60 mm Hg. This act lead to an increase in blood volume, as venous drainage was severely impaired, but arterial blood could still enter the limb. It was the venous system which swelled to take the extra blood volume, hence the largest increase in attenuation was at 778 nm corresponding

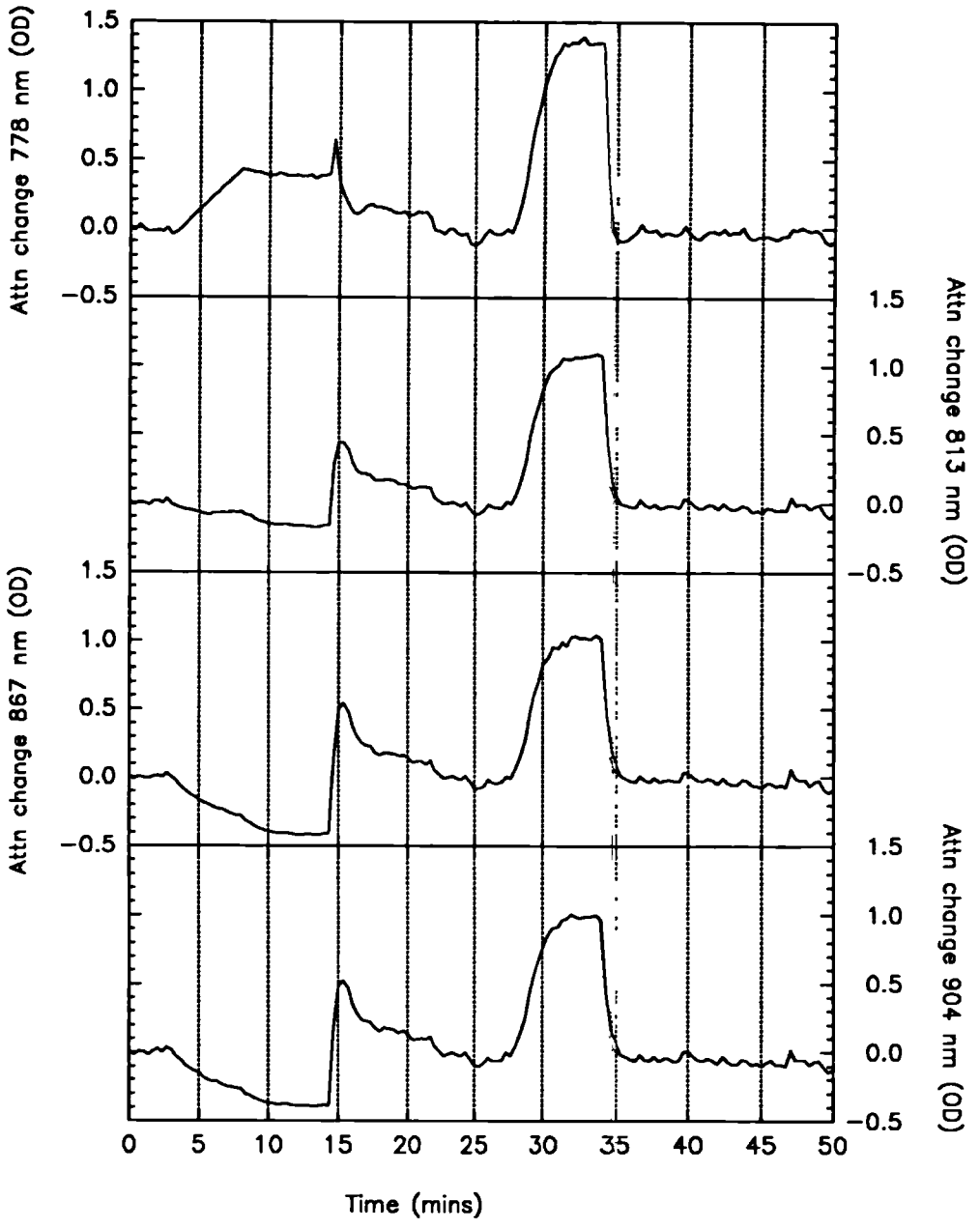

Figure 5.31 Changes in attenuation across 6.5 cm of adult forearm for both ischaemia and a partial block of venous return.

to absorption by Hb. After the cuff was released the arm returned to normoxia once more.

The discussion of the experiment above has been purely qualitative but the following chapters will look at methods of converting this attenuation data into quantitative changes in the concentration of oxy- and deoxy-haemoglobin and the redox state of cytochrome c oxidase and the interpretation of this information in terms of the oxygenation changes taking place in

both the blood and the tissues.

5.12 CHAPTER SUMMARY

This chapter has covered the construction and testing of a clinical near infrared spectrophotometer. With the aid of pulse pile-up error correction, the system has been shown to match the design specifications over a dynamic range in attenuation of +1.0 OD to –0.7 OD. The drift performance could still be improved from its current value of ±0.005 OD/hour after an initial PMT cooler stabilisation period of one hour and a laser diode stabilisation period of 8 minutes. The 904 nm diode signal is inherently sensitive to ambient temperature with a drift of 0.005 OD $°C^{-1}$ and it is fortunate that Special Care Baby Units are temperature controlled.

The data obtained on the adult forearm demonstrated the maximum range of the signals that can be expected and the physiological monitoring possibilities which the instrument offers.

CHAPTER 6

HAEMOGLOBIN AND CYTOCHROME C OXIDASE: SPECTRA AND INTERPRETATION

Chapter 5 followed the development of a clinically usable NIR spectroscopy system up to the point where changes in optical density could be measured at four near infrared wavelengths across the head of a newborn infant. This data must be converted into the corresponding changes in the concentrations of the oxygen dependent chromophores oxy- and deoxy-haemoglobin and cytochrome c oxidase. A simple three wavelength method for doing this has already been outlined in Section 4.1 in Equation 4-4 and this topic will be expanded upon in Chapter 7.

As outlined in the introductory chapter, the approach taken in this thesis has been to measure the absorption spectra of Hb, HbO_2 and cytochrome c oxidase in non-scattering solutions, and to account for tissue scattering by its effect upon the effective optical pathlength. To take this approach, accurate specific absorption spectra of the three chromophores Hb, HbO_2 and cytochrome c oxidase are first required. Obtaining these accurate spectra is the first problem discussed in this chapter. The optical properties of cytochrome c oxidase are more complicated and for that reason its spectra are measured both "in-vitro" and "in-vivo".

6.1 OXY- AND DEOXY-HAEMOGLOBIN

The near infrared spectrum of blood is taken to arise wholly from oxy- and deoxy-haemoglobin. The effects of carboxy- and sulf-haemoglobin and haemiglobin have been seen (Section 2.2.3) to produce only small errors in normal patients. Additionally the near infrared specific absorption spectra of the oxy- and deoxy- forms of fetal haemoglobin appears to be indistinguishable from those of adult haemoglobin[97]. There is also no evidence in the substantial amount of data on this topic to indicate that the optical properties of haemoglobin in-vivo in the red blood cell or in-vitro in solution should be any different. Therefore the haemoglobin spectra were measured in-vitro in clear solutions.

6.1.1 Measurement of the absorption spectrum of haemoglobin

Figure 6.1 shows the NIR specific extinction coefficient spectrum of oxy- and deoxy-haemoglobin obtained from three references Horecker[62], van Assendelft[94] and Barlow[170]. The spectra of oxy-haemoglobin from Horecker and Barlow are almost identical, within the error of manual digitisation of the data from the original publications, while the data points of van Assendelft are somewhat different. More variability is evident in the three spectra of deoxy-haemoglobin. Differences between the spectra could result from many sources such as incorrect scaling, baseline spectrophotometer drifts and sample turbidity. Extremely accurate haemoglobin spectra are required for this work, and experiments were therefore performed to establish precise spectra. The experimental method is now described.

6.1.1.1 *Methods*

Human blood from an adult volunteer was freshly removed into a heparinised container, centrifuged at 3500 rpm to separate the red cells from the plasma and white cells, and the supernatant removed and discarded. The red cells were then washed with 0.9% saline, separated again by centrifugation and the supernatant removed. This washing process was repeated a total of 4 times. The red blood cells were then free from the clotting proteins which were originally present in the plasma. The red cells were then lysed using an equal volume of distilled water to packed red cell volume and then buffered by a phosphate buffer to

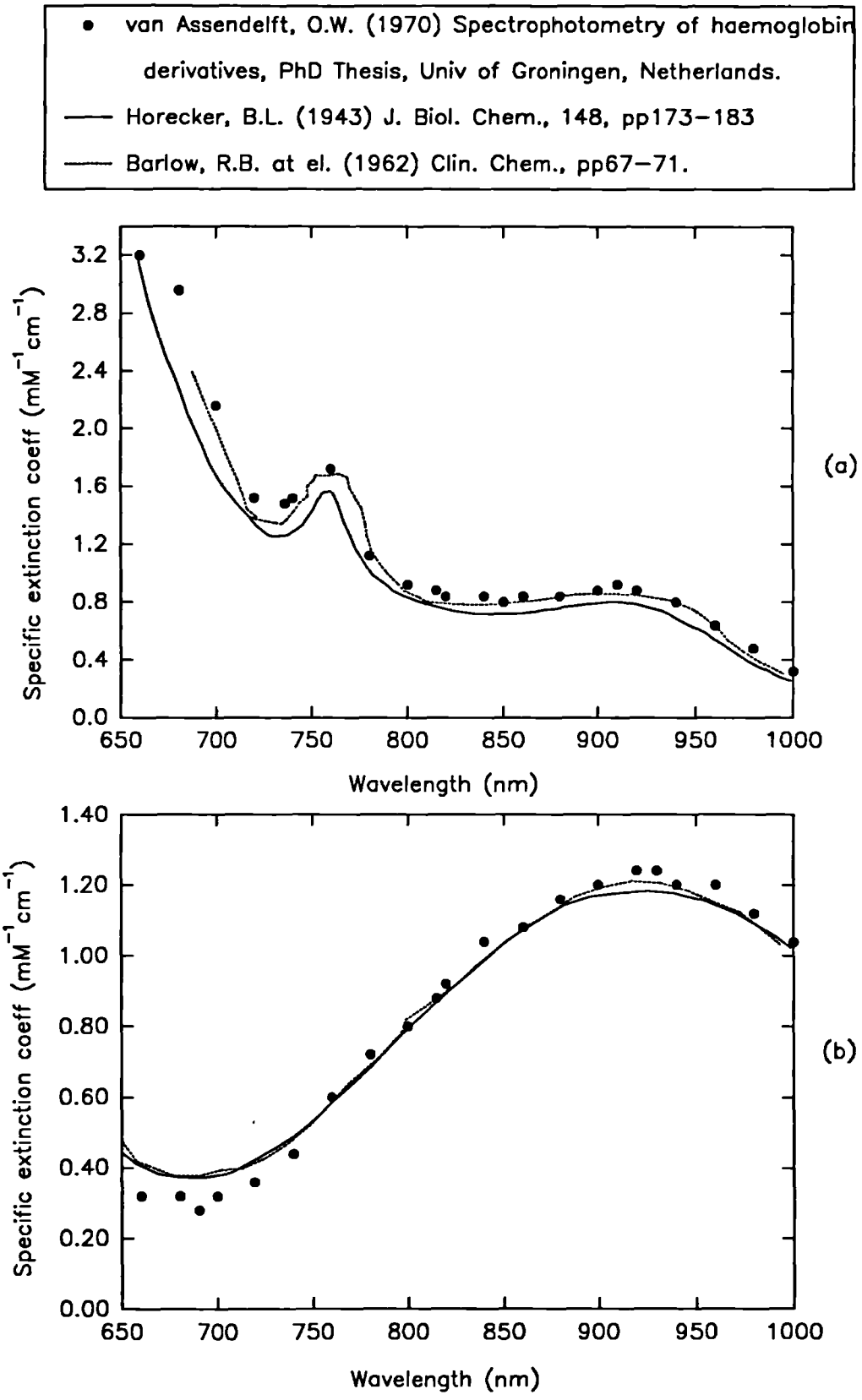

Figure 6.1 Various (a) deoxyhaemoglobin and (b) oxyhaemoglobin spectra, taken from the three publications indicated.

approximately pH 7.2. A small amount of trichloroethylene was then added and the mixture, shaken well to dissolve the red cell membranes left after lysing. The mixture was then centrifuged at 5000 rpm for 15 minutes. The haemoglobin solution was then drawn off into a syringe and passed through a 0.2 μm cellulose nitrate filter. To perform measurements of the NIR spectrum, the haemoglobin solution was first diluted to give an extinction coefficient of approximately 0.3 OD cm^{-1} at 800 nm (this corresponded to the original packed red blood cells diluted by approximately 1 part in 15).

The measurement of the oxy- and deoxy-haemoglobin spectra were performed on separate samples. The oxy-haemoglobin spectrum was the easiest to obtain. The haemoglobin solution was first bubbled with 100% O_2, then passed again through a 0.2 μm cellulose nitrate filter into a 1 cm pathlength glass cuvette. Its attenuation was compared to an identical 1 cm cuvette containing filtered, distilled water. Spectra were measured on a total of 9 different blood samples.

The pure deoxygenated form of haemoglobin was prepared by equilibration of a 5 ml filtered sample of haemoglobin solution with O_2 free nitrogen (O_2 < 5 ppm) for 45 minutes in a tonometer (Instrument Laboratories, IL237). The deoxygenated solution was then transferred to a previously evacuated anaerobic cuvette of 1 cm path length for the determination of its attenuation spectrum. Following the collection of this spectrum, the solution was slowly oxygenated by adding small volumes of oxygen, then gently shaking the cuvette. This procedure allowed spectra to be taken at various intermediate levels of haemoglobin saturation in order to accurately determine the isobestic point which was known to be near 800 nm (literature values have been quoted between 800 and 815 nm). Bubbling gas through the solution was deliberately avoided as it tended to lead to changes in the concentration of the haemoglobin solution as a result of evaporation of water. Spectra were measured on 8 different samples.

6.1.1.2 *Results*

The quality of the isobestic point near 800 nm can be seen in Figure 6.2. The position of the isobestic wavelength is 798 ±1.5 nm. This absolute value of the isobestic wavelength is marginally lower than values reported elsewhere in the literature (Horecker 800 nm, Barlow 805 nm, van Assendelft 815 nm). There are good reasons for the variations in wavelength of this isobestic point quoted by different authors. At the isobestic point the slope of the oxy-

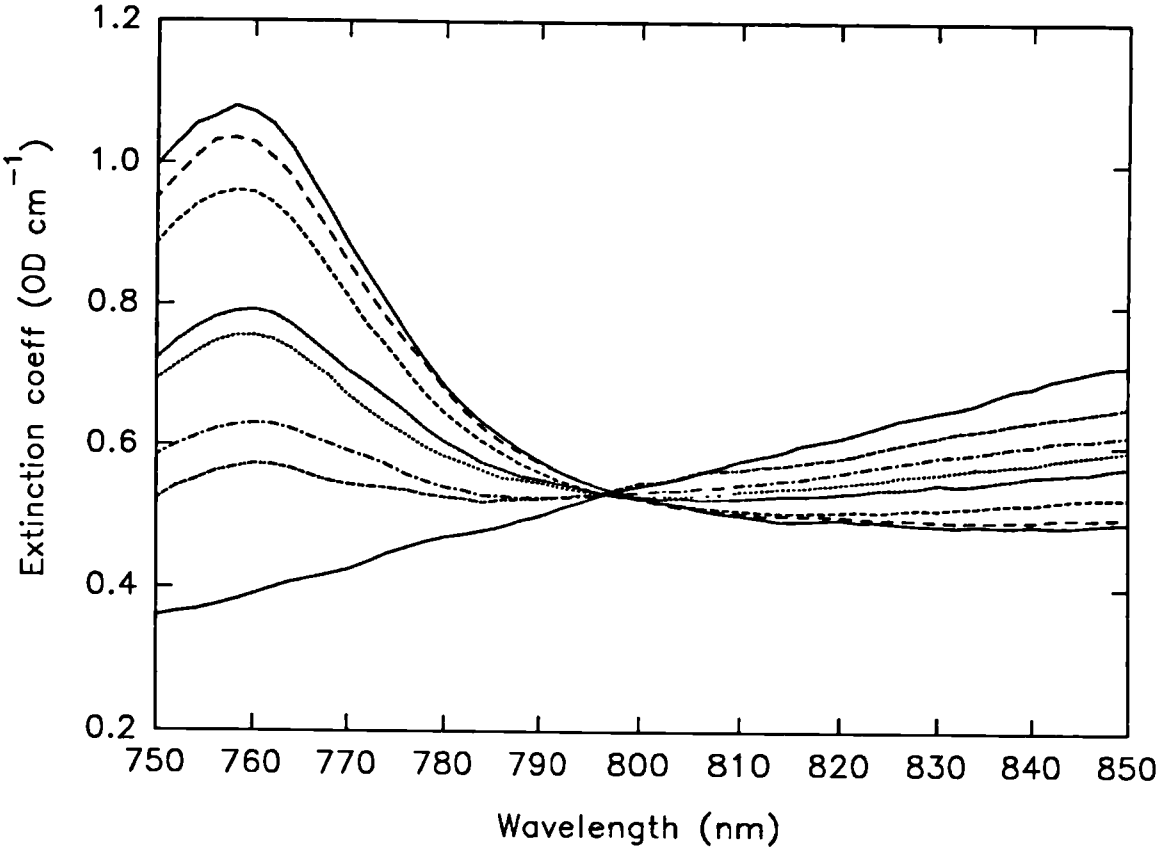

Figure 6.2 Spectra of haemoglobin solution taken at various degrees of oxygen saturation, indicating the near infrared isobestic point for oxy- and deoxy-haemoglobin.

and deoxy-haemoglobin curves are very shallow and a small error (<1%) in the concentration of haemoglobin, instrumental baseline drift or changes in sample turbidity between the spectra can lead to a relatively large (>10 nm) error in the position of the isobestic wavelength.

The methodology of determining the isobestic wavelength that was used here avoided concentration changes caused by water evaporation during bubbling. Most importantly, scattering changes were also avoided. Haemoglobin can become denatured and precipitate (producing scattering) if it is deoxygenated vigorously, or remains deoxygenated for long periods. Deoxygenation by vacuum was found to be particularly bad from this point of view. Even tonometry with nitrogen for periods in excess of one hour was found to produce a small increase in the amount of scattering. It was also observed that deoxygenation by excess sodium dithionite frequently caused increased scattering. Dithionite deoxygenation is the technique commonly used to obtain the deoxygenated spectrum of haemoglobin e.g. van

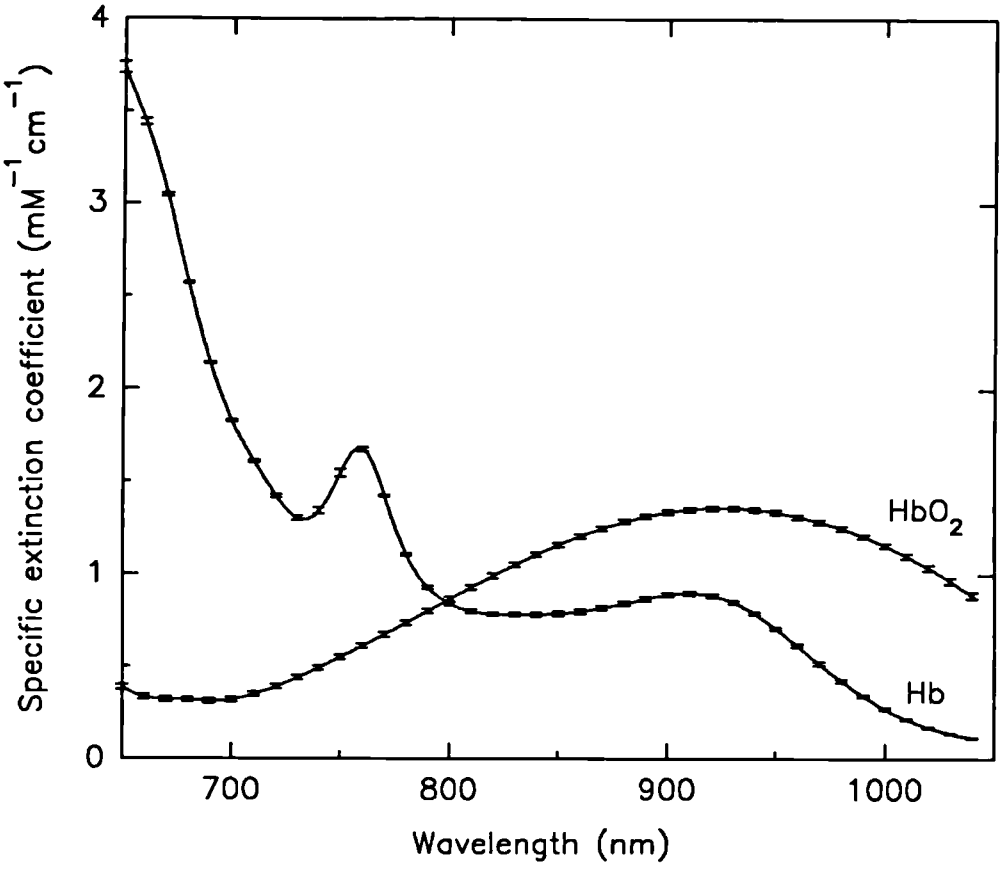

Figure 6.3 Experimentally measured specific extinction spectra of oxy- and deoxy-haemoglobin. Error bars indicate one standard deviation.

Assendelft[94] and Barlow[170]. With dithionite deoxygenation, the first spectrum which is measured is the oxygenated one. A small amount of dithionite is then added producing the deoxy- spectrum, and in our experience some additional degree of scattering, perhaps due to denaturation[†]. Observation of Figure 6.2 shows that an additional amount of attenuation caused by scattering in the deoxy- spectrum artificially pushes the isobestic point towards the longer wavelengths. The results presented here are taken in the opposite order, first deoxy- then oxy- spectra. Addition of oxygen is not likely to add to any scattering which might already be present.

The averaged spectra of oxy- and deoxy-haemoglobin are shown in Figure 6.3. The error bars indicate one standard deviation. Each individual sample contained a different and

[†] The method of denaturing could be a combination of high acid pH (especially if the dithionite is added in the solid phase) and peroxide ions. Better results should be obtained if sodium dithionite is first dissolved in oxygen free water and buffered to a neutral pH.

unknown concentration of haemoglobin, therefore each individual spectrum required scaling before averaging could be performed. Scaling of individual deoxyhaemoglobin spectra was performed such that the difference in attenuation between 700 and 1000 nm was the same, and for oxyhaemoglobin spectra the two wavelengths selected for scaling were 930 and 690 nm. Finally the averaged spectra were themselves scaled such that the extinction coefficient at 798 nm (the isobestic point) was the same as that quoted by other authors, 0.8524 $mM^{-1}cm^{-1}$.

The accuracy of these spectra appear to be very good, the standard deviation being approximately 1% of the mean value. Tabulated values are given in Appendix B. They could possibly be improved further, particularly the deoxy-haemoglobin spectrum, the sample ideally should be filtered after deoxygenation has taken place and not before deoxygenation as was done here. This operation would minimise any scattering effects.

6.1.2 Haemoglobin, its interpretation as blood oxygenation in-vivo

The sum of the oxy- and deoxy-haemoglobin concentrations ($HbO_2 + Hb$) can be interpreted as a cerebral blood volume measurement which is rather easy to visualise. The difference in concentrations ($HbO_2 - Hb$) can be interpreted as a measure of cerebral blood saturation measurement. However, the situation is more complicated than measuring for instance arterial blood saturation with a pulse oximeter. Here, the measured parameter is an averaged value for the blood in all the arterial, capillary and venous vascular systems in the brain. Interpretation of this requires some knowledge of cerebral haemodynamics, a subject which was introduced in Section 1.2.4. Further discussion is more conveniently performed with reference to clinically measured data and is therefore left until later, Section 7.6.

6.2 CYTOCHROME C OXIDASE (EC 1.9.3.1)

Monitoring the redox state of cytochrome c oxidase provides unique information on the status of intracellular oxygenation. If it can be shown that its redox state can be measured reliably in-vivo it could prove to be an important new parameter in clinical measurements. It is therefore worth expending considerable effort to try to achieve this objective. The in-vivo

monitoring of cytochrome c oxidase is however a far more complex problem than the monitoring of haemoglobin. For this reason this section contains an extensive discussion of the existing literature prior to a description of the measurement of its absorption spectrum. This discussion also points out a number of problems relating to the optical characteristics of the enzyme as well as problems of interpreting its redox state in-vivo.

One major difference between the monitoring of haemoglobin and cytochrome c oxidase in-vivo is that the concentration of all the respiratory enzymes can be assumed not to change over a period of hours. Any extinction coefficient change observed in the tissue is therefore not the result of a change in the enzyme's concentration but merely its redox state (i.e. $Cyt_{Ox} + Cyt_{Rd}$ is constant). Therefore it is only the difference spectrum between the oxidised and reduced forms ($Cyt_{Ox} - Cyt_{Rd}$) which is required and not the absolute spectrum of both forms. This is not the case for oxy- and deoxy-haemoglobin as the total blood volume ($HbO_2 + Hb$) can and does change.

The NIR difference spectrum of blood free brain tissue (normoxia minus hypoxia) is examined in this chapter. Theoretically this "in-vivo cytochrome c oxidase difference spectrum" should approximate to, but should not exactly match, the difference spectrum of the in-vitro isolated enzyme. Primarily, this is because it is the complete respiratory chain that is being measured in-vivo and not purely cytochrome c oxidase. However, from the literature available, it is predicted that the other respiratory chain enzymes should have negligible NIR extinction coefficients, see Figure 2.9. Hopefully, the redox states of the respiratory chain enzymes move in unison during changes in cellular oxygenation, so that a single spectrum will still be observed which is indicative of changes in tissue oxygenation in-vivo.

The two pieces of information that we thus require in order to use cytochrome c oxidase as an optical marker of tissue metabolism are: firstly, an accurate optical difference spectrum; and secondly, knowledge of the factors which affect its redox state in-vivo.

6.2.1 Cytochrome c oxidase: the literature

This enzyme is undoubtedly complex. There is a voluminous literature about it involving many studies using different methods of both chemical and physical analysis. Additionally, it is possible to study the enzyme in many different environments such as the isolated enzyme, in mitochondria, in liposomes and in-vivo.

The broad range of specialised analytical techniques that have been used to study

cytochrome c oxidase, has lead to the field becoming unwieldy and fragmented, a rather unfortunate outcome. Even definitive statements of "known" and "agreed" features of the optical characteristics of the cytochrome c oxidase enzyme are still being resolved. Explanations of some of the discrepancies between measured data could be due either to the sensitivity of the enzyme to the different experimental methods employed, or possibly the environment in which the enzyme is observed. The approach taken in this discussion of the literature has been firstly to look at how the respiratory enzymes behave when isolated in-vitro and then to apply that knowledge to data observed in isolated intact mitochondria and then finally in-vivo.

6.2.1.1 *The isolated solubilised enzyme*

Isolated cytochrome c oxidase is generally purified from tissue rich in mitochondria (e.g. heart tissue), and stored frozen in a buffer containing a non-ionic detergent such as Tween 80 in order to keep it in solution[171 172]. The detergent presents a similar hydrophobic environment to that found in the inner mitochondrial membrane. Information in the literature on various purified enzyme preparations do show some differences between preparations[173], mainly in the electron paramagnetic spectra (EPR) and the positions of the UV Soret band absorptions identified by NO and fluoride binding studies[174]. These variations are usually explained by the existence of different conformational states of the enzyme, and the fact that each preparation method will result in a different mixture of these conformations. There is evidence that after a cycle of reduction and oxygenation, all the preparations exist, at least temporarily, in the same conformations[175]. There have been suggestions[173] that the different preparation procedures can explain some of experimentally observed measurements on the untreated isolated enzyme, and that the raw isolated, solubilised, enzyme may be partially reduced, the degree of reduction depending upon the method of preparation[176]. This has enormous implications when trying to compare experimental results from different workers, since it implies that there is no "authentic isolated cytochrome oxidase". For further reading, see the opposing opinions of Powers[177] and Hartzell[178].

Despite the possibility of conformational heterogeneity, the enzyme is known to contain two haem groups (Cyt a, Cyt a_3) and two copper atoms (Cu_A, Cu_B), all of which may give rise to absorption bands in the UV/VIS/NIR regions. There is also some evidence of the

presence of an extra copper Cu_x[179], zinc[180] and magnesium[181] atom. The overall metal content of the cytochrome c oxidase dimer (the naturally occurring form) is 5 (possibly 6) Cu, 4 Fe, 2 Zn and 2 Mg atoms. The Cyt a site is in close association with Cu_A and together they are described as being the electron acceptor site from cytochrome c. Cyt a_3 is closely associated with Cu_B, forming what is known as the binuclear centre, which is the oxygen (and other ligand) binding site[182].

The strong 605 nm absorption band, see Figure 2.9, in the reduced minus oxidised spectrum of cytochrome c oxidase is, by consensus of opinion, considered to have an 80 ± 10% contribution from Cyt a and a 20 ± 10% contribution from Cyt a_3. These values are in overall agreement between three different groups using different analysis techniques[183 184 185]. There are some dissenting voices regarding the relative contributions to the 605 nm band, suggesting a 50:50 contribution,[186 187] but when all the evidence is taken into consideration an 80:20 contribution for Cyt a:Cyt a_3 is accepted by a large majority[99]. The equivalent values for the Soret band at 445 nm are 50 ± 10% for Cyt a and 50 ± 10% for Cyt a_3, these values are not greatly disputed. A large part of the evidence in this argument comes from experiments where the cytochrome c oxidase is bound to either carbon monoxide (CO) or cyanide (HCN) ligands. Both of these ligands will compete with oxygen at the binuclear centre. CO will only bind to a reduced binuclear centre leaving (in the absence of light) stable reduced Cyt a_3 and Cu_B sites with the Cyt a, Cu_A sites free to change their redox state. Cyanide inhibits catalytic O_2 reduction, but it has not been unambiguously proven whether it binds to the Cyt a_3 or Cu_B site or both[188]. It has been shown that HCN only binds rapidly with the half reduced enzyme (electron acceptor site reduced, binuclear site oxidised), binding being some 100 000 times slower with either the fully reduced or oxidised forms[189]. The HCN complex formed in the reaction is considered to have the binuclear site oxidised leaving Cyt a and Cu_A free to change their redox state[190]. The effects on the UV/VIS optical spectrum of this ligand binding is described elsewhere[171]. A recent publication questions the HCN binding described above[191] though its conclusions are again complicated by the possibility of differing preparation techniques.

Performing independent optical spectroscopic observations on the redox state of the binuclear site is much more difficult than studying the electron acceptor site. There is a small absorption shoulder reported for Cyt a_3 at 650 nm, which appears in the oxidised state. It is quoted as being "the most unambiguous manifestation of the a_3 component"[215].

The 830 nm absorption band of the oxidised enzyme was first discovered by Griffiths

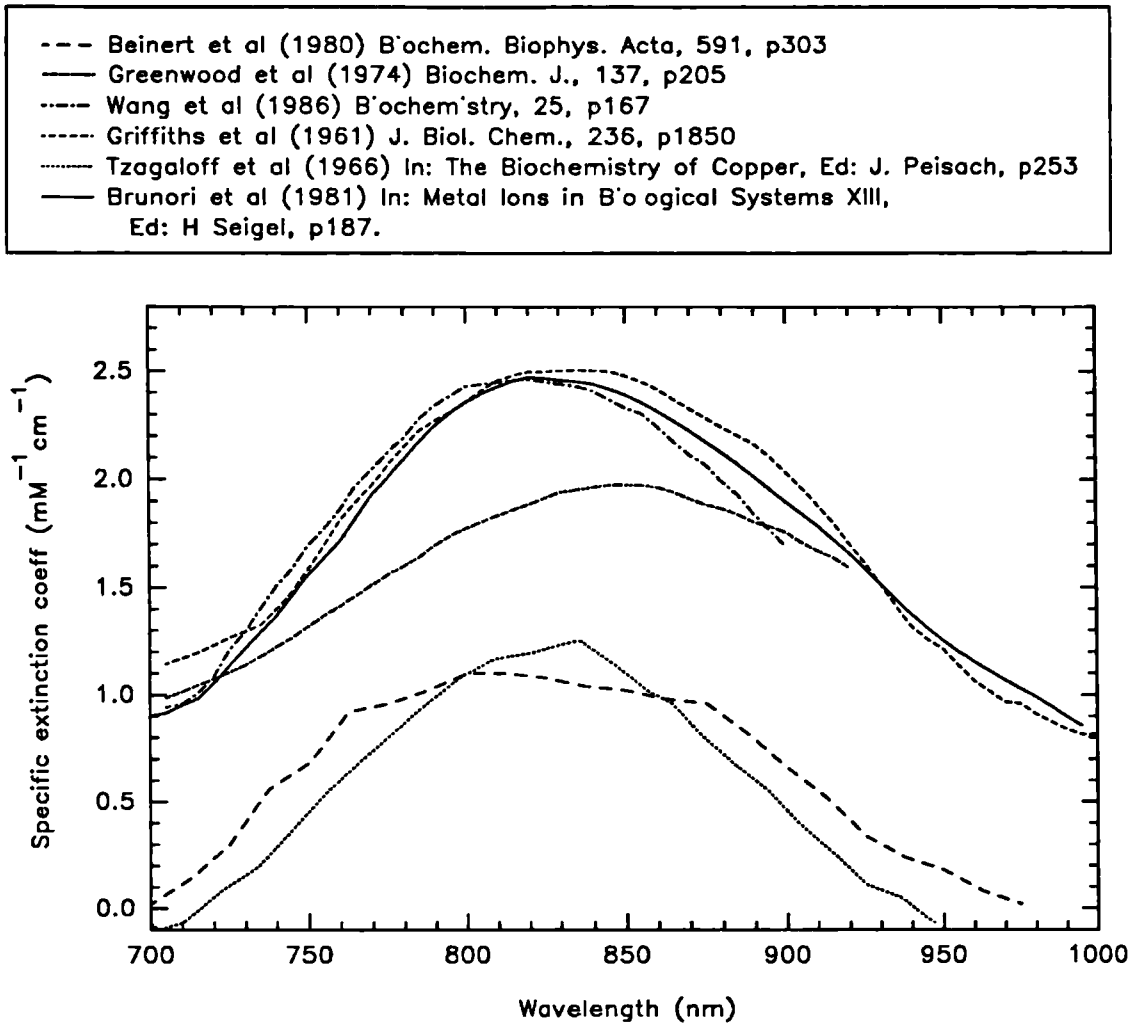

Figure 6.4 Various difference spectra of cytochrome aa_3 (oxidised minus reduced) taken from the references indicated. The vertical axis has been scaled to approximate to the true extinction coefficient.

and Wharton in 1961[192]. Since then, a number of authors have published spectra of the purified enzyme in its oxidised and reduced states or of its difference spectrum. A number of these purified cytochrome c oxidase enzyme spectra collected from various authors are shown in Figure 6.4[99 192 193 194 195 196]. These illustrate the differences observed on what should be the same compound. The overall shape of the 830 nm band does not appear to differ greatly between authors but there is a noticeable difference in the offset of the band from the zero attenuation line. The magnitude of this offset is important unless derivative spectroscopy

is being used for the analysis†.

Early evidence suggested that the 830 nm band was due to the copper atoms in the enzyme. There is now overwhelming evidence that not only is the 830 nm band due to the copper, but more specifically it is the copper atom (Cu_A) at the electron acceptor site. A recent paper devoted to this topic[195] comes to the conclusion that the spectral contribution of Cu_B, associated with Cyt a_3, lies in the range 0-15%. The majority of this evidence comes from electron paramagnetic resonance (EPR) studies[195 197 198]. Here the magnitude of the 830 nm absorption band is compared with that of the EPR signal from the oxidised Cu_A atom, the only EPR visible copper in cytochrome c oxidase. New evidence also comes from work on cytochrome c oxidase prepared from the bacteria Pseudomonas Am 1. When grown normally, the cytochrome c oxidase in this bacteria has the same spectroscopic properties as mammalian cytochrome c oxidase[199], but when grown in a copper deficient medium, the enzyme lacks Cu_A and the 830 nm band disappears[200]. The Cu_A deficient enzyme can still turn over electrons and reduce oxygen (albeit at a lower rate), and can also bind with carbon monoxide.

There is one group of publications[201 202] which claim a major contribution by Cu_B to the 830 nm band††. They are very much on their own, and the same data has been re-analyzed by others[195] to suggest a maximum contribution from Cu_B of 15%. The suggestion of a major Cu_B contribution arose in conjunction with earlier work on low temperature kinetics[203], where copper absorption bands at 744 and 782 nm were discovered. Absorption bands at these wavelengths are characteristic of type I copper centres, for example stellacyanine[202]. Similar kinetic work by another investigator at room temperature has not found evidence for these 744 and 782 nm bands[204]. There have also been suggestions of a haem contribution at near infrared wavelengths[196 205], though later work implied that the contribution may be insignificant[206]. In summary, the general opinion of investigators worldwide is that is that the 830 nm band is associated with the Cu_A site of the cytochrome c oxidase enzyme with the possibility of up to 15% interference, possibly from a combination of Cu_B, Cyt a and Cyt a_3.

As the 830 nm band monitors the redox state of Cu_A, its use as a monitor of tissue

---

† Derivative spectroscopy is not practical with the 830 nm band due to its broad featureless characteristics.

†† The later of these two publications does allow for the possibility of a 15% (minimum) contribution of Cu_B to the 830 nm band[202].

oxygenation is more interesting and more complicated than if it was the Cu_B site. Cu_A is one step away from the oxygen receptor site, the binuclear centre, and as such is not a simple indicator of oxygen availability. In a situation where the enzyme is turning over electrons, the Cyt a_3 site is considered to have a very high affinity for oxygen with a K_m (50% of maximum O_2 turnover) of 1 μM O_2 (0.08 kPa)[207], the enzyme probably initially forming an O_2^{2-} complex[204] and being in rapid equilibrium with the available oxygen. At low temperatures[203] and with fast kinetics studies[204], an oxygenated cytochrome c oxidase complex (analogous to oxy-haemoglobin) has been reported with a very much higher K_m of approximately 300 μM (≈ 38 kPa) and this is considered to be the initial and highly reversible binding step of O_2 with Cyt a_3. The rather large discrepancy between these two K_m values is regarded by Chance[203] to be the result of a much faster electron entry into the Cyt a_3 site than the rate at which O_2 can leave the site unreduced. Alternatively, Petersen[207] suggests that in the steady state, high O_2 affinity is caused by the rather slow turnover of the enzyme compared to the O_2 binding and electron transfer rates.

During electron turnover, the electron acceptor site, being one step down the chain, must be at a more positive redox potential than the binuclear centre. Thus the 830 nm band is not only dependent upon local O_2 concentration, but additionally upon the rate of electron transport down the chain and the rate of internal electron transfer between the electron acceptor site and the binuclear centre. Changes in the redox state of Cu_A are to be expected with changes in electron turnover independent of oxygen availability. A separate examination is therefore required into what controls electron flux down the respiratory chain, the rate constants of electron transport within cytochrome c oxidase itself, in addition to local O_2 concentrations.

The rate constants of electron transport through the cytochrome c oxidase enzyme are complicated. There is good evidence of at least two different mechanisms for passing electrons from the electron acceptor site to O_2. One of these mechanisms is significantly faster than the other, and the spectroscopic properties of the enzyme during the slow and fast turnover mechanisms are also different. Various reactions schemes and associated intermediate compounds between the fully reduced and oxidised forms have been described, but there is as yet no generally agreed scheme.

The first intermediate compound was reported by Okunuki[208] and named "oxygenated oxidase". Subsequent work on intermediate compounds have referenced this original "oxygenated oxidase" (e.g. Williams[209]), or new intermediates like Compounds A,

B, C described by Chance[210] and "pulsed oxidase" described by Brunori[211] and Wilson[175]. Many of these intermediate compounds have only been observed at cryogenic temperatures, and have milliseconds lifetimes at room temperature. As such they are unlikely to exist in significant concentrations in-vivo. The one intermediate which has been shown to have a significant lifetime at room temperature is the so called "pulsed" enzyme. In this thesis, the convention of Brunori is used to describe this cytochrome c oxidase intermediate rather than the use of the term "oxygenated" oxidase. The term "pulsed" is generally preferred as it is now considered that the original "oxygenated" oxidase of Okunika is firstly not the O_2 adduct, and secondly it can be formed with other oxidising agents such as HCN.

The kinetics of electron transfer in the "resting" enzyme has been studied by numerous groups, and several good reviews exist[99 212 213]. One paper which specifically looks at the 830 nm band in addition to the 605 nm band is by Wilson et al.[214]. They found that under fast kinetic situations, where electrons are available from reduced cytochrome c (and before they can be passed on to Cu_B and Cyt a_3), the changes observed at the 830 nm band tend to marginally lag events at the 605 nm band, and that both these sites accept one electron from reduced cytochrome c. Their major conclusions are that:

i) the electron entrance site in cytochrome c oxidase is the Cyt a site,

ii) the 2nd electron acceptor site (Cu_B) is in rapid equilibrium with Cyt a,

iii) the transfer of electrons from Cu_A to the oxygen binding site is the rate limiting step between cytochrome c and O_2,

iv) blocking the O_2 binding site does not affect the initial electron transfer into the Cyt a, Cu_A sites. It only slows down the transfer between Cu_A and the O_2 binding site.

Some of the above conclusions have also been drawn from EPR studies[215] and from other kinetic studies under anaerobic conditions[185] which also revealed the following:

v) In an initial fast phase, only 2 electrons are transferred from cytochrome c to cytochrome c oxidase. In low ionic strength conditions, electron entry rates into Cyt a are between 200 and 600 s^{-1} dependent upon the cytochrome c: cytochrome c oxidase ratio. A typical second order rate constant is 2×10^8 $M^{-1}s^{-1}$. These electrons are accepted by the Cyt a and Cu_B sites equally.

vi) Under anaerobic conditions, the full 4 electron reduction of cytochrome c oxidase is very slow. Transfer of electrons to the Cyt a_3 site is $\approx$ 2-4 s^{-1}. (In aerobic conditions typical rates are 100 to 400 s^{-1}). The anaerobic rate can be slowed even further by

incubation of cytochrome c oxidase with cyanide. This indicates that either Cyt a_3 in the "resting" state will not accept electrons unless it is bound to O_2, or that the enzyme must be "activated" by turnover.

vii) The electron transfer rate between cytochrome c and Cyt a is strongly affected by ionic strength (and lipid concentration). From 200 s^{-1} with a cytochrome c: cytochrome c oxidase ratio of 4:1 and near zero ionic strength solutions to 0.07 s^{-1} under the same conditions plus 0.5 M NaCl.

viii) Significantly, increasing the reducing power of cytochrome c by exchanging the iron ion for cobalt made no difference to the ability to transfer electrons to the Cyt a_3 site.

An internal electron transfer rate between Cyt a and Cyt a_3 of approximately 4 s^{-1} has been observed by numerous groups for the "resting" enzyme. As pointed out earlier, this value is considerably below the maximum observed rate of cytochrome c oxidase turnover which is nearer 400 s^{-1} [216] when the phospholipid, cytochrome c and ionic concentrations are optimised. A method of explaining this much faster electron transfer is through the formation of the "pulsed" enzyme. In experimental comparisons, electron turnover rates up to 70 times quicker have been reported for the "pulsed" over the "resting" enzyme[217]. In-vivo enzyme turnover rates are up to 10 times higher† than those reported for the "resting" enzyme.

The exact chemical species of the "pulsed" enzyme is still disputed, but it is considered to exist when a red shift is observed from the typical "resting" oxidase spectrum. This results in displacement of the 418 nm absorption bands to 428 nm and a red-shift of approximately 5 nm for the 598 nm band of oxidised cytochrome c oxidase together with an increase in absorption coefficient of 20%. Spectral differences between "resting" and "pulsed" forms in the near infrared (830 nm band) have not been reported in the literature. It is generally accepted that the "resting" to "pulsed" changeover affects only the Cyt a_3 site and that a conformational change is the most likely explanation. As well as optical spectrum variations, there are EPR detectable changes in going from resting to pulsed forms[218]. There is currently a great deal of discussion regarding the structure, ligand binding and redox states of the metal ions in the "pulsed" form, therefore it appears more sensible just to concentrate on its experimentally measured properties rather than its possible structure.

---

† The oxygen utilisation of brain tissue is 1.6 to 5.0 μM/g wet wt/min and typical concentration of cytochrome a are 10 nM/g wet wt. This puts the electron turnover rate at 10.7 to 33 s^{-1}.

The formation of the "pulsed" enzyme from fully reduced oxidase is very rapid (approximately 1 ms). It is also slowly generated from the "resting" oxidised enzyme (time constants vary between seconds to minutes) as it starts to turn over electrons, for example in the aerobic reduction of cytochrome c oxidase by ascorbate and cytochrome c[211]. The conversion time back from "pulsed" to "resting" forms is as yet unknown. In the absence of cytochrome c it appears to be very slow[219 220], possibly hours.

A kinetic model has been presented[221] to account for some of the in-vitro findings observed in turnover experiments on the isolated enzyme. This paper predicts a continuous changeover from "resting" to "pulsed" forms (and vice-versa), dependent upon the availability of oxygen and the electron transport rate. Low O_2 favours the "pulsed" enzyme and high O_2 favours the resting enzyme. These authors (and others[194]) additionally speculated that as cytochrome c oxidase is a proton pumping site, then proton gradients and electric potential across mitochondrial membrane may also affect the inter-conversion between "resting" and "pulsed" forms.

6.2.1.2 *The enzyme in mitochondria*

In mitochondria (or liposomes) there is an additional factor which can affect the redox state of the Cu_A redox centre. This is the proton motive force (Δp) across the mitochondrial membrane which is made up of an electrical gradient ($\Delta\varphi$) and a pH gradient (ΔpH), see Section 1.2.3. It is well known that the proton motive force has a strong controlling influence over the rate of respiration such that increased Δp leads to a decreased respiration rate. This has been shown in rat liver cells[222]. It can also be shown that an increased energy demand in brain tissue, will lead to a change in the redox state of Cu_A.

The magnitude of the proton motive force is determined by the relative rates at which protons are pumped out of and return into the mitochondria. For the passage of two electrons down the respiratory chain, protons are pumped out at each of three different sites: four protons between NADH-ubiquinol oxidoreductase: four at the cytochrome bc_1 complex and two at cytochrome c oxidase[223]. The most important mechanisms of proton return are: the phosphorylation of ADP to ATP (producing high energy metabolites); via antiporters with Na^+, K^+ and Ca^{2+} (ion exchangers against a metal ion gradient) and membrane leakage (energy wastage).

What is most important to note is that the respiration rate is controlled by ATP usage

(energy consumption) and not vice-versa[224]. For example, if energy demand in the brain increases then the cytosolic ADP level increases. This stimulates the phosphorylation of ADP in the mitochondria, which requires the movement of protons across the mitochondrial membrane into the mitochondria to provide the required energy. This in turn lowers the proton motive force across the membrane lowering the inhibition of the respiratory chain and hence increasing electron turnover and the rate at which protons are pumped out of the mitochondria. The new redox state adopted by the individual redox centres of the respiratory chain enzymes in this higher electron turnover state is more difficult to predict. This is because the proton motive force inhibits the respiratory chain at all three proton pumping sites mentioned above, and the degree of inhibition at each site is not known. Therefore the change of the Cu_A redox state as a function of proton motive force cannot be easily predicted.

This problem has been looked at experimentally with isolated mitochondria and in cytochrome c oxidase vesicle preparations, however some inconsistencies exist which may reflect difficulties in the preparation of the cytochrome c oxidase vesicles[225]. We must also infer results for the Cu_A (830 nm) band based upon the cytochrome a (605 nm) and cytochrome c (550 nm) bands, as the 830 nm has rarely been directly studied. The inference is somewhat problematic for two reasons: firstly, the sequence of electron transfer from cytochrome c to the binuclear centre is not known and secondly the position of the proton pump within cytochrome c oxidase is also not known. Therefore it is not possible to say, under all circumstances, whether the 830 nm band will follow cytochrome c, Cyt a or neither. However in contrast to previous evidence, it has recently been suggested that Cu_A is the electron acceptor site and that the proton pumping site is somewhere between Cu_A and oxygen[226]. Thus suggesting that the 830 nm band follows cytochrome c more closely than Cyt a.

In coupled mitochondria, Chance and Williams[227] found that the Cyt a (605 nm) band became reduced with higher ADP levels (lower Δp) while cytochrome b and cytochrome c became more oxidised. Using cytochrome c oxidase vesicles, where the effect of Δp can be studied on a single proton pumping site, lowering Δp lead to both cytochrome a and cytochrome c becoming more oxidised[225]. However, the situation is further complicated because it appears that it is the potential gradient part of Δp that affects the speed of electron transfer between cytochrome c and Cyt a and that it is the pH gradient that affects the internal electron transfer within cytochrome c oxidase[228]. Additionally, it was found that increasing the internal mitochondrial pH inhibited electron turnover of cytochrome c oxidase and made

Cyt a more reduced[225 233].

6.2.1.3 *The enzyme in-vivo*

There have been shown to be five possible influences on Cu_A redox state in brain tissue: (a) oxygen concentration; (b) energy (ATP) usage; (c) substrate (NADH) supply; (d) pH and (e) the relative population of the "pulsed/resting" forms of cytochrome c oxidase. Each of these will be considered in turn:

(a) The sensitivity of solubilised cytochrome c oxidase to oxygen concentration has already been discussed, where a K_m of 0.08 kPa (1 μM) has been found. In single cell preparations[229] and in mitochondria[230 231], values of K_m for oxygen are in the range 0.008-0.16 kPa and are a function of the proton motive force, increased Δp leading to an increased K_m[232].

Figure 6.5, data taken from Wilson[229], shows the redox state of cytochrome c and the respiratory rate as a function of oxygen partial pressure. Note that respiratory rate is less sensitive to oxygen partial pressure than the cytochrome c redox state. For pO_2 values from 16 kPa down to 1 kPa, cytochrome c is an insensitive indicator of mitochondrial pO_2, changing its redox state by only 15% over this range. In the mitochondrial pO_2 range from 1 to 0 kPa cytochrome c is very sensitive to oxygen, its redox state changing by 65%. The half maximal reduction level of cytochrome c ($p50_c$) is less than 0.1 kPa in these coupled mitochondria. Using more sensitive O_2 probes, Wilson et al[233] confirmed these measurements on coupled mitochondria and also found that in uncoupled mitochondria, cytochrome c is totally insensitive to pO_2 down to 0.1 kPa with a $p50_c$ less than 0.008 kPa. As stated earlier, Cu_A (830 nm) is expected to respond in a similar manner to cytochrome c, but the question of whether Cu_A is a sensitive indicator of tissue pO_2, depends very much upon the typical pO_2 values in normoxic brain tissue.

Quantitative measurements of tissue pO_2 in cerebral cortex are usually made using polarographic electrodes either single microelectrodes advanced into the brain tissue[234] or multi-wire surface electrodes place on the brain surface[235]. Multiple measurements are normally made at numerous (greater than 100) sites and plotted as a function of position or as a histogram of pO_2 values. A typical histogram has a mean of 3 kPa and a distribution from 0-12 kPa, see Figure 6.6, taken from Lübbers[236]. The percentage of values less than the

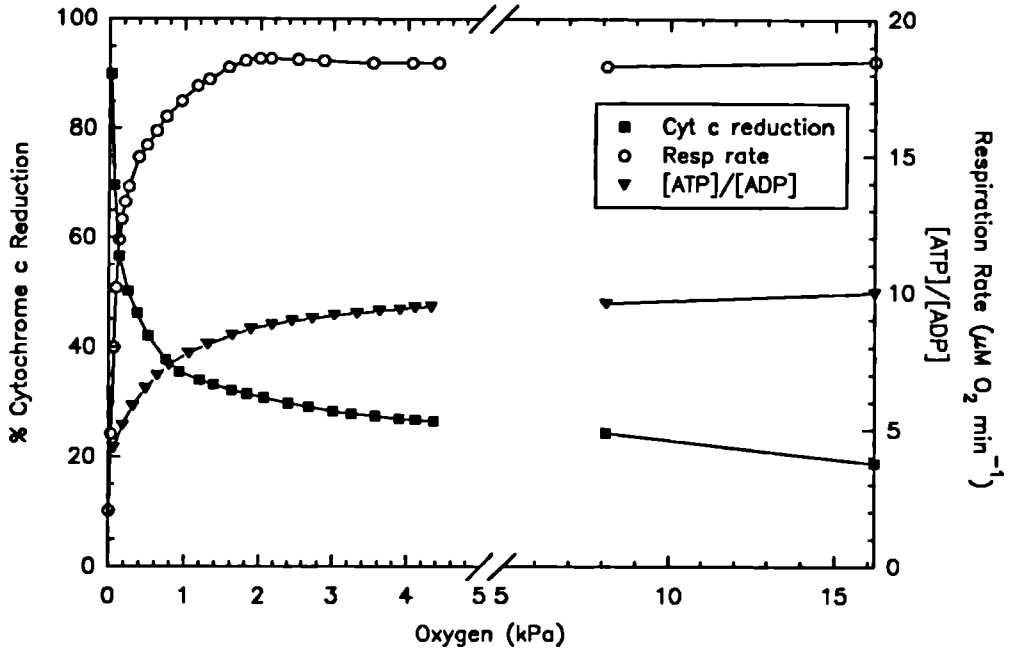

Figure 6.5 The effect of oxygen concentration on respiration rate, ATP/ADP ratio and cytochrome c redox state in cultured neuroblastoma cells, taken from Wilson[229].

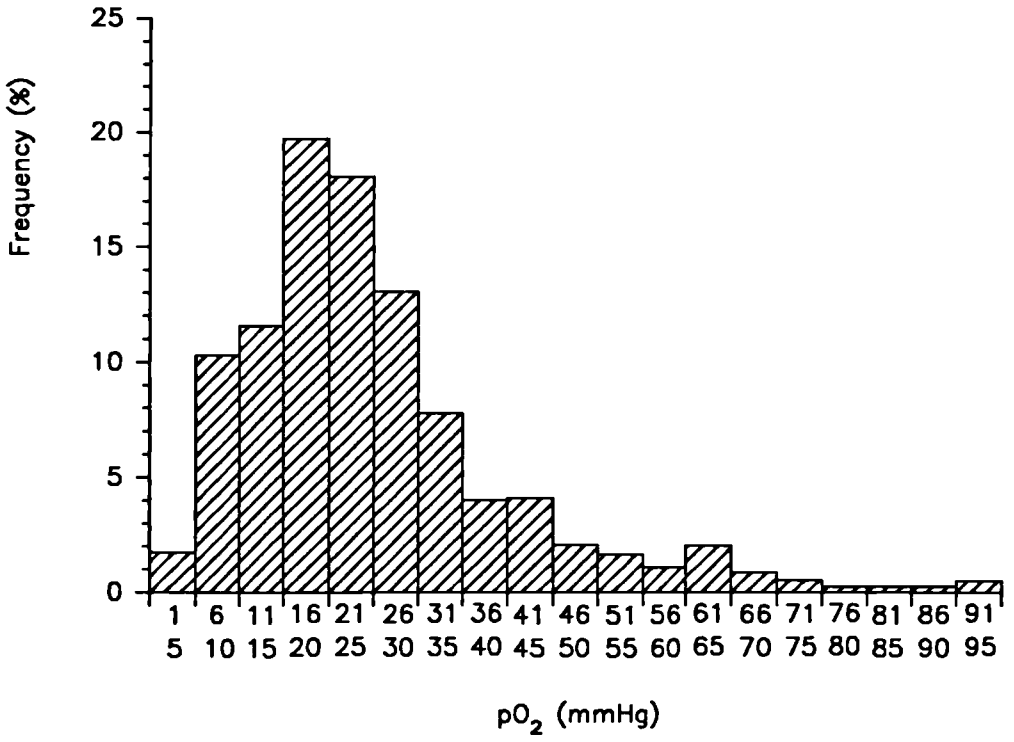

Figure 6.6 Histogram of grey matter pO_2 values of guinea pig brain. Taken from Lübbers[236], total number of values 2010, mean 21 mmHg. Note that 1 kPa≡7.5 mmHg.

critical 1 kPa is around 5%.

The majority of reported brain pO_2 data broadly agree with the above, but with some variations. Both Silver[234] and Erdmann[237] found a similar range of values as a function of depth into the rat brain cortex (no histogram given). In cat brain, Nair[238] found a mean value of 5 kPa, with 8% of values less than 1 kPa but a much broader distribution. However, there are some major discrepancies reported in two other publications so some caution must be used in interpreting the data. The first is from Erdmann[239] which contradicts all his other work by saying that 50% of pO_2 values in the adult rat cortex are less than 0.8 kPa. It is a great pity that this data is difficult to believe as it also quotes data on fetal and neonatal mouse and guinea pig brain, where the mean pO_2 decreases from a peak of 2.4 kPa to 0.13 kPa with increasing age in the mouse. The second is from Kreismann[240], he reported increasing pO_2 with age with 25% of values being less than 0.5 kPa in 10 day old rats and contradicts Erdmann's result regarding changes in tissue pO_2 with development.

The majority of information on tissue pO_2 implies that less than 5% of the brain has a pO_2 less than 1 kPa. Therefore, when taken in conjunction with the data in Figure 6.5 on the percentage reduction of cytochrome c in single cells, the conclusion is that Cu_A in cytochrome c oxidase will only indicate changes in tissue pO_2 near anoxia and will be a very insensitive indicator of brain tissue pO_2 during normoxia. It also suggests that in normoxia oxygen availability is not the rate limiting factor in tissue respiration. The caveat to this conclusion is that insufficient data is available on tissue pO_2 levels in the newborn (especially the human newborn).

This conclusion, that oxygen is not rate limiting in tissue, was expressed, amongst others, by Jöbsis[241] in 1972. However, since that time Jöbsis and his group have collected a large amount of in-vivo data which disagrees with the in-vitro findings[242 243 244 245]. In these publications, there appears to be no critical pO_2 for brain tissue, cytochrome c oxidase redox state being almost linearly related to oxygen supply, as determined by the concentration of oxyhaemoglobin in the tissue.

One explanation of these experimental findings is that their experimental technique of dual wavelength spectroscopy contained artifacts, such that the cytochrome c oxidase signal (typically 605 nm minus 590 nm) was contaminated by haemoglobin. Problems with dual wavelength spectroscopy at these wavelengths have been demonstrated[246]. In this latter publication, a three wavelength measurement system was recommended to eliminate haemoglobin artifacts. More recently, two further publications from this group have

contradicted earlier ones. One publication uses a three wavelength system[247] and the other a haemoglobin free preparation[248]. These data show that there is a critical pO_2, the critical inspired oxygen level being an F_iO_2 of 11% (p_aO_2 6.5 kPa) for the normally perfused adult rat. The cytochrome c oxidase signal being an excellent indicator of the brain's main energy reserve, phosphocreatine. This result is much more in agreement with in-vitro results and also the opinions of other workers in the field, for example Tamura[249] and Chance[250]. Thus it is likely that cytochrome c oxidase, in conjunction with an arterial oxygen monitor, will be a good indicator of critical oxygen delivery to the brain but probably not of changes in tissue pO_2 in normoxia. The above arguments may however not apply in abnormal physiological states which may exist in the neonatal brain following birth asphyxia/ischaemia.

(b) The effect of ATP turnover on cytochrome c oxidase redox state has been investigated in animals. Results show that increased neuronal activity leads to Cyt a becoming more oxidised in the exposed cortex of normoxic rats, and more reduced in anoxic rats. This has been shown during both electrical stimulation[251] and induced seizures[252]. However, some doubt must again be put on these results as the measurement method was dual wavelength spectroscopy of the 605 nm band.

(c) NADH supply is largely controlled by glucose supply and intracellular Ca^{2+}. Increases in mitochondrial Ca^{2+} can occur during periods of intense neuronal activity and hence can lead to NADH stimulated increases in respiratory chain turnover and alterations in cytochrome redox states[253].

(d) It has already been shown that decreases in intracellular pH can be expected to lead to an oxidation of cytochrome c oxidase[225 233]. This is most likely to occur with increasing carbon dioxide levels and with increased lactate production during anoxia.

(e) The "pulsed/resting" influence will be ignored, as recent discussions amongst investigators in the cytochrome c oxidase field suggest that only the "pulsed" form exists in-vivo. However, at present this information is unpublished and requires further clarification.

6.2.1.4 *Literature survey, a summary*

Summarising the evidence from isolated cytochrome c oxidase work:

i) Greater than 85% of the absorption occurring in the near infrared 830 nm region follows the redox state of Cu_A associated with Cyt a. The remainder (less than 15%) is from the other metal centres.

ii) The affinity of the binuclear centre for oxygen is very high and it will be fully oxidised at oxygen levels greater than a few micromolar (0.2 kPa).

iii) In the working enzyme (during electron turnover), the redox state of Cyt a, Cu_A is likely to be significantly more reduced than that of Cu_B, Cyt a_3. The steady state degree of reduction of Cu_A may be high as the transfer of electrons between the electron acceptor site and the binuclear centre is the rate limiting step in the reduction of oxygen from cytochrome c.

iv) A change in the relative population of cytochrome c oxidase in the "pulsed" and "resting" forms would alter the redox state of Cu_A at the same electron turnover rate.

Thus the magnitude of the 830 nm band is a function of the redox state of the Cu_A redox centre, which in turn is a function of the oxygen availability, the rate of supply of electrons (from cytochrome c) and the relative amounts of the "resting" and "pulsed" species. Published spectra of the 830 nm band appear to be inconsistent and therefore the measurement of these spectra need to be repeated.

The mitochondrial and liposome studies show that any change in metabolic rate in brain tissue has the ability to affect the Cu_A redox state via the electric potential and pH difference across the mitochondrial membrane. Inadequate data does not allow an exact prediction of the effect of $\Delta\varphi$ and ΔpH on Cu_A redox state, but the indirect evidence already presented suggests that lowering Δp will make Cu_A more oxidised. The intracellular pH also appears to affect the redox state of Cyt a and from this we can predict that decreasing intracellular pH will also make Cu_A more oxidised[225].

In-vivo tissue pO_2 measurements suggest that Cu_A will be a good indicator of critical oxygen delivery. A large change in Cu_A redox state occurring in conjunction with a change in arterial haemoglobin saturation would be a sign of a poorly oxygenated brain. The effect o a change in arterial carbon dioxide partial pressure is more difficult to interpret as this will lead to both increased cerebral blood flow and blood volume, thereby increasing oxygen

supply, and a decrease in the intracellular pH which also affects the cytochrome enzymes redox state.

Other factors have also been shown to have a potential influence on Cu_A redox state. These are any other factors modulating intracellular pH (e.g. lactate levels), NADH concentration (mainly affected by glucose supply and intracellular Ca^{2+}) and ATP usage (energy demand). Thus despite the interpretation of Cu_A redox state being a complex problem, is it potentially a powerful sensor of changes in cellular metabolism.

6.2.2 Measurement of "in-vivo" cytochrome c oxidase spectrum, attempt 1

This study was carried out on adult rats, the aim being to accurately measure the near infrared oxygen dependent spectrum of blood free brain tissue (which should approximate to the in-vitro spectrum of cytochrome c oxidase). An instrument was constructed for this purpose which measured over a continuum of wavelengths as opposed to the clinical spectrophotometer which only measured attenuation at four discrete wavelengths. Measuring the full spectra allows: (a) comparisons to be made with other cytochrome c oxidase spectra; (b) the examination of errors which may arise due to any wavelength dependent scattering in tissue; and (c) the absorption by the other cytochrome enzymes in the respiratory chain to be examined.

The animal model chosen was convenient both because of its size and the wealth of physiological information already available. Transillumination of the rat head (approximately 15 mm across) results in an optical loss of 4.3 OD when using 3 mm diameter optical fibre bundles both for light input and collection. This amount of attenuation represents the upper limit of attenuation which can be coped with by a good quality bench top spectrophotometer.

Bench top spectrophotometers are themselves not practical for use in this type of study as they tend not to interface to fibre optics and usually use slow scanning monochromators (especially slow on the 4 OD range where little light is available). There are some suitable instruments available commercially but initially, due to cost limitations, an instrument was constructed from much of our existing equipment. This instrument is described in the following section and is called the ROFIN SYSTEM. At a later date more funds became available and the ROFIN SYSTEM was replaced with a vastly improved OMA CCD SYSTEM to perform the same function.

6.2.2.1 *The animal spectrophotometer, Mark I, "The ROFIN SYSTEM"*

This system was built at low cost using as many pieces of existing equipment as possible, many of which were already incorporated into the NIR clinical spectrophotometer. The system was capable of recording a single spectrum in a few milliseconds and of averaging many single spectra to obtain an improved signal to noise ratio. Rapid scanning was an important design consideration as the speed of oxygenation changes in the brain of small animals can be up to 0.5 s. Fast optical scanning and averaging resulted in the measurement of an averaged optical spectrum of all the oxygenation changes which occurred during an acquisition. Slowly scanning the whole spectrum during an oxygenation change would have led to a distorted spectrum.

A schematic diagram of the ROFIN SYSTEM is shown in Figure 6.7. A quartz-halogen light source was selected as being the most suitable for providing illumination in the 600 nm to 1000 nm wavelength range. Although arc lamps were known to produce higher radiance in the near infrared region (see Section 4.2.4), their large emission peaks would have made the overall system design more difficult due to the higher dynamic range required. A lamp

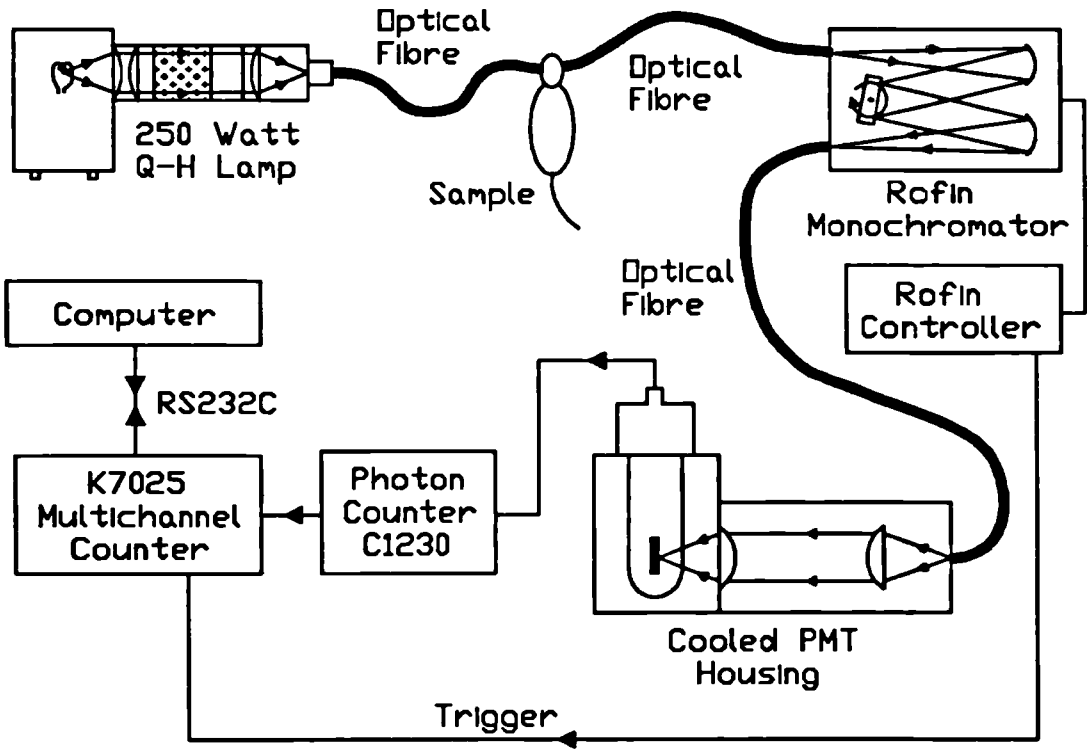

Figure 6.7 Schematic diagram of the ROFIN low light level, continuous scanning, near infrared spectrophotometer.

housing (Oriel 66195, USA) was used which consisted of a fan cooled lamp holder for bulbs of up to 250 W and a condenser lens (F/1, f = 38 mm) followed by a water filter of 5 cm pathlength. The heat filtered collimated beam then passed through a 2 inch filter holder to a focusing lens (F/0.85, f = 32 mm) and finally into an optical fibre bundle of 3 mm diameter. The amount of optical power available from such a piece of equipment has been shown previously in Figure 4.6.

The light source used in this single beam instrument needed to have a very stable output level with time (unlike dual beam spectrophotometers). This was achieved by using optical feedback of the bulb's output to the d.c. power supply. The optical output showed a drift of less than 0.25% over four hours after an initial 15 minute stabilisation period. The a.c. component of the optical signal was 1% rms which was higher than expected, however averaged over many seconds this a.c. component was not important. Its origin appeared to be mechanical vibration in the lamp housing caused by the forced air cooling.

Transmitted light was detected by a 3 mm diameter fibre bundle made of optical fibres identical to those described in Figure 4.2. This fibre optic carried transmitted light from the rat's head to the input of a rapidly scanning monochromator (Rofin 6040, U.K.). The throughput of the monochromator was not very high, the grating size being 12.5 mm square, 1200 $l\,mm^{-1}$, blazed at 750 nm (F/6, focal length 74 mm, dispersion 10 $nm\,mm^{-1}$). The small size of the grating allowed it to be spun continuously at 8 revolutions per second. Rapid scanning was essential for the reasons outlined earlier in this section.

The ROFIN SYSTEM monochromator scanned at a preset angular velocity, therefore the wavelength of the light exiting the output slit was a non-linear function of time. It was calibrated in units of "wavemarkers" (digital pulses, which were linear in time). These wavelength markers (W_m) were related to the true wavelength (λ) by

$$\lambda = 1604.1 \sin\left[19.8997^\circ + 0.038^\circ\left(W_m - 546\right)\right] \qquad [Units: nm] \qquad \text{6-1}$$

A slight adjustment (±10%) of the scan rate was possible which allowed a scan rate of one wavemarker per 8 µs to be set, thus the portion of the optical spectrum between 650 nm and 950 nm could be captured in approximately 2.5 ms.

The light output from the monochromator was collected by the same fibre optic bundle and detection circuit that was used in the NIR clinical spectrophotometer, see Section 5.5.1. The only major differences were the temperature of the GaAs PMT (−10°C) to lower the dark count, and no gating of the detector because of the continuous light source. The use of fibre

optics between the monochromator output and the photomultiplier tube was obviously not as efficient as direct coupling. However it allowed the same optical detector to be easily interchanged for use with both the NIR clinical spectrophotometer and the ROFIN SYSTEM.

The light intensity of an individual spectrum was so low that many thousands of spectra had to be averaged over many minutes. The light intensity was however of the correct order of magnitude so that photon counting was practical, and the multichannel photon counter (K7025) of the NIR clinical spectrophotometer, operating in a slightly different mode, was ideal for this purpose. The 64 counting channels were used to store counts at fixed wavemarker intervals, the first counter was started at a preselected wavemarker and the incoming photon pulses switched to the next counter after a preselected time. In all the work reported in this section the time between counters was 40 μs, corresponding to 5 wavemarkers. The photon counts from individual spectra were summed in the multichannel photon counter until a preset number of scans (N_{cycles}) had been taken and the summed data was then transferred to the same Olivetti M24 microcomputer as before to be stored on disk.

The spectra stored on disk were the summed photon counts over the allotted acquisition time against channel number l (l = 0 to 63). Channel number was converted to the centre wavelength for that channel using the knowledge of the wavemarker which triggered channel 0 (W_0) to start a sweep, and the fact that the gap between adjacent counter channels (ΔW_m) was 5 wavemarkers. The relationship between channel number l and its equivalent wavemarker W_{ml} was derived using

$$W_{ml} = W_0 + (l + 0.5)\Delta W_m; \quad \text{for } l = 0 \text{ to } 63 \qquad 6\text{-}2$$

and the correct wavelength of counter channel l was obtained by inserting W_{ml} in Equation 6-1.

The system response for a neutral absorber and a normoxic rat head is shown in Figure 6.8. The maximum count rate was kept below 1 MHz, to minimise pulse pile-up errors, by inserting neutral density filters in front of the photomultiplier tube. To obtain a signal to noise ratio of 100:1 (10000 counts) on the counter channel corresponding to the maximum count rate, 250 scans were necessary which took a total of 30 seconds. Obtaining a signal to noise ratio better than 100:1 over a broad band (down to 10% of the peak response) required an acquisition time of 5 minutes.

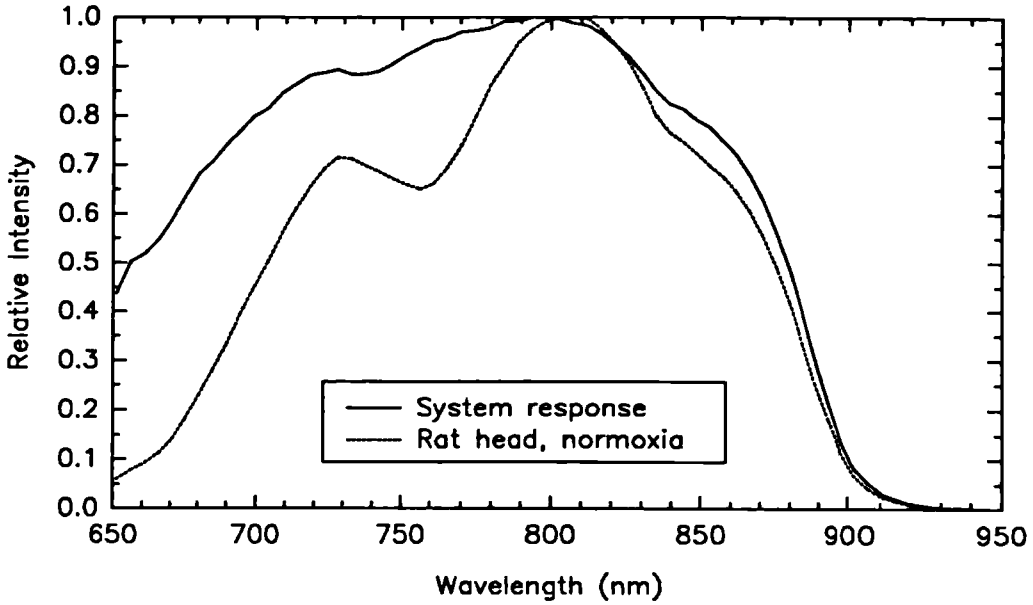

Figure 6.8 The relative sensitivity of the ROFIN system: (solid line) baseline response; (broken line) transillumination of a normoxic rat head.

6.2.2.2 *The experimental method, Mark I*

As only the difference spectrum of cytochrome c oxidase was required, it became plausible to measure it in-vivo in an animal's brain. For accurate measurements, a change in cytochrome c oxidase redox state needed be brought about without any change in the oxygenation of the haemoglobin. Since this was physiologically not possible, the haemoglobin had to be removed from the circulation and replaced with a blood substitute. A commercially available perfluorocarbon emulsion blood substitute, FC-43 (Green Cross Corp, Japan), was thus used to replace the haemoglobin in the blood stream of the rats. In the rat, serial exchange transfusion of the circulating blood volume by between 150 and 200 ml of FC-43 achieved a very low final haematocrit. The required volume of exchange to reduce haemoglobin absorption to negligible values was determined experimentally.

FC-43 is a colourless suspension of small perfluorocarbon particles (approximately 0.2 μm diameter) in saline and is capable of dissolving 2.3 times the amount of oxygen compared to plasma at the same partial pressure[254]. Optically, it acts as a Rayleigh scattering suspension and does not change its optical properties (scattering or absorption) with oxygenation. Other authors have shown that in the rat it can maintain normal cerebral function

for long periods[255].

The procedure employed in the experiments to measure the in-vivo spectrum of cytochrome c oxidase was as follows. Male Wistar rats weighing 300 to 500 g were anaesthetised with urethane (ethyl carbonate 36% w/v solution, 0.5 ml/100 g body weight intra-peritoneal). Tracheostomy was performed and a femoral artery and vein cannulated. The spleen was isolated by sutures around its supplying blood vessels. The skull was then exposed by an incision along the top of the head lengthwise, the scalp tissues reflected and the temporal muscles removed. Cautery sealed the exposed tissue to prevent blood loss. The head was immobilised in a stereotactic holder and two optical fibre bundles positioned either side of the rat's skull in contact with the parietal bones. A clear gel was used between the optical fibres and the skull to improve optical coupling. This enabled transillumination of the 1.4 cm width (approximately) of the rat's brain. Electroencephalographic (EEG) electrodes to monitor cerebral function were placed in burr holes made in the skull. Ventilation was performed with 100% oxygen and the animal paralysed with tubocurare (intra-venously 0.2 ml of 1.5 mg/ml solution, additional doses given throughout when required). Anaesthesia was maintained throughout by giving 0.2 ml of 24% urethane intra-venously every 2 to 3 hours. Body temperature was maintained at 37 ± 1°C via a heated bed. Arterial blood pressure was monitored continuously by a transducer (Elcomatic model 750, U.K.) attached to the arterial catheter.

The existing blood was exchange transfused with the fluorocarbon blood substitute, perfluorotributlylamine (FC-43, Green Cross Corp, Japan) prepared as prescribed by the manufacturer and pre-warmed to 37°C. The rate of the exchange was approximately 2 ml/min, equal volumes of FC-43 being added to the circulation via the femoral vein and diluted blood removed via the femoral artery. A slight net input of volume, approximately 1 ml for every 50 ml exchanged appeared to be required to maintain the blood pressure at its starting value. A total volume greater than 100 ml of fluorocarbon was exchanged.

Following the exchange transfusion the difference spectrum of cytochrome c oxidase could then be measured in the absence of haemoglobin. To do this, the spectrum of the head was first taken when the cytochrome c oxidase in the head was largely oxidised. This was obtained with an inspired F_iO_2 of 100% and normal EEG activity. The inspired gas was then changed to 100% nitrogen, the circulation failed and the EEG waveform disappeared. The spectrum obtained in these circumstances contained the contribution of totally reduced cytochrome c oxidase. Taking the log ratio of these two spectra yielded the difference

spectrum of in-vivo cytochrome c oxidase.

6.2.2.3 *Results, Mark I*

The major aim of this initial series of experiments was to characterise the difference spectrum of cytochrome c oxidase (and any other members of the respiratory chain) in-vivo. It was important therefore to determine the minimum amount of FC-43 exchange that was acceptable to ensure that at the end of the transfusion, the concentration of residual haemoglobin was such that its absorption coefficient was negligible compared to the absorption coefficient of cytochrome c oxidase.

In publications from others authors, some studies had used only a little FC-43, approximately 38 ml[256], while other authors used a much larger exchange volume, over 100 ml[257]. Examination of these publications suggested that a 38 ml exchange was insufficient, as the difference spectrum of haemoglobin was still visible, while a 100 ml exchange looked, by simple observation of the lack of haemoglobin spectral features, to be sufficient. A simple experiment was therefore carried out to find the minimum amount of perfluorocarbon to exchange.

Figure 6.9 shows the effect on light transmission across the rat head at 798 nm during the exchange transfusion, starting from a normal haemoglobin concentration of 15 g/dl. The absolute change in attenuation at the isobestic wavelength of 798 nm, caused by the removal of haemoglobin, was 0.45 OD (averaged over 6 results, standard deviation 0.25 OD). The magnitude of the standard deviation may well represent physiological variations in cerebral blood volume between the animals due to different starting blood gas values for carbon dioxide and pH. A rough estimate from this graph indicated that an exchange volume greater than 120 ml would be sensible, but the correct amount was determined with a better accuracy as follows.

In one animal, blood samples were taken after every 5 ml of exchange and the concentration of haemoglobin was measured in-vitro via the absorbance of the lysed solution at the wavelengths 798 nm or 576 nm depending upon the haemoglobin concentration in the sample. Measurements of the packed cell volumes (PCV) were also performed when the PCV was greater than 6% (at values less than 6% this technique was too inaccurate). The experimental results were compared to a simple simulation of the exchange transfusion assuming a starting haemoglobin concentration of Hb_0 mM, and a starting circulating volume

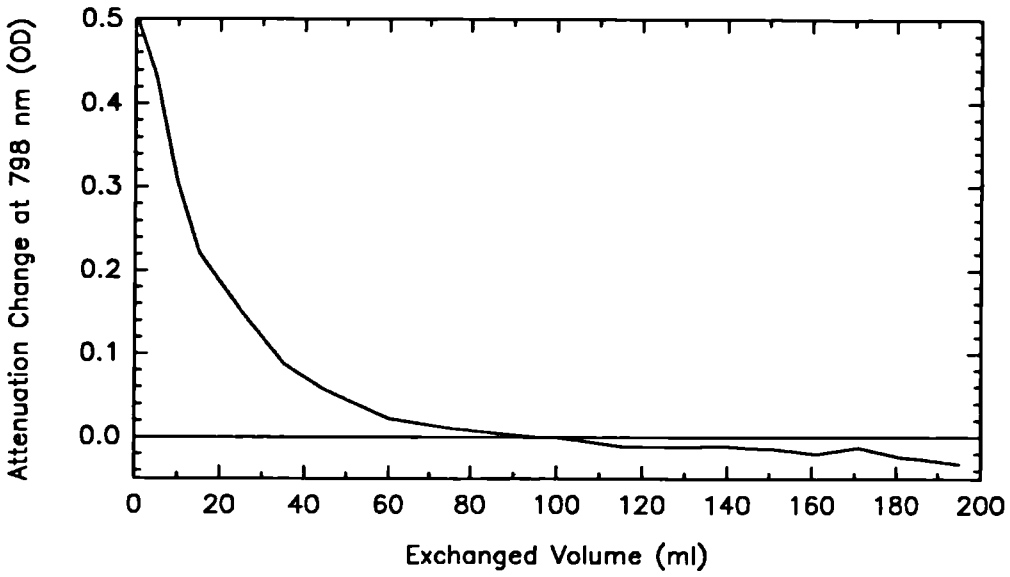

Figure 6.9 The change in attenuation, at 798 nm, across a rat head resulting from an exchange transfusion of blood with FC-43 perfluorocarbon blood substitute. Data normalised at an exchanged volume of 100 ml.

of y ml of blood. In this simulation, one millilitre of perfluorocarbon was added to the circulating fluid and allowed to distribute evenly, diluting the circulating fluid to $y/(y+1)Hb_0$ mM. One millilitre of fluid was then removed. This process was repeated n times for n ml exchanged blood. Thus after n ml, the circulating haemoglobin concentration was $[y/(y+1)]^n Hb_0$ mM. This equation represented an exponential curve which was fitted to the experimental data to determine the unknown values of Hb_0 and y. The experimental data and the theoretical fit are shown in Figure 6.10. Further experiments would be necessary to confirm this simple model but this is not central to this work, the intention was only to estimate a minimum volume required for the perfluorocarbon exchange.

The other parameter which was required in order to calculate the minimum exchange volume was the maximum residual extinction coefficient of haemoglobin that could be tolerated. Equation 4-3 showed that the expected signal from cytochrome c oxidase was 0.07 OD across 14 mm of a rat's head. This value agreed with results from other authors[256] who found a value near 0.08 OD. From this information a maximum contribution from haemoglobin of 5% of the expected cytochrome signal was set (equivalent to 0.004 OD). The average change in attenuation at 798 nm for a full exchange has already been shown to be 0.45 OD. Therefore the haemoglobin concentration in the blood stream required reducing to

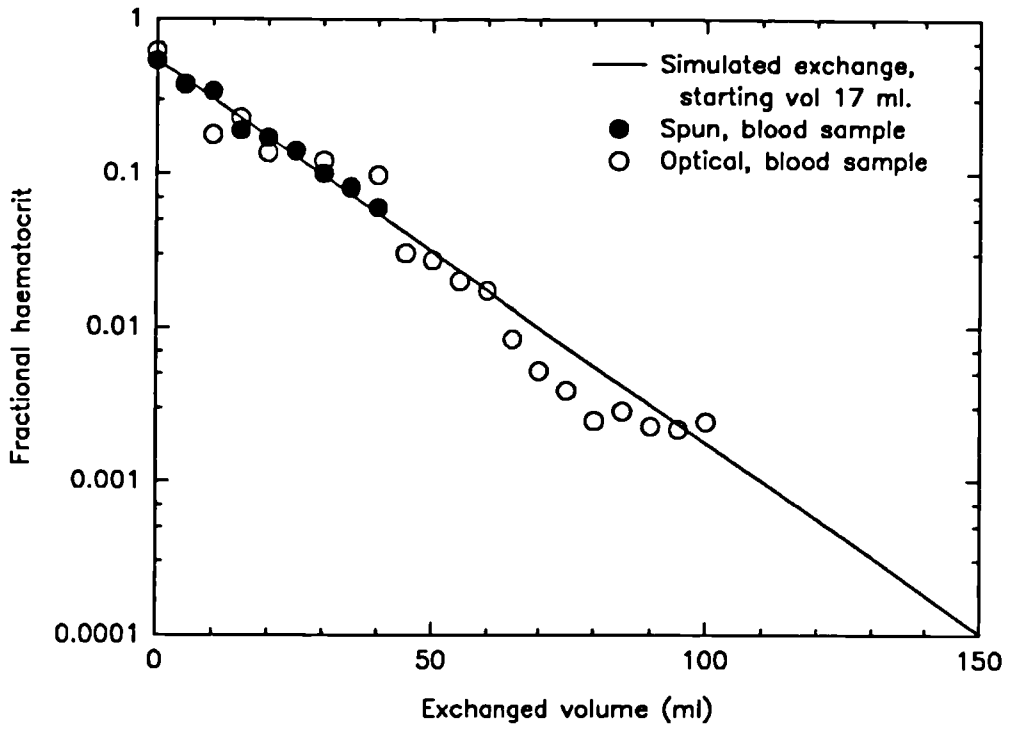

Figure 6.10 Comparison of experimental results and theoretical predictions for the haematocrit in the large vessels of a rat, as a function of the exchanged volume of FC-43.

less than 1% of its original value (0.004/0.45) to have a interference in the cytochrome spectrum of less than 5%. After allowing a safety factor of two, the equivalent final haematocrit should therefore be 0.22% (or 12 μM) in the blood stream and a haemoglobin concentration of 0.4 μM in brain tissue. Figure 6.10 showed that this point was reached after 96 ml of exchange, slightly less than the 120 ml suggested by Figure 6.9. Figure 6.10 could also be used to find the amount of haemoglobin interference which would be obtained at other exchange volumes.

Typical full spectra taken during the exchange transfusion are shown in Figure 6.11. These spectra were "flat fielded" to the response of the spectroscopy system with no sample in its path, but note that the y-axis zero was arbitrary. These spectra showed a gradual decrease in attenuation at all wavelengths as the haemoglobin (both oxygenated and deoxygenated) was removed from the blood stream and replaced with perfluorocarbon blood substitute. Initially, at the start of the exchange, the attenuation was approximately flat with wavelength, with a small peak at 760 nm due to deoxygenated haemoglobin (not very apparent

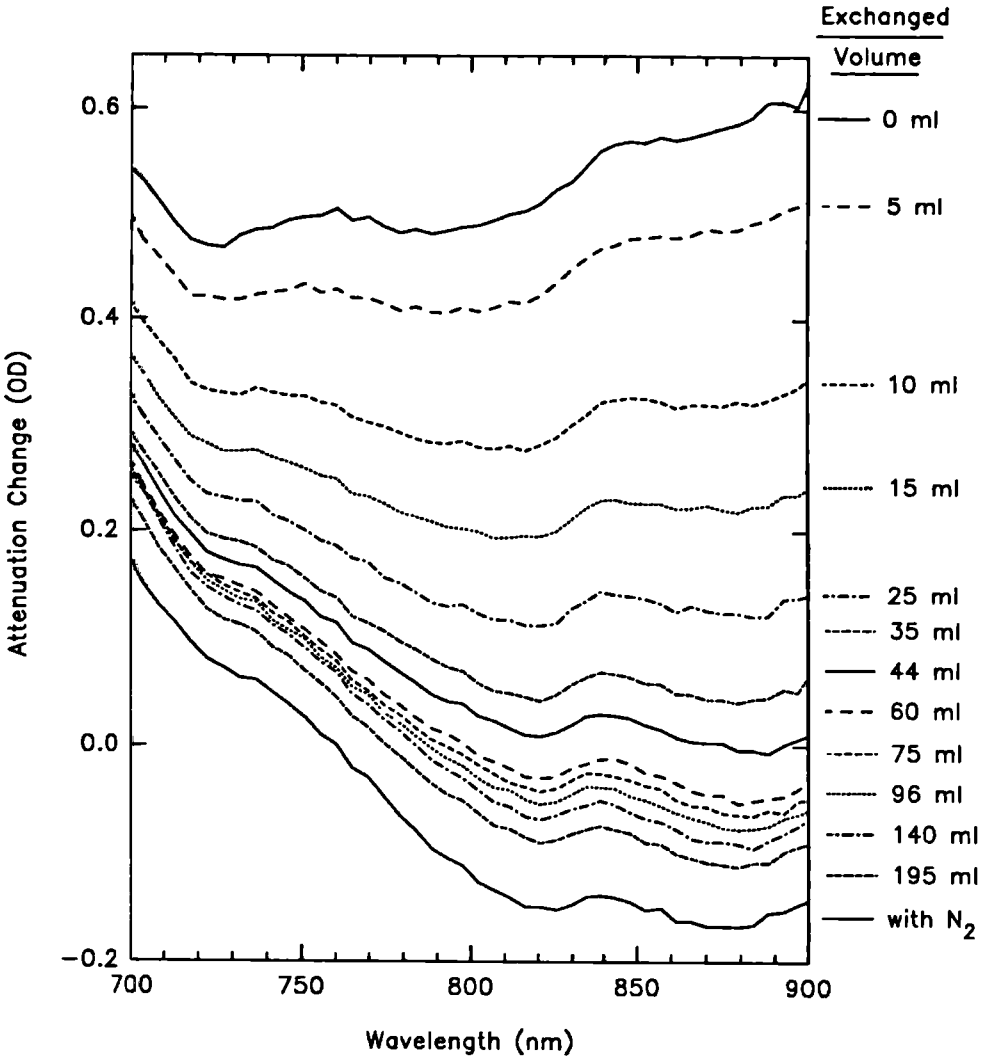

Figure 6.11 Spectra across a rat's head taken at various levels of exchange transfusion of FC-43. The last two spectra are at the same level of transfusion but at an F_iO_2 of 100% and 0%.

in this animal as the starting p_aCO_2 was very high and the F_iO_2 was 100%). The other small ripples at 750 and 840 nm were due to water absorption. As the exchange progressed, the largest attenuation losses were at the higher wavelengths (near 900 nm) compared to the shorter wavelengths (near 700 nm). This was consistent with the fact that it was mainly oxy-haemoglobin which was being removed.

The most important stage of this experiment came in the last 15 minutes, following the exchange transfusion which typically took 2.5 to 3.0 hours. A spectrum was taken just

before and just after the animal was exchanged from breathing 100% oxygen to 100% nitrogen. The difference spectrum between these two states was taken to be the difference spectrum of the respiratory chain in-vivo. A problem arose however due to the poor time resolution of the spectrometer, which took 5 minutes to record a broadband spectrum with 0.004 OD rms noise and which was therefore too slow to follow all the changes that took place. In addition to collecting the full spectrum, a signal was available from the system which was a sum of all the detected photons at all wavelengths, and this was updated every second with about 0.02 OD rms noise. This signal was a little difficult to interpret as it was weighted not only by the transmission of the rat's brain, but also by the wavelength sensitivity of the instrument. Despite the interpretation difficulty, this signal was invaluable experimentally as an indicator of rapid attenuation changes in the brain and revealed a problem inherent in using an instrument with a 5 minute data acquisition time.

This effect can be best explained by reference to Figure 6.12 which shows the summed photon count plotted against time during the period when nitrogen was administered. Period 'A' was the time before nitrogen was given, when the brain had an adequate oxygen supply. Immediately upon giving nitrogen, the summed photon count increased rapidly over a period

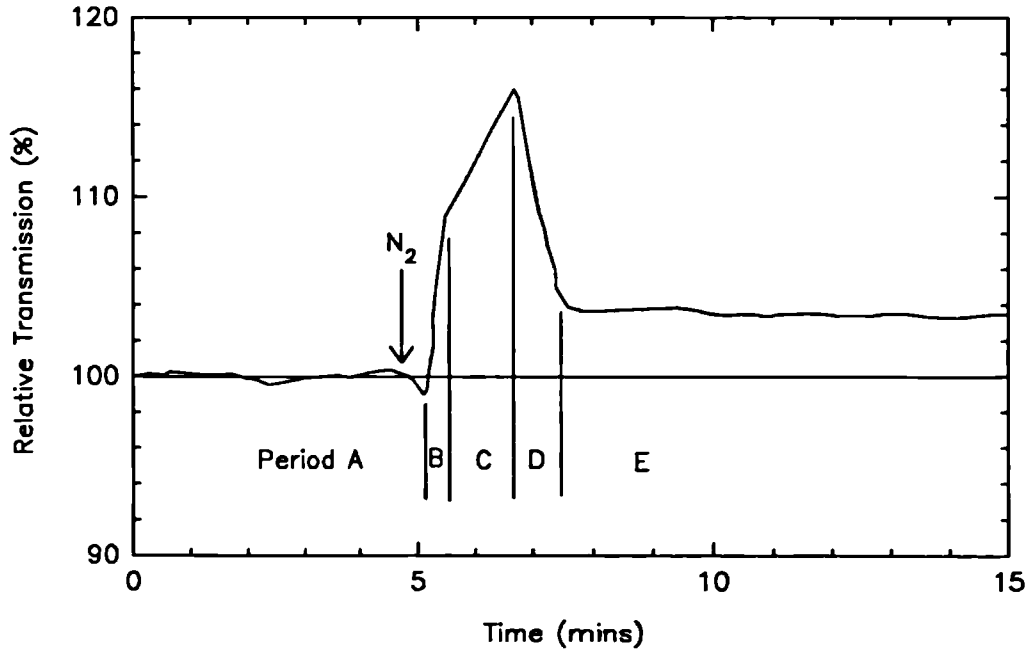

Figure 6.12 Reproduction of a chart recording, indicating complex changes in the relative intensity of light (summed between 700-900 nm) transmitted across a rat's head at death in a haemoglobin free preparation.

of 20 seconds by 9% or –0.037 OD (Period 'B'). A much slower increase in transmission then occurred over the next 90 seconds (Period 'C') to a peak of 16% (–0.065 OD) which then dropped back over a period of 60 seconds (Period 'D') to a value 3.4% (or –0.015 OD) greater than the pre nitrogen value. The final plateau value was held for many minutes (Period 'E'). This general response was found in all animals except one in which it was suspected that the brain was not well oxygenated during 'A'. Period 'C' was often flatter than indicated in this example. On simple inspection, it looked as if at least two separate processes were taking place during death and this indicated that the ROFIN SYSTEM, with its 5 minute acquisition time, merely produced data on an average of all these changes. What were these two processes likely to be?

Period 'B', the initial increase in transmission was almost certainly due to the conversion of oxidised to reduced cytochrome c oxidase with 'C' probably being a slower continuation of 'B'. The problem lies in explaining period 'D', the much slower decrease in transmission which occurred over a period of one minute and then period 'E'. In order to gain further information on this effect, in five animals three separate spectra were collected during death. The first was taken in period 'A', the second an average of periods 'B' and 'C', the third an average of periods 'D' and 'E'. The timing of each collection was based on the time course of the summed photon count. Due to the limited time available for the second spectrum, its signal to noise ratio was reduced.

The three spectra are shown as three pairs of difference spectra in Figure 6.13: A – (B + C), A –(D + E), (B + C)–(D + E). From this limited evidence it was possible to conclude that cytochrome c oxidase was not changing its redox state during periods D and E. This conclusion was based upon the curvature of the resulting spectra (i.e. their 1st differential). Both A –(B + C) and A –(D + E) exhibited the same broad 830 nm absorption band of cytochrome c oxidase with identical curvature. (B + C)–(D + E) showed no such curvature which indicated that something else was happening which was largely wavelength independent within the resolution of these spectra and over this wavelength range.

The question therefore arises as to what this second process could be. On this point, only speculation is possible, based on two pieces of evidence. Firstly the wavelength independent nature of the attenuation change and secondly, the 60-90 second delay from the start of anoxia. The author believes this evidence points to an increase in the scattering properties of the brain tissue as the cellular ion pumps fail and the cells swell due to the effects of osmotic pressure. The almost wavelength independent change is consistent with this

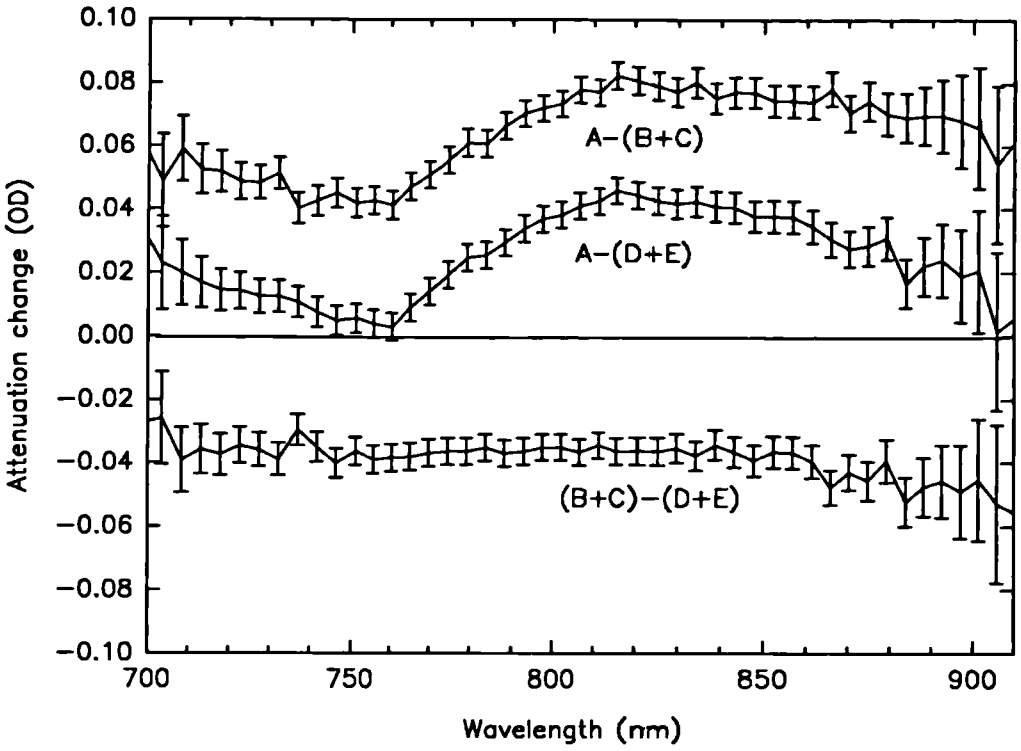

Figure 6.13 Spectral changes in light transmitted across a rat's head near death in a haemoglobin free preparation. Refer to the text and Figure 6.12 for details and timing.

speculation. These changes are the subject of a later discussion on scattering changes observed in neurons, see Section 7.5.3.2.

For the reasons given above, it was obviously better to take the cytochrome c oxidase difference spectra to be the spectrum A –(B + C) rather than A –(D + E). In fact the (B + C)–(D + E) spectrum can be considered as arising from a "fourth compound" which ought strictly to be taken into account when analysing tissue spectra. However, the only time that this effect was seen was around the time of cell death. Therefore it would rarely be observed in normal clinical circumstances, but if it did occur it would be very important.

The final difference spectrum of the respiratory chain A–(B+C) is shown in Figure 6.14. This was an average from five animals with a mean exchanged volume of 160 ml (min. 97, max. 195 ml). Before averaging, each individual spectrum was scaled so that the area under the curve of all the spectra was identical. This process takes into account variations in the concentration of cytochrome c oxidase between animals without the need for matching all the spectra at one specific wavelength. The error bars represented one standard deviation

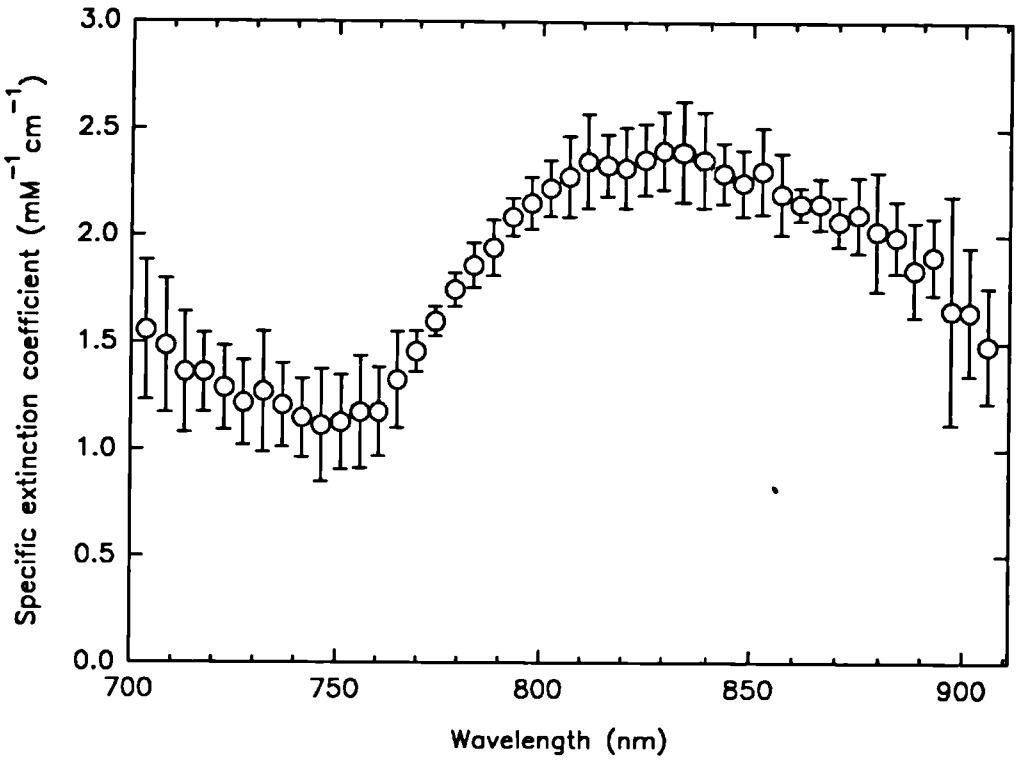

Figure 6.14 The difference spectrum of "in-vivo" cytochrome aa_3, measured across a rat's head in a haemoglobin free preparation. Mean and standard deviations from 5 animals. Data scaled to in-vitro extinction coefficients.

of the five scaled spectra. The vertical axis of the spectrum in Figure 6.14 has also been scaled to match the NIR extinction peak reported for the in-vitro enzyme[99].

A comparison of this spectrum with similar data from Ferrari[256] and Jöbsis[257] is shown in Figure 6.15. Apart from the spectrum of Ferrari (which contained a high degree of haemoglobin contamination), the shape of the 830 nm bands were similar. However, despite their similar shape, the curvatures were different and this was probably due to discrepancies in the correct position of the baseline. Choosing the correct position for the baseline has already been shown to be difficult, see Figure 6.13, due to the complex changes in light transmission that occur around death and which are inconsistent with a simple single spectral change due to cytochrome c oxidase reduction. Therefore, some uncertainty must still exist regarding the accuracy of these in-vivo spectra.

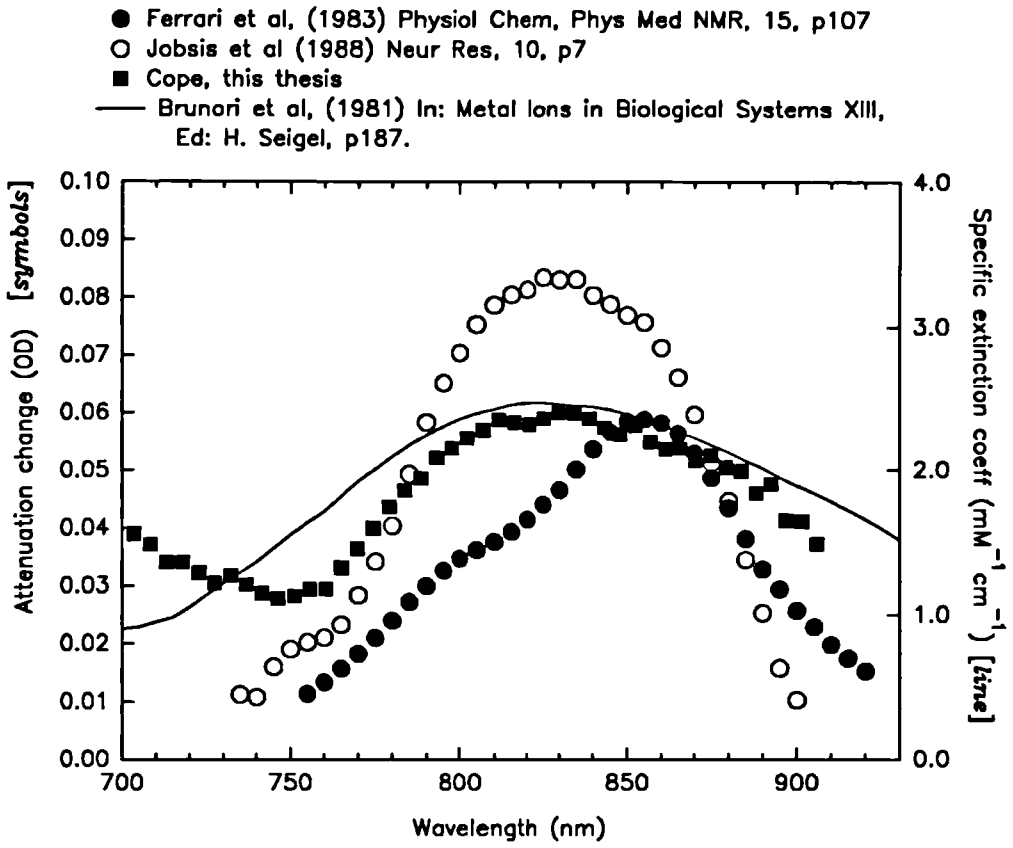

Figure 6.15 Comparison of the "in-vivo cytochrome aa_3" spectrum measured in this thesis with other "in-vivo spectra" published data from Ferrari and Jöbsis. One in-vivo spectrum of Brunori is also shown.

6.2.3 Measurement of "in-vivo" cytochrome c oxidase spectrum, attempt 2

The measurements described in the previous section suffered from the lack of speed and the sensitivity of the spectrophotometer and as a result did not produce spectra of the quality that was really required. A new spectrophotometer was subsequently constructed which overcame these problems and the measurement of the "in-vivo" cytochrome c oxidase difference spectrum was repeated. The new spectrophotometer collected NIR spectra across a rat's head with lower noise, at an increased wavelength resolution (<2 nm) in a time of only one second. Using this equipment the previous animal experiments were repeated. The spectral changes occurring during the periods labelled 'A' to 'E' in Figure 6.12 were then followed with a time resolution of one second.

6.2.3.1 *The animal spectrophotometer, Mark II, "The OMA CCD SYSTEM."*

The principles of operation of this spectrophotometer and the reasons for the improved performance of this Optical Multichannel Analyzer Charge Coupled Device System (OMA CCD SYSTEM) have already been discussed[258]. There is little point in entering into great details here, but a schematic diagram of the system is given in Figure 6.16. Note that the grating no longer rotates during a spectral acquisition but moves merely to place a different spectral region onto the array detector. Most of the components for this system were bought commercially and then assembled in the laboratory to form the complete instrument. The major advantages of the system lie in the use of a liquid nitrogen cooled silicon CCD imaging detector in the focal plane of a high throughput spectrograph which can therefore view a band of visible/NIR light simultaneously with high resolution.

The characteristics of the system are summarised below for the case of transillumination of a rat's head. The spectral irradiance entering the head (via a 3 mm diameter fibre optic bundle, NA 0.5) was 90 $\mu W\ mm^{-2}nm^{-1}$ (at 800 nm), which resulted in an output spectral irradiance of 14 $pW\ mm^{-2}nm^{-1}$ being available to the spectrometer from a similar 3 mm diameter fibre optic bundle, NA 0.5:

i) An acquisition time of 1 s for high signal to noise spectra (350:1 at the peak wavelength), photon noise limited.

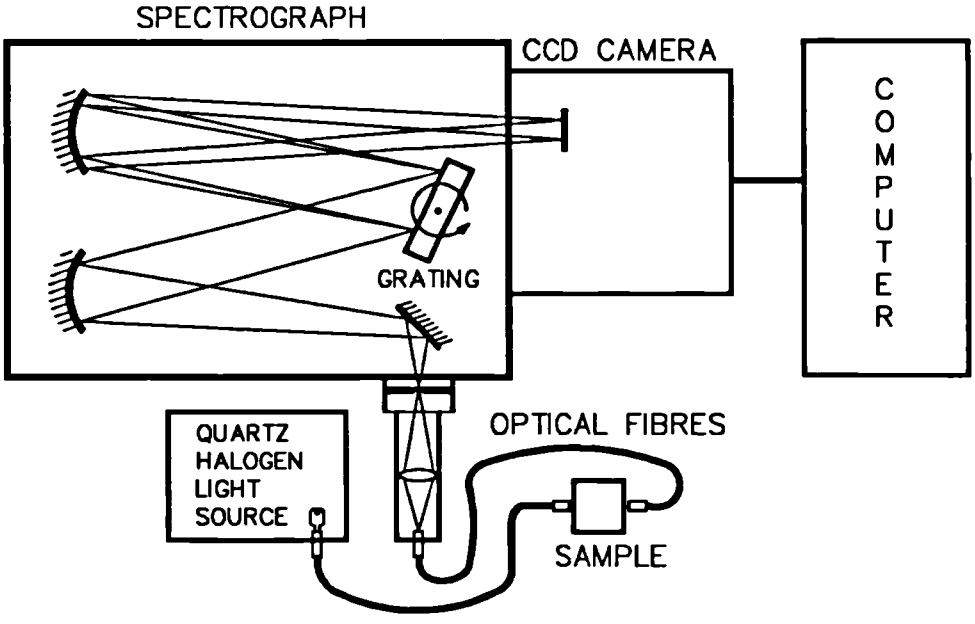

Figure 6.16 Schematic diagram of the OMA CCD SYSTEM.

ii) Better than 2 nm resolution, 0.5 nm accuracy.

iii) Extended near infrared response to 1050 nm.

vii) Recorded any 400 nm wide region of the spectrum between 450 nm and 1050 nm simultaneously.

viii) Fibre optic coupled, usable near NMR magnets.

6.2.3.2 *Experimental method, Mark II*

The experimental method was essentially identical to that described in Section 6.2.2.2. The differences were:

i) The animals were not given the muscle relaxant, tubocurare.

ii) The exchange transfusion was performed in a shorter period by simultaneous infusion of FC-43 into a femoral vein and withdrawal from a femoral artery.

iii) The OMA CCD SYSTEM was used as the spectrophotometer.

There was no doubt that in this second set of studies the experimental procedure was better, the overall condition of the animal after 150 ml of exchange was improved upon that in the first studies. This was probably because of a much reduced exchange transfusion time. The OMA CCD SYSTEM, with its 1 second time resolution, also allowed transient periods (20 to 40 seconds) of anoxia, breathing 100% N_2, followed by recovery on 100% O_2 to be studied. Thus, normally three or four anoxic dips were performed per animal prior to death by anoxia as described in Section 6.2.2.2. In this way the repeatability of the oxygenation dependent tissue difference spectra could be compared both within one animal and between animals.

6.2.3.3 *Results, Mark II*

A typical set of spectra taken before, during and after a 30 second period of breathing 100% N_2 (going from and returning to 100% O_2) are shown in Figure 6.17. They were normalised to the first spectrum taken while breathing 100% O_2. The spectra show the general features of a cytochrome c oxidase difference spectrum. Upon breathing N_2 a narrow peak at 605 nm was formed, while at the same time the broad trough of the 830 nm band appeared. Note that only periods 'A, B & C' of Figure 6.12 were visible in this experiment as recovery of the animal was achieved within 30 seconds. The recovery phase showed spectra returning

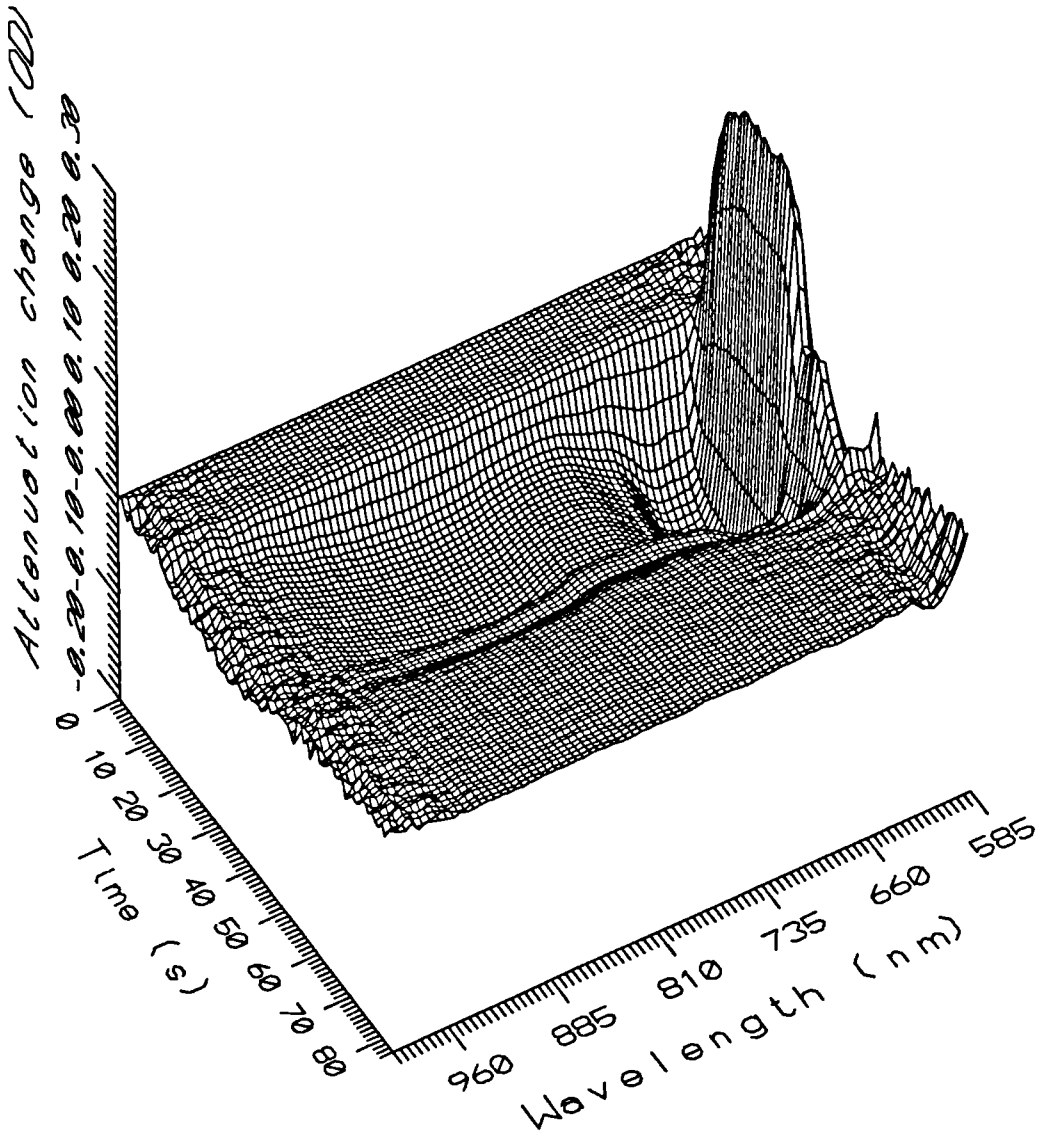

Figure 6.17 In-vivo difference spectra, relative to normoxia, of a blood free rat brain during 30 seconds of nitrogen inspiration. The F_iO_2 was 100% before and after the transient hypoxia.

back to their original pre-N_2 values except for a slightly more oxidised 605 nm band. This was commonly seen and could be due to low ADP, lower intracellular pH or increased cerebral blood flow all of which would be expected during the beginning of the recovery period.

Figure 6.18 shows a similar set of spectra, except that in this case the animal continued to breath N_2 until death. The initial 30 second response was identical to Figure 6.17, but at 70 seconds the complete spectrum (at all wavelengths) increased in attenuation (Period

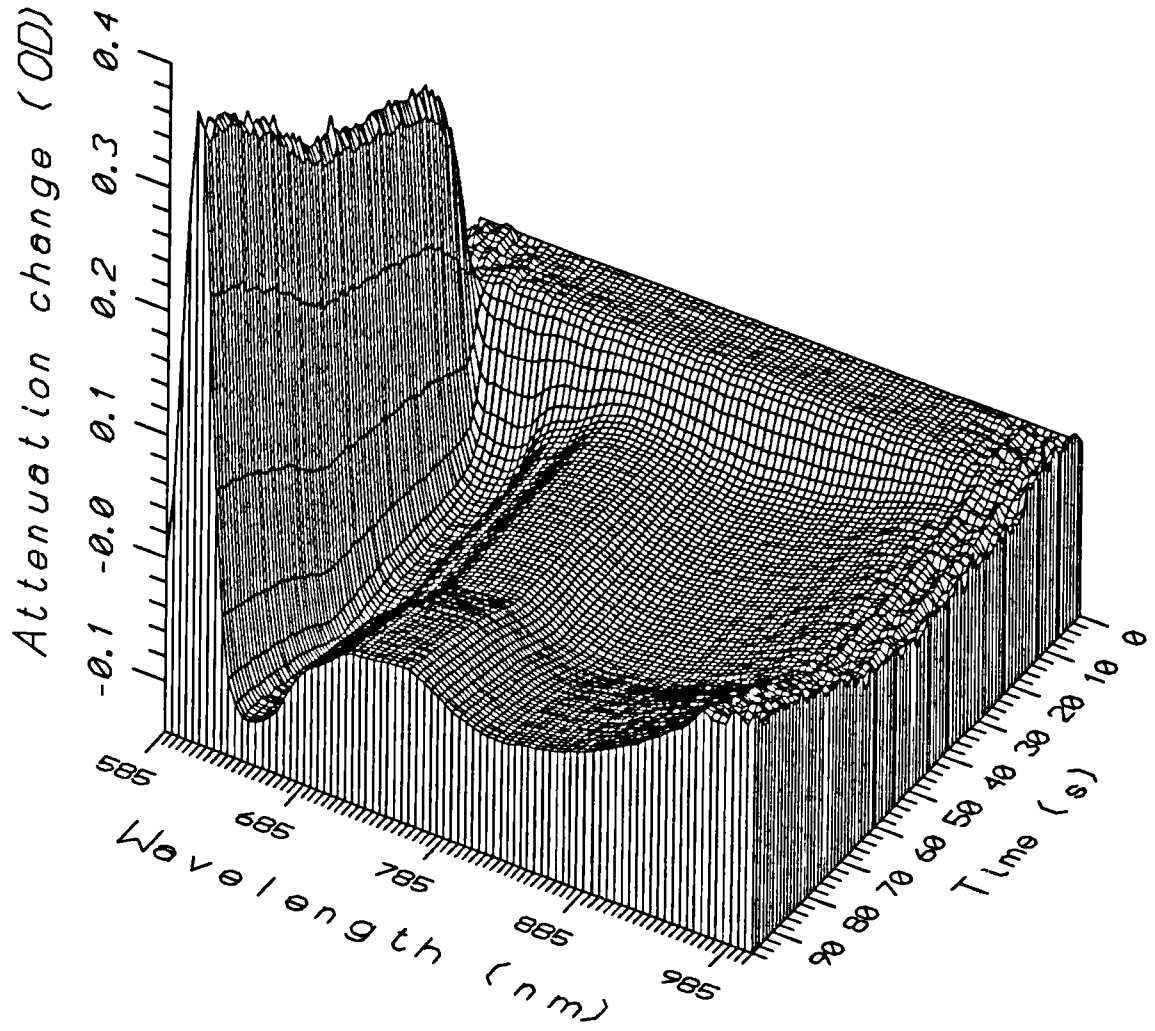

Figure 6.18 In-vivo difference spectra, relative to normoxia, of a blood free rat brain in changing the inspired gases from 100% oxygen to 100% nitrogen. Nitrogen respiration continued until death.

'D' of Figure 6.12) for about 40 seconds and then continued at the new level. The changes in spectral characteristics over this period were broadly wavelength independent, with a small additional increase in the 605 nm peak (approximately 5% of the total 605 nm peak).

The kinetics of the initial 15 second period at selected wavelengths can be seen in Figure 6.19. The upper graph, Figure 6.19(a) is the raw attenuation change data, while in Figure 6.19(b) the same data has been normalised so that the scaled attenuation change, at each wavelength, is positive and unity at 15 seconds. Figure 6.19(b) showed that, the kinetics had three distinct phases: an initial fast stage for the first 15 seconds; a second slow phase

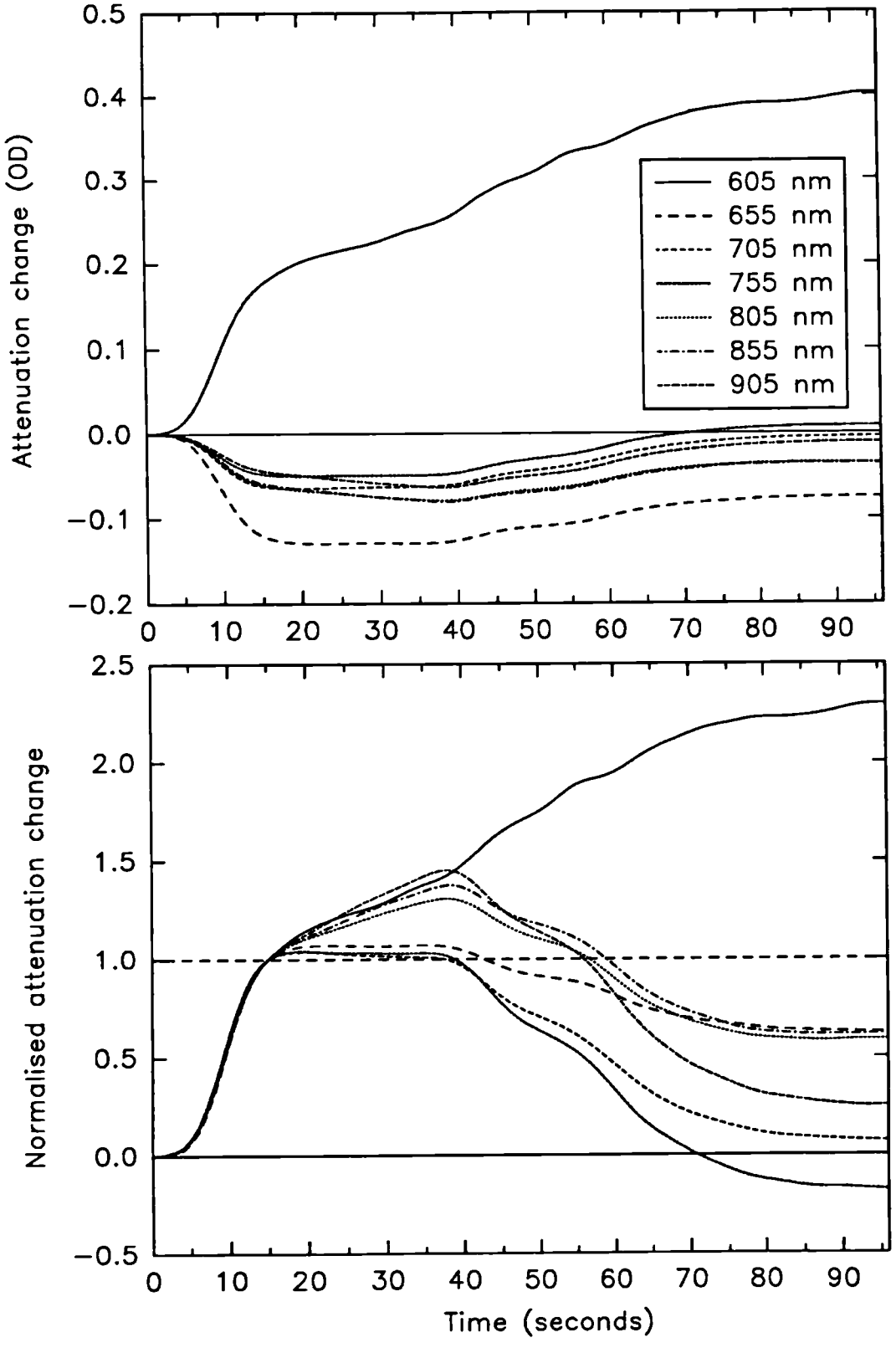

Figure 6.19 The kinetics of attenuation changes in a blood free rat brain (spectra relative to normoxia). The inspired gases were changed from 100% oxygen to 100% nitrogen. Nitrogen respiration continued until death.

between 15 and 40 seconds; and a third phase from 40 seconds onwards. All wavelengths behaved similarly in the first phase, however in the second phase (this corresponds to the previously defined Period 'C') the 605 nm peak and all wavelengths longer than 780 nm responded differently from all the other wavelengths between 650 and 770 nm. All this preceded the tertiary phase (Period 'D') of essentially wavelength independent changes in attenuation seen after 40 seconds. The magnitude of the attenuation changes in the 15-40 second slow phase were about 30% of the attenuation changes seen during the initial fast phase and hence would be more difficult to detect, especially in the presence of haemoglobin. Currently, this slow phase spectrum will be ignored as possibly arising from an additional compound. However it does point to the existence of another spectral component which may be associated with the binuclear centre of cytochrome c oxidase.

The almost wavelength independent increase in attenuation at death (Period 'D') was always seen. Its magnitude was in the range 0.03-0.06 OD, typically 60% of the absolute attenuation change seen at 830 nm due to the cytochrome c oxidase reduction. The spectral changes were not completely wavelength independent during this period and there was evidence of a continuing small increase in the magnitude of the 605 nm peak. This effect was therefore a very significant spectral component which occurred at cell death and was almost certainly related to scattering changes occurring with neuronal depolarisation.

An average spectrum of the respiratory chain in-vivo was constructed using data from seven animals with an average of 4.4 (min. 3, max. 6) N_2 dips performed per animal. Averaging was performed in three stages:

i) For each N_2 dip an average spectrum was taken from the **first 15-20 seconds** of the appearance of the 605 nm peak. During this period, a "near" isobestic wavelength was observed between 617 and 618 nm. A few spectra were rejected on the basis of the lack of a "near" isobestic wavelength. This averaged "N_2dip" was passed onto stage (ii). Averaging for just the first 15-20 seconds of spectra avoided the complexities of the slower second phase reduction.

ii) An average spectrum was then formed for **each animal** representing an average of all the "N_2dip" spectra from that animal. Each "N_2dip" spectrum was firstly scaled so that the absolute area under the spectrum between 585 nm and 995 nm was identical. Typical standard deviations within one animal were 1-2% of the mean values across the complete spectrum.

iii) An average was then performed **between animals** after first scaling the one averaged

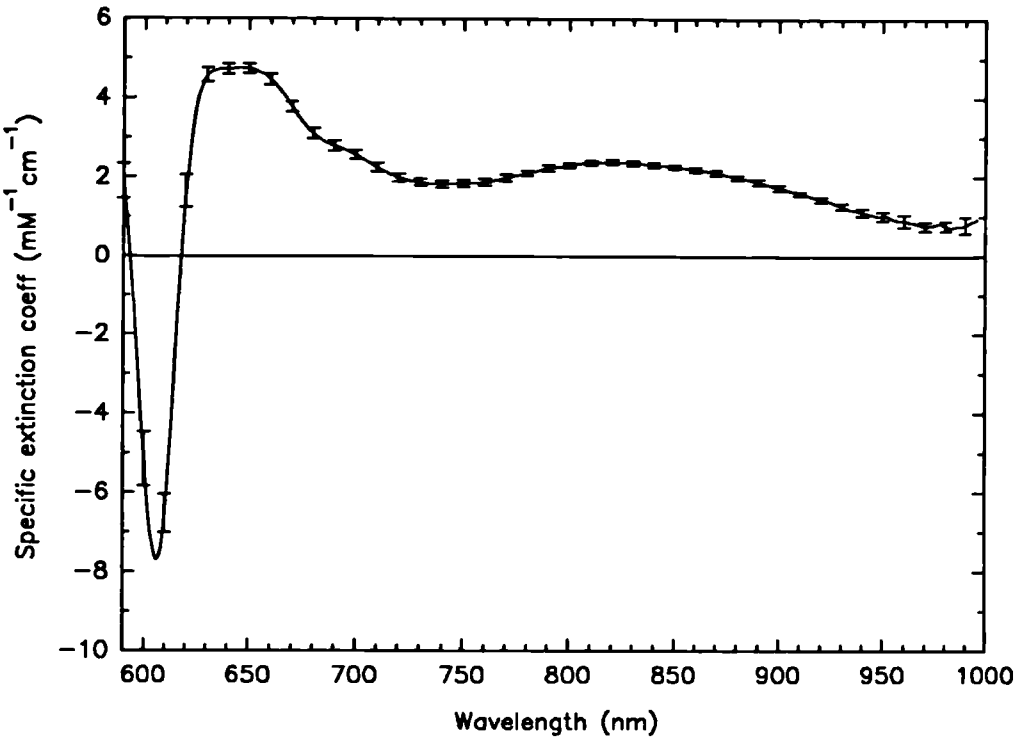

Figure 6.20 The difference spectrum of a blood free rat brain, indicating the mean value and one standard deviation taken from many results. Data is scaled to the extinction coefficient of in-vitro cytochrome c oxidase at 830 nm.

spectrum from each animal, again using the absolute area under the curve. This spectrum can be seen in Figure 6.20 together with error bars showing one standard deviation, the magnitude of the standard deviation was in the range of 3-5% of the mean, slightly larger than the same quantity measured on one animal.

Small inaccuracies in the absolute wavelength position lead to the larger standard deviations seen near the sharp 605 nm peak. Otherwise it is fair to say that for a physiological measurement the spectral responses were remarkably similar. It is of interest to compare this result with a measurement on isolated solubilised in-vitro cytochrome c oxidase.

6.2.4 Measurement of in-vitro cytochrome c oxidase

Purified, cytochrome c oxidase enzyme was kindly supplied by Dr. M.T. Wilson, (Biochemistry Dept., Essex University) prepared from ox heart using the method of Yonetani[171]. The previous discussion on the properties of this enzyme, Section 6.2.1, has shown that it exhibits different spectra (in the visible region) from two different oxidised forms, one called "resting" and the other "pulsed" when it is rapidly turning over electrons, and that it now appears that it is the "pulsed" form which exists in-vivo. Thus measuring the in-vitro difference spectrum of the enzyme in this same state was most relevant.

The reduced state was obtained in a manner which mimicked cytochrome c oxidase reduction by anoxia, an excess of electrons were supplied to the enzyme at a rate which exceeded the oxygen supply. The enzyme was eventually reduced because of inadequate oxygen delivery.

The purified cytochrome c oxidase enzyme was first unfrozen and diluted with phosphate buffer at pH 7.0 containing a trace of detergent, Tween 80 (polyoxyethylene sorbitan). The working enzyme concentration was 22 μM. The solution was then filtered using a disposable 0.2 μM cellulose acetate filter (Micropore), to leave a clear liquid and then transferred to a self masking cuvette of 1 cm path length.

The spectrophotometer used was the OMA CCD SYSTEM so that fast undistorted spectra could be taken as the enzyme redox state changed. The reductant sodium ascorbate was first added to produce a concentration of 10 mM. Electron flow to cytochrome c oxidase began at this time but at a negligible rate. To increase the rate of electron transfer slightly, a mediator tetramethyl-*p*-phenylenediamine dihydrochloride (TMPD) was added at a concentration of 40 μM which resulted in a full reduction of cytochrome c oxidase in 10.5 minutes. Spectra were not taken during this first reduction cycle which merely served to ensure the generation of the "pulsed" enzyme. Oxygen was then shaken into the solution to re-oxidise the sample and spectra then collected at 1 second intervals during the second reduction cycle. The very slow donation of electrons from TMPD in this experiment meant that the Cyt a, Cu_A site remained essentially fully oxidised for 8 minutes until oxygen supply became limiting. At this point it became increasingly more reduced over a period of 2 minutes, this phase of reduction can be seen in the 3-dimensional plot of Figure 6.21. The set of difference spectra were normalised to the (approximately) fully oxidised state during the 8 minutes of steady state before reduction began. There appeared to be only one spectral component in all these

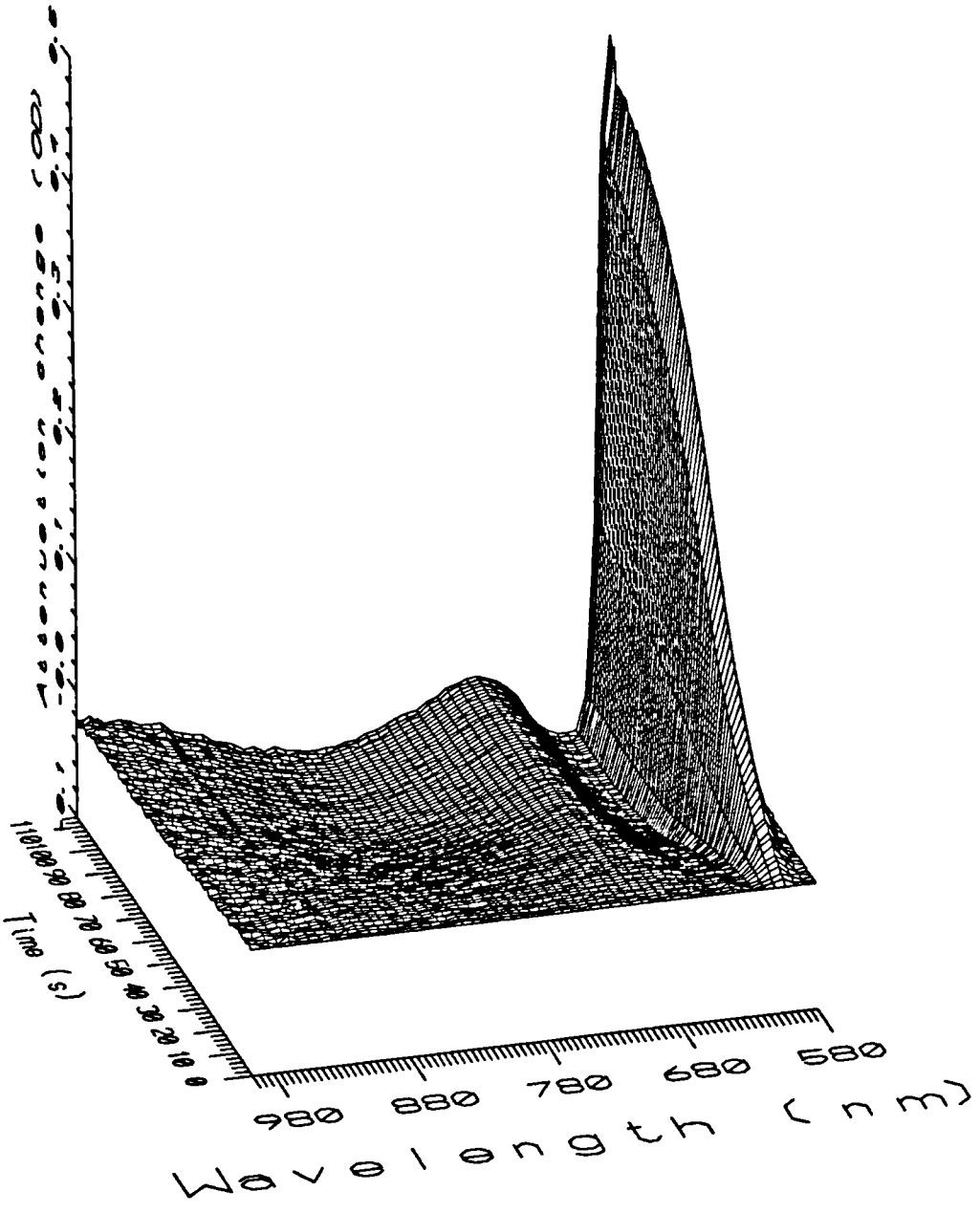

Figure 6.21 Difference spectra, relative to time zero, of isolated solubilised "pulsed" cytochrome c oxidase taken during reduction by sodium ascorbate and TMPD in the presence of a diminishing oxygen supply.

difference spectra, the kinetics at all wavelengths being identical.

6.2.5 Differences between in-vivo and in-vitro data

The in-vivo difference spectra obtained from the anoxic minus normoxic rat brain of Figure 6.20 should have closely matched those of the cytochrome c oxidase, cytochrome c, and cytochrome b components of mitochondria unless there was some other oxygenation dependent chromophore in the tissue. This supposition was tested by comparing the in-vivo difference spectrum against a linear sum of the in-vitro difference spectra of cytochrome c oxidase (Figure 6.21), cytochrome c and b (Figure 2.9), at ratios estimated to exist in rat brain tissue. Literature values of these ratios have already been discussed in Section 1.2.3, and are approximately 1:1.6:1.42 for cyt aa_3:cyt b:cyt c. However, it should be remembered that the steady state reduction levels of the cytochrome enzymes in normoxic brain are not necessarily identical and therefore these values have to be treated as estimates.

The result of the comparison of the "in-vitro simulated mitochondrial difference spectra" and the in-vivo rat brain difference spectrum is shown in Figure 6.22(a). Below this, in Figure 6.22(b), the relative contribution of the cytochrome enzymes at the ratios indicated above for the "simulated mitochondria" are shown. There are two important points to notice. Firstly, the match of the two spectra in Figure 6.22(a) is excellent, the major difference being at shorter wavelength, particularly around the 605 nm peak. This is to be expected, as both the scattering and absorption coefficients of brain tissue are slowly varying functions over the 630-900 nm wavelength range[151]. Shorter effective optical pathlengths are expected at shorter and longer wavelengths outside this range where tissue absorption coefficients (caused by the cytochromes and water) are higher and this agrees qualitatively with the results observed here. The second point is that the contribution of cytochrome c oxidase dominates the other cytochrome enzymes by an order of magnitude in the 750-950 nm spectral range.

The conclusion can therefore be reached that the attenuation change observed across a rat brain, in changing from normoxia to anoxia, can be explained by the cytochrome enzymes of the mitochondria and further that in the 750-950 nm range this is dominated by cytochrome c oxidase.

A tabulated version of the "simulated mitochondrial spectrum" in Figure 6.22 is given in Appendix B, where the extinction coefficient values have been scaled to the in-vitro extinction coefficients of the 830 nm band of cytochrome c oxidase[99].

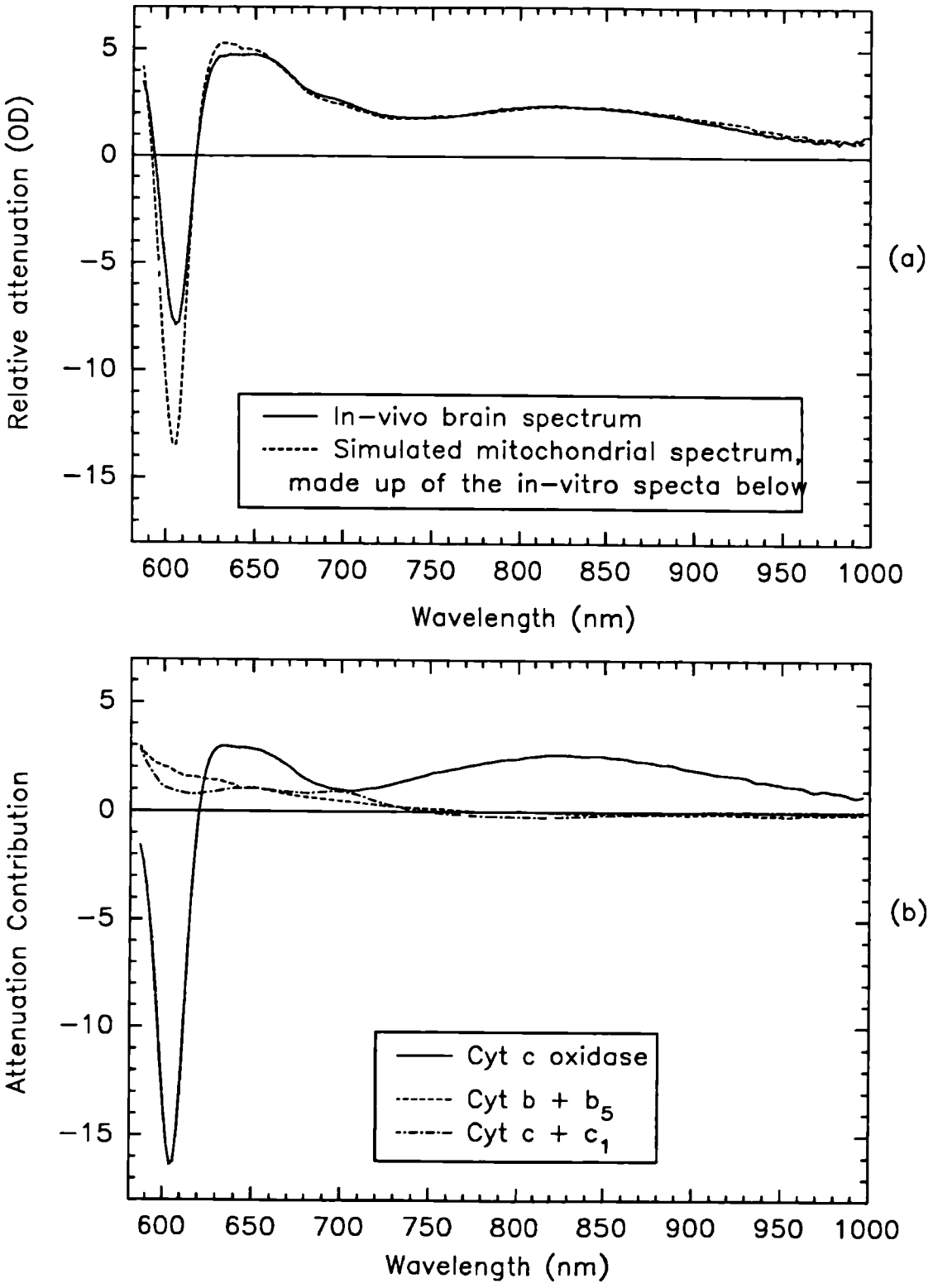

Figure 6.22 (a) Comparison between the in-vivo rat brain spectra of Figure 6.20 and a "mitochondria" made up of cytochromes c oxidase, b and c. (b) Relative contribution of the cytochromes to the spectrum in (a).

6.2.6 Chapter summary

The extinction coefficients for haemoglobin and cytochrome c oxidase (mitochondrial enzymes) measured in this chapter have been shown to be of acceptable accuracy to be used in calculating the chromophore concentration in tissue. In the wavelength region of interest, 750 to 950 nm, it has been shown that there is no appreciable difference between cytochrome c oxidase measured in-vitro and in-vivo. This also adds a degree of confidence to the assumption that the effective optical pathlength is only slowly varying in this spectral region.

One possible problem has arisen, the possibility of additional "compounds" which are only apparent around the time of cell death. The signal magnitude from these "compounds" is in the range of 30-50% of the total attenuation signal resulting from cytochrome c oxidase alone. These effects require further investigation but as they occur at such high levels of cytochrome reduction (close to cell death) they will be ignored in the data analysis which is the subject of the following chapter.

CHAPTER 7

NIR SPECTROSCOPY DATA ANALYSIS

The clinical spectrophotometer described in the previous chapters provides data on brain tissue attenuation changes at four discrete wavelengths from the heads of newborn infants. Additionally continuous NIR spectra, over a spectral range of 400 nm, are available from the OMA CCD SYSTEM, across up to 3 cm of brain tissue in laboratory animals. Accurate specific extinction coefficient spectra of isolated deoxyhaemoglobin (Hb), oxyhaemoglobin (HbO_2) and the difference spectrum of cytochromes (Cyt) have also been measured. Data analysis methods (or "algorithms") are now needed which will permit tissue concentrations of Hb, HbO_2 and Cyt to be calculated from these specific extinction coefficient spectra. Any algorithm should ideally also incorporate a means of estimating the size of possible errors in the calculated concentrations.

At the outset, the aim of this project was to provide quantitative data in non-arbitrary units. The various techniques used to achieve this goal are described in this chapter and the measured values for ΔHb, ΔHbO_2 and ΔCyt concentrations in tissue are compared to other published data. Finally, possible methods of refining the algorithm are discussed.

Some of the data analysis procedures discussed in this chapter have been presented previously[259].

7.1 THE PROVISIONAL ALGORITHM

7.1.1 Method

There are two distinct steps in an algorithm which produces chromophore concentrations in relative, quantified and non-arbitrary units: Stage I, is the conversion of the measured attenuation change spectrum [Units: OD] into an extinction coefficient spectrum [Units: $OD\,cm^{-1}$ effective optical pathlength]; Stage II, is the splitting of the extinction coefficient spectrum into the relative contributions of the constituents i.e. ΔHb, ΔHbO_2 and ΔCyt concentration changes. Please note that all attenuation spectra and resulting concentration data discussed here are **changes** unless explicitly stated as being **absolute.**

7.1.1.1 *Stage I: conversion of attenuation into extinction coefficient*

In the provisional algorithm a simplifying approximation is made in Stage I; attenuation changes are taken to be linearly related to changes in extinction coefficient. It has already been shown that over a wide extinction coefficient range that this assumption is likely to be incorrect (see Section 3.4.2). The assumptions made in the provisional algorithm are:

i) The validity of the modified Beer-Lambert law of Equation 3-19, in which additionally the differential pathlength (DP) has a constant value, both as a function of tissue extinction coefficient and of wavelength.

ii) The scattering coefficient of the tissue does not change over a single monitoring period.

iii) The separation of the OPTODES does not change during a single monitoring period.

Expressed mathematically the conversion is simply

$$\Delta K = \frac{\Delta A}{Bd} \qquad 7\text{-}1$$

where ΔA is the attenuation change, ΔK is the extinction coefficient change and the DP [Units: cm], is $\beta = Bd$, the DPF (B) multiplied by the OPTODE spacing (d). Later in this chapter, a non-linear conversion of attenuation to extinction coefficient is discussed which should improve conversion accuracy.

7.1.1.2 *Stage II: conversion of extinction coefficient into chromophore concentrations*

Having determined the extinction coefficient change ΔK, Stage II is the conversion of ΔK into its three components; ΔHbO_2, ΔHb and ΔCyt. This stage is a truly linear process, the total extinction coefficient is simply a linear sum of the extinction coefficients of its constituent parts. To derive the contributions of the components, a minimum set of three simultaneous equations, at three different wavelengths is required, see Equation 4-4. When more than three wavelengths are used, multilinear regression can be employed to "fit" the component spectra and the accuracy of the fit can be checked using analysis of variance. This process assumes that:

i) The only changes in tissue attenuation that can occur are caused by changes in the concentration of oxy- and deoxy-haemoglobin and redox changes of the cytochromes.

ii) The concentration of cytochrome enzymes in the tissue does not change over a single monitoring period (many hours).

Therefore only three independent variables will be assumed in the analysis ΔHb, ΔHbO_2 and ΔCyt. This hypothesis has been tested in a limited number of circumstances in the rat brain using principle component analysis[260]. However, it is convenient to first set out the mathematics of the analysis in general terms allowing for the possibility of any number of oxygen dependent chromophores being present in the brain tissue.

The general form of a multilinear regression calculates an **estimate set** ($\boldsymbol{C}$), which contains elements C_i, where C_i is the concentration change of the i^{th} independent chromophore in the tissue, for $i = 1$ to m chromophores, [Units: mM]. Expressed in vector form this is

$$\boldsymbol{C} = (C_1, C_2, ..., C_m) \qquad 7\text{-}2$$

The estimate is based upon a **data set** ($\boldsymbol{K}$), the elements, (K_j) of which are the

extinction coefficient changes† observed in the tissue as a function of wavelength, for $j=1$ to n wavelengths, [Units: OD cm^{-1} effective optical path]. In vector form this is

$$K=(K_1, K_2, ..., K_n) \qquad 7\text{-}3$$

The estimate relies on an error free **design set** (α), whose elements are the specific extinction coefficients of the oxygen sensitive chromophores at the same wavelengths that are used to generate the data set

$$\alpha=\begin{vmatrix} \alpha_{11} & \alpha_{21} & . & . & \alpha_{m1} \\ \alpha_{12} & \alpha_{22} & . & . & . \\ . & . & . & . & . \\ \alpha_{1n} & \alpha_{2n} & . & . & \alpha_{mn} \end{vmatrix} \qquad 7\text{-}4$$

Here element α_{ij} is the specific extinction coefficient of chromophore i at wavelength j [Units: mM^{-1}cm^{-1}]. These specific extinction coefficient spectra should be accurately measured in non-scattering media containing the isolated purified compounds.

The estimate set is never exact, as each point in the data set will have a noise component superimposed upon its mean value and hence the problem to be solved can be expressed as

$$\begin{aligned} K_1 &= \alpha_{11}C_1+\alpha_{21}C_2+ \ldots . \alpha_{m1}C_m+e_1 \\ K_2 &= \alpha_{12}C_1+\alpha_{22}C_2+ \ldots . \alpha_{m2}C_m+e_2 \\ . &= . \quad . \quad . \quad . \quad . \\ K_n &= \alpha_{1n}C_1+\alpha_{2n}C_2+ \ldots . \alpha_{mn}C_m+e_n \end{aligned} \qquad 7\text{-}5$$

where the error set (E) contains elements which are the residual errors at each wavelength

$$E=(e_1, e_2, ..., e_n) \qquad 7\text{-}6$$

Note that there is no constant term in the analysis. This is based on the physical fact that the regression must go through the origin. Zero attenuation change implies a zero change in the chromophore concentrations.

Equation 7-5 is expressed in matrix form as

---

† For simplicity in the matrix expressions K is used instead of ΔK from this point and similarly for C.

$$K = \alpha C + E \tag{7-7}$$

A solution for this set of equations can be found only if $n \geq m$ and α is non singular. If $n = m$ then the solution is found by simultaneous equations. If $n > m$ then the solution is found by a least-square multilinear regression, where the matrix C is found such that the sum of the squares of the residual error terms (*SSE*) is minimised where

$$SSE = \sum_{j=1}^{n} e_j^2 \tag{7-8}$$

When the variance of the error terms at each wavelength is the same and independent of all other wavelengths i.e. var(E)=$I\sigma^2$,where I is the identity matrix and σ^2 the variance. A minimum value for the *SSE* is found by the partial differentiation of the *SSE* with respect to all the C_i and in matrix form yields[261]

$$C = (\alpha'\alpha)^{-1}\alpha' K \tag{7-9}$$

where $(\alpha'\alpha)^{-1}\alpha'$ is the pseudo-inverse of α and α' is the transpose of α. The residual errors are given by

$$E = K - \alpha C \tag{7-10}$$

The reconstructed data derived from the multilinear regression is $\kappa = \alpha C$, calculated from the estimate set C. The total sum of squares (*SST*) of the input data is made up of the regression sum of squares (*SSR*), the sum of squares explained by the model, plus the *SSE*

$$SST = SSR + SSE$$
$$\sum_{j=1}^{n} K_j^2 = \sum_{j=1}^{n} \kappa_j^2 + \sum_{j=1}^{n} e_j^2 \tag{7-11}$$

As stated at the beginning of this section, the provisional algorithm assumes that only three compounds are present in brain tissue which can give rise to oxygen dependent attenuation changes. A table of the specific extinction coefficients of Hb, HbO_2 and Cyt are given in Appendix B and this data is inserted into the design set. For example, when multilinear regression is used in conjunction with the NIR clinical spectrophotometer with its four wavelengths 778, 813, 867 and 904 nm, and the Hb, HbO_2 and Cyt estimate set, the

matrix $(\alpha'\alpha)^{-1}\alpha'$ can be precalculated as

$$(\alpha'\alpha)^{-1}\alpha' = \begin{vmatrix} 1.784 & -1.337 & -0.861 & 0.776 \\ -0.830 & -0.616 & 0.389 & 1.267 \\ -0.238 & 1.018 & 0.302 & -0.868 \end{vmatrix} \qquad \textbf{7-12}$$

Calculation of the chromophore concentration set C is then a simple (and fast) matrix multiplication of this matrix and the tissue extinction coefficient matrix K, with the residual errors E calculated from Equation 7-6.

With a correct model, the variance of the estimate set Var(C) can be predicted from the variance-covariance matrix $(\alpha'\alpha)^{-1}$ as $\text{Var}(C)=(\alpha'\alpha)^{-1}\sigma^2$. Where σ^2 is the (identical) variance of each element of the input data vector K. Expressed in matrix form this is

$$\text{Var}(C) = \begin{vmatrix} v_{11} & v_{21} & \cdot & v_{m1} \\ v_{12} & v_{22} & \cdot & \cdot \\ \cdot & \cdot & \cdot & \cdot \\ v_{1m} & v_{2m} & \cdot & v_{mm} \end{vmatrix} \sigma^2 \qquad \textbf{7-13}$$

and the v_{ij} are elements of the variance-covariance matrix $(\alpha'\alpha)^{-1}$.
The variance of the estimate of chromophore C_i is σ_{Ci}^2,

$$\sigma_{Ci}^2 = v_{ii}\sigma^2; \qquad \text{for } i=0,1,\ldots m \qquad \textbf{7-14}$$

while the covariance of C_i with C_j is σ_{CiCj}^2,

$$\sigma_{CiCj}^2 = v_{ij}\sigma^2; \qquad \text{for } i \neq j \qquad \textbf{7-15}$$

An unbiased estimate of the value of σ^2 is obtained from s^2, where

$$s^2 = \frac{SSE}{n-m} \qquad \textbf{7-16}$$

and n and m are (as before) the number of wavelengths and the number of chromophores in the regression analysis. Confidence limits for the estimate set can also be found, based on the

values of the v_{ii}, s^2 and the relevant statistical 't' and 'F' tables[261].

The elements of the variance-covariance matrix $(\alpha'\alpha)^{-1}$ are very important. The diagonal elements multiply the variance of the data set to give the variance of the chromophore concentrations. The off-diagonal elements indicate the degree of covariance (or crosstalk) between the error of any two chromophores. For the four wavelength clinical spectrophotometer the variance-covariance matrix of C is

$$Var(C) = \begin{vmatrix} 6.315 & -0.008 & -2.720 \\ -0.008 & 2.825 & -1.412 \\ -2.720 & -1.412 & 1.938 \end{vmatrix} \qquad \text{7-17}$$

In general, a lower variance in the chromophore concentration estimates could be obtained by making more wavelength measurements (increasing n) or by using another wavelength region with larger extinction coefficients. A lower covariance is also obtained by increasing n and by selecting a wavelength region where the specific extinction spectra do not overlap as markedly as they do in the near infrared region. However, one must balance the use of a larger wavelength region and greater variations in specific extinction coefficients against the increased non-linearity that will occur in the Stage I of the algorithm, the conversion of the tissue attenuation (ΔA) into the tissue extinction coefficient (ΔK) data. Hence using a larger wavelength region tends to increase the errors in Stage I and decrease the errors in Stage II of the algorithm. This suggests that an optimum choice of wavelength region must exist.

Note that multilinear regression analysis relies upon two important features of the input data; firstly that the noise in the data set K is normally distributed and secondly that the variance of each K_j is identical and independent of all other wavelengths. The first requirement is met as long as the input noise intensity is small compared to the mean intensity at each wavelength, which is the case in these NIR measurements. The second requirement is almost met, in that the intensities (and therefore the variance) at each wavelength are approximately the same. If there are wide variations in detected intensity at the wavelengths used in the regression analysis then a weighted multilinear least squares analysis should be used[261]. In this case the variance of the error matrix is given by

$$\mathrm{Var}(E) = U = \begin{vmatrix} u_1^2 & 0 & . & 0 \\ 0 & u_2^2 & . & . \\ . & . & . & . \\ 0 & 0 & . & u_n^2 \end{vmatrix} \qquad 7\text{-}18$$

whereas in the analysis above U has been taken to be an identity matrix. Equation 7-7 is then premultiplied by a diagonal matrix $W = (U^{1/2})^{-1}$ to make the variance of each element identical, giving

$$K^* = \alpha^* C + E^* \qquad 7\text{-}19$$

where $K^* = WK$, $\alpha^* = W\alpha$ and $E^* = WE$. The solution of the weighted multilinear regression problem, the variance-covariance matrix is then the same as before with the variables K^*, α^* and E^* replacing K, α, and E in the equations above i.e.

$$C = (\alpha^{*\prime}\alpha^*)^{-1}\alpha^{*\prime}K^* \qquad 7\text{-}20$$

with similar expressions for the variance-covariance matrix.

7.1.2 Algorithm testing methods

The residual error set E is very important, as it indicates the adequacy of the model. The model is the supposition that the data set (the tissue extinction spectrum) is made up of a linear sum of rows of the design set (the individual chromophore spectra). Figure 7.1 is a hypothetical example of such an error set plotted as a function of wavelength. Figure 7.1(a) is an example of a model which is exact, and the error set is observed to be a random function of wavelength. Figure 7.1(b) is an example where the model is incorrect and does not account for all deviations of the data set. In this case the error set is not random, and the model obviously needs refining.

The above test is a visual one, but for a rigorous analysis mathematical tests should be used. The standard test of regression analysis is the coefficient of multiple determination (R^2) which is defined as the proportion of the total sum of squares explained by the regression

parameters.

$$R^2 = \frac{SSR}{SST} \qquad 7\text{-}21$$

For a perfect model and noiseless data, R^2 approaches unity.

In testing the algorithms here, the primary interest is the "lack of fit" of the model, the aim being to develop an algorithm which generates an error set as shown in Figure 7.1(a) where there is no systematic error. One mathematical test which realises this aim splits the sum of the squares of the errors (*SSE*) into a part which is pure noise in the input data and a part which is the systematic error due to the model being incorrect. With all of the NIR optical data we are in the very fortunate position of knowing the variance of the elements of the data set K based on the number of photons per measurement and Poisson statistics. It is therefore possible to calculate from Equations 4-7 and 7-1 the elements u_j of the variance

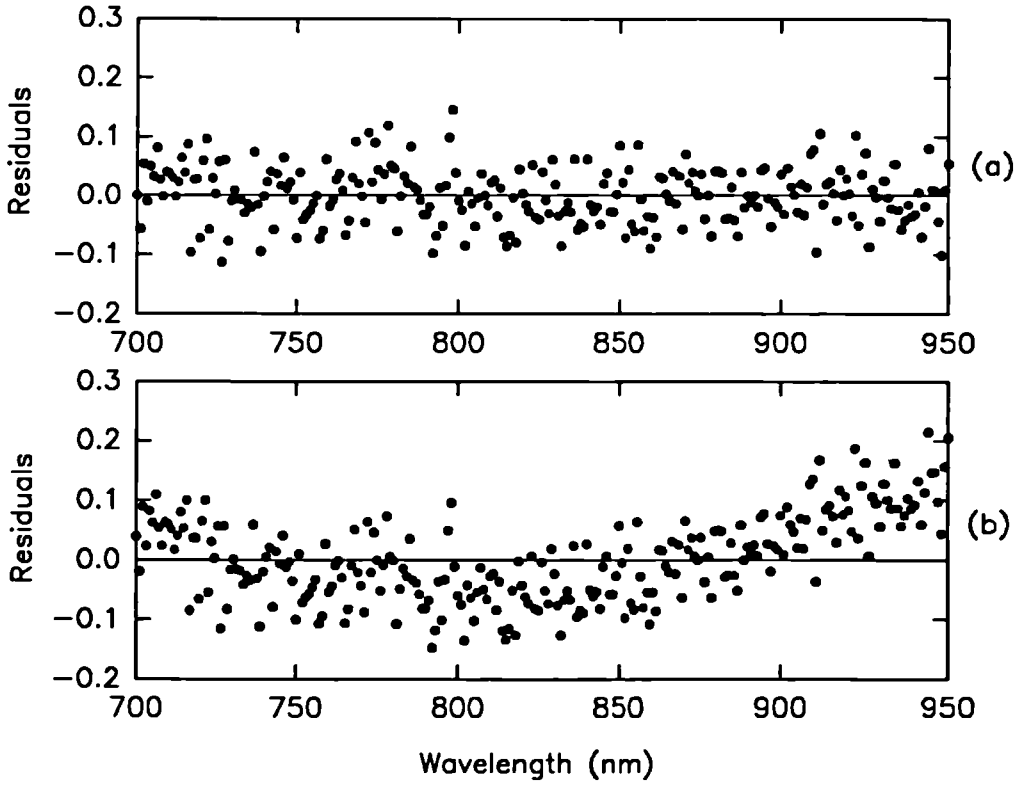

Figure 7.1 Examples of the residual error vector E, the noise is normally distributed with a standard deviation of 0.05 (a) ideal case, on a zero background (b) non-ideal case, on a quadratic background.

matrix U, and hence the weights matrix W needed to perform weighted multilinear regression:

$$\mathrm{var}(K_j) = u_j^2 = \left(\frac{\lg(e)}{\beta_j}\right)^2 \left(\frac{1}{\mu_j} + \frac{1}{\mu_{j0}}\right) \qquad 7\text{-}22$$

where β_j is the differential pathlength and μ_j and μ_{j0} are the mean number of photons detected at wavelength j during the relevant time interval and at the normalisation time ($t=0$) respectively. Weighted multilinear regression is strictly necessary in order to accurately calculate the expected value of the SSE^* arising from the noise of the input data ($\mathcal{E}(SSE^*)$) which from Equation 7-16 is given by

$$\mathcal{E}(SSE^*) = (n-m) \qquad 7\text{-}23$$

This expected value can be compared to the actual value of SSE^* found from the weighted multilinear regression analysis, using Equation 7-8. For an absolutely correct algorithm one would expect $\mathcal{E}(SSE^*) = SSE^*$. For the same input data set, the accuracy of different algorithms can be tested by examining the degree of systematic error measured by $SSE^* - \mathcal{E}(SSE^*)$.

7.1.3 Results

The NIR clinical spectrophotometer with its limited number of wavelengths was not the best system with which to test out the proposed algorithm. Instead, the continuous wavelength OMA CCD SYSTEM provided much better data with its measurement of attenuation at hundreds of wavelengths spread continuously over a 400 nm band.

In order to examine the adequacy of the proposed model, a number of sets of test data were collected using the OMA CCD SYSTEM. This data was measured across the heads of anaesthetised adult rats, prepared in the same manner as described in Section 6.2.2.2 and with a femoral arterial canula in place. Two different types of experiment were performed to cause variations in attenuation across the brain. The first experiment consisted of 96 spectra taken at 1 second intervals during changes in F_iO_2. At the start of the collections the animal was breathing 100% oxygen, after 7 seconds the inspired gas was changed to 100% nitrogen for a 30 second period and then returned to 100% oxygen. The second experiment consisted of 115 spectra measured at 2 second intervals during which time the animal was breathing 21% oxygen. 12 seconds after the start of the collection the animal was given a bolus injection of

bicuculline which caused an immediate large increase in arterial blood pressure from 95 to 140 mmHg. A large increase in EEG activity, accompanied by general seizures, followed some 36 seconds after the injection and lasted for 28 seconds.

Stage I of the algorithm used a constant value for the differential pathlength of 7.82 cm, at all wavelengths, based on measurements which are described later in this chapter. In Stage II, the weighted multilinear regression analysis, used the component spectra in Appendix B which have been measured in non-scattering media and are therefore undistorted by tissue scattering characteristics. The analysis was performed over the spectral region of 700-900 nm at 1.111 nm intervals, therefore $m=3$ and $n=180$. Wavelengths longer than 900 nm were avoided because of the large variations in the differential pathlength that would be expected to occur due to the large water absorption peak at 975 nm. Wavelengths shorter than 700 nm were avoided because of significantly reduced signal to noise ratios in the attenuation spectrum.

The results of the multilinear regression analysis are shown in Figure 7.2 and Figure 7.3. The second and third boxes in these figures are the calculated chromophore concentration changes as a function of time. The error bars show one standard deviation based on the SSE^* and the covariance matrix. The bottom box contains the $\mathcal{E}(SSE^*)$, SSE^* and SSR^*, and indicate the accuracy of the multilinear regression in fitting the ΔK data. The top box shows one of the input extinction spectra from the rat brain, taken at the time indicated, together with the residual spectrum E (multiplied by 10).

The R^2 values for the regressions were typically in excess of 0.997. However the SSE^* values were up to 10 times higher than the $\mathcal{E}(SSE^*)$ which indicated that the model was not correct. Therefore the error bars on the haemoglobin and cytochrome traces could not be treated as being strictly correct and must be viewed with caution. The top box in these figures also showed the lack of fit of the model, the residuals (E) were clearly not distributed evenly about zero. Note that the spectrum displayed in the top box was chosen for the worst case, when the SSE^* was largest.

The magnitude and timing of the changes in the haemoglobin and cytochrome concentrations were not unreasonable, the cytochrome trace was towards the high end of the expected concentration range of 1-5 μM, see Section 1.2.3. The accuracy of this data is discussed later in conjunction with other data calculated using a different algorithm.

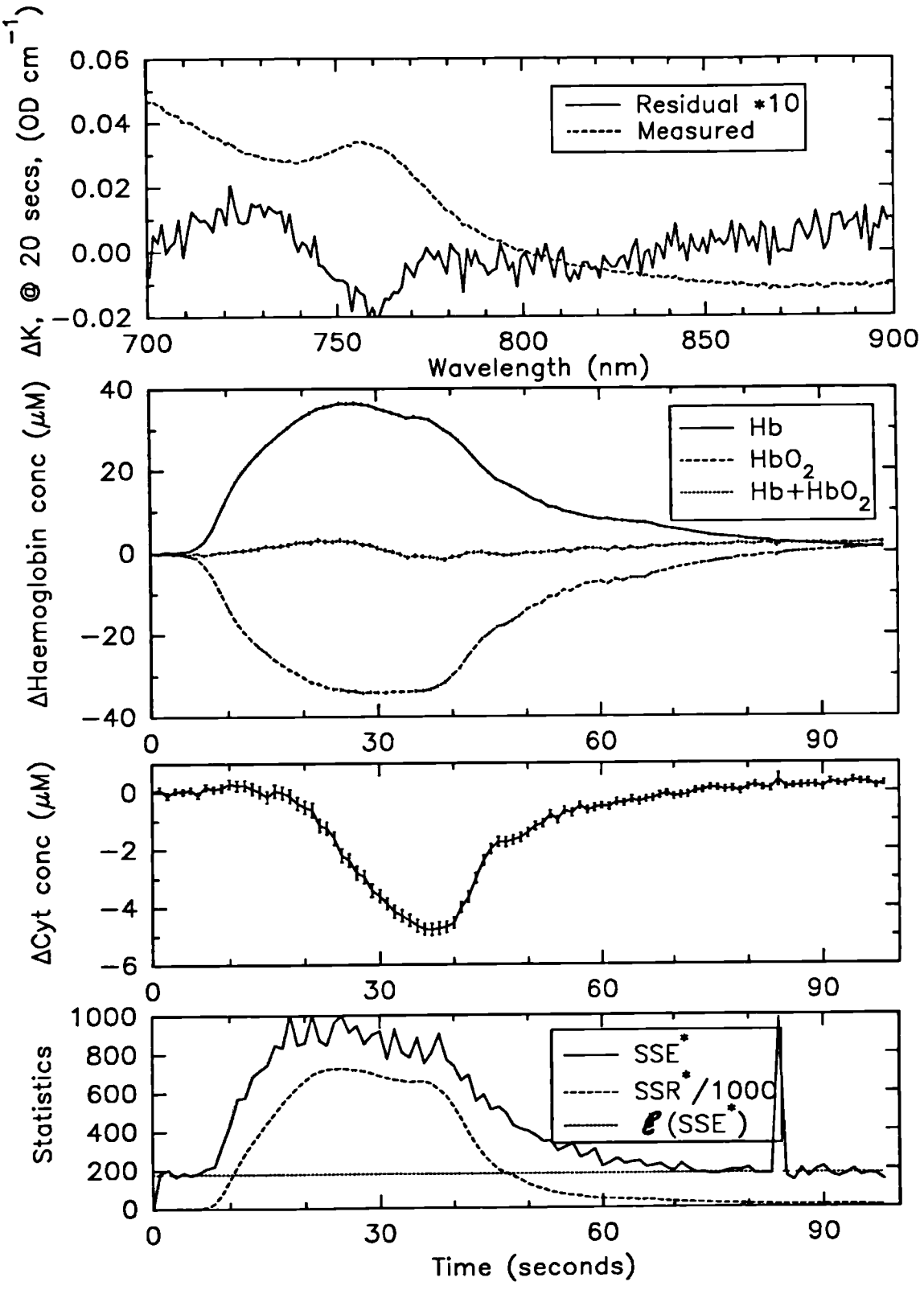

Figure 7.2 Test of the provisional algorithm using a data set measured across a rat head during a dip in the inspired oxygen level to 0%.

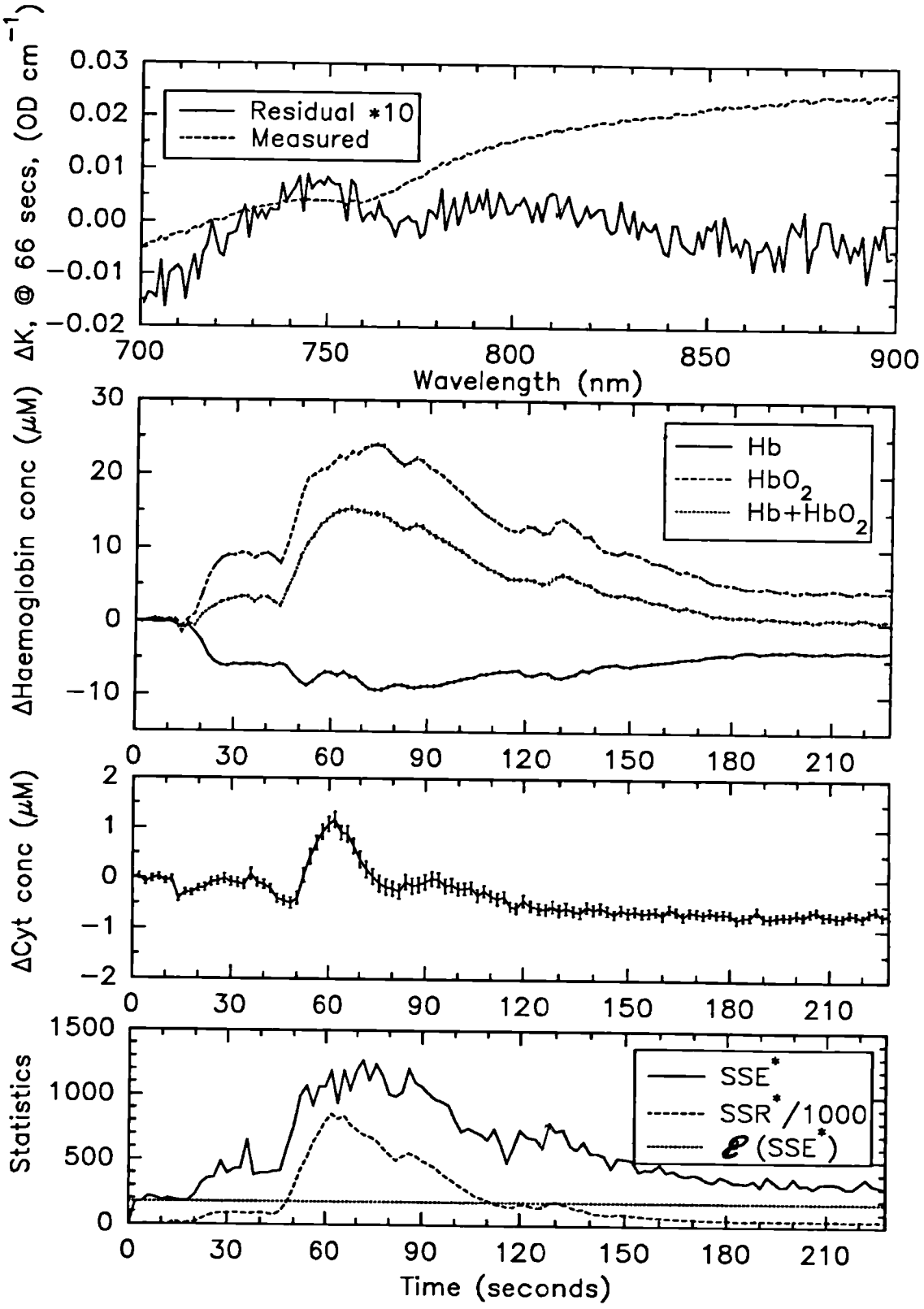

Figure 7.3 Test of the provisional algorithm using a data set measured across a rat head when the animal had seizures caused by an injection of bicuculline.

7.2 THE DIFFERENTIAL PATHLENGTH (DP) IN SCATTERING MEDIA

A lack of knowledge of the differential pathlength is the major reason for the inability of near infrared spectroscopy techniques to quantify chromophore concentrations in tissue. Variations in optical pathlength, either as a function of wavelength or of tissue extinction coefficient lead to errors in the preliminary algorithm of Section 7.1. Many methods of determining the differential pathlength in tissue have therefore been investigated.

The first of these was described in Section 3.4.2 in which known amounts of absorber were added to a scattering solution whose optical properties resembled those of brain tissue, the DPF from this experiment was 5.0. A method of determining this value in newborn infant's brain was sought and three methods of doing this are described in the following sections.

7.2.1 Plasma markers in known concentration

The first approach to the problem of the DP measurement was very simple, and is similar to the quantitative techniques used in positron emission tomography. Here, a small amount of an extra optical absorber is injected into the blood stream. After approximately 30 seconds, it is evenly distributed throughout the plasma and will have added a measurable change to the tissue attenuation, ΔA_t (Units: OD). A blood sample is taken at this time to measure the attenuation caused by the dye across 1 cm of clear plasma, ΔA_p (Units: OD cm^{-1}). The DP (β) is then given by the equation

$$\beta = \frac{\Delta A_t}{\Delta A_p CPV} \quad [cm] \qquad 7\text{-}24$$

where CPV is the fractional cerebral plasma volume in millilitres of plasma per millilitre of wet brain tissue.

This experiment was performed on adult male Wistar rats with their heads prepared in the same manner as described in Section 6.2.2.2 and a femoral arterial canula inserted. The dye used was Cardiogreen (Indocyanine Green, Sigma U.S.A.). This dye had the advantage of being available as a clinically tested material, and also had a large broad near infrared absorption peak. Its disadvantage was that it was rapidly removed from the blood stream by

the liver, making the timing between the collection of the blood sample and the brain tissue spectrum critical. The OMA CCD SYSTEM was not available at the time these measurements were made and the ROFIN SYSTEM was too slow. Instead therefore single wavelength measurements were made at 813 nm (using an interference filter) across both the rat's head and the plasma samples.

Only two successful measurements were made on one animal, and the DP for a 1.4 cm head was estimated at 10.5 cm, based on a *CPV* of 2 ml/100 ml of brain[262]. The accuracy of this method was poor because small errors in the *CPV* were magnified approximately 50 fold in the calculation of the differential pathlength. Also the *CPV* would have been a function of the arterial carbon dioxide partial pressure amongst other things.

Cardiogreen was not the ideal plasma marker for these measurements. The liver was too effective at removing it from the blood stream before it had the opportunity to distribute itself evenly through the circulatory system. The measurements above had therefore to be made after infusion of very high doses of cardiogreen, so high that the liver became poisoned and its ability to extract the cardiogreen from the blood was severely diminished. Using cardiogreen, this is obviously not a plausible technique for use on patients.

7.2.2 Tissue markers in known concentration

This idea for measuring the DP is based on a similar principle to the plasma marker method. The idea for the technique arose whilst using the OMA CCD SYSTEM, which is capable of measuring absorption caused by the water in brain tissue at 975 nm. Water is a naturally occurring absorber in the brain tissue whose concentration is both well known, and which varies by only a few percent in normal physiological conditions. The concept is not to inject additional water, but to non-invasively determine its absolute attenuation in tissue by differential spectroscopy of the tissue attenuation against wavelength around the relatively narrow 975 nm water absorption peak. This method was also tested on the rat head.

The attenuation of the rat head was first measured relative to a neutral absorber, see the solid line of Figure 7.4(a), the baseline for this curve was arbitrary. To remove the problem of the arbitrary baseline and of other absorbers (e.g. haemoglobin) with broader absorption peaks at these wavelengths, the second differential of this curve was taken (see the solid line of Figure 7.4(b)). This second differential curve for the tissue attenuation was then regressed against the second differential of the extinction spectrum for pure water to yield a

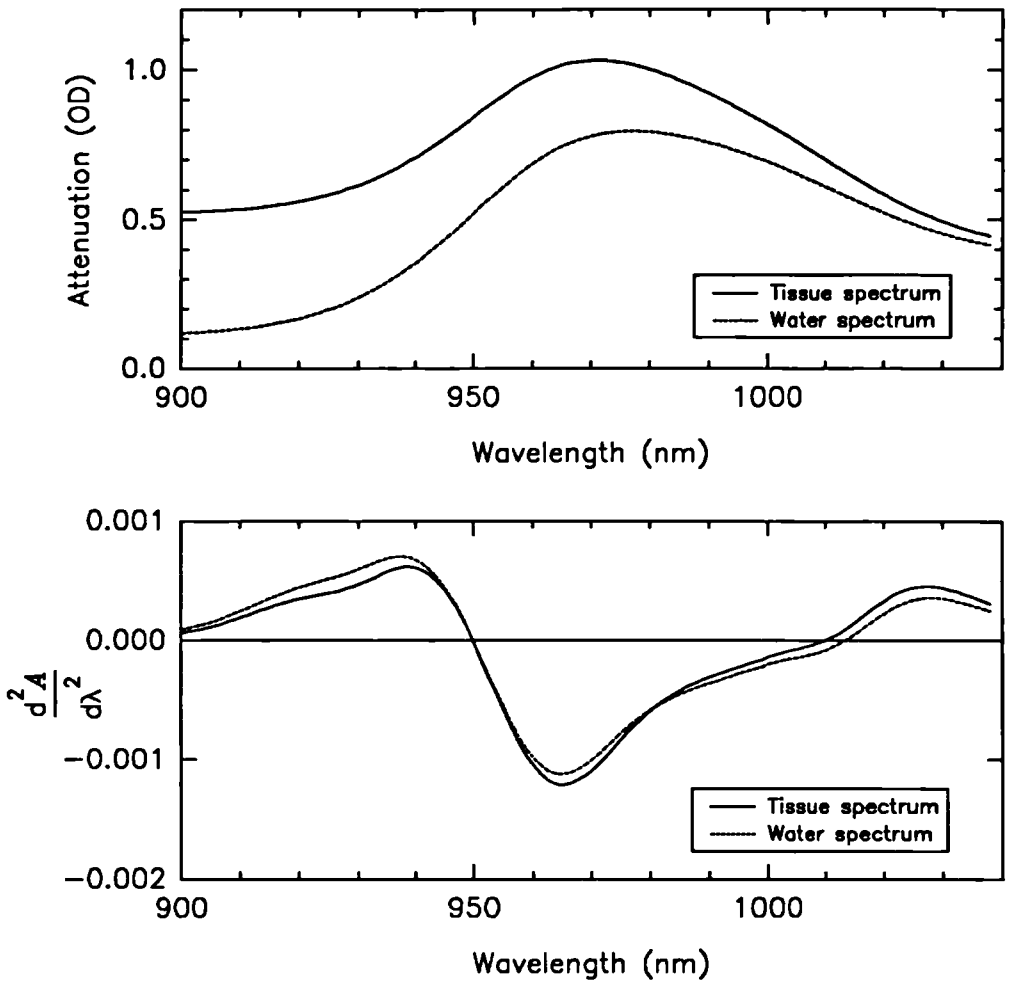

Figure 7.4 (a) attenuation spectra of a rat head and 4.11 cm of distilled water, baseline corrected for the spectral response of the spectrophotometer, (b) second differential spectra of the attenuation spectra in (a).

value for the quantity of water in the tissue spectrum. The curves for the calculated amount of water in the attenuation spectrum and the second differential were then generated, see Figure 7.4(b), and the R^2 for the regression was typically 0.95. The differential pathlength (DP) was then found by dividing the quantity of water found by the regression by 0.82[263], the volume fraction of the brain which is water. This process was identical to that illustrated in Equation 7-24 using a plasma marker except that the second differential spectra were divided.

Theoretically the effect of lipids should also be taken into account at these wavelengths but in practice they could not be observed. It is a matter of speculation if brain lipids have the same NIR absorption peaks as pork fat, as shown in Figure 2.5, or if other problems exist with this methodology.

Values of DP were measured on 10 animals giving a mean value and standard deviation of 4.71 ±0.27 cm for a 1.4 cm rat head.

The main problems of this method are:

i) That the DP is assumed to be a constant in the 900-1050 nm region. This is not going to be true because of the large variations of the water extinction coefficient. Thus this technique will always result in an underestimation of the true DP in this wavelength region.

ii) The inhomogeneity of water distribution in the surface tissues, the skull, and the white and grey matter of brain tissue make it difficult to select a single fractional water content value.

iii) The DP is only found in a single wavelength region, extending it to other wavelengths would not be possible.

However, using water absorption does have inherent advantages over the use of plasma markers because of its much higher percentage volume in brain and its low percentage variability plus the totally non-invasive nature of the measurement. There remains the possibility that with the use of correction factors, this technique may provide a practical method of developing a self calibrating quantitative spectrophotometer.

7.2.3 Photon transit times in scattering media

This section describes the most informative method of examining optical pathlengths in a scattering medium. As previously stated, light which travels through a scattering medium takes a convoluted path, much longer than the direct "straight line" path. One method of observing the distribution of all these paths taken by the light is to directly measure the time of flight of a very short (picosecond) optical input pulse which has passed through the medium and thus derive optical paths as the light velocity multiplied by the time of flight.

The units of time (t) and distance (l) will be freely interchanged throughout this section by using the simple relationship

$$l = \frac{c}{n} t \qquad 7\text{-}25$$

where c is the velocity of light in vacuo and n the refractive index of the scattering medium.

7.2.3.1 *Pilot experiment*

This qualitative pilot experiment was performed in a very limited amount of time whilst visiting Hamamatsu Photonics K.K., Japan. It serves to demonstrate the differential pathlength factor of multiply scattered light traversing a scattering medium of diluted milk, and also illustrates the effects of the addition of an absorbing dye.

The laser used was a frequency doubled modelocked Nd:Yag, synchronously pumping a dye laser which produced light pulses of approximately 5 picosecond duration at 630 nm, at a repetition rate of 82 MHz. The detector was a synchroscan streak camera (Hamamatsu Photonics K.K., C1587 & M1955). The synchroscan streak camera is a very fast optical oscilloscope with a 10 ps resolution and a one dimensional (slit) imaging capability. It could average the incoming pulses over periods from 1 second to a few minutes to increase signal to noise ratios at low light levels[264].

The laser beam was expanded to about 1 cm diameter and passed through a beaker of 8 cm diameter, before being incident upon the entry slit of the streak camera. Water was placed in the beaker to a depth such that the 1 cm beam was split, part travelling through the water and part through the air above the surface of the water. By careful alignment, parts of both beams were arranged to enter the input slit of the synchroscan streak camera. The overall time resolution obtained was 20 picoseconds because of excessive pulse to pulse jitter of the laser source.

Initially the beaker contained only water. Two pulses were detected by the streak camera, one going through the water and the other going an identical distance in air, see the streak image in Figure 7.5(a)†. The time difference between the pulses resulted from the refractive index difference between air and water. The refractive index calculated from this experiment was the reassuring value of 1.33. The difference in the heights of the two peaks reflected the intensity of light reaching the entry slit from each component of the beam. The absolute intensity value in this experiment was irrelevant and the first peak arriving at the streak camera (through the air) served merely as a time reference.

Milk was then added to the water to make it a scattering solution. The resulting loss in light intensity was many orders of magnitude and this was compensated for by increasing

---

† The streak camera image profile shown is similar to an oscilloscope picture, light intensity on the vertical axis and time on the horizontal axis.

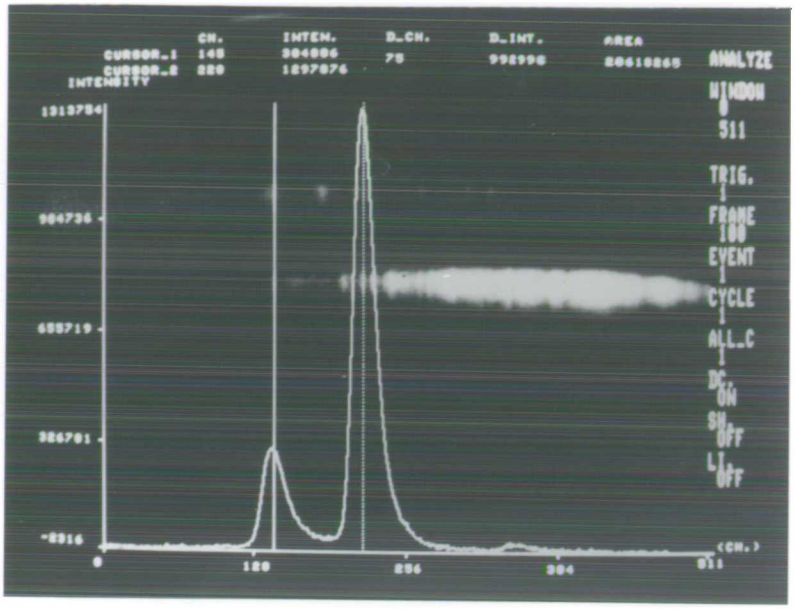

(a) Streak camera profiles of a light pulse crossing an 8 cm beaker containing water. The first pulse is always a time reference pulse across the water surface through air, the second pulse is delayed by the additional refractive index of water.

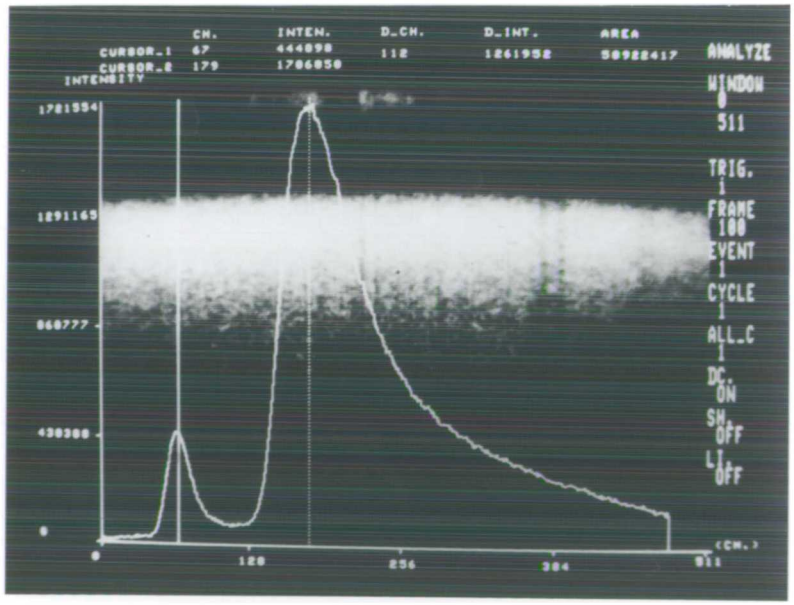

(b) Streak camera profiles with a scattering medium (milk) added to (a). Note the added delay and the broadening of the light pulse through the scattering med um.

Figure 7.5 Pilot experiment to measure the optical pathlengths taken by light passing through a scattering medium (Part I). Note that one channel is equivalent to 1.3 ps.

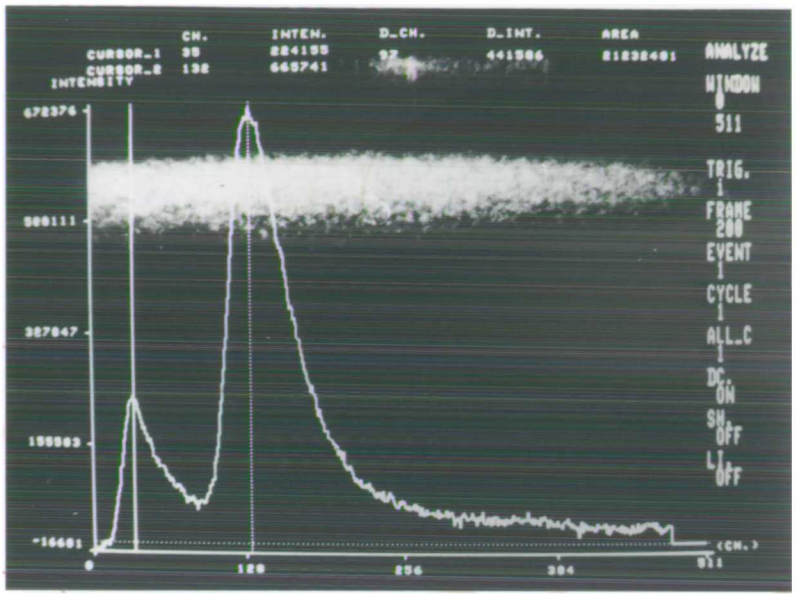

(a) Streak camera profiles but with an absorbing dye added to Figure 7.5(b). Note that the broad pulse in Figure 7.5(b) has been narrowed by the addition of an absorber, mainly at the longest pathlengths.

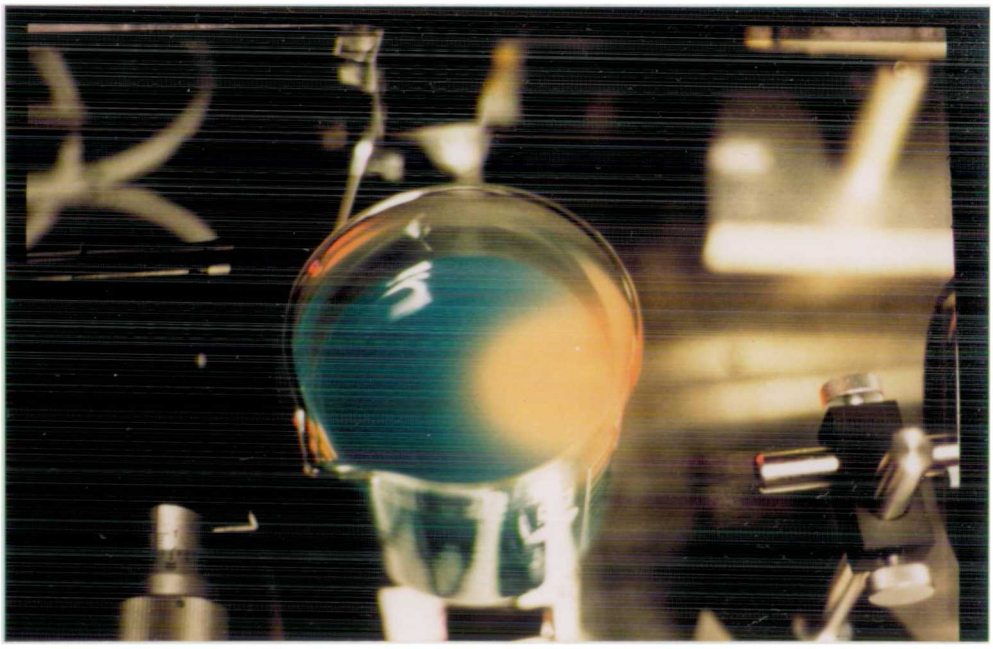

(d) Photograph of the beaker, showing the diffuse laser beam radiation in the scattering medium (containing dye).

Figure 7.6 Pilot experiment to measure the optical pathlengths taken by light passing through a scattering medium (Part II). Note that one channel is equivalent to 1.3 ps.

the gain of the streak camera and attenuating the reference beam across the water surface. The effects of multiple scattering can be clearly seen in Figure 7.5(b). The scattering solution added a significant delay to the mode of the photon path distribution, a factor of 1.5 longer than the time of flight in clear water. The pulse was also broadened significantly, the intensity was still significant at times corresponding to 3 to 4 times the physical pathlength.

Addition of a green absorbing dye to the scattering solution resulted in a further decrease in signal size which required the gain of the system to be increased again. The shape of the temporally dispersed light pulse also changed dramatically, see Figure 7.6(a). This resulted from the logarithmic attenuation of light intensity with pathlength (i.e. time). Now, light which had travelled very long distances was highly attenuated and as a result the distribution of the photons paths was shortened in time. Addition of absorber thus moved the mode of the distribution to a slightly earlier time. The light distribution which was obtained with both the absorber and scatterer present is shown in Figure 7.6(b).

The situation encountered here with both an absorber and scatterer present in the solution is similar to that observed in brain tissue. Unfortunately the degree of scattering and absorption used in this experiment were unknown, but were undoubtedly less than that of brain tissue. This simple experiment did however show two principle features:

i) The existence of the differential pathlength factor which effectively increases the optical path length of light in a scattering media.

ii) The differential pathlength factor is a function, amongst other things, of the extinction coefficient of the medium.

These results lead to the conclusion that it would be fruitful to investigate light transport and absorption in a scattering media by simultaneously measuring attenuation and pathlength with a time of flight measurement system. In conjunction with a number of colleagues, a purpose built system was therefore constructed for this purpose.

7.2.3.2 *Experimental methods*

The apparatus constructed is shown in Figure 7.7. Optical pulses of approximately 4 ps duration at a repetition rate of 76 MHz are produced by an actively modelocked ion laser coupled to a synchronously pumped dye laser (Coherent, U.S.A. K3000, K701-3). The average optical power available is 150 mW at wavelengths between 750 nm and 810 nm (Oxazine 750

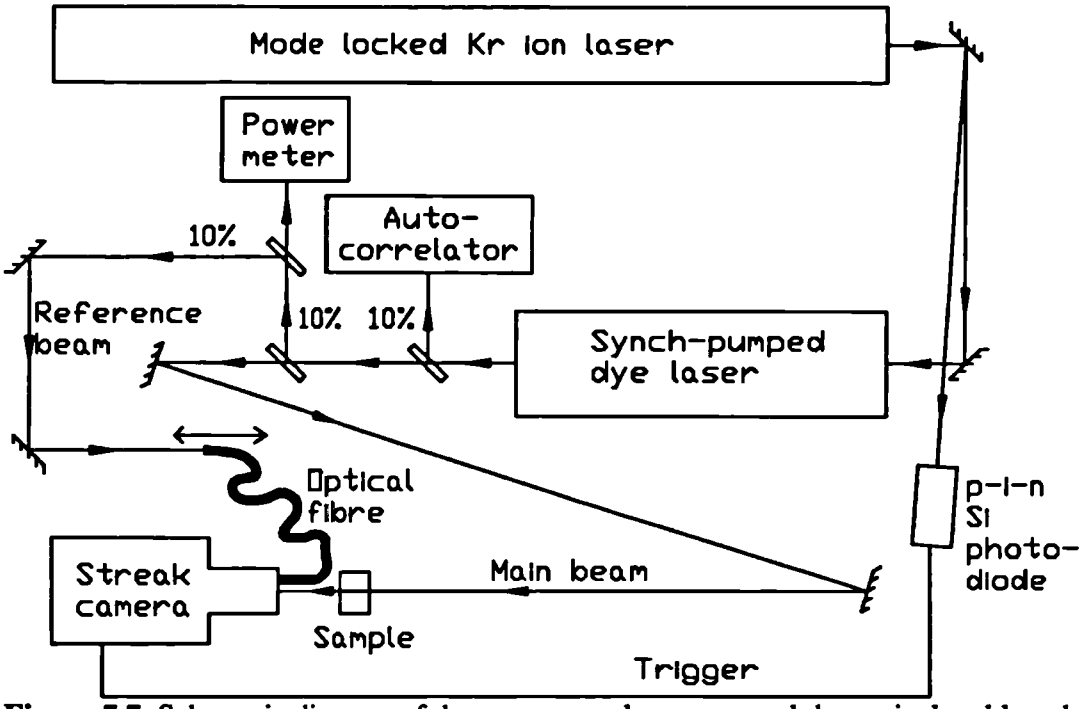

Figure 7.7 Schematic diagram of the system used to measured the optical pathlength distributions (TPSFs) of scattering media.

dye). Other wavelengths could be generated using different laser dyes and optics.

The picosecond pulses are sampled by three beamsplitters before going to the test sample. The first removes 10% of the beam for pulse width examination in an autocorrelator; the second 10% of the remaining power is sampled to measure the average optical power, and a further 10% is employed as a "zero time reference" for the streak camera. Beam steering mirrors reflect the main beam towards the synchroscan streak camera (Hamamatsu Photonics K.K., C1587 & M1955).

Time zero is defined as the time at which light enters the sample, the time reference beam allows the time delay added by the sample to be measured independent of drifts which occur in the synchronisation of the laser and the streak camera.

Various improvements to the optical arrangements of this system have been made over the years, the latest of which has been to make both the laser and the streak camera fibre optic coupled.

7.2.3.3 *The relationship between the differential pathlength and the optical pathlength distribution*

Figure 3.14 implies that the differential pathlength is a unique distance for any given set of experimental conditions such as wavelength, absorption and scattering coefficients and geometry. However, Figure 7.5 shows that in reality that there is no unique optical path through a scattering medium but rather a distribution of paths. The differential pathlength represents an "effective optical pathlength" which is some function of the actual optical pathlength distribution. Finding a function which generates the differential pathlength from the optical pathlength distribution would be of the great importance to quantitative spectroscopy since, if such a function exists, it could form the basis of a non-invasive method of determining the differential pathlength.

The methodology which describes how this was achieved has been published[265]. Both Monte Carlo modelling and experimental measurement of the differential pathlength (DP) and the optical pathlength distribution in a scattering medium were performed. The optical pathlength distribution was named the Time Point Spread Function (TPSF) analogous to the line point spread function in imaging. Sample attenuation and the TPSF were measured and modelled for a wide range of scattering and absorption coefficients.

A number of functions of the TPSF were then compared with the DP. It was found that the mean time delay of the TPSF (converted to a distance using Equation 7-25) corresponded on a 1:1 basis to the DP, to within the experimental error. This is shown in both the Monte Carlo and the experimental data from Delpy et al.[265] which is reproduced in Figure 7.8. Most importantly the 1:1 relationship held over a large range of scattering coefficients.

Hence a non-invasive method of measuring the DP had been found which could be applied to quantitative spectroscopy of any tissue.

7.2.3.4 *The mean optical pathlength in rat brain*

The time of flight technology was first applied to the adult rat head and the experimental apparatus used in these studies has been described in Section 7.2.3.2. Nine male Wistar rats mean weight 288 g were prepared in the standard manner. They were anaesthetised, tracheostomised, and the femoral artery and vein cannulated. The scalp tissues were reflected to allow direct access to the parietal bones on the sides of the skull.

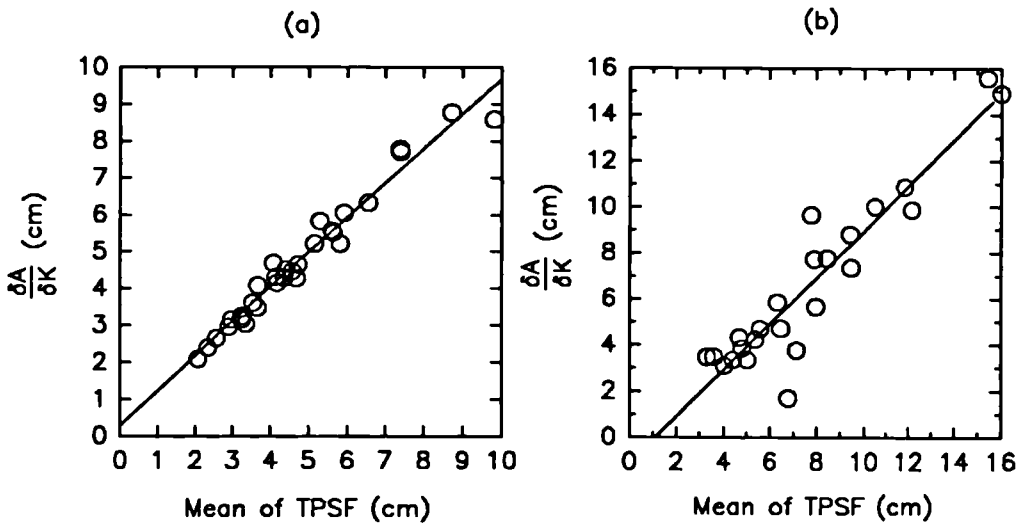

Figure 7.8 Verification of the 1:1 relationship between the DP ($\delta A/\delta K$) and the mean of the TPSF, from Delpy et al[265]. (a) Modelled, (b) experimental data.

Picosecond light pulses at 783 nm were incident on one side of the skull and the light emerging from the far side of the head was detected both by the streak camera and a separate 1 mm diameter fibre optic. Changes in attenuation across the head were calculated by measuring the ratio of the input laser beam intensity to that of the emerging light intensity measured via this fibre optic. Hence changes in attenuation were recorded at the same time as the TPSF on the streak camera.

The experimental protocol was to measure the TPSF and the changes in the overall attenuation at different arterial oxygenation levels by altering the inspired gas mixture in the sequence: 100% oxygen; 90% oxygen, 10% carbon dioxide; 21% oxygen, 89% nitrogen; 12% oxygen, 88% nitrogen; 100% oxygen again; 100% nitrogen at cell death; 15 minutes post mortem and 24 hours post mortem. The idea behind this protocol was to examine the variation in the TPSF over the maximum physiological range of brain oxygenation and blood volume.

Three example TPSFs are shown in Figure 7.9 for F_IO_2 values of 100%, 21% and 12% balance nitrogen. The abscissa was converted into distance assuming an (approximate) average refractive index for brain tissue of 1.4[266,267], the mode of each TPSF was normalised to unity. The input pulse width is shown at time zero. The second pulse is a hypothetical one corresponding to the TPSF which would have been obtained if the rat's head had been non-scattering. It emphasises the magnitude of the pulse delay and the broadening caused by the scattered light in the brain tissue. Scattering was obviously much larger than that observed in

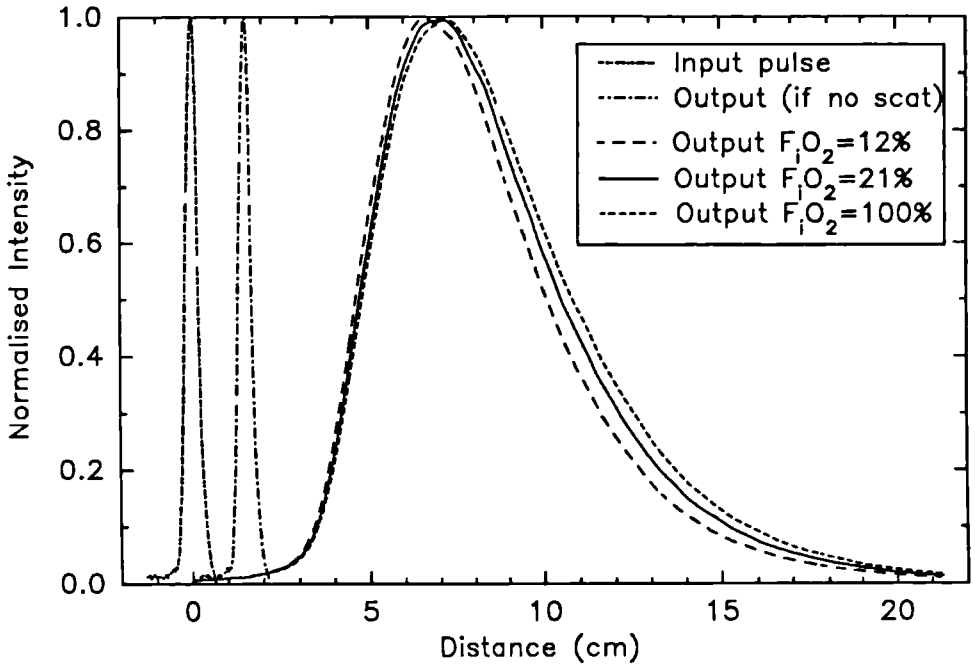

Figure 7.9 Normalised optical pathlength distributions measured across a rat's head in various states of oxygenation. The "non-scat" output pulse corresponds to the hypothetical case of non-scattering rat head.

the pilot experiment of Figure 7.5. Additionally there was the expected systematic decrease in the optical pathlengths as the tissue absorption coefficient increased (at 783 nm) with decreased F_iO_2 (i.e. decreased haemoglobin oxygen saturation).

The average data of the results for all of the experiments is tabulated in Table 7.i. The table parameters are dimensionless as the calculated pathlengths were divided by the mean distance across the rat head. Hence the parameter marked as the mean was the differential pathlength factor (DPF). In normoxia this had the value of 5.3 but was also oxygenation dependent. This experimentally measured value compared favourably with the value of 5.0 obtained in the simulation of neonatal brain tissue in Section 3.4.2. Note that the first 5% of light did not exit the tissue until 2.5 times the physical tissue thickness and the last 5% exited after travelling greater than 9.5 times the physical tissue thickness.

The relationship between changes in tissue attenuation per centimetre of tissue and the percentage change in the DP is shown in Figure 7.10. The maximum variation in the DP over the physiological range was 10% at 783 nm. A linear regression line through the data points indicated a slope of –32% per OD cm^{-1} change in tissue attenuation. This data has also been presented previously[268].

Table 7.i Statistical parameters of the rat brain TPSFs, mean and standard deviations of all animals. Values are dimensionless, having been normalised for the transit time of the physical head size (1.45 cm, n=1.4).

All animals	100% O_2	10% CO_2, 90% O_2	21% O_2, 79% N_2	12% O_2, 88% N_2	Post mortem			All data
					0 min	15 min	22 hrs	
Mean								
5th percentile	2.61	2.57	2.55	2.50	2.43	2.60	2.87	2.59
50th percentile	5.07	4.98	4.95	4.78	4.60	4.83	5.18	4.91
95th percentile	9.62	9.47	9.40	9.04	8.68	8.96	9.41	9.23
Mean	5.43	5.35	5.31	5.12	4.93	5.16	5.52	5.26
Standard deviation								
5th percentile	0.27	0.25	0.28	0.26	0.24	0.22	0.30	0.28
50th percentile	0.24	0.24	0.25	0.25	0.24	0.26	0.41	0.31
95th percentile	0.23	0.31	0.28	0.27	0.26	0.34	0.52	0.44
Mean	0.23	0.24	0.24	0.24	0.24	0.26	0.41	0.31

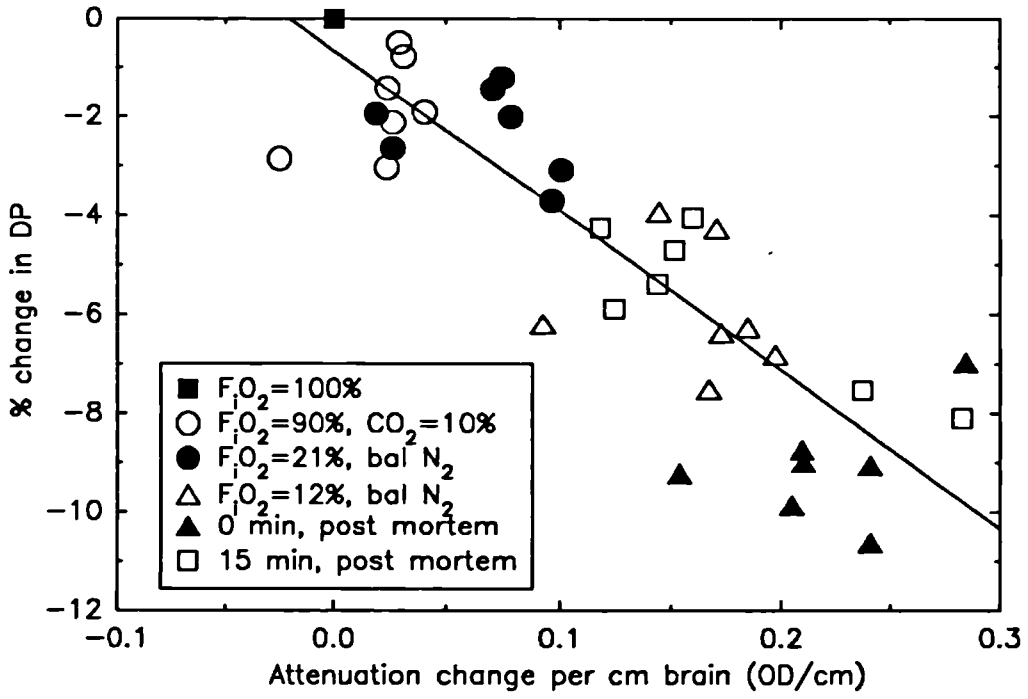

Figure 7.10 The percentage change in the differential pathlength measured across 7 rat heads as a function of the attenuation change per cm of brain tissue in different states of oxygenation.

7.2.3.5 *The differential pathlength of human infant brain*

The DP across the head of post mortem human infants has been measured and the results published[158 269]. The first publication[158] reported measurements on 6 infants of between 23 and 26 weeks gestation. The light entry and exit points were at 180° to each other, on opposite sides of the head and the effective OPTODE separations were between 4.5 and 5.7 cm. The measurements were made at between 12 and 72 hours post mortem. The mean DPF for all the measurements was 4.39 ±0.28 (standard deviation).

The results of the second publication[269] are shown in Figure 7.11. Ten infants were studied in this group between gestations of 24 to 38 weeks. Optical fibres were used to couple light both into the head from the laser and also from the head to the streak camera. This added flexibility meant that measurements could be easily made at any OPTODE separation. The angle between the OPTODE and the skin surface was always kept at near 90° and the OPTODE separation varied.

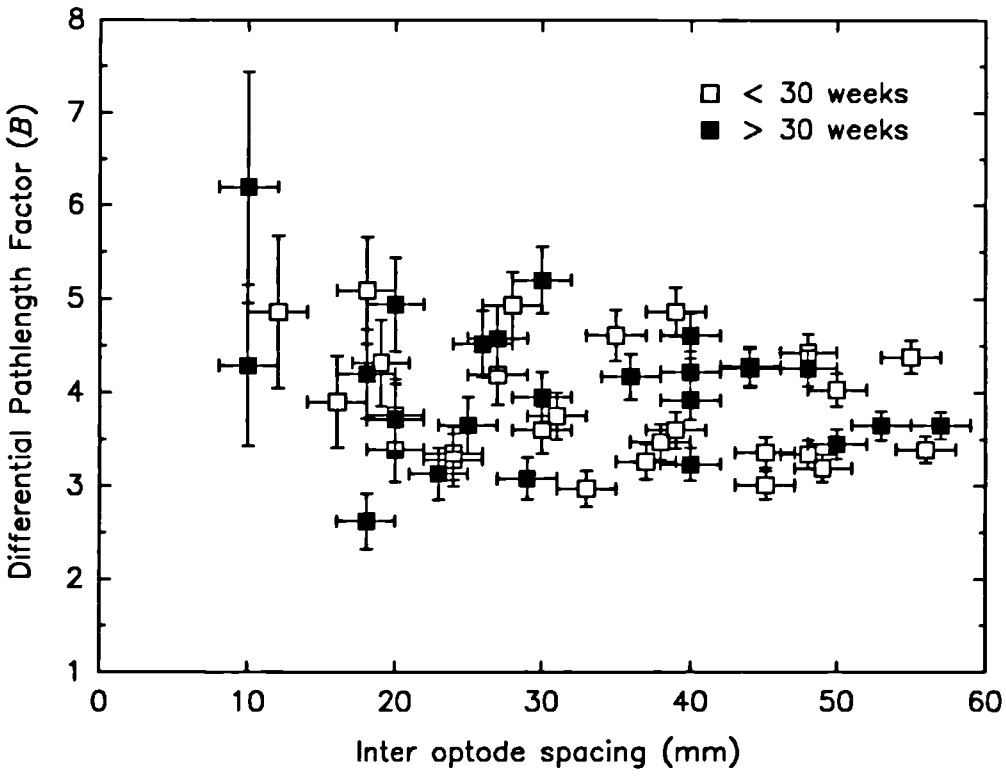

Figure 7.11 Differential pathlength factor for post mortem human infant brain as a function of inter OPTODE spacing.

The mean value and standard deviation of the DPF for this data was 3.85 ±0.57. This value was somewhat smaller than the value of 4.39 ±0.28 reported in the previous publication but the difference was not statistically different. There was also no statistically significant variation found between the two groups of infants of different gestational ages, although this may be masked by the large experimental errors.

The rather large spread of values was somewhat disappointing and probably related to two main factors:

i) OPTODE separation measurement inaccuracies: it was particularly difficult to accurately measure the inter OPTODE separation with callipers. The oedematous state of the surface tissues often added to this problem.

ii) Experimental inaccuracies: this technology is rather complex to use. The long time period (2 years) it took to accumulate this data and the large number of different personnel involved undoubtedly led to some systematic experimental errors.

The use of post mortem tissue is not ideal but it was not practical to make these measurements on patients. Table 7.i showed that in the rat, the difference between 24 hours post mortem and normoxic values of the DPF were small.

Future measurements would benefit from the laying down of a strict measurement protocol and the construction of a stereotactic holder for more accurate measurements of OPTODE separation. The same measurements made within a few days on the heads of a group of adult volunteers[269] showed much less variation with an average DPF of 5.93 ±0.42.

7.2.4 Summary

Three different methods have been described for measuring the DP of brain tissue. The first, used a plasma marker, was invasive, very inaccurate but had the advantage of requiring simple technology. The second, used water absorption, still used relatively simple technology, but had the disadvantage of always under-reading the correct DP and was only capable of measuring the DP in the 975 nm region. The third method, used very expensive technology but provided the DP, non-invasively and at any wavelength which was available from the picosecond laser source.

The mean values for the DPF of the rat head obtained by these three methods were 7.5 (at 813 nm), 3.37 (at 975 nm) and 5.3 (at 783 nm) for the plasma, water and time of flight

methods respectively. The plasma marker value was, for reasons explained earlier, very inaccurate. The water peak value always under read but was consistent across many animals and may be of practical use with correction factors. The time of flight method is going to provide the most accurate values and is also flexible, as theoretically it can be used at any wavelength. However, state of the art picosecond laser sources limit the wavelength range available.

The most accurate value of the DPF found for post mortem infant brain was 3.85 ±0.57. This value is used in the quantitative data of Section 7.6.

A fourth possible method of measuring the DP has recently been reported[270], but which still requires validation. This method is capable of making measurements similar to those of the time of flight system but in the frequency domain instead of the time domain. A continuous laser source is used but is intensity modulated in the 100 MHz to 1 GHz range. The phase change and loss of depth of modulation of the modulation signal is detected.

7.3 AN IMPROVED NON-LINEAR ALGORITHM

The provisional algorithm of Section 7.1 was based on a number of assumptions some of which have now been confirmed as only approximately correct. The DP is not a constant as expressed in Equation 7-1, but has been shown to vary by up to 10% over the physiological range of extinction coefficients observed in the rat head. Additionally, the fact that the DP is a function of the tissue scattering and absorption coefficient means that it must also be a function of wavelength, while in the provisional algorithm it was assumed to be wavelength independent.

A more general form of the equation describing the relationship between tissue attenuation and extinction coefficient, as seen in Figure 3.14, would be:

$$A = G(\mu_s) + \int_0^K \beta(k, \mu_s)\, dk \qquad 7\text{-}26$$

where A is the **absolute** tissue attenuation, K is the **absolute** extinction coefficient, β is the DP, and G is the attenuation due to the scattering coefficient (μ_s) when $K = 0$. Note that both

β and G will additionally be dependent upon the geometry of the sample.

Finding a general solution to this equation for tissue attenuation is a long term problem and not the topic of this thesis. The equation is much simplified by measuring tissue attenuation changes at a fixed OPTODE geometry and determining relative changes in attenuation as a function of time compared to a fixed NORMALISATION time. Assuming that tissue scattering properties are time independent, the first term in Equation 7-26 drops out, simplifying the expression to

$$\Delta A = \int_0^{\Delta K} \beta(k, \mu_a)\, dk \qquad 7\text{-}27$$

The most accurate solution to Equation 7-27 would be obtained with an instrument that could measure both tissue attenuation and the DP at a number of wavelengths in real time, but unfortunately such an instrument does not exist at present, though it may soon be available using frequency domain measurements. In the meantime a practical methodology has been developed based upon the modelling of light transport in tissue using the diffusion equation and incorporating experimentally measured reduced scattering coefficients ($\mu'_s = \mu_s(1-g)$) and absorption coefficients μ_a of post mortem rat brain. (An introduction to diffusion theory was given in Section 3.3.2).

7.3.1 Diffusion approximation derivation of tissue attenuation and differential pathlength

The diffusion approximation for a point source in tissue is

$$-\gamma^2 \nabla^2 \phi + \mu_a c \phi = \delta(r - r') \qquad 7\text{-}28$$

where ϕ is the space irradiance, ∇^2 is the Laplacian operator, c the velocity of light in the tissue, $\delta(r - r')$ is a delta function source at the point $r = r'$ and γ^2 is the diffusion coefficient given by[271]:

$$\gamma^2 = \frac{c}{3(\mu_a + \mu'_s)} \qquad 7\text{-}29$$

The solution to Equation 7-28 in a spherically symmetric infinite geometry is a Green's

function

$$\phi = \frac{1}{(2\pi)^{3/2}} \frac{1}{\rho \gamma^2} \exp\left(-\frac{\rho}{\Gamma}\right) \qquad 7\text{-}30$$

where $\rho = (r - r')$ and $\Gamma = \gamma/(\mu_a c)^{1/2}$ is the penetration depth. Thus given μ_a and μ'_s it is possible to calculate the space irradiance at a distance ρ from the source. The intensity at position ρ is therefore

$$I = -\gamma^2 \nabla\phi = \frac{1}{(2\pi)^{3/2}} \frac{\left(1 + \frac{\rho}{\Gamma}\right)}{\rho^2} \exp\left(-\frac{\rho}{\Gamma}\right) \qquad 7\text{-}31$$

where $\nabla\phi$ is the gradient of ϕ. Here it is convenient to describe tissue attenuation on a natural log scale ($N = \ln[I_0/I]$), where I_0 is the intensity when $\mu_a = 0$, as

$$N = \frac{\rho}{\Gamma} - \ln\left(1 + \frac{\rho}{\Gamma}\right) \qquad 7\text{-}32$$

The DP (β) is calculated from Equation 7-32 by differentiating with respect to μ_a, giving

$$\beta = \frac{dN}{d\mu_a} = \left(\frac{\rho}{2\gamma}\sqrt{\frac{c}{\mu_a}}\right)\left(1 + \frac{3\gamma^2\mu_a}{c}\right)\left(1 - \frac{1}{1 + \frac{\rho}{\Gamma}}\right) \qquad 7\text{-}33$$

The dominant term in this expression $(c/\mu_a)^{1/2}\rho/2\gamma$ is the same as the dominant term in the expression for the mean optical pathlength developed by Patterson[272] for a slab geometry. The second term is caused by the diffusion constant γ^2 being a function of μ_a, and the third term is geometry dependent.

The equations above will be used to describe light transport in a rat's head. The theory outlined above is strictly only applicable to a point source at the centre of an infinite sphere and is therefore only a rough approximation to the physical reality. This is a common problem in using the diffusion approximation and for a more accurate result a more realistic model should be sought.

Accurate values of $\mu'_s(\lambda)$ and $\mu_a(\lambda)$ are required in conjunction with the equations

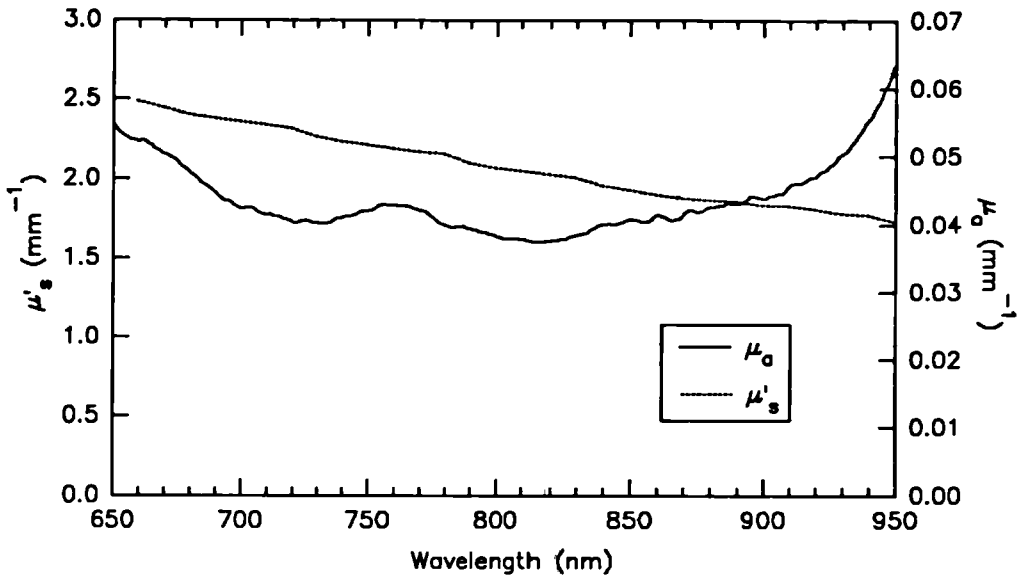

Figure 7.12 Experimentally measured values of μ_a and μ'_s (mm^{-1}) for post mortem rat brain. The data is an average of grey and white matter across a slice.

developed above. These are notoriously difficult to measure. Figure 7.12 shows the data used in this paper. These are preliminary values from one animal and measured using an integrating sphere technique on a thin slice of post mortem rat brain[273]. They represent an average value for both white and grey matter.

The $\mu'_s(\lambda)$ data in Figure 7.12, which is considered to be time invariant, when taken together with tissue thickness ρ (14 mm for a rat head), allows an attenuation versus extinction coefficient curve of the form of Figure 7.13 to be calculated for each wavelength using Equation 7-32†. Two values of reduced scattering coefficients have been chosen which represent the maximum and minimum values in the 650 nm to 950 nm band. The start point on each curve (at time 0) is taken to be $K_0(\lambda)$ (data from Figure 7.12) and is assumed to be the normoxic value in the rat brain. The **absolute** attenuation during normoxia, at time 0, $A_0(\lambda)$ is also calculated from Equation 7-32. The tissue spectrophotometer measures changes in tissue attenuation $\Delta A_k(\lambda)$ at time k (a change in attenuation relative to normoxia at time 0). Therefore the absolute attenuation at time t_k is $A_k(\lambda) = A_0(\lambda) + \Delta A_k(\lambda)$. The absolute absorption

† Confusion can arise due to the different units traditionally used in spectroscopy and the diffusion equation. Remember that attenuation (A) and natural attenuation (N) are related by $A = \log_{10}(e)N$ and extinction coefficient (K, cm^{-1}) and absorption coefficient (μ_a, mm^{-1}) by $K = 10\log_{10}(e)\mu_a$.

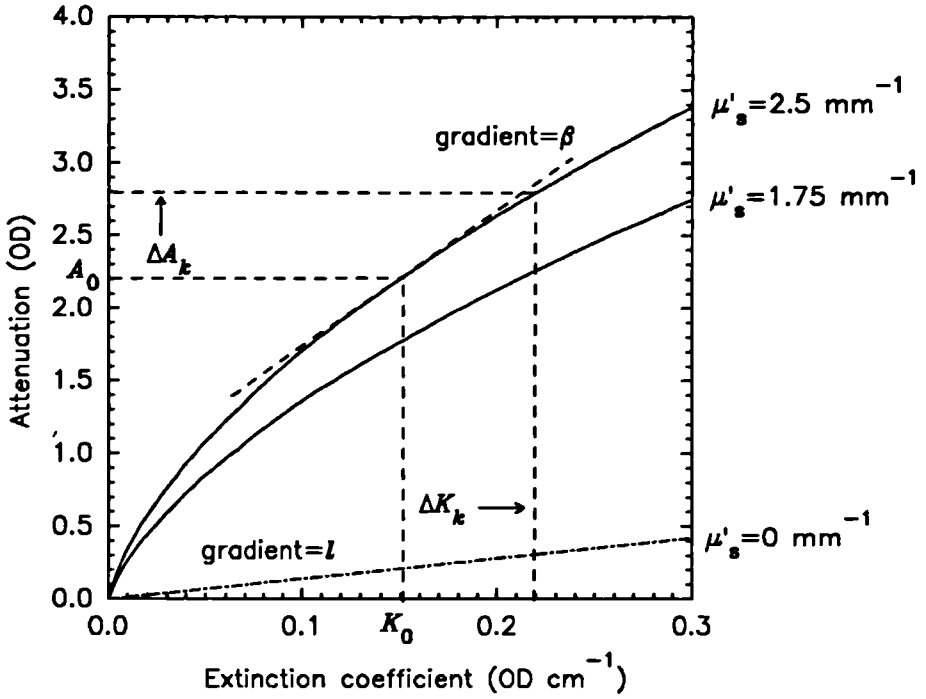

Figure 7.13 Attenuation versus absorption coefficient for the range of scattering coefficients predicted in rat brain between 650 and 950 nm, brain thickness 14 mm, diffusion approximation model.

coefficient K_k at time t_k is found by solving Equation 7-32 for K_k assuming μ'_{s0} and tissue thickness (ρ) are constant at each wavelength. The change in absorption coefficient $\Delta K_k(\lambda)$ corresponding to $\Delta A_k(\lambda)$ is then simply given by $\Delta K_k(\lambda) = K_k(\lambda) - K_0(\lambda)$. The solution of Equation 7-32 is found using a Newton-Raphson root finding algorithm utilising Equation 7-33, so that the maximum allowed error in the attenuation measurement is < 0.00004 OD.

7.3.2 Verification of the attenuation to absorption coefficient conversion

The above method has been verified using data obtained from various measurements on the rat brain. As a first test of the method a simulated rat brain attenuation spectrum was generated, using Equation 7-32, for a head size of 14 mm and the coefficients μ_a and μ_s' of Figure 7.12. This is shown by the solid line of Figure 7.14(a). On the same graph, shown for comparison, are a set of three equivalent baseline corrected spectra, measured across a rat

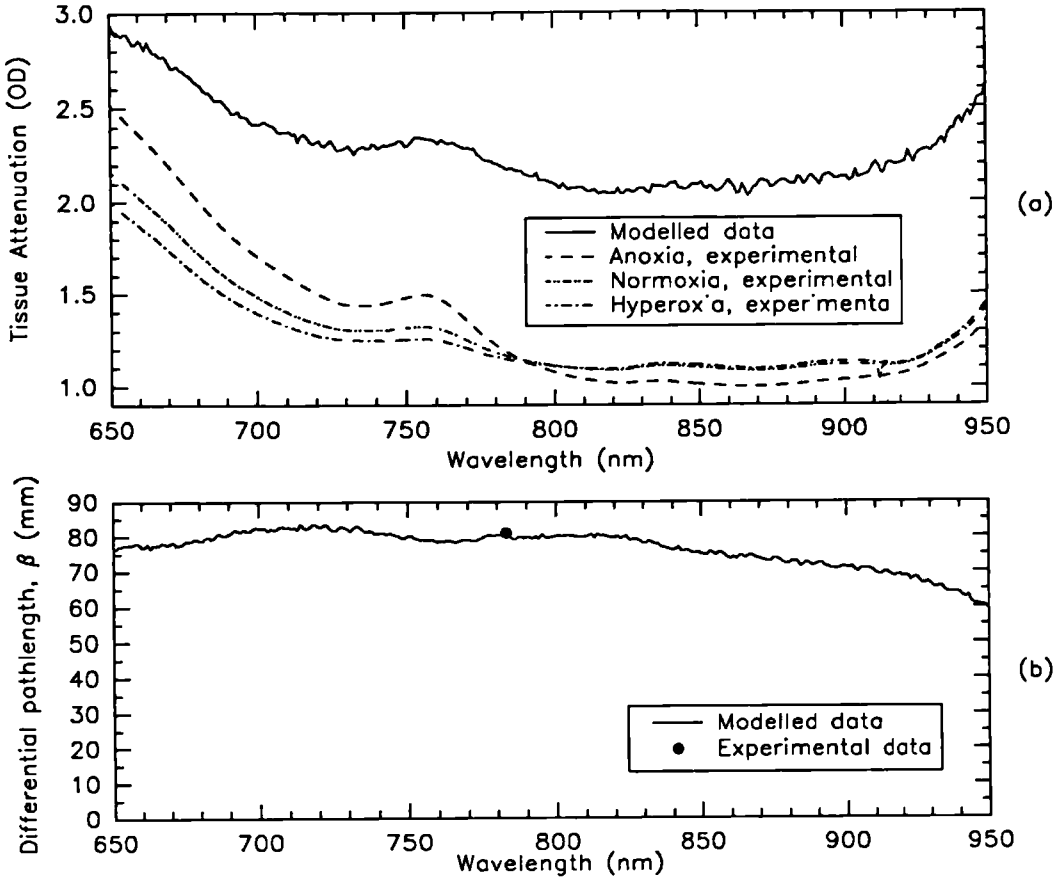

Figure 7.14 Comparison of diffusion equation modelled tissue attenuation and differential pathlength with experimental data.

brain in hyperoxia, normoxia and anoxia†. The offset in attenuation between the measured and calculated spectra is arbitrary. The normoxic attenuation spectrum was the closest match to the modelled attenuation spectrum. Unfortunately the state of haemoglobin oxygenation in the rat brain slice used for the μ_a, μ_s' measurements was not known. The brain was 28 hours post mortem and had been stored in oxygenated saline at 4°C before the measurements were made. Taking into account the different conditions under which the data were measured and the preliminary nature of the μ_a and μ_s' data, there was a good agreement between the measured and calculated attenuation spectra. The second test was a comparison of the differential pathlength. The DP was calculated using the diffusion approximation, Equation 7-33, and the experimentally measured μ_a and μ_s'. The results are shown in Figure 7.14(b). They indicate

† An optical fibre coupled spectrophotometer was used with optical fibres placed on opposite sides of the head and directly against the parietal bones, after removal of the surface tissues.

a 20% variation of the DP in the spectral region 650-900 nm. Larger variations were predicted at shorter and longer wavelengths primarily because of absorption by haemoglobin and water respectively. The modelled value of the DP at 783 nm was 79 mm and was nearly identical to the experimentally determined value of 81 mm measured using mean time of flight techniques, on 24 hour post mortem rat brain, see Table 7.i.

The good agreement shown here between the modelled and experimentally measured tissue attenuation spectra and differential pathlength was encouraging and suggested that the above method lead to results which were consistent with the available experimental data.

7.3.3 Results

The same two data sets used in Section 7.1.3 were reanalysed to see if the application of a wavelength dependent DP and a non-linear attenuation/extinction coefficient relationship could improve upon the value of the SSE^* determined in Section 7.1.3.

Stage I of the algorithm was performed as described in Section 7.3.1. Stage II , the weighted multilinear regression was identical to that covered in Section 7.1.3, using the same wavelength range, the same raw input data (ΔA) and extinction coefficient table. Only the input data (ΔK) was different.

The results for the nitrogen dip data are shown in Figure 7.15 while those for the bicuculline administration are given in Figure 7.16. The format of these figures is identical to that of Figure 7.2 and Figure 7.3. Note that the fixed optical pathlength of 7.82 cm used in Section 7.1.3 represented the average pathlength value between 700 and 900 nm of Figure 7.14(b). Hence the nitrogen dip data in Figure 7.15 and Figure 7.2 and the bicuculline data in Figure 7.16 and Figure 7.3 can be compared quantitatively.

The nitrogen dip data of Figure 7.15 showed an almost identical response to Figure 7.2 for both the haemoglobin and cytochrome signals. The main difference was the magnitude of the cytochrome reduction which was slightly larger for the provisional algorithm compared to the improved algorithm. The SSE^* for the improved algorithm was much less than that for the provisional algorithm. During the large attenuation changes, the SSE^* increased by a factor of 2.5 above the $\mathcal{E}(SSE^*)$ when using the improved algorithm, but by a factor of 6 with the provisional algorithm. Hence performing the non-linear conversion greatly reduced the systematic error in the regression. This improvement was also visible when the residual spectra in the top boxes of Figure 7.15 and Figure 7.2 were compared. The R^2 values with the

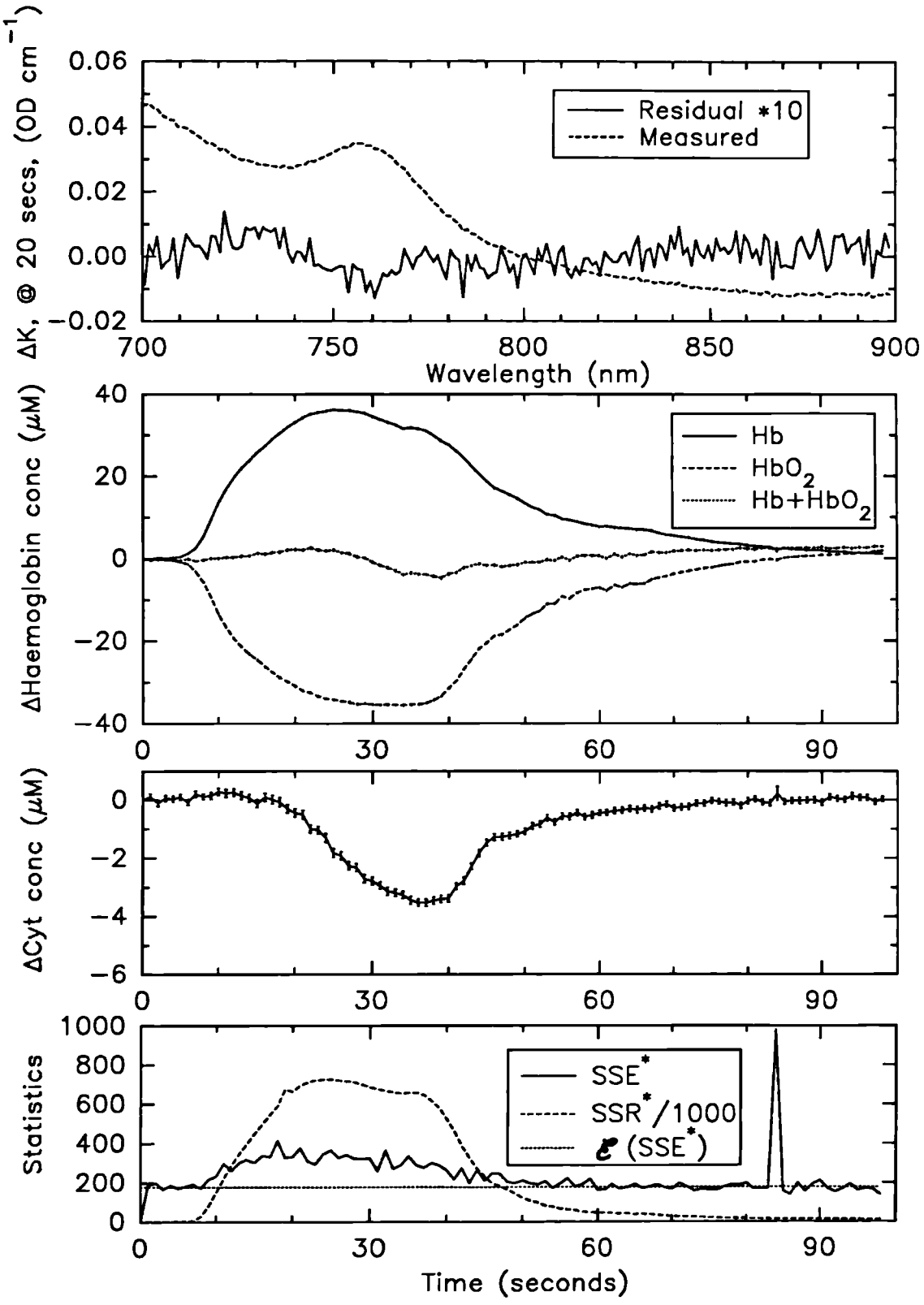

Figure 7.15 Test of the improved "non-linear" algorithm using a data set measured across a rat head during a dip in the inspired oxygen level to 0%.

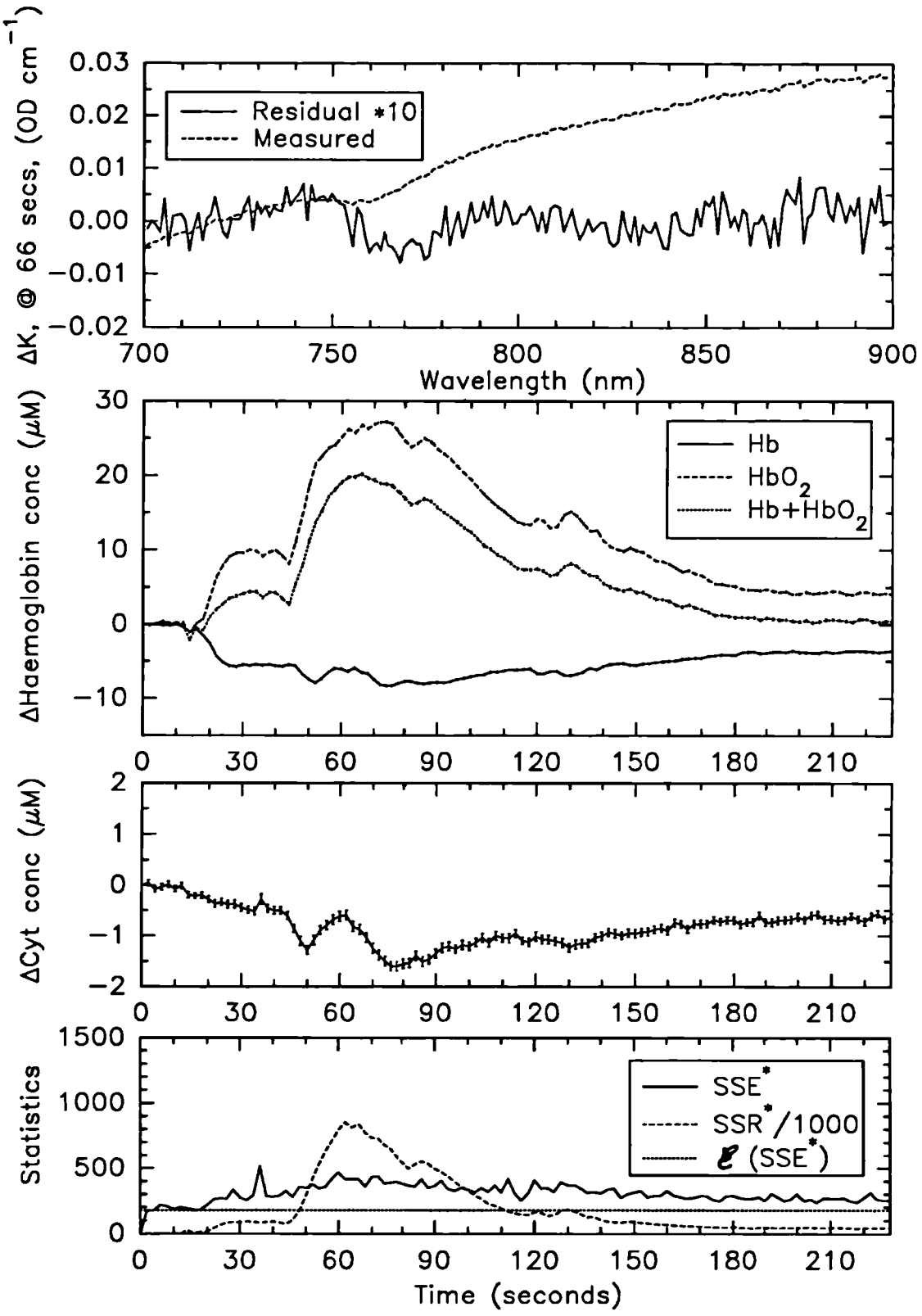

Figure 7.16 Test of the improved "non-linear" algorithm using a data set measured across a rat head when the animal had seizures caused by an injection of bicuculline.

improved algorithm were greater than 0.999.

The SSE^* for the non-linear bicuculline data in Figure 7.16 showed a similar pattern to that for the nitrogen dip, with a significantly improved SSE^* for the non-linear analysis compared to the linear analysis in Figure 7.3. However, in this data set there were large differences in the cytochrome data between the linear and non-linear cases. Based on the statistical evidence of the magnitude of the SSE^*, the non-linear method is a significantly more accurate technique for NIR data analysis.

It is interesting to note the independence of the cytochrome and haemoglobin signals. In the nitrogen dip, cytochrome became reduced at a much later time than haemoglobin became deoxygenated, indicating that in the anaesthetised adult animal cytochrome reduction is largely unaffected by oxygen availability down to very low concentrations. The bicuculline data indicated a general reduction of the cytochromes following the injection, but with a period of increased oxidation which coincided with the increased EEG activity and seizures.

7.4 DISCUSSION ON DATA ANALYSIS METHODS

The non-linear conversion of attenuation to extinction coefficient in the improved algorithm significantly improves the residuals generated by the multilinear regression analysis. Ideally the SSE^* should follow the $\mathcal{E}(SSE^*)$ and be independent of the SSR^* which would lead to the residual extinction coefficients exhibiting a random variation about zero. This is obviously not the case for the linear conversion where the SSE^* follows the SSR^*, but is vastly improved in the non-linear case. It is therefore apparent that the basic approach of the improved algorithm appears to be successful, but that further work is required which may possibly lead to: refinements of the values of μ_a and μ'_s; refinements of the specific absorption coefficients; or modifications to the diffusion approximation to more closely match the physical situation.

The magnitudes of the micromolar changes in HbO_2, Hb and Cyt are all within a physiologically reasonable range. In Figure 7.15, the nitrogen dip data, a 36 μM drop in HbO_2 and a 3.5 μM drop in Cyt occur. The Cyt value is only fractionally higher than that reported for adult rat brain[25].

The haemoglobin concentration signals are largely but not completely insensitive to the choice of the linear or non-linear conversion methods. The same is not however true of the calculated cytochrome concentrations. However it is interesting to note that in the nitrogen dip data, the cytochrome signals differed by only a small degree with the different conversion methods, whereas they differed significantly in the bicuculline administration data. In the nitrogen dip data, the analysis had only to separate the (HbO_2–Hb) and the Cyt spectra since there were minimal blood volume changes. In the bicuculline data the analysis had also to cope with large changes in blood volume, mainly an HbO_2 increase. The separation of the two similar spectra of HbO_2 and Cyt, may be much more difficult in the presence of systematic errors. Note that the error bars on the cytochrome displayed in these figures are much smaller than the actual difference in the cytochrome traces obtained using the two different algorithms. This reinforces the point that the error bars must be viewed with caution in the presence of systematic errors in the model.

7.5 DATA ANALYSIS PROBLEMS

The non-linear algorithm has the capability, given the correct information, of taking into consideration a differential pathlength which is both wavelength dependent and extinction coefficient dependent. Leaving only a few remaining problems with the data analysis. These will be addressed in turn.

7.5.1 OPTODE movement

Developing an algorithm that can compensate for changes in OPTODE separation is an interesting problem, for which currently there is no solution. The diffusion equation approximation can obviously describe what happens to tissue attenuation and this may be the best approach. However, currently it is best to minimise the possibility of OPTODE movement. The developing interest of obstetricians in monitoring cerebral oxygenation during delivery makes seeking a solution to this problem all the more urgent since OPTODE movement on the fetal scalp during labour will be difficult if not impossible to prevent.

7.5.2 Additional compounds

The only evidence of an additional absorbing compound arose in Section 6.2.3.3. Towards the end of the reduction in rat brain oxygenation what appeared to be an additional unexpected spectral response was observed. It was speculated that it might be associated with the binuclear centre of cytochrome c oxidase. Fortunately its extinction coefficient change was small, compared to the main cytochrome signal and it occurred after the primary reduction of the cytochrome enzymes. It should therefore pose only minimal problems but ideally it should be investigated further.

7.5.3 Changes in scattering coefficient

This factor poses the largest theoretical difficulties in the near infrared data analysis methods. There are a number of possible sources of scattering changes namely changes in red blood cell density (blood volume), mitochondrial volume and intracellular and extracellular volumes. This section looks at some of the relevant literature but the solution to this problem would form a new research project on tissue scattering coefficient changes and their effects upon tissue attenuation.

7.5.3.1 *Red blood cells*

One possible source of scattering coefficient changes in brain tissue is variation in the red blood cell density in the tissue. An increases in blood volume would mean a higher red cell density and therefore a higher tissue scattering coefficient. What is difficult to predict is the effect this that will have upon tissue attenuation. Section 3.2.3 showed that red blood cells form only a small fraction of the total brain scattering coefficient whereas they are a major part of the brain tissue absorption coefficient. Hopefully therefore, the only measurable effect of red cell density variation will be caused by their absorption and not their scattering properties. However, this source of uncertainty requires investigation.

7.5.3.2 Brain tissue

Section 6.2.3.3 indicated that some cerebral NIR spectral changes observed in the haemoglobin free rat brain at death may be caused by a scattering increase. Separate studies in thin slices of brain cortex confirm that changes in light scattering occur in conjunction with membrane depolarisation[130]. In a similar manner perfused retinas show a scattering decrease when the osmolarity of the suspending medium is reduced (and vice-versa)[274]. In fact this is a rather common observation, not only in tissue sections but also in mitochondria[275], erythrocytes[276] and the axons of crustacea[277] and appears to be related to cell (or organelle) volume. Increased volume, resulting from osmosis, generally leads to decreased scattering. Interestingly, when membrane depolarisation in the isolated perfused retina is initiated via spreading depression†, a scattering increase is observed[274] which is opposite to the scattering decrease observed in cortical slices[130]. This is despite evidence of an increase of intracellular volume and the presence of all the other electrolyte changes associated with membrane depolarisation. This discrepancy was commented upon by the author who added that the exact origin of the scattering changes in tissue was not known.

There are a number of possible explanations as to why the two observations above do not agree but none are conclusive. The studies were on different species and different excitable tissues, one was studied in reflectance (180°) the other at approximately 45°. Also it is not known whether the experimental situations were akin to single or multiple scattering as data on the tissue thicknesses were not given. Work performed on the basic optical effects observed in the crab nerve trunk and the isolated giant squid axon may provide some answers.

Changes in light scattering occur with the action potential. The magnitude of these changes are typically reported to be between 10^{-5} and 10^{-4} of the resting scattering amplitude[278 279 280]. These early studies were performed on the leg nerve trunks of crabs which are approximately 0.5 mm in diameter, containing individual nerve fibres of mean diameter 2 μm, many of which are "unmyelinated".

The origin of one scattering changes was found in studies performed on isolated giant squid axons. Scattering changes were observed to be somewhat slower than the action potential, and their magnitude was found to be proportional to the integral of the current flow

† Spreading depression is a wave of membrane depolarisation which can be initiated by a local disturbance, possibly mechanical, or chemical, and which results in biochemical effects similar to those observed in anoxia.

across the membrane[281]. The resting scattered intensity from a giant squid axon (myelinated) is, like that of thin slices of brain tissue, highly forward peaked[282]. Scattering changes were measured at three scattering angles, 10°, 25° and 90° and different scattering characteristics were found for each angle. The most obvious feature was that changes in 90° scattering were always of opposite sign to that of scattering of 10° and 25° (at normal extracellular refractive index), the magnitude of $\Delta I/I_r$ at 90° was 10 times larger than that at small angles[281]. Current flow into the cell produced decreased scattering at 10° and 25° and increased scattering at 90°, outwards current flow produced scattering changes of opposite signs. Furthermore, the time course at each of the 3 angles was different. At 25° the scattering change followed the time course of the integral of membrane current through the current pulse, then returned towards the baseline with a time constant of approximately 10 ms. At 90°, the response was much slower with an initial delay followed by a rise with a time constant of 2-3 ms, then falling with a time constant of ≈ 94 ms. Although the scattered intensity at this angle did not follow the integral of membrane current, its peak intensity was directly proportional to the current integral. Unlike 25° scattering, light scattering at 10° did not reach its peak until after the passage of the current, and then decayed to the baseline with a very long time constant (greater than 150 ms). This was the only angle at which scattering was affected by changes in the extracellular refractive index. The different responses of scattering angles may well account for the conflicting scattering changes seen by other authors on brain slices and the retina.

Explanation of these observations is difficult and inconclusive. Cohen makes much of the periaxonal region, a 10 nm gap between the axon membrane and the Schwann cell. Cohen's explanation for the observations at 90° states that the periaxonal space is responsible for these effects. The periaxonal space swells/shrinks in response to outward/inward currents resulting in a decrease/increase in scattering. This interpretation is a possibility but a more logical explanation would be that the origin of this effect is the very small particles (less than 200 nm), such as neurofibrils, microtubules, granules etc. within the axoplasm. These are Rayleigh scatterers, whose scattering properties are proportional to axoplasm refractive index and hence independent of external refractive index. Scattering by these particles should increase as the axoplasm is diluted by osmosis. For an inward membrane current flow, axons would swell, water following the ion movement, decreasing intracellular refractive index and therefore increasing scattering by axonal inclusions. The opposite effect would occur for an outward current flow.

The scattering effects described above have been shown to be associated with the movement of ions during an action potential. Upon anoxia large movement of ions also occur in the brain[283] equivalent to a net inward current. By comparison with the data above this would be expected to produce an increase in large angle scattering and a decrease in small angle scattering. Over many millimetres of tissue the increase in large angle scattering would tend to dominate over the decrease in small angle scattering producing an overall increase in scattering. These effects may well account for the observations seen at cell death in Section 6.2.3.3.

7.6 CLINICAL RESULTS

At University College Hospital over two hundred infants have now been studied and many clinical publications have arisen from the use of the clinical NIR spectrophotometer described in Chapter 5 and the commercial instrument which has since replaced it (NIR1000, Hamamatsu Photonics K.K., Japan). A list of these publications is given in Appendix C. Two of these papers are particularly important because they describe how **absolute** cerebral blood volume[157] and **absolute** cerebral blood flow[284] can be derived.

In this section two sets of data are used to demonstrate two different clinical situations and illustrate how the measured ΔHb, ΔHbO_2 and ΔCyt data can be interpreted. A separate monitor of arterial oxygenation (either S_aO_2 or p_aO_2) was recorded during the NIRS measurements together with arterial carbon dioxide partial pressure. The clinical details of the infants on whom this data has been measured are in Table 7.ii. The provisional algorithm was

Table 7.ii Relevant clinical details of two infants studied using the clinical spectrophotometer, whose data is described in this section.

	Sex	Gestation (weeks)	Age at study (days)	Birth weight (kg)	Clinical diagnosis at birth	Ultrasound appearance at birth	Outcome at 4 years
Figure 7.17	M	30	2	1.6	Hyaline membrane disease, Pneumothorax	Normal	Normal
Figure 7.19	M	39	4	2.7	Meconium aspiration, Listeria septicaemia	Normal	Normal

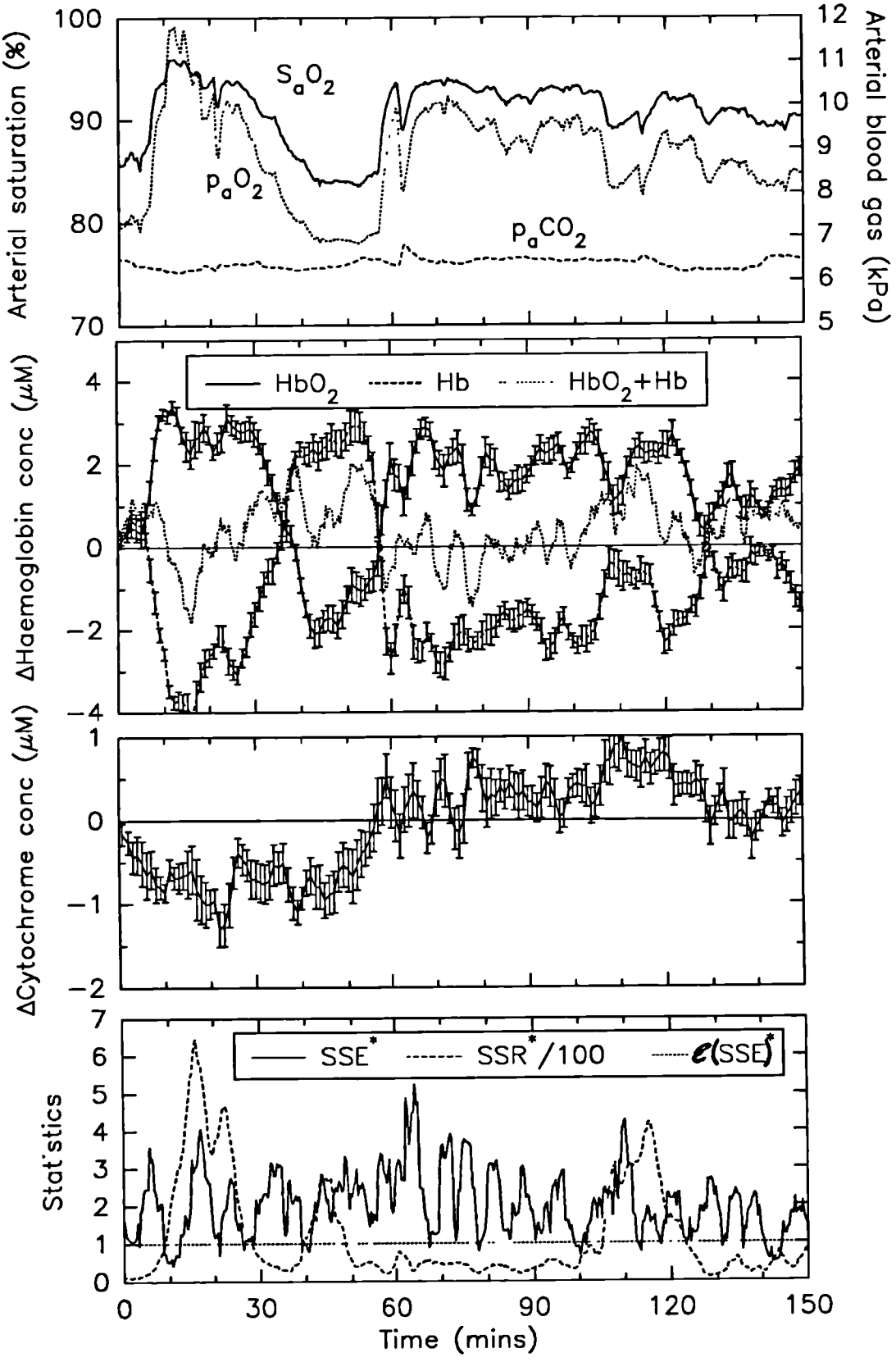

Figure 7.17 Results of a changes in arterial saturation upon the concentration of haemoglobin and cytochrome in the brain of a newborn infant.

used to analyse the data with a fixed differential pathlength factor of 3.85[269]. It was likely therefore that some inaccuracies would still occur with the newborn infant cytochrome data, but no reliable values of μ_a and μ'_s for neonatal brain were available. The regression analysis was weighted for the variance of the measured attenuation changes at each wavelength as described in Section 7.1.1.2 using the specific extinction coefficients in Appendix B. The results are presented in Figure 7.17 and Figure 7.19 in a similar manner to those previously measured on the head of the adult rat. Error bars on the ΔHb, ΔHbO_2 and ΔCyt traces represented one standard deviation based on the variance-covariance matrix and the actual SSE^* of the regression analysis (not $\mathcal{E}(SSE^*)$, the estimated SSE^* based on the input data variance which in this case was unity).

Figure 7.17 showed the simple case of slow variations of arterial saturation within the range of 85% to 95%. The data was smoothed with a time constant of 3 minutes to reduce the noise level. Arterial saturation (S_aO_2) was calculated from Equation 1-2 using measured p_aO_2 values from a transcutaneous arterial oxygen sensor. The blood volume ($HbO_2 + Hb$) remained relatively constant as Hb and HbO_2 went in equal and opposite directions with

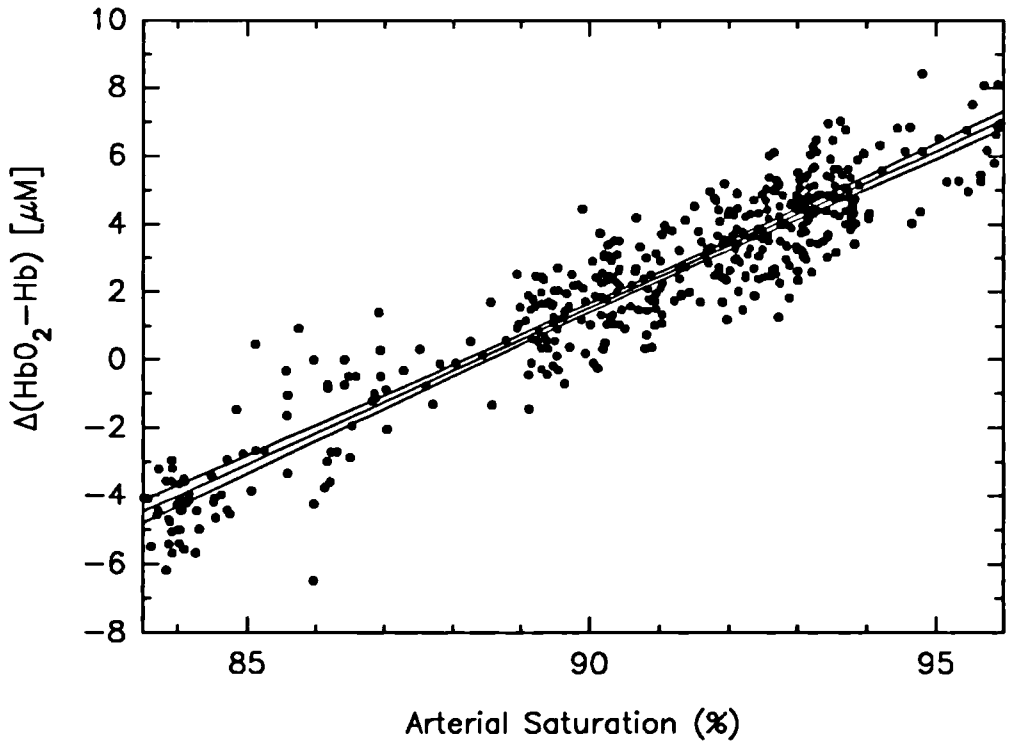

Figure 7.18 The relationship between the NIRS blood oxygenation index (HbO_2–Hb) and the S_aO_2 data in Figure 7.17 with its regression line and 99% confidence limits.

changes in S_aO_2. The small variation in blood volume was expected because of the relative stability of the p_aCO_2 trace. The cytochrome trace is discussed separately later.

Figure 7.18 shows the HbO_2–Hb data (NIRS blood oxygenation index) and the S_aO_2 data from Figure 7.17 plotted against each other. A linear relationship between these two independently measured parameters was found. The slope of the linear regression line through the data has been used to calculate the absolute haemoglobin concentration[157] using:

$$Hb_t = \frac{\Delta(HbO_2 - Hb)}{2\,\Delta S_aO_2} \qquad [\mu M] \qquad 7\text{-}34$$

where ΔS_aO_2 should be expressed as a fraction (<1.0) and not as a percentage. From this figure the absolute blood volume was calculated to be 41 μM. This appeared to be a typical value for the newborn infant, see Ref. 6 Appendix B, and is approximately half the value quoted earlier for the adult and fractionally smaller than that quoted for the newborn piglet (see Section 1.2.4). Here, the measurement of arterial saturation proved itself to be important for two reasons: firstly it allowed the quantification of absolute haemoglobin saturation; and secondly it allowed the conclusion to be reached that the data represented a normal physiological response to a change in arterial haemoglobin saturation.

Figure 7.19 shows a more complex situation when the arterial carbon dioxide concentration (p_aCO_2) of a term infant changed markedly Note that problems were encountered with the arterial blood gas sensors, hence the gaps in the data, and that the NIRS data was smoothed with a 100 second time constant.

The blood volume data followed the p_aCO_2 data closely and this was the expected physiological response in a normal brain. Additionally, we have found that in the birth asphyxiated infant the CO_2 responsiveness was often lost in the first few days of life. Note that the change in blood volume was almost completely due to changes in HbO_2, Hb was almost a constant during the p_aCO_2 changes. This observation was explained by the fact that CO_2 increased cerebral blood flow and blood volume by dilation of the arteriolar system, which of course, contained arterial blood.

Summarising the interpretation of the haemoglobin traces discussed above:

i) an increase in arterial oxygen saturation causes an equal increase and decrease in the cerebral HbO_2 and Hb concentration respectively (and vice versa).

ii) an increase in cerebral blood flow leads to an increase in cerebral blood volume which

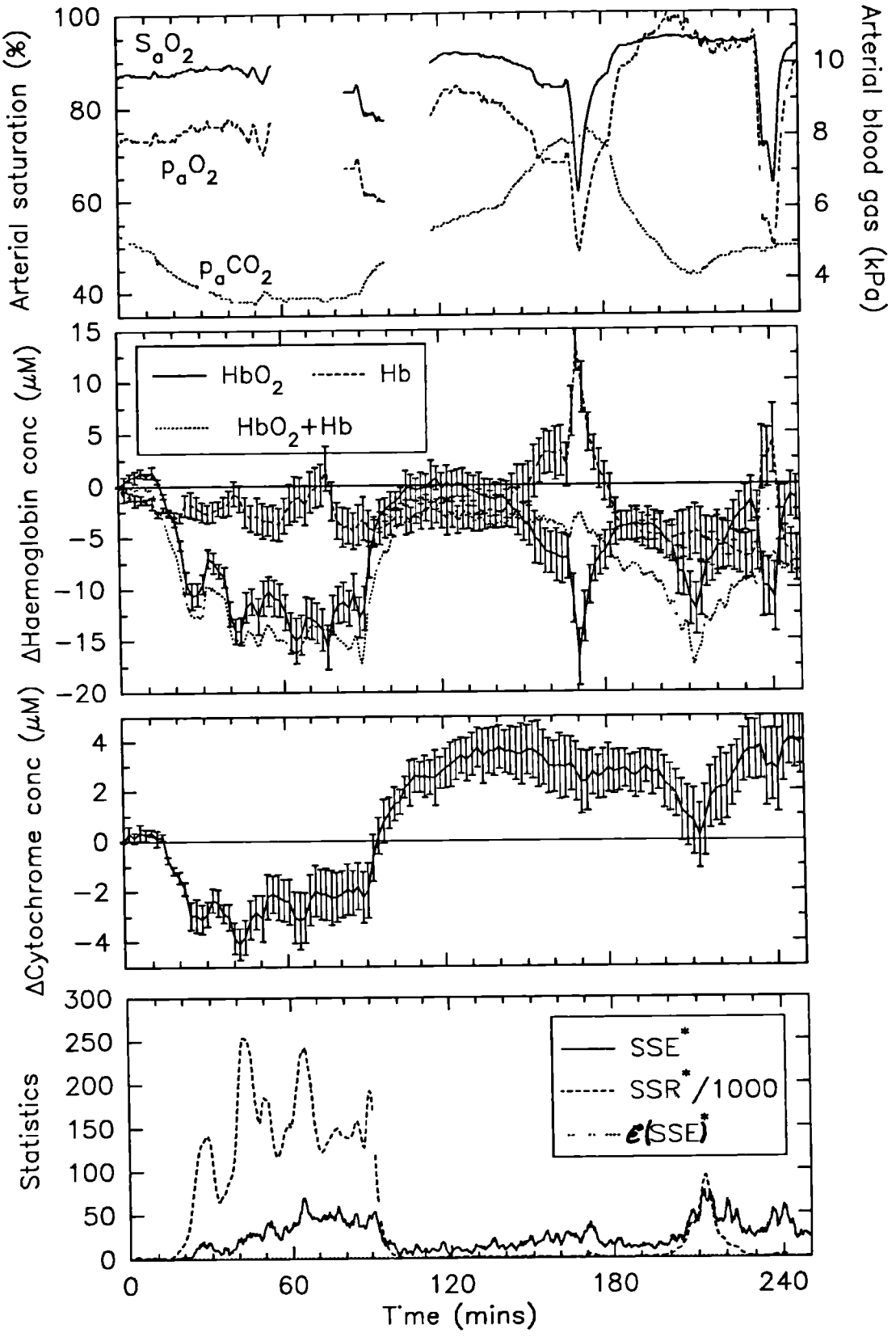

Figure 7.19 Results of large variations in p_aCO_2 upon the concentration of haemoglobin and cytochrome in the brain of a newborn infant.

is largely taken up by the HbO_2 concentration (and vice versa).

Additionally:

iii) an increase in cerebral oxygen consumption would lead to an equal decrease and increase in the cerebral HbO_2 and Hb concentration respectively (and vice versa). Note that an arterial saturation monitor would allow this effect to be differentiated from case (i) above.

iv) an increase in blood pressure in the venous system (i.e. blocking venous return) would lead to an increase in blood volume in the venules, a much larger fraction of which would be made up of Hb in comparison with case (ii) above. Deliberately increasing venous pressure has been suggested as a method of measuring absolute venous saturation[157].

With these methods of interpretation it has been possible to investigate many clinical situations and the effects of drugs upon cerebral haemodynamics, see the references in Appendix C.

The cytochrome trace in Figure 7.17 showed variations which broadly followed but did not exactly match those of the HbO_2 trace. This result would not have been predicted from the previous rat data which showed that cytochrome did not become significantly reduced until the HbO_2 trace had dropped 30 μM from normoxia. However, there is the possibility that the brain of this infant was abnormally perfused or that the response of the newborn is different to that of the adult rat.

The cytochrome trace of Figure 7.19 showed very large variations of redox state which tracked the p_aCO_2 and blood volume traces. The direction of the cytochrome redox change with CO_2 found here would have been predicted from the earlier literature survey on the effect of pH on the mitochondrial cytochrome redox state. Also the magnitude of the blood volume drop in the first 90 minutes was very large 15 μM, in 50 μM and hence a lower cytochrome redox state would be consistent with these events. However these redox state changes were very large, a range of 6 μM, and larger than the expected concentration of cytochrome enzymes in neonatal brain tissue. Hence there is still some doubt over the accuracy of these cytochrome traces and further work is required on the remaining uncertainties of the data analysis before unequivocal proof of the accuracy of the cytochrome data can be shown.

The *SSE* of Figure 7.17 was only a factor of two larger than the $\mathcal{E}(SSE)$ indicating a low systematic error. However the *SSE* of Figure 7.19 was very large and hence the degree

of systematic error in the model was significantly worse. In general, the provisional algorithm appeared to generate the largest systematic errors when fitting data which contained large shifts in blood volume compared to large desaturations of haemoglobin. Hopefully, the application of the improved algorithm using the diffusion model for light propagation in tissue to the newborn infant brain and the advent of clinical NIR spectrophotometers that can measure the differential pathlength in real time at all wavelengths will cure this problem.

CONCLUDING REMARKS

The project has on the whole been a successful one. A clinically useful instrument has been designed and constructed and from this prototype, two commercial instruments have now been manufactured through a collaboration between UCL and Hamamatsu Photonics K.K., (Japan) the NIR1000 and the NIR500. To date, ten NIR1000 instruments have been constructed and are being used in hospitals worldwide both in clinical trials and general use. A more compact version of the instrument, the NIR500, will be available in the next few months.

Data analysis has been approached in a scientific manner and a non-linear data analysis procedure derived based upon the differential pathlength. Currently the analysis relies upon the use of the diffusion approximation and separately measured μ_a and μ'_s data, which unfortunately are not currently available for the newborn infant brain. However values should be available soon. Future NIR instruments using time of flight or phase modulation measurements will be able to measure in real time both changes in tissue attenuation and the differential pathlength of each wavelength. This will a make prior knowledge of tissue thickness, μ_a and μ'_s and the use of the diffusion approximation unnecessary.

The major remaining uncertainties relate to changes in tissue scattering coefficient and this problem requires further investigation.

All the direct spectroscopic data in this thesis relate to measurements of **changes** in chromophore concentrations. The overall goal is still to produce **absolute** chromophore concentration measurements. Again, time of flight instruments offer the best possibilities of achieving this goal[285].

A further obvious extension of this work is the localisation of the volume of brain tissue under study and the imaging of the distribution of chromophore concentrations in the brain. This thesis has not discussed the question of the volume of brain tissue interrogated by the NIR light, but it can probably best be defined as a fat fuzzy banana shaped region placed between the OPTODES[286]. There is a large amount of work taking place in the field of near infrared imaging which examines the localisation problem[287 288 289 290 291 292].

APPENDIX A

MONTE CARLO SIMULATION OF PULSE PILE-UP ERROR

A computer program was written in the 'C' language which simulated the pulse pile-up error observed in photon counting photomultiplier tube systems. The basic flowchart of the program is shown in Figure A.1. The PMT deadtime τ_p and the discriminator deadtime τ_d are the characteristics of the detector, the light pulse length is t_p and n_p is the mean photoelectron generation rate at the detector during the period of the light pulses. The photoelectron generation rate is assumed to be zero at all other times. The precision of the Monte Carlo simulation depends upon the number of photoelectrons detected and the required number of detected photoelectrons (N_r) is also entered as an input parameter. The time variable (t) measures time from the beginning of each new light pulse.

The time between light pulses was assumed to be greater than both τ_p and τ_d so that the detector was always ready to accept the first photoelectron of any light pulse. This was achieved by setting the time of the last photoelectron (T_{lp}) and the time of the last detection (T_{ld}) variables to a number less than $-\tau_p$ and $-\tau_d$ respectively at the beginning of each new light pulse. N_i counted the number of input photoelectrons, N_d counted the number of these input photoelectrons which were detected and N_p the total number of light pulses. The simulation ended when N_i exceeded N_r at the end of a light pulse.

The photon statistics of the arrival of the photons were assumed to be Poissonian and originating from a non-polarised random light source. The cumulative probability function for the time between photoelectrons was then given by

$$F_0(t) = 1 - e^{-n_p t} \qquad \text{A-1}$$

Equating F_0 to a random number, which is evenly distributed between 0.0 and 1.0, gave the time to the arrival of the next photoelectron

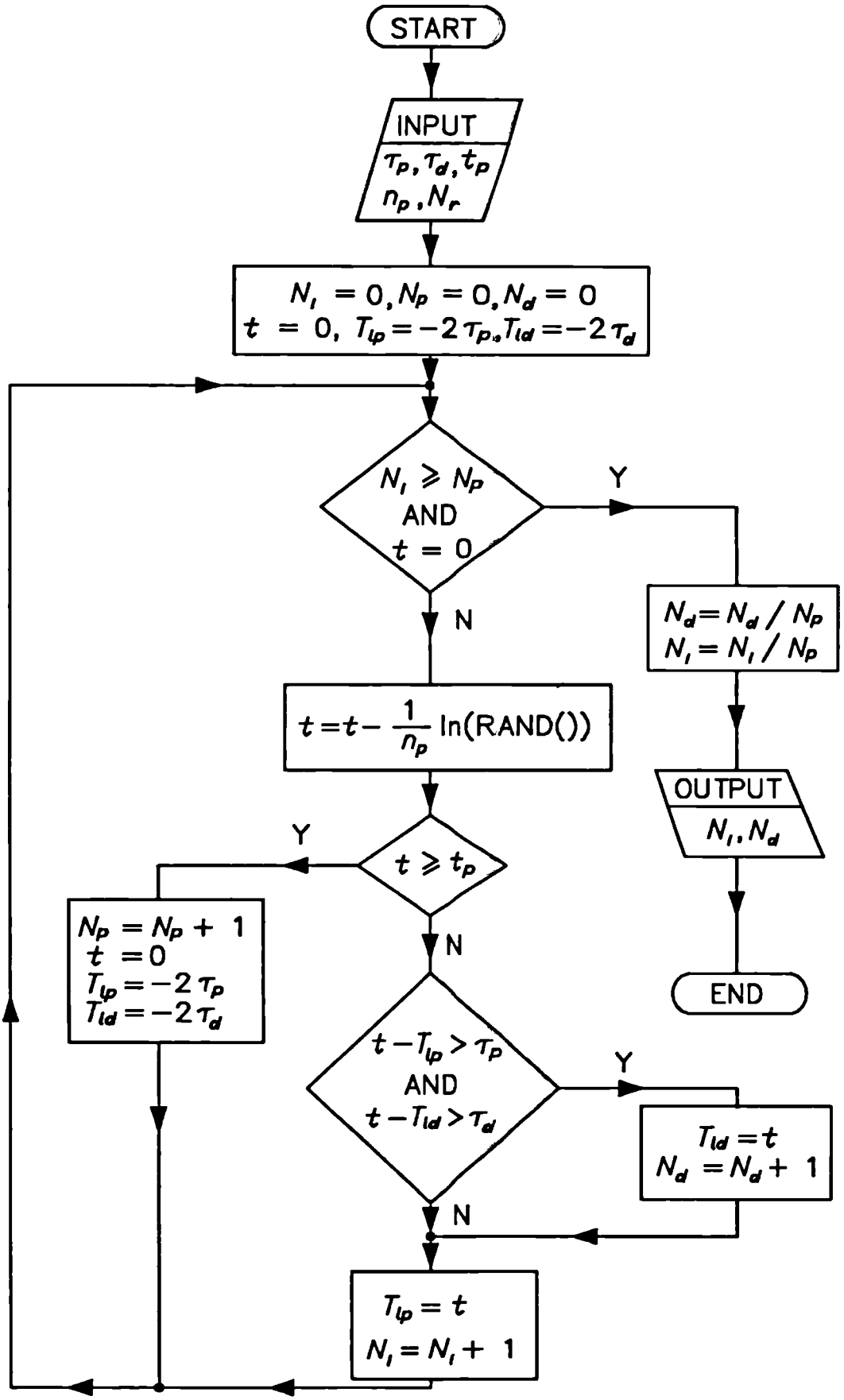

Figure A.1 Flowchart of program for the Monte Carlo simulation of pulse pile-up error in a photon counting detector.

$$t_n = -\frac{1}{n_p}\ln(\text{RAND}) \qquad \text{A-2}$$

The time of the next photoelectron was calculated using Equation A-2 and tested to see if it fell within the period of the light pulse, If it did, the program then checked to see if it would have been detected based upon the last photoelectron arrival and the last detection time. See Figure A.1 for the program details.

Monte Carlo simulations were performed for the photon counting detector used in this thesis ($\tau_p = 30$ ns, $\tau_d = 109$ ns) and for light pulse lengths (t_p) between 100 and 240 ns at 10 ns steps. The mean input photoelectron rate (n_p) was varied between 10^5 and 10^9 s^{-1} with 99 points per decade and the accuracy (N_r) was set for 100000 photoelectrons. The simulations took 48 hours of CPU (Central Processing Unit) time on a SUN4 workstation (Sun, USA).

Figure A.2 shows the results of the Monte Carlo simulation together with experimentally measured data from a 100 ns pulse width (FWHM) LA-68 laser diode and a 185 ns pulse width (FWHM) LA-8 laser diode, the experimental details have been described in Section 5.11.3.1. The simulated data in Figure A.2(a) showed the expected response, with increased optical pulse width leading to a lower pulse pile-up error at the same input photon per pulse rate and the 100 ns simulation followed the exponential response predicted by Equation 5-11.

Figure A.2(b) showed that the noise on the experimental data was high at the low photon per pulse rates. However, the simulated data was a good approximation to the experimental data. The 100 ns pulse width experimental data only deviated at very high rates, probably because it was a non rectangular pulse which was wider than 109 ns at its base. The experimental results of the 185 ns, LA-8, laser diode did not exactly follow a single curve in Figure A.2. The data peaked at a lower photon per pulse value and most closely matched the Monte Carlo simulation of the 170 ns optical pulse width. There could be a number of reasons for this, but the most likely reason was that the Monte Carlo model was an over simplification of the PMT, the amplifier and the discriminator characteristics. For example, the Monte Carlo simulation assumed that all pulses (optical and electronic) were square and of the same height and shape, while this was far from the case in reality. However the 170 ns simulated optical pulse results were a good approximation to the data from the LA-8 185 ns pulse, so the Monte Carlo 170 ns optical pulse data was used as a look-up table to correct the clinical data presented in this thesis.

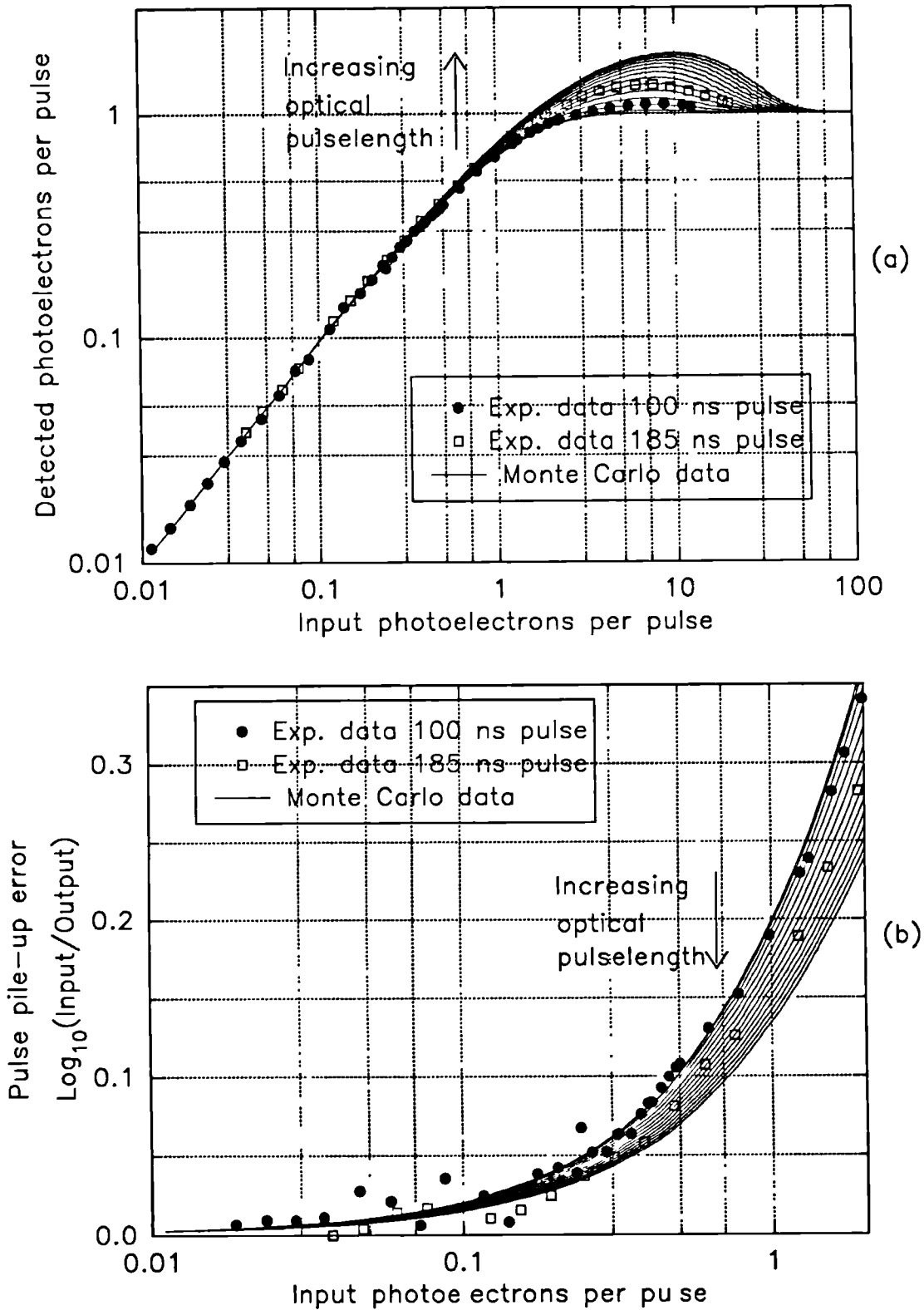

Figure A.2 Results of the Monte Carlo simulation (see the text for the simulation parameters), together with experimentally measured data. (a) Input versus output photoelectrons per pulse; (b) pulse pile-up error.

APPENDIX B

EXTINCTION COEFFICIENT TABLE FOR HB, HbO_2 AND CYT

Figure B.1 and Table B.i contain the specific extinction coefficients (measured in non-scattering solutions) that were used in this thesis for the Hb, HbO_2 and Cyt spectra. Note that the haemoglobin coefficients are quoted for a molecular weight of 64450 and hence are four times larger than values which are quoted as "per equivalent". The Cyt data represents a difference spectrum (oxidised minus reduced) not only of cytochrome c oxidase but also of cytochromes b and c. However, cytochrome c oxidase dominates the spectrum above 770 nm and the specific extinction coefficient values are quoted per functional unit of cytochrome c oxidase i.e. for 2 haem groups.

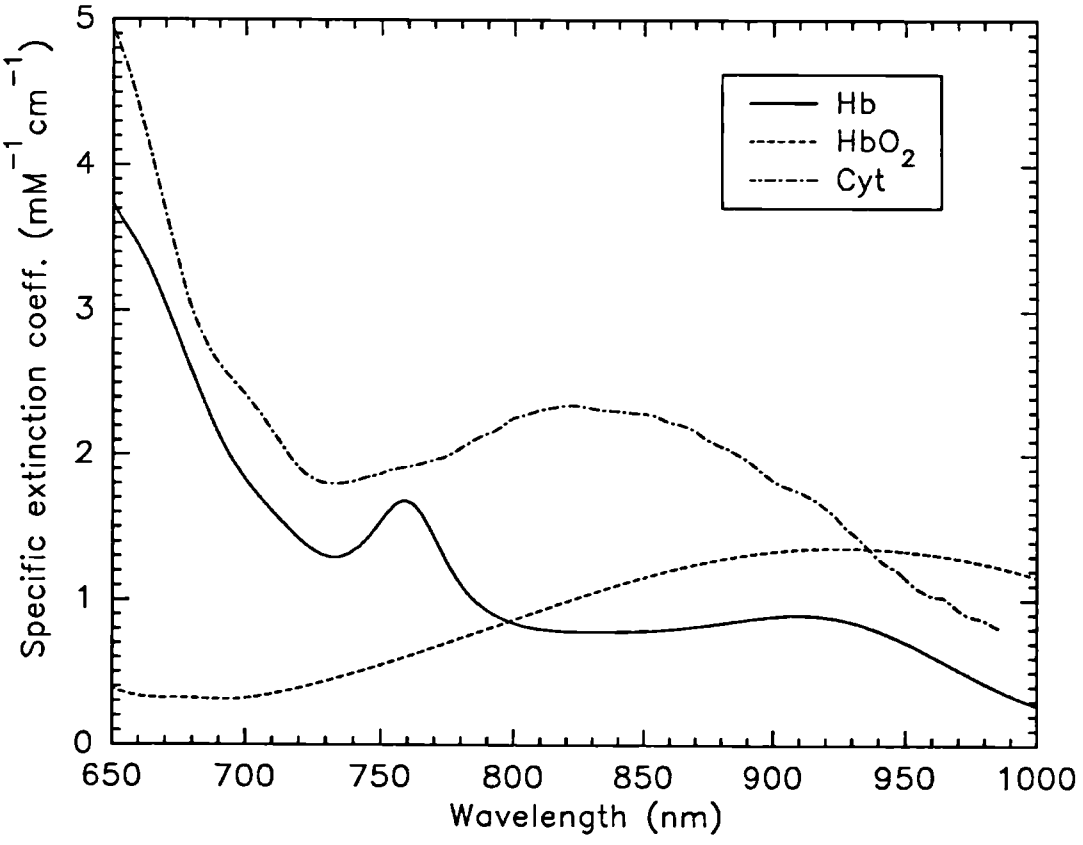

Figure B.1 Specific extinction coefficients of deoxyhaemoglobin, oxyhaemoglobin and the total tissue cytochrome enzyme difference spectrum as used in this thesis.

Table B.i Specific extinction coefficients of deoxyhaemoglobin, oxyhaemoglobin and the total tissue cytochrome enzyme difference spectrum as used in this thesis.

Wav (nm)	Hb ($Mm^{-1}cm^{-1}$)	HbO_2 ($mM^{-1}cm^{-1}$)	Cyt ($mM^{-1}cm^{-1}$)	Wav (nm)	Hb ($mM^{-1}cm^{-1}$)	HbO_2 ($mM^{-1}cm^{-1}$)	Cyt ($mM^{-1}cm^{-1}$)
650	3.7351	0.3869	4.9308	675	2.8087	0.3211	3.3224
651	3.7039	0.3793	4.8939	676	2.7606	0.3208	3.2527
652	3.6727	0.3722	4.8570	677	2.7124	0.3206	3.1841
653	3.6414	0.3659	4.8083	678	2.6652	0.3205	3.1156
654	3.6126	0.3601	4.7595	679	2.6183	0.3201	3.0562
655	3.5841	0.3545	4.7045	680	2.5713	0.3194	2.9968
656	3.5555	0.3495	4.6495	681	2.5248	0.3186	2.9496
657	3.5269	0.3451	4.5893	682	2.4788	0.3181	2.9024
658	3.4982	0.3410	4.5291	683	2.4329	0.3173	2.8623
659	3.4695	0.3376	4.4652	684	2.3870	0.3163	2.8223
660	3.4408	0.3346	4.4012	685	2.3436	0.3157	2.7859
661	3.4062	0.3318	4.3331	686	2.3004	0.3151	2.7494
662	3.3717	0.3294	4.2650	687	2.2572	0.3140	2.7180
663	3.3371	0.3276	4.1928	688	2.2162	0.3135	2.6866
664	3.2990	0.3260	4.1206	689	2.1772	0.3126	2.6597
665	3.2582	0.3245	4.0456	690	2.1382	0.3123	2.6328
666	3.2174	0.3234	3.9705	691	2.0997	0.3122	2.6093
667	3.1762	0.3227	3.8983	692	2.0656	0.3122	2.5857
668	3.1327	0.3220	3.8261	693	2.0315	0.3123	2.5662
669	3.0891	0.3216	3.7529	694	1.9974	0.3125	2.5468
670	3.0455	0.3213	3.6797	695	1.9665	0.3130	2.5240
671	2.9993	0.3212	3.6073	696	1.9370	0.3140	2.5013
672	2.9519	0.3212	3.5349	697	1.9076	0.3148	2.4806
673	2.9045	0.3214	3.4635	698	1.8791	0.3164	2.4599
674	2.8569	0.3214	3.3921	699	1.8530	0.3181	2.4376

continued ....

Wav (nm)	Hb ($mM^{-1}cm^{-1}$)	HbO_2 ($mM^{-1}cm^{-1}$)	Cyt ($mM^{-1}cm^{-1}$)	Wav (nm)	Hb ($mM^{-1}cm^{-1}$)	HbO_2 ($mM^{-1}cm^{-1}$)	Cyt ($mM^{-1}cm^{-1}$)
700	1.8270	0.3199	2.4154	725	1.3456	0.4133	1.8357
701	1.8010	0.3219	2.3922	726	1.3352	0.4181	1.8261
702	1.7777	0.3243	2.3690	727	1.3249	0.4230	1.8180
703	1.7548	0.3269	2.3438	728	1.3146	0.4281	1.8099
704	1.7319	0.3296	2.3185	729	1.3081	0.4332	1.8058
705	1.7099	0.3323	2.2955	730	1.3029	0.4383	1.8017
706	1.6887	0.3352	2.2725	731	1.2976	0.4435	1.8010
707	1.6675	0.3386	2.2446	732	1.2946	0.4488	1.8004
708	1.6464	0.3418	2.2167	733	1.2950	0.4540	1.7999
709	1.6267	0.3450	2.1889	734	1.2953	0.4593	1.7994
710	1.6070	0.3485	2.1612	735	1.2959	0.4646	1.8010
711	1.5873	0.3524	2.1362	736	1.3028	0.4700	1.8026
712	1.5677	0.3564	2.1112	737	1.3096	0.4754	1.8045
713	1.5481	0.3602	2.0821	738	1.3164	0.4811	1.8064
714	1.5285	0.3639	2.0530	739	1.3277	0.4865	1.8107
715	1.5093	0.3680	2.0255	740	1.3411	0.4920	1.8150
716	1.4907	0.3724	1.9980	741	1.3545	0.4976	1.8213
717	1.4721	0.3765	1.9736	742	1.3697	0.5032	1.8275
718	1.4535	0.3807	1.9492	743	1.3887	0.5089	1.8337
719	1.4365	0.3854	1.9274	744	1.4078	0.5147	1.8399
720	1.4197	0.3899	1.9055	745	1.4268	0.5203	1.8451
721	1.4029	0.3943	1.8879	746	1.4501	0.5259	1.8502
722	1.3875	0.3988	1.8703	747	1.4736	0.5317	1.8543
723	1.3733	0.4035	1.8578	748	1.4971	0.5376	1.8585
724	1.3592	0.4083	1.8453	749	1.5212	0.5436	1.8635

continued ....

Wav (nm)	Hb ($mM^{-1}cm^{-1}$)	HbO_2 ($mM^{-1}cm^{-1}$)	Cyt ($mM^{-1}cm^{-1}$)	Wav (nm)	Hb ($mM^{-1}cm^{-1}$)	HbO_2 ($mM^{-1}cm^{-1}$)	Cyt ($mM^{-1}cm^{-1}$)
750	1.5458	0.5495	1.8685	775	1.2481	0.7038	1.9952
751	1.5703	0.5554	1.8768	776	1.2175	0.7101	2.0037
752	1.5938	0.5613	1.8851	777	1.1870	0.7166	2.0155
753	1.6142	0.5672	1.8917	778	1.1566	0.7229	2.0273
754	1.6346	0.5731	1.8983	779	1.1298	0.7297	2.0387
755	1.6549	0.5791	1.9019	780	1.1050	0.7360	2.0500
756	1.6646	0.5856	1.9055	781	1.0803	0.7422	2.0612
757	1.6733	0.5912	1.9086	782	1.0571	0.7485	2.0724
758	1.6820	0.5974	1.9117	783	1.0372	0.7549	2.0851
759	1.6816	0.6031	1.9148	784	1.0173	0.7613	2.0979
760	1.6745	0.6096	1.9178	785	0.9975	0.7681	2.1081
761	1.6674	0.6157	1.9206	786	0.9822	0.7743	2.1183
762	1.6566	0.6219	1.9235	787	0.9668	0.7808	2.1271
763	1.6343	0.6283	1.9285	788	0.9515	0.7874	2.1360
764	1.6121	0.6345	1.9335	789	0 9385	0.7941	2.1433
765	1.5898	0.6407	1.9391	790	0.9264	0.8005	2.1506
766	1.5582	0.6469	1.9446	791	0.9143	0.8070	2.1572
767	1.5259	0.6535	1.9498	792	0.9034	0.8134	2.1638
768	1.4935	0.6596	1.9549	793	0.8939	0.8197	2.1763
769	1.4590	0.6658	1.9602	794	0.8844	0.8264	2.1887
770	1.4229	0.6720	1.9656	795	0.8752	0.8330	2.2015
771	1.3869	0.6785	1.9705	796	0.8676	0.8392	2.2142
772	1.3513	0.6849	1.9754	797	0.8600	0.8458	2.2279
773	1.3169	0.6911	1.9810	798	0.8524	0.8524	2.2416
774	1.2825	0.6974	1.9867	799	0.8461	0.8588	2.2518

continued ....

Wav (nm)	Hb ($mM^{-1}cm^{-1}$)	HbO_2 ($mM^{-1}cm^{-1}$)	Cyt ($mM^{-1}cm^{-1}$)	Wav (nm)	Hb ($mM^{-1}cm^{-1}$)	HbO_2 ($mM^{-1}cm^{-1}$)	Cyt ($mM^{-1}cm^{-1}$)
800	0.8399	0.8653	2.2619	825	0.7809	1.0211	2.3429
801	0.8338	0.8716	2.2666	826	0.7808	1.0273	2.3403
802	0.8285	0.8780	2.2713	827	0.7806	1.0333	2.3369
803	0.8237	0.8845	2.2762	828	0.7805	1.0393	2.3335
804	0.8190	0.8909	2.2812	829	0.7804	1.0449	2.3300
805	0.8146	0.8973	2.2870	830	0.7804	1.0507	2.3265
806	0.8111	0.9038	2.2927	831	0.7804	1.0564	2.3233
807	0.8075	0.9102	2.2991	832	0.7804	1.0621	2.3200
808	0.8040	0.9164	2.3055	833	0.7804	1.0680	2.3174
809	0.8014	0.9227	2.3114	834	0.7805	1.0739	2.3148
810	0.7987	0.9291	2.3172	835	0.7805	1.0797	2.3131
811	0.7961	0.9354	2.3212	836	0.7806	1.0851	2.3113
812	0.7941	0.9416	2.3253	837	0.7807	1.0907	2.3106
813	0.7922	0.9478	2.3281	838	0.7809	1.0962	2.3098
814	0.7904	0.9539	2.3309	839	0.7812	1.1018	2.3090
815	0.7888	0.9603	2.3335	840	0.7815	1.1072	2.3081
816	0.7874	0.9666	2.3361	841	0.7817	1.1128	2.3062
817	0.7861	0.9728	2.3388	842	0.7820	1.1182	2.3043
818	0.7849	0.9789	2.3415	843	0.7823	1.1233	2.3019
819	0.7842	0.9848	2.3442	844	0.7827	1.1286	2.2995
820	0.7834	0.9911	2.3469	845	0.7833	1.1339	2.2972
821	0.7827	0.9973	2.3478	846	0.7839	1.1391	2.2948
822	0.7822	1.0032	2.3486	847	0.7845	1.1442	2.2934
823	0.7817	1.0091	2.3471	848	0.7850	1.1494	2.2919
824	0.7812	1.0153	2.3455	849	0.7856	1.1547	2.2912

continued ....

Wav (nm)	Hb ($mM^{-1}cm^{-1}$)	HbO_2 ($mM^{-1}cm^{-1}$)	Cyt ($mM^{-1}cm^{-1}$)	Wav (nm)	Hb ($mM^{-1}cm^{-1}$)	HbO_2 ($mM^{-1}cm^{-1}$)	Cyt ($mM^{-1}cm^{-1}$)
850	0.7861	1.1596	2.2905	875	0.8285	1.2678	2.1029
851	0.7871	1.1645	2.2879	876	0.8310	1.2710	2.0930
852	0.7880	1.1694	2.2853	877	0.8336	1.2746	2.0846
853	0.7890	1.1742	2.2805	878	0.8361	1.2781	2.0763
854	0.7901	1.1790	2.2757	879	0.8387	1.2814	2.0684
855	0.7912	1.1842	2.2685	880	0.8412	1.2846	2.0606
856	0.7923	1.1885	2.2613	881	0.8438	1.2878	2.0530
857	0.7935	1.1934	2.2527	882	0.8463	1.2907	2.0454
858	0.7949	1.1980	2.2442	883	0.8489	1.2938	2.0359
859	0.7963	1.2026	2.2373	884	0.8516	1.2971	2.0265
860	0.7977	1.2071	2.2303	885	0.8542	1.3000	2.0164
861	0.7993	1.2114	2.2259	886	0.8568	1.3027	2.0063
862	0.8009	1.2156	2.2214	887	0.8594	1.3058	1.9959
863	0.8025	1.2200	2.2170	888	0.8620	1.3084	1.9855
864	0.8044	1.2245	2.2127	889	0.8645	1.3108	1.9725
865	0.8063	1.2286	2.2069	890	0.8670	1.3137	1.9594
866	0.8082	1.2325	2.2010	891	0.8694	1.3165	1.9467
867	0.8102	1.2367	2.1941	892	0.8718	1.3189	1.9340
868	0.8122	1.2407	2.1872	893	0.8742	1.3210	1.9203
869	0.8143	1.2449	2.1773	894	0.8765	1.3235	1.9066
870	0.8166	1.2490	2.1674	895	0 8787	1.3262	1.8916
871	0.8189	1.2529	2.1529	896	0 8807	1.3283	1.8766
872	0.8213	1.2565	2.1384	897	0 8827	1.3304	1.8619
873	0.8237	1.2601	2.1256	898	0.8846	1.3323	1.8472
874	0.8261	1.2641	2.1128	899	0.8863	1.3341	1.8343

continued ....

Wav (nm)	Hb (mM ^{1}cm ^{1})	HbO_2 (mM $^{1}cm^{-1}$)	Cyt ($mM^{-1}cm^{-1}$)	Wav (nm)	Hb ($mM^{-1}cm^{-1}$)	HbO_2 ($mM^{-1}cm^{-1}$)	Cyt (mM $^{1}cm^{-1}$)
900	0.8880	1.3365	1.8213	925	0.8691	1.3602	1.5495
901	0.8897	1.3385	1.8113	926	0.8655	1.3604	1.5292
902	0.8910	1.3403	1.8012	927	0.8613	1.3603	1.5106
903	0.8923	1.3420	1.7933	928	0.8571	1.3599	1.4919
904	0.8936	1.3435	1.7854	929	0.8528	1.3600	1.4772
905	0.8944	1.3452	1.7784	930	0.8480	1.3595	1.4625
906	0.8952	1.3467	1.7713	931	0.8432	1.3593	1.4480
907	0.8959	1.3478	1.7649	932	0.8382	1.3590	1.4335
908	0.8962	1.3496	1.7585	933	0.8324	1.3584	1.4161
909	0.8965	1.3507	1.7523	934	0.8265	1.3577	1.3988
910	0.8968	1.3514	1.7460	935	0.8207	1.3569	1.3800
911	0.8964	1.3528	1.7362	936	0.8143	1.3557	1.3613
912	0.8957	1.3542	1.7265	937	0.8080	1.3549	1.3427
913	0.8951	1.3553	1.7167	938	0.8016	1.3545	1.3241
914	0.8942	1.3562	1.7068	939	0.7945	1.3533	1.3053
915	0.8931	1.3570	1.6970	940	0.7874	1.3520	1.2865
916	0.8920	1.3578	1.6873	941	0.7802	1.3511	1.2724
917	0.8904	1.3582	1.6735	942	0.7727	1.3502	1.2583
918	0.8885	1.3587	1.6597	943	0.7651	1.3487	1.2471
919	0.8866	1.3585	1.6456	944	0.7575	1.3468	1.2360
920	0.8844	1.3590	1.6315	945	0.7493	1.3453	1.2258
921	0.8817	1.3598	1.6172	946	0.7410	1.3445	1.2156
922	0.8790	1.3602	1.6029	947	0.7327	1.3428	1.2014
923	0.8760	1.3602	1.5863	948	0.7241	1.3410	1.1871
924	0.8726	1.3602	1.5697	949	0.7154	1.3394	1.1698

continued ....

Wav (nm)	Hb ($mM^{-1}cm^{-1}$)	HbO_2 ($mM^{-1}cm^{-1}$)	Cyt ($mM^{-1}cm^{-1}$)	Wav (nm)	Hb ($mM^{-1}cm^{-1}$)	HbO_2 ($mM^{-1}cm^{-1}$)	Cyt ($mM^{-1}cm^{-1}$)
950	0.7068	1.3374	1.1525	975	0.4691	1.2692	0.8863
951	0.6982	1.3354	1.1350	976	0.4597	1.2656	0.8813
952	0.6896	1.3332	1.1175	977	0.4504	1.2624	0.8773
953	0.6810	1.3313	1.1009	978	0.4413	1.2590	0.8733
954	0.6715	1.3293	1.0843	979	0.4323	1.2549	0.8670
955	0.6616	1.3263	1.0745	980	0.4233	1.2513	0.8606
956	0.6517	1.3240	1.0648	981	0.4146	1.2470	0.8505
957	0.6420	1.3217	1.0539	982	0.4061	1.2430	0.8403
958	0.6324	1.3199	1.0429	983	0.3975	1.2393	0.8292
959	0.6229	1.3172	1.0356	984	0.3892	1.2351	0.8180
960	0.6133	1.3144	1.0282	985	0.3810	1.2305	0.8093
961	0.6037	1.3123	1.0256	986	0.3729	1.2260	0.8005
962	0.5941	1.3099	1.0229	987	0.3648	1.2219	
963	0.5843	1.3070	1.0222	988	0.3567	1.2173	
964	0.5745	1.3042	1.0215	989	0.3487	1.2133	
965	0.5647	1.3018	1.0087	990	0.3409	1.2087	
966	0.5550	1.2995	0.9959	991	0.3334	1.2043	
967	0.5453	1.2966	0.9804	992	0.3259	1.1992	
968	0.5357	1.2928	0.9649	993	0.3187	1.1939	
969	0.5261	1.2900	0.9484	994	0.3117	1.1893	
970	0.5166	1.2868	0.9319	995	0.3047	1.1848	
971	0.5071	1.2838	0.9198	996	0.2978	1.1789	
972	0.4976	1.2807	0.9078	997	0.2909	1.1733	
973	0.4880	1.2773	0.8995	998	0.2841	1.1694	
974	0.4785	1.2735	0.8913	999	0.2776	1.1637	

APPENDIX C

CLINICAL REFERENCES

1. Wyatt, J.S., Cope, M., Delpy, D.T., Wray, S., Reynolds, E.O.R. (1986) Quantification of cerebral oxygenation and haemodynamics in sick newborn infants by near infrared spectrophotometry. *Lancet*, **2**, pp1063-1066.

2. Delpy, D.T., Cope, M., Cady, E.B., Wyatt, J.S., Hamilton, P.A., Hope, P.L., Wray, S., Reynolds, E.O.R. (1987) Cerebral monitoring in newborn infants by magnetic resonance and near infrared spectroscopy. *Scand. J. Clin. Lab. Invest.*, **47, suppl. 88**, pp9-17.

3. Edwards, A.D., Wyatt, J.S., Richardson, C.E., Delpy, D.T., Cope, M., Reynolds, E.O.R. (1988) Cotside measurement of cerebral blood flow in ill newborn infants by near infrared spectroscopy. *Lancet*, **ii**, pp770-771.

4. Reynolds, E.O.R., Wyatt, J.S., Azzopardi, D., Delpy, D.T., Cady, E.B., Cope, M., Wray, S. (1988) New non-invasive methods for assessing brain oxygenation and haemodynamics. *Brit. Med. Bull.*, **44(4)**, pp1052-1075.

5. Wyatt, J.S., Cope, M., Delpy, D.T., van der Zee, P., Arridge, S.R., Edwards, A.D., Reynolds, E.O.R. (1989) Measurement of optical pathlength for cerebral near infrared spectroscopy in newborn infants. *Dev. Neuroscience.*, **12**, pp140-144.

6. Wyatt, J.S., Cope, M., Delpy, D.T., Richardson, C.E., Edwards, A.D., Wray, S.C., Reynolds, E.O.R. (1990) Quantitation of cerebral blood volume in newborn infants by near infrared spectroscopy. *J. Appl. Physiol.*, **68(3)**, pp1086-1091.

7. Edwards, A.D., Wyatt, J.S., Richardson, C., Potter, A., Cope, M., Delpy, D.T. and reynolds, E.O.R. (1990) Effects of indomethacin on cerebral haemodynamics in very preterm infants, *Lancet*, **335**, pp1491-1495.

8. Hutchinson, I.L., Cope, M., Delpy, D.T., Richardson, C.E. and Harris, M. (1990) The investigation of osteoradionecrosis of the mandible by near infrared spectroscopy, *Br. J. Oral Maxillo. Surg.*, **28**, pp150-154.

9. Cheatle, T.R., Potter, L.A., Cope, M., Delpy, D.T., Coleridge-Smith, P.D., Scurr, J.H. (1990) Near infrared spectroscopy in peripheral vascular disease, *Brit. J. Surg.*, (In Press).

REFERENCES

1. Powell, T.G., Pharoah, P.O.D. and Cooke, R.W.I. (1986) Survival and morbidity in a geographically defined population of low birthweight infants, *Lancet*, **i**, pp539-543.
2. Stewart, A.L., Reynolds, E.O.R. and Lipscomb, A.P. (1981) Outcome for infants of very low birthweight: Survey of world literature, *Lancet*, **i**, pp1048-1041.
3. Stewart, A.L., Reynolds, E.O.R., Hope, P.L., Hamilton, P.A., Baudin, J., Costello, A.M. de L., Bradford, B.C. and Wyatt, J.S. (1987) Probability of neurodevelopmental disorders estimated from ultrasound appearance of brains of very preterm infants, *Dev. Med. Child Neurol.*, **29**, pp3-11.
4. McCormick, M.C. (1989) Long term follow-up of infants discharged from neonatal intensive care units, *J. Am. Med. Assn.*, **261**, pp1767-1772.
5. Stewart A.L., Thorburn R.J., Hope P.L., Goldsmith M., Lipscomb A.P. and Reynolds E.O.R. (1983) Ultrasound appearance of the brain in the very preterm infants and neurodevelopmental outcome at 18 months of age. *Arch. Dis. Child.* **58**, pp598-604.
6. Alberman, E., (1982) The epidemiology of congenital defects: A pragmatic approach, In: *Clinics in developmental medicine, No. 83*, Eds: M. Adinolfi et al., Spastics International Medical Publications, Heinemann, (London, U.K.).
7. Fujimori, M. and Seryu, J-I (1977) Velocity of head growth during the perinatal period, *Arch. Dis. Child.*, **52**, pp105-112.
8. Pape, K.E. and Wrigglesworth, J.S. (1979) Haemorrhage, ischaemia and the perinatal brain, For: *Spastics International Medical Publications*, Heinemann (London).
9. Ganong, W.F. (1979) Review of Medical Physiology, Lange Medical Publications, California (USA).
10. Godfrey, S. (1979) *In: Clinical Paediatric Physiology*, Eds: Godfrey, S. and Baum, J.D., Blackwell Scientific Publications (Oxford, U.K.).
11. Kokholm, G. (1990) Simultaneous measurements of blood pH, pCO_2, pO_2 and concentrations of hemoglobin and its derivatives- A multicentre study, *Scand. J. Clin. Lab. Invest.*, **Suppl.**, In press.
12. Gibbs, E.L., Lennox, W.G., Nims, L.F. and Gibbs, F.A., (1942) Arterial and cerebral venous blood, arterial-venous differences in man, *J. Biol.Chem.*, **144**, pp325-332.
13. Rooth, G. (1963) Foetal respiration, *Acta. Paediat. (Stockh)*, **52**, p22-35.

14. Hoffbrand, A.V. and Pettit, J.E. (1980) Essential Haematology, Blackwell Scientific Publications, Oxford (U.K.).

15. Biological Handbooks, (1971) Respiration and Circulation, Eds: P.L. Altman and D.S. Dittmer, Federation of American Societies for Experimental Biology, Bethesda, (U.S.A.).

16. Hinkle P.C. and McCarty, R.E. (1978) How cells make ATP, *Scientific American*, **238(3)**, pp104-123.

17. Erecinska M. and Silver I.A. (1989) Review: ATP and brain function, *J. Cereb. Blood Flow. and Metab.*, **9(1)**, pp2-19.

18. Siesjo, B.K. (1978) Brain energy metabolism. Wiley N.Y (U.S.A.).

19. Bachelard, H.S. (1975) Energy utilized by neurotransmitters, In: *Brain: The coupling of function, metabolism & blood flow in brain*, Eds: D.H. Ingvar et al., Munksgaard, Copenhagen (Denmark).

20. Tzagoloff, A. (1982) Mitochondria, Plenum Press (N.Y.), p106.

21. Sato, N., Kamada, T., Abe, H., Suematsu, T., Kawano, S., Hayashi, N., Matsumura, T. and Hagihara, B. (1977) Simultaneous measurement of mitochondrial and microsomal cytochrome levels in human liver biopsy, *Clinica Chimica Acta*, **80**, pp243-251.

22. Chepelinsky, A.B. and Arnaiz, G.R. de Lores (1970) Levels of cytochromes in rat-brain mitochondria during post-natal development, *Biochim. Biophys. Acta.*, **197**, pp321-323.

23. Sato, N., Hagihara, B., Kamada, T. and Abe, H. (1976) A sensitive method for the quantitative estimation of cytochromes a and a_3 in tissues, *Anal. Biochem.*, **74**, pp105-117.

24. Gregson, N.A. and Williams, P.L. (1969) A comparative study of brain and liver mitochondria from new-born and adult rats, *J. Neurochem.*, **16**, pp717-626.

25. Dallman, P.R. and Schwartz, H.C. (1964) Cytochrome c concentrations during rat and guinea pig development, *Pediatrics*, **33**, pp106-110.

26. Woodard, H.Q. and White, D.R. (1986) The composition of body tissues, *Br. J. Radiol.*, **59**, pp1209-1219.

27. Frackowiak, R.S.J., Lenzi, G.L., Jones, T. and Heather, J.D. (1980) Quantitative measurement of regional cerebral blood flow and oxygen metabolism in man using ^{15}O and positron emission tomography: theory, procedure, and normal values. *J. Comput. Assist. Tomogr.*, **4**, pp727-736.

28. Lammertsma, A.A., Wise, R.S.J., Heather, J.D., Gibbs, J.M., Leenders, K.L., Frackowiak, R.S.J., Rhodes, C.G. and Jones, T. (1983) Correction for the presence of intravascular oxygen-15 in the steady state technique for measuring regional oxygen extraction from the brain: 2. Results in normal subjects and brain tumour and stroke patients, *J. Cereb. Blood Flow Metab.*, **3**, pp425-431.

29. Lassen, N.A. (1974) Control of the cerebral circulation in health and disease, *Circ. Res.*, **34**, pp749-760.

30. Siesjö, B.K., Jóhannson, H., Norberg, K. and Salford, L. (1975) Brain function, metabolism and blood flow in moderate and severe hypoxia, *In: Brain: The coupling of function, metabolism & blood flow in brain*, Eds: D.H. Ingvar et al., Munksgaard, Copenhagen.

31. Sakai, F., Nakazawa, K., Tazaki., Y., Ishii, K., Hidetada, H., Igarashi, H., and Kanda, T. (1985) Regional Cerebral Blood Volume and Haematocrit Measured in Normal Human Volunteers by Single-Photon Emission Computed Tomography, *J. Cereb. Blood. Flow and Metabolism*, **5**, pp207-213.

32. Lammertsma, A.A., Brooks, D.J., Beaney, R.P., Turton, D.R., Kensett, M.J., Heather, J.D., Marshall, J. and Jones, T. (1984) In vivo measurement of regional cerebral haematocrit using Positron Emission Tomography, *J. Cereb. Blood Flow Metab.*, **4**, pp317-322.

33. Leenders, K.L., Perani, D., Lammerstsma, A.A., Heather, J.D., Buckingham, P., Healy, M.J.R., Gibbs, J.M., Wise, R.J.S., Hatazawa, J., Herold, S., Beaney, R.P., Brooks, D.J., Spinks, T., Rhodes, C., Frackowiak, R.S.J. and Jones, T. (1990) Cerebral blood flow, blood volume and oxygen utilization: Normal values and the effect of age, *Brain*, **113**, pp27-47.

34. Herold, S., Brown, M.M., Frackowiak, R.S.J., Mansfield, A.O., Thomas, D.J. and Marshall, J. (1988) Assessment of cerebral haemodynamic reserve: correlation between PET parameters and CO_2 reactivity measured by intravenous ^{133}Xenon injection technique, *J. Neurol.*, **51**, pp1045-1050.

35. Volpe, J.J., Herscovitch, P., Perlman, J.M. and Raichle M.E. (1983) Positron Emission Tomography in the newborn: Extensive impairment of regional cerebral blood flow with intraventricular haemorrhage and haemorrhagic intracerebral involvement, *Pediatrics*, **5**, pp569-601.

36. Jaggi, J.L., Lipp, A.E. and Duc, G. (1989) Measuring cerebral blood flow with the non-invasive Xenon-133 method in preterm infants, *In: Physiologic foundations of perinatal care, Vol III*, Eds: L. Stern, M. Orzalesi and B. Friis-Hansen, Elsevier (N.Y.), pp231-242.

37. Greisen, G. (1986) Cerebral blood flow in preterm infants during the first week of life, *Acta. Paed. Scand.*, **75**, pp43-51.

38. Greisen, G. and Trojaborg, W. (1987) Cerebral blood flow, $PaCO_2$ changes, and visual evoked potentials in mechanically ventilated, preterm infants, *Acta. Paed. Scand.*, **76**, pp394-400.

39. Linderkamp, O., Berg, D., Betke, K., Köferi, F., Kriegel, H. and Kriegel, K.P. (1980) Blood volume and hematocrit in various organs in newborn piglets, *Pediatr. Res.*, **14**, pp1324-1327.

40. Severinghaus, J.W. (1986) Historical development of oxygenation monitoring, *In: Pulse Oximetry*, Eds: J.P. Payne and J.W. Severinghaus, Springer-Verlag, Heidelburg (FRG).

41. Nicolai, L. (1932) Über Sichtbarmachung, Verlauf und chemische Kinetic der Oxyhemoglobinreduktion im lebendum Gewebe, besonders in der menschlichen Haut, *Arch. Ges. Physiol*, **229**, p372.

42. Matthes, K. (1935) Untersuchungen über die Sauerstoffsättigungen des menschlichen Arterienblutes, *Arch. Exp. Path. Pharmakol.*, **179**, pp698-711.

43. Kramer, K. (1935) Ein Verfahren zur fortlaufenden Messung des Sauerstoffgehaltes im stromenden Blute an uneröffneten Gefassen, *Z. Biol.*, **96**, pp61-75.

44. Matthes, K. and Gross, F. (1939) Untersuchungen über die Absorption von rotem und ultrarotem Licht durch kohlenoxydgesättigtes und reduziertes Blut, *Arch. Exp. Pathol. Pharmakol.*, **191**, p369.

45. Matthes, K. and Gross, F. (1939) Fortlaufende Registrierung der Lichtabsorption des Blutes in zwei verschiedenen Spektralbezirken, *Arch. Exp. Pathol. Pharmakol.*, **191**, p381.

46. Kramer, K., Elam, J.O., Saxton, G.A. and Elam, W.N. Jnr (1951) Influence of oxygen saturation, erythrocyte concentration and optical depth upon the red and near-infrared light transmittance of whole blood, *Am. J. Physiol.*, **165**, pp229-246.

47. Brown, L.J., (1980) A new instrument for the simultaneous measurement of total hemoglobin, % oxyhemoglobin, % carboxyhemoglobin, % methemoglobin, and oxygen content in whole blood, *IEEE Trans. Biomed. Eng.*, **BME-27:3**, pp132-138.

48. Millikan, G.A. (1942) The oximeter, an instrument for measuring continuously oxygen saturation of arterial blood in man, *Rev. Sci. Instrum.*, **13**, pp434-444.

49. Wood, E. and Geraci, J.E., (1949) Photoelectric determination of arterial oxygen saturation in man, *J. Lab. Clin. Invest.*, **34**, p387.

50. Nakajima, S., Hirai, Y., Takase, H., Kuse, A., Aoyagi, S., Kishe, M. and Yamaguchi, K. (1975) New pulsed type earpiece oximeter, *Kokyu To Junkan*, **23**, pp709-713.

51. Brinkman, R., Zijlstra, W.G. and Koopmans, R.K. (1950) A method for continuous observation of percentage oxygen saturation in patients, *Arch. Chir. Needl.*, **1**, pp333-334.

52. Wilkinson, A.R., Phibbs, R.H. and Gregory, G.A. (1978) Continuous measurement of oxygen saturation in sick newborn infants, *J. Pediatrics*, **93(6)**, pp1016-1019.

53. Chance, B. and Williams, G.R. (1955) A method for the localization of sites for oxidative phosphorylation, *Nature*, **176**, pp250-254.

54. Chance, B. (1972) Principles of Differential Spectrophotometry with Special Reference to the Dual Wavelength Method, *In: Methods in Enzymology (Part B)*, pp322-335.

55. Jöbsis, F.F. (1972) Oxidative metabolism at low pO_2, *Fed Proc*, **31**, pp1404-1413.

56. Schwickardi, D. (1968) Konzentration und Kinetic der Atmungsfermente am isoliert perfundierten Meerschweinchengehirn in vivo und Hypothermie von 18°C, *Dissertation*, Marburg (Germany).

57. Figulla, H.R., Hoffmann, J. and Lübbers, D.W. (1984) Evaluation of reflection spectra of the isolated heart by multicomponent spectra analysis in comparison to other evaluating methods, *Adv. Exp. Med. Biol.*, **169**, pp821-830, Plenum (N.Y.).

58. Hoffman, J. and Lübbers, D.W. (1986) Estimation of concentration ratios and the redox states of the cytochromes from noisy reflection spectra using multicomponent analysis methods. *Adv. Exp. Med. Biol.*, **200**, pp119-124.

59. Hoffman, J. and Lübbers, D.W. (1986) Improved quantitative analysis of reflection spectra obtained from the surface of the isolated perfused guinea pig heart. *Adv. Exp. Med. Biol.*, **200**, pp125-130.

60. Kubelka, K. (1948) New contributions to the optics of intensely light scattering materials, part I, *J. Opt. Soc. Am.*, **38**, p448.

61. Kubelka, K. (1954) New contributions to the optics of intensely light scattering materials, part II, *J. Opt. Soc. Am.*, **44**, p330.

62. Horecker, B.L. (1943) The absorption spectra of hemoglobin and its derivatives in the visible and near infra-red regions, *J. Biol. Chem.*, **148**, pp173-183.

63. Wharton D.C. and Tzagoloff. (1964) Studies of the Electron Transfer System: LVII. The near infrared absorption band of cytochrome oxidase, *J. Biol. Chem.*, **239(6)**, pp2036-2041.

64. Chance, B. (1966) Spectrophotometric observations of absorbance changes in the infrared region in suspensions of mitochondria and in submitochondrial particles, *In: The Biochemistry of Copper*, Eds: Peisach et al., Academic Press, N.Y (U.S.A.).

65. Jöbsis, F.F. (1977) Noninvasive, infrared monitoring of cerebral and myocardial oxygen sufficiency and circulatory parameters, *Science*, **198**, pp1264-1267.

66. Ferrari, M., Giannini, I., Sideri, G. and Zanette, E. (1985) Continuous non invasive monitoring of human brain by near infrared spectroscopy, *Adv. Exp. Med. Biol.*, **191**, pp873-882.

67. Ferrari, M., Zanette E., Giannini, I, Sideri, G, Fieschi, C. and Carpi, A. (1986) Effects of carotid compression test on regional cerebral blood volume, haemoglobin oxygen saturation and cytochrome-c-oxidase redox level in cerebrovascular patients, *Adv. Exp. Med. Biol.*, **200**, pp213-222.

68. Ferrari, M.,De Marchis, C., Giannini, I., Nicola, A., Agostino, R., Nodari, S. and Bucci, G. (1986) Cerebral blood volume and haemoglobin oxygen saturation monitoring in neonatal brain by near IR spectroscopy, *Adv. Exp. Med. Biol.*, **200**, pp203-212.

69. Brazy J.E., Lewis D.V., Mitnick, M.H. and Jöbsis vander Vliet, F.F. (1985) Noninvasive monitoring of cerebral oxygenation in preterm infants: Preliminary observations, *Paediatrics*, **75(2)**, pp217-225.

70. Brazy, J.E. and Lewis, D.V. (1986) Changes in cerebral blood volume and cytochrome aa_3 during hypertensive peaks in preterm infants, *J. Pediatr.*, **108(6)**, pp983-987.

71. Brazy, J.E., Lewis, D.V., Mitnick, M.H. and Jöbsis vander Vliet (1985) Monitoring of cerebral oxygenation in the intensive care nursery, *Adv. Exp. Med. Biol.*, **191**, pp843-848.

72. British Standard (1983) Radiation safety of laser products and systems, BS4803 Part 2, British Standard Institution, (U.K.).

73. Gadian, D.G. (1982) Nuclear magnetic resonance and its application to living systems, Clarendon Press (Oxford, U.K.).

74. Cady, E.B., Dawson, M.J., Hope, P.L., Tofts, P.S., Costello, A.M. de L., Delpy, D.T., Reynolds, E.O.R. and Wilkie, D.R. (1983) Non-invasive investigation of cerebral metabolism in newborn infants by phosphorus nuclear magnetic resonance spectroscopy, *Lancet*, **i**, pp1059-62.

75. Hope, P.L., Cady, E.B., Tofts, P.S., Hamilton, P.A., Costello, A.M. de L., Delpy, D.T., Chu, A. and Reynolds, E.O.R. (1984) Cerebral energy metabolism studied with phosphorus NMR spectroscopy in normal and birth-asphyxiated infants, *Lancet*, **ii**, pp366-370.

76. Volpe, J.J., Herscovitch, P., Perlman, J.M., Kreusser, K.L. and Raichle M.E. (1985) Positron Emission Tomography in the asphyxiated term newborn: Parasagittal impairment of cerebral blood flow, *Ann. Neurol.*, **17**, pp287-296.

77. Barber, D.C. and Brown, B.H. (1984) Review article: applied potential tomography, *J. Phys. E.*, **17(9)**, pp723-733.

78. Brown, B.H. and Seagar, A.D. (1987) The Sheffield data collection system, *Clin. Phys. Physiol. Meas.*, **8, suppl. A**, pp91-97.

79. Barber, D.C. and Brown, B.H., (1988) Errors in reconstruction of resistivity images using a linear reconstruction technique, *Clin. Phys. Physiol. Meas.*, **9, suppl. A**, pp101-104.

80. Breckon, W.R. and Pidcock, M.K. (1988) Data errors and reconstruction algorithms in electrical impedance tomography, *Clin. Phys. Physiol. Meas.*, **9 suppl. A**, pp105-109.

81. Murphy, D., Burton, P., Coombs, R., Tarassenko, L. and Rolfe, P. (1987) Impedance imaging in the newborn, *Clin. Phys. Physiol. Meas.*, **8, suppl. A**, pp131-140.

82. Jöbsis-van der Vliet, F.F. (1985) Non-invasive, near infrared monitoring of cellular oxygen sufficiency in vivo, *In: Adv. Exp. Med. Biol.*, **191**, pp833-841.

83. Beer, A. (1852) Bestimmung der Absorption des rothen Lichts in farbigen Flüssigkeiten, *Ann. Phys. u. Chem.*, **163**, p78.

84. Vierordt, K. (1873) Die Anvendung des Spectralapparates zur Photometrie der Absorptionsspectren un zur Quantitativen Chemischen Analyse, *H. Laupp'schen Buchhandlung*, Tübingen.

85. Lothian, G.F. (1969) Absorption Spectrophotometry, Adam Hilger, London (U.K.).

86. Brodersen, S. (1954) Slit-width effects, *J. Opt Soc. Am.*, **44**, pp22-25.

87. Glick, D., Engstrom, A. and Malmstrom, Bo G. (1951) A critical evaluation of quantitative histo- and cytochemical microscopic techniques, *Science*, **114**, pp253-258.

88. Duysens, L.N.M. (1956) The flattening of the absorption spectrum of suspensions, as compared to that of solutions, *Biochim. Biophys. Acta.*, **19**, pp1-12.

89. Barer, R. (1955) Spectrophotometry of clarified cell suspensions, *Science*, **121**, pp709-715.

90. Fillerup, D.L. and Mead, J.F. (1967) The lipids of the aging human brain, *Lipids*, **2(4)**, pp295-298.

91. Hale, G.M. and Querry, M.R. (1973) Optical Constants of Water in the 200-nm to 200-μm wavelength region, *App. Opt.*, **12(3)**, pp555-563.

92. Conway, J.M., Norris, K.H. and Bodwell, C.E. (1984) A new approach for the estimation of body composition: infrared interactance, *Am. J. Clin. Nutri.*, **40**, pp1123-1130.

93. Handbook of Clinical Laboratory Data (1968) Eds: W.R. Faulkner, J.W. King & H.C. Damm, The Chemical Rubber Co. (Cleveland, USA).

94. van Assendelft, O.W. (1970) Spectrophotometry of haemoglobin derivatives, *PhD Thesis*, Univ. of Groningen, The Netherlands.

95. Zwart, A., Buursma, A., van Kampen, E.J., Oeseburg, B., van der Ploeg, P.H.W. and Zijlstra, W.G. (1981) A multi-wavelength spectrophotometric method for the simultaneous determination of five haemoglobin derivatives, *J. Clin. Chem. Clin. Biochem.*, **19**, pp457-463.

96. International Committee for Standardisation in Haematology, (1967) Recommendation for haemoglobinometry in human blood, *Br. J. Haemat.*, **13**, Suppl., 71.

97. Mendelson, Y. and Kent, J.C. (1989) Variations in optical absorption spectra of adult and fetal haemoglobins and its effect on pulse oximetry, *IEEE Trans. Biomed. Eng.*, **36(8)**, pp844-848.

98. Anderson, R.R. and Parrish, J.A. (1981) The optics of the human skin, *J. Invest. Dermat.*, **77**, pp13-19.

99. Brunori, M., Antonini, E. and Wilson, M.T. (1981) Cytochrome c oxidase: an overview of recent work, In: *Metal Ions in Biological Systems XIII*, Ed: H. Siegel, Marcel Dekker, (New York, U.S.A.).

100. Wilson, M.T., *Personal Communication*, Dept. of Biological Chemistry, University of Essex, Colchester, U.K.

101. Tzagaloff, A. (1982) Mitochondria, Plenum Press N.Y. (USA).

102. Ragan, C.I. (1976) NADH-ubiquinone oxidoreductase, *Biochim. Biophys. Acta.*, **456**, pp249-290.

103. Davis, K.A. and Hatefi, Y. (1971) Succinate dehydrogenase. I. Purification, molecular properties, and substructure, *Biochemistry*, **10(13)**, pp2509-2516.

104. Rieske, J.S. (1976) Composition and function of complex III of the respiratory chain, *Biochim. Biophys. Acta.*, **456**, pp195-247.

105. Wolbarsh, M.L., Walsh, A.W. & George, G. (1981) Melanin, a unique biological absorber, *App. Optics*, **20(13)**, pp2184-2186.

106. Wan, S., Parrish, J.A., Anderson, R. and Madden, M. (1981) Transmittance of nonionizing radiation in human tissues, *Photochem. Photobiol.*, **34**, pp679-681.

107. Wang, Z., Noyszewski, E.A. and Leigh Jr, J.S. (1990) In vivo measurement of deoxymyoglobin in human forearm, *Mag. Res. Med*, **14**, pp562-567.

108. Bachrach, R.Z. and Brown, F.C. (1970) Exciton optical properties of TlBr and TlCl, *Phys. Rev.*, **B1**, pp818-831.

109. Jenkins, F.A. and White, H.E. (1976) Fundamentals of Optics, McGraw Hill, (London).

110. Singham, S.B. and Bohren, C.F. (1988) Light scattering by an arbitrary particle: the scattering-order formulation of the coupled-dipole method, *J. Opt. Soc. Am. A.*, **5** pp1867-1872.

111. Bohren C.F. and Huffman D.R. (1983) Absorption and Scattering of Light by Small Particles, J. Wiley (New York).

112. Ross, K.F.A. (1967) Phase contrast and interference microscopy for cell biologists, Edward Arnold (London).

113. Galavazi, G. (1963) *Doctoral Dissertation*, University of Leiden (Holland).

114. Documenta Geigy, scientific tables (1956) Ciba Geigy (Basle Switzerland).

115. Ponder, E. (1948) Hemolysis and related phenomena, Grune and Stratton Inc, (N.Y., U.S.A.).

116. Chadwick, R.S. and Chang, I.D. (1973) A laser study of the motion of particles suspended in a slow viscous shear flow, *J. Colloid. Interface Sci.*, **42**, pp516-534.

117. Steinke, J.M. and Shepherd, A.P. (1988) Comparison of Mie theory and the light scattering of red blood cells, *App. Opt.*, **27(19)**, pp4027-4033.

118. Tortora, G.J. and Anagnostakos, N.P. (1990) *Principles of anatomy and physiology*, HarperCollins (N.Y., USA).

119. Clouet, D.H. and Gaitonde, M.K. (1956) The changes with age in the protein composition of the rat brain, *J. Neurochem.*, **1**, pp126-133.

120. Brant, G. (1949) Studies on lipids in the nervous system with special reference to quantitative chemical determination and topical distribution, *Acta. Physiol. Scand. Suppl.*, **18 Suppl 63**.

121. Fawcett, D.W. (1966) The cell, its organelles and inclusions, Saunders (Philadelphia, U.S.A.).

122. von Zglinicki, T., Bimmler, M. and Krause, W. (1987) Estimation of organelle water fractions from frozen-dried cryosections, *J. Microscopy*, **146(1)**, pp67-75.

123. Darley-Usmar, V.M., Rickwood, D. and Wilson, M.T. (1987) Transport across membranes, *In: Mitochondria, a practical approach*, Eds: V.M. Darley-Usmar, D. Rickwood & M.T. Wilson, IRL Press (Oxford, U.K.), pp313-315.

124. Dahl, D.R. and Samson, F.E. (1959) Metabolism of rat brain mitochondria during postnatal development, *Am. J. Physiol.*, **196(2)**, pp470-472.

125. Samson Jr, F.E., Balfour, W.M., Jacobs, R.J. (1960) Mitochondrial changes in the developing rat brain, *Am. J. Physiol.*, **199(4)**, pp693-696.

126. Gregson, N.A. and Williams, P.L. (1969) A comparative study of brain and liver mitochondria from new-born and adult rats, *J. Neurochem*, **16**, pp617-626.

127. Lehninger, A.L. (1975) Biochemistry, Worth (New York, U.S.A.), pp302-306.

128. Cuzner, M.L., Davison, A.N. and Gregson, N.A. (1965) The chemical composition of vertebrate myelin and microsomes, *J. Neurochem.*, **12**, pp469-481.

129. Kong, Jin Au., (1986) Electromagnetic wave theory, J. Wiley (N.Y., U.S.A.).

130. Lipton, P. (1973) Effects of membrane depolarization on light scattering by cerebral cortical slices, *J. Physiol.*, **231**, pp365-383.

131. van der Zee, P. and Delpy, D.T. (1988) Computed point spread functions for light in tissue using a measured volume scattering function, *Adv. Exp. Med. Biol.*, **215**, Plenum Press (N.Y., U.S.A.), pp191-198.

132. Ganong W.F. (1979) Review of Medical Physiology, Lange Medical Publication (California, U.S.A.)

133. Fris-Hansen, B. (1971) Body composition during growth, *Paediatrics*, **47**, pp264-274.

134. van der Hulst, H.C. (1980) Multiple light scattering: Tables, formulas and applications Vols I & II, Academic Press (N.Y., U.S.A.).

135. Ishimaru, A. (1978) Wave propagation and scattering in random media, Academic Press, (N.Y., U.S.A.).

136. Twersky, V. (1970) Absorption and multiple scattering by biological suspensions, *J. Opt. Soc. Am.*, **60**, pp1084-1093.

137. Chandrasekhar, S. (1960) Radiative transfer, Dover (N.Y., U.S.A.).

138. Patterson, M.S., Wilson, B.C., & Wyman, D.R., The propagation of optical radiation in tissue. *In: Adv. Laser Biophys.*, Ed: M.J. Colles, JAI Press, (In press).

139. Svaasand, L.O. (1987) On the properties of light propagation in tissue, *In: Abstracts of the Clayton Foundation Conference on Photodynamic Therapy, Los Angeles.*

140. Kubelka, P. and Munk, F. (1931) Ein Beitrag zur Optik der Farbanstriche, *Z. Tech. Phys.*, **12**, pp593-601.

141. Star, W.M. (1989) Comparing the P3-approximation with diffusion theory and with Monte Carlo calculations of light propagation in a slab geometry, *SPIE 1035-42.*

142. Duderstadt, J.J. and Hamilton, L.J. (1976) Nuclear Reactor Analysis. Wiley, (N.Y., U.S.A.).

143. Star, W.M., Marijnissen, J.P.A. and van Gemert, M.J.C. (1988) Light dosimetry in optical phantoms and tissues I. Multiple flux and transport theory, *Phys. Med. Biol.*, **33**, pp437-454.

144. Steinke, J.M. and Shepherd, A.P. (1986) Role of light scattering in whole blood oximetry, *IEEE Trans. Biomed. Eng.*, **BME-33**, pp294-301.

145. Twersky, V. (1962) Multiple scattering of waves and optical phenomena, *J. Opt. Soc. Am.*, **52**, pp145-171.

146. Twersky, V. (1970) Interface effects in multiple scattering by large, low-refracting, absorbing particles, *J. Opt. Soc. Am.*, **60**, pp908-914.

147. Anderson, N.M. and Sekelj, P. (1967) Light-absorbing and scattering properties of non-haemolysed blood, *Phys. Med. Biol.*, **12**, pp173-182.

148. Anderson, N.M. and Sekelj, P. (1967) Reflection and transmission of light by thin films of non-haemolysed blood, *Phys. Med. Biol.*, **12**, pp183-192.

149. Loewinger, E., Gordon, A., Weinreb, A. and Gross, J. (1964) Analysis of a micromethod for transmission oximetry of whole blood, *J. Appl. Phys.*, **19**, pp1179-1184.

150. Svaasand, L.O. and Ellingsen, R. (1983) Optical properties of human brain, *Photochem. Photobiol.*, **38(3)**, pp293-299.

151. Sterenborg, H.J.C.M., van Gemert, M.J.C., Kamphorst, W., Wolbers, J.G. and Hogervorst, W. (1990) The spectral dependence of the optical properties of human brain, *Lasers Med. Sci.*, **4**, pp221-227.

152. Wilson, B.C., Patterson, M.S., Flock, S.T. & Moulton, J.D. (1988) The optical absorption and scattering properties of tissues in the visible and near infrared wavelength range, *In: Proceedings of the 2nd Congress of the European Society of Photobiology*, In Press.

153. Preuss, L.E., Bolin, F.P. and Cain, B.W. (1982) Tissue as a medium for laser light transport implications for photoradiation therapy, *SPIE 357*, pp77-84.

154. Keilin, D. and Hartree, E.F. (1949) Effect of low temperature on the absorption spectra of haemodynamics: with observations on the absorption spectrum of oxygen, *Nature*, **164**, pp254-259.

155. Butler, W.I. and Norris, K.H. (1960) The spectrophotometry of dense light scattering material, *Arch. Biochem. Biophys.*, **87**, pp31-40.

156. Arridge, S., van der Zee, P., Delpy, D.T. and Cope, M. (1989) Particle sizing in the Mie scattering region: singular-value analysis, *Inverse Problems*, **5**, pp671-689.

157. Wyatt, J.S., Cope, M., Delpy, D.T., Wray, S. and Reynolds, E.O.R. (1986) Quantitation of cerebral oxygenation and haemodynamics in sick newborn infants by near infrared spectrophotometry, *Lancet*, **ii**, pp1063-1066.

158. Wyatt, J.S., Cope, M., Delpy, D.T., van der Zee, P., Arridge, S., Edwards, A.D. and Reynolds, E.O.R. (1990) Measurement of optical pathlength for cerebral near infrared spectroscopy in newborn infants, *Dev. Neurosci.*, **12**, pp140-144.

159. Jöbsis, F.F. (1980) Method and apparatus for monitoring metabolism in body organs in vivo, *U.S. Patent*, **4223680.**

160. Keyes, R.J. (1977) Optical and Infrared Detectors, Springer Verlag (Berlin, F.R.G.).

161. Seib D.H., and Aukerman L.W. (1973) Photodetectors for the 0.1 to 1.0 μm spectral region, *Adv. Electronics Electron Phys.*, **34**, pp95-221.

162. Brown, R.G.W., Jones, R., Rarity, J.G. and Ridley, K.D. (1987) Characterization of silicon avalanche photodiodes for photon correlation measurements. 2: Active quenching. *App. Opt.* **26** pp2383-2389.

163. Cope, M. and Delpy, D.T. (1988) A system for long term measurement of cerebral blood and tissue oxygenation in newborn infants by near infrared illumination. *Med. Biol. Eng. & Comp.*, **26**, pp289-294.

164. British Standards Institute, (1983) Safety on medical electrical equipment, *BS5724*, London U.K.

165. International Electrotechnical Commission (1979) Safety of medical electrical equipment, *IEC601-1*, IEC (Geneva, Switzerland).

166. Hospital Physicist's Association, Safe design and construction of electromedical equipment, Ed: R.H. Smallwood, London U.K.

167. Cope, M. (1988) Optical Examination Apparatus, UK Patent Application, **8902562.1**

168. EG&G Princeton Applied Research, (1984) *Photon Counting*, P.O. Box 2565, Princeton, NJ 08540, U.S.A.

169. Bédard, G. (1967) Dead-time corrections to the statistical distribution of photoelectrons, *Proc. Phys. Soc.*, **90**, pp131-141.

170. Barlow, R.B. and Polanyi, M.L. (1962) Absorption measurements for oxygenated and reduced hemoglobin in the range 0.6-1.88 microns, *Clin Chem*, **8**, pp67-71.

171. Yonetani, T. (1960) Studies on cytochrome oxidase I. Absolute and difference absorption spectra, *J. Biol. Chem.*, **235**, pp845-852.

172. Hartzell, C.R. and Beinert, H. (1974) Components of cytochrome c oxidase detectable by EPR spectroscopy, *Biochim. Biophys. Acta.*, **368**, pp318-338.

173. Brudwig, G.W., Stevens, T.H., Morse R.H. and Chan, S.I. (1981) Conformations of oxidised cytochrome c oxidase, *Biochemistry*, **20**, pp3912-3921.

174. Stevens, T.H., Brudwig, G.W., Bocian, D.F. and Chan, S.J. (1979) Structure of cytochrome a_3-Cu_{a3} couple in cytochrome c oxidase as revealed by nitric oxide binding studies, *Proc. Natl. Acad. Sci.*, **76**, pp3320-3324.

175. Wilson, M.T., Jensen, P., Aasa, R., Malmström, B.G. and Vänngård T. (1982) An investigation by e.p.r. and optical spectroscopy of cytochrome oxidase during turnover, *Biochem. J.*, **203**, pp483-492.

176. Young, J.Y. and Palmer, G. (1986) Redox-cycled oxidase, *J. Biol. Chem.*, **261**, pp13031-13033.

177. Powers, L., Chance, B., Ching, Y.C. and Lee, C.P. (1987) Structure of the copper sites in membrane bound cytochrome c oxidase, *J. Biol. Chem.*, **262**, pp3160-3164.

178. Hartzell C.R., Beinert, H., Babcock, G.T., Chan, S.I., Palmer, G. and Scott, R.A. (1988) Heterogeneity in an isolated membrane protein, has the 'authentic cytochrome oxidase' been identified?, *FEBS. Letts.*, **236**, pp1-4.

179. Steffens, G.C.M., Biewald, R. and Buse, G. (1987) Cytochrome c oxidase is a three-copper, two-heme-protein, *Eur. J. Biochem.*, **164**, pp295-300.

180. Einersdóttir, O. and Caughey, W.S. (1984) Zinc is a constituent of bovine heart cytochrome c oxidase preparations, *Biochem. Biophys Res. Comm.*, **124**, pp836-842.

181. Einersdóttir, O. and Caughey, W.S. (1985) Possible roles for "adventitious" copper, zinc and magnesium in bovine heart cytochrome c oxidase, *Fed. Proc.*, **44**, p1780 (Abstract).

182. Keilin, D. and Hartree, E.F. (1939) Cytochrome and cytochrome oxidase, *Proc. Roy. Soc., Ser. B*, **127**, pp167-191.

183. Vanneste, W.H. (1966) The stoichiometry and absorption spectra of components a and a_3 in cytochrome c oxidase, *Biochemistry*, **5**, pp838-848.

184. Greenwood, C., Brittain, T., Wilson, M.T. and Brunori M. (1976) Studies on partially reduced mammalian cytochrome oxidase reactions with ferrocytochrome c, *Biochem. J.*, **157**, pp591-598.

185. Antalis, T.M. and Palmer G. (1982) Kinetic characterisation of the interaction between cytochrome oxidase and cytochrome c, *J. Biol. Chem.*, **257**, pp6194-6206.

186. Tiesjama, R.H., Muijsers, A.O. and van Gelder, B.F. (1973) Biochemical and biophysical studies on cytochrome c oxidase. X. Spectral and potentiometric properties of the hemes and coppers, *Biochim. Biophys. Acta.*, **305**, pp19-28.

187. Wilson, D.F. and Leigh, J.S. (1974) Heme-heme interaction between the cytochromes of the mitochondrial respiratory chain, *Ann. N.Y. Acad. Sci.*, **227**, pp630-635.

188. Antonini, E., Brunori, M., Greenwood, C., Malmström B.G. and Rotilio, G.C. (1971) The interaction of cyanide with cytochrome oxidase, *Eur. J. Biochem.*, **23**, pp396-400.

189. Jones, M.G., Bickar, D., Wilson, M.T., Brunori, M., Colisimo, A. and Sarti, P. (1984) A re-examination of the reactions of cyanide with cytochrome c oxidase, *Biochem. J.*, **220**, pp57-66.

190. Ellis, W.R., Wang, H., Blair, D.F., Gray, H.B., Chan, S.I. (1986) Spectroelectrochemical study of the cytochrome a site in carbon monoxide inhibited cytochrome c oxidase, *Biochemistry.*, **25**, pp161-167.

191. Musatov, A. and Konstantinov, A.A. (1988) Conformational change of cytochrome a_3 induced by oxidised cytochrome c, *FEBS. Letts.*, **238**, pp295-299.

192. Griffiths, D.E. and Wharton, D.C. (1961) Studies of the electron transport system. XXXV. Purification and properties of cytochrome oxidase, *J. Biol. Chem.*, **236**, pp1850-1856.

193. Tzagaloff A. and MacLennan, D.H. (1966) The copper protein component of cytochrome c oxidase, In: *The Biochemistry of Copper*, Ed: J. Peisach, Academic Press, pp253-265.

194. Wang, H., Blair, D.F., Ellis, W.R., Gray, H.B., Chan, S.I. (1986) Temperature dependence of the reduction potential of Cu_A in carbon monoxide inhibited cytochrome c oxidase, *Biochemistry*, **25**, pp167-171.

195. Beinert, H., Shaw, R.W., Hansen, R.E. and Hartzell, C.R. (1980) Studies of the origin of the near infrared (800-900 nm) absorption of cytochrome c oxidase, *Biochim. Biophys. Acta.*, **591**, pp458-470.

196. Greenwood, C., Wilson, M.T. and Brunori, M. (1974) Studies on partially reduced mammalian cytochrome oxidase, *Biochem. J.*, **137**, pp205-215.

197. Greenwood, C., Hill, B.C., Barber, D., Eglington, D.G., and Thompson, A.J. (1983) The optical properties of Cu_A in bovine cytochrome c oxidase determined by low-temperature magnetic-circular-dichroism spectroscopy, *Biochem. J.*, **215**, pp303-316.

198. Babcock, G.T., Vickery, L.E. and Palmer, G. (1978) The electronic state of heme in cytochrome oxidase II, *J. Biol. Chem.*, **253**, pp2400-2411.

199. Fukumori, Y., Nakayama, K., and Yamanaka T. (1985) Cytochrome c oxidase of Pseudomonas AM 1: Purification and molecular and enzymatic properties, *J. Biochem.*, **98**, pp493-499.

200. Fukumori, Y., Nakayama, K., and Yamanaka T. (1985) One of the two copper atoms is not necessary for the cytochrome c oxidase activity of Pseudomonas AM 1 cytochrome aa_3, *J. Biochem.*, **98**, pp1719-1722.

201. Powers, L., Blumberg, W.E., Chance, B., Barlow, C.H., Leigh Jnr, J.S., Smith, J., Yonetani, T., Vik, S. and Peisach, J. (1979) The nature of the copper atoms of cytochrome c oxidase as studied by optical and X-ray absorption edge spectroscopy, *Biochim. Biophys. Acta.*, **546**, pp520-538.

202. Powers, L., Chance, B., Ching, Y. and Angiolillo, P. (1981) Structural features and the reaction mechanism of cytochrome oxidase: Iron and copper X-ray absorption fine structure, *Biophys. J.*, **34**, pp465-498.

203. Chance, B., Saronio, C., Leigh Jnr, J.S., Ingledew, W.J. and King, T.E. (1978) Low-temperature kinetics of the reaction of oxygen and solubilized cytochrome oxidase, *Biochem. J.*, **171**, pp787-798.

204. Hill, B.C. and Greenwood C. (1984) The reaction of fully reduced cytochrome c oxidase with oxygen studied by flow-flash spectrophotometry at room temperature, *Biochem. J.*, **218**, pp913-921.

205. Andréasson, L.E., Malmström, B.G., Strömberg, C. and Vänngård, T. (1972) The reaction of ferrocytochrome c with cytochrome oxidase: a new look, *FEBS Lett.*, **28**, pp297-301.

206. Boelens, R. and Wever, R. (1980) Redox reactions in mixed-valence cytochrome c oxidase, *FEBS Lett.*, **116**, p223-226.

207. Petersen, L.C., Nicholls, P. and Degn, H. (1976) The effect of oxygen concentration on the steady state kinetics of the solubilised cytochrome c oxidase, *Biochim. Biophys. Acta.*, **452**, pp59-65.

208. Okunika, K., Hagihara, B., Sekuzu, I. and Horio, T. (1958) Studies on cytochrome oxidase, In: *Proc. Intern. Symp. Enzyme mistry. Tokyo and Kyoto, Maruzen, Tokyo*, Ed: K. Schihara, Academic press (N.Y.), pp264.

209. Williams, G.R., Lemberg, R. and Cutler, M.E. (1968) The oxidized forms of cytochrome oxidase, *Can. J. Biochem.*, **46**, pp1371-1379.

210. Chance, B., Saranio, C. and Leigh Jnr., J.S. (1975) Functional intermediates in the reaction of membrane-bound cytochrome oxidase with oxygen, *J. Biol. Chem.*, **250**, pp9226-9237.

211. Brunori, M., Colosimo, A., Rainoni, G., Wilson, M.T. and Antonini E. (1979) Functional intermediates of cytochrome oxidase, *J. Biol. Chem.*, **254**, pp10769-10775.

212. Malmström, B.G. (1979) Cytochrome c oxidase, structure and catalytic activity, *Biochim. Biophys. Acta.*, **549**, pp281-303.

213. Erecinska, M., and Wilson, D.F. (1978) Cytochrome c oxidase: A synopsis, *Arch. Biochem. Biophys.*, **188**, pp1-14.

214. Wilson, M.T., Greenwood, C., Brunori, M. and Antonini, E. (1975) Kinetic studies on the reaction between cytochrome c oxidase and ferrocytochrome c, *Biochem. J.*, **147**, pp145-153.

215. Hartzell, C.R., Hansen, R.E. and Beinert, H. (1973) Electron carriers of cytochrome c oxidase detectable by electron paramagnetic resonance and their relationship to those traditionally recognised in this enzyme, *Proc. Nat. Acad. Sci.*, **70**, pp2477-2481.

216. Yonetani, T. (1966) Cytochrome oxidase from beef heart muscle, *Biochem. Prep.*, **11**, pp14-20.

217. Reichardt, J.K.V. and Gibson, Q.H. (1982) Spectra of intermediates in oxidation and reduction of cytochrome c oxidase, *J. Biol. Chem.*, **257**, pp9268-9270.

218. Rosén, S., Bränden, R., Vänngård, T. and Malmström, B.G. (1977) EPR evidence for an active form of cytochrome c oxidase different from the resting enzyme, *FEBS. Letts.*, **74**, pp25-30.

219. Myer, J.P. (1971) Conformation of cytochromes: V. cytochrome c oxidase, *J. Biol. Chem.*, **246**, pp1241-1248.

220. Tiesjema, R.H., Muijers, A.O., and Van Gelder, B.F. (1972) Biochemical and biophysical studies on cytochrome aa_3: IV. Some properties of oxygenated cytochrome a_3, *Biochim. Biophys. Acta.*, **256**, pp32-42.

221. Wilson, M.T., Peterson, J., Antonini, E., Brunori, M., Colosimo, A. and Wyman, J. (1981) A plausible two-state model for cytochrome c oxidase, *Proc. Natl. Acad. Sci.*, **78**, pp7115-7118.

222. Brown, G.C., Lakin-Thomas, P.L. and Brand, M.D. (1990) Control of respiration and oxidative phosphorylation in isolated rat liver cells, *Eur. J. Biochem.*, **192**, pp335-362.

223. Brown, G.C. and Brand, M.D. (1988) Proton/electron stoichiometry of mitochondrial complex I estimated from the equilibrium thermodynamic force ratio, *Biochem. J.*, **252**, pp473-479.

224. Lowry, O.H. (1975) Energy metabolism in brain and its control, In: *The Coupling of Function, Metabolism and Blood Flow in Brain*, Eds: D.H. Ingvar and N.A. Lassen, Munksgaard (Copenhagen), pp49-63.

225. McGovern Moroney, P., Scholes, T.A. and Hinckle, P.C. (1984) Effect of membrane potential and pH gradient on electron transfer in cytochrome oxidase, *Biochemistry*, **23**, pp4991-4997.

226. Rich, P.R., West, I.C. and Mitchell, P. (1988) The location of Cu_A in mammalian cytochrome c oxidase, *FEBS Lett.*, **233(1)**, pp25-30.

227. Chance, B. and Williams, G.R. (1965) The respiratory chain and oxidative phosphorylation, *Adv. Enzymol.*, **17**, pp65-134.

228. Antonini, G., Brunori, M., Malatesta, F., Sarti, P. and Vallone B. (1990) Transient kinetics and regulation of cytochrome c oxidase, In: *Structure, function and biogenesis of energy transfer systems*, Eds: E. Quagliariello, S. Papa, et al., Elsevier (Holland), pp27-30.

229. Wilson, D.F., Erecińska, M., Drown, C. and Silver, I.A. (1979) The oxygen dependence of cellular metabolism, *Arch. Biochem. Biophys.*, **195**, pp485-493.

230. Kessler, M. and Lübbers, D.W. (1964) Bestimmung des kritischen Sauerstoffdruckes an isolierten Lebermitochondrien, *Pflügers Arch. Ges. Physiol.*, **281**, p50, (Abstract).

231. Sugano, T., Oshino, N. and Chance, B. (1974) Mitochondrial functions under hypoxic conditions. The steady states of cytochrome c reduction and of energy metabolism, *Biochim. Biophys. Acta.*, **347**, p340-358.

232. Wilson, D.F. and Rumsey, W.L. (1988) Factors modulating the oxygen dependence of mitochondrial oxidative phosphorylation, *Adv. Exp. Med. Biol.*, **222**, Plenum Press (N.Y.), pp121-131.

233. Wilson, D.F., Rumsey, W.L., Green, T.J. and Vanderkooi, J.M. (1988) The oxygen dependence of mitochondrial oxidative phosphorylation measured by a new optical method for measuring oxygen concentration, *J. Biol. Chem.*, **263(6)**, pp2712-2718.

234. Silver, I.A. (1965) Some observations on the cerebral cortex with an ultramicro, membrane-covered, oxygen electrode, *Med. Electron. Biol. Engng.*, **3**, pp377-387.

235. Kessler, M. and Lübbers, D.W. (1966) Aufbau und Anwendungsmöglichkeiten verschiedener PO_2-Electroden, *Pflügers Arch. ges. Physiol.*, **291**, R82.

236. Lübbers, D.W. (1973) Local tissue PO_2: its measurement and meaning (introductory paper), *In: Oxygen Supply*, Eds: Kessler et al., Urban and Schwarzenberg (München-Berlin-Wein), pp151-155.

237. Erdmann, W., Kunke, S.T. and Krell, W. (1973) Tissue PO_2 and cell function - An experimental study with multimicroelectrodes in the rat brain, *In: Oxygen Supply*, Eds: Kessler et al., Urban and Schwarzenberg (München-Berlin-Wein), pp169-174.

238. Nair, P., Whalen, W.J. and Buerk, D. (1975) PO_2 of cat cerebral cortex: Response to breathing N_2 and 100% O_2, *Microvas. Res.*, **9**, pp158-165.

239. Erdmann, W. (1978) Microelectrode studies in the brain of fetal rats and new born rats, *Adv. Exp. Med. Biol.*, **94**, Plenum Press (N.Y.), pp455-461.

240. Kreismann, N.R., Olson, J.E., Horne, D.S. and Holtzman, D. (1989) Cerebral oxygenation and blood flow in infant and young adult rats, *Am. J. Physiol.*, **256**, R78-85.

241. Jöbsis, F. (1972) Oxidative metabolism at low pO_2, *Fed. Proc.*, **31(5)**, pp1404-1413.

242. Rosenthal, M., LaManna, J.C., Jöbsis, F.F., Levasseur, J.E., Kontos, H.A. and Patterson, J.L. (1976) Effects of respiratory gases on cytochrome a in intact cerebral cortex: Is there a critical pO_2?, *Brain Res.*, **108**, pp143-154.

243. Kariman, K., Hempel, F.G., and Jöbsis, F.F. (1983) In vivo comparison of cytochrome aa_3 redox state and tissue pO_2 in transient anoxia, *J. Appl. Physiol.*, **55(4)**, pp1057-1063.

244. Piantadosi, C.A., Hemstreet, T.M. and Jöbsis-Vandervliet, F.F. (1986) Near-infrared spectrophotometric monitoring of oxygen distribution to intact brain and skeletal muscle tissues, *Crit. Care Med.*, **14(8)**, pp698-706.

245. Mook, P.H., Proctor, H.J., Jöbsis, F. and Wildevuur, Ch.R.H. (1984) Assessment of brain oxygenation: a comparison between an oxygen electrode and near-infrared spectrophotometry, *Adv. Exp. Med. Biol.*, **169**, Plenum Press (N.Y.), pp841-847.

246. Kariman, K. and Burkhart, D.S. (1985) Non-invasive in vivo spectrophotometric monitoring of brain cytochrome aa_3 revisited, *Brain Res.*, **360**, pp203-213.

247. Sylvia, A.L., Piantadosi, C.A. and Jöbsis-vander Vliet, F.F. (1985) Cerebral bioenergetics and in-vivo cytochrome c oxidase redox relationships, *Adv. Exp. Med. Biol.*, **191**, Plenum Press (N.Y.), pp815-821.

248. Sylvia, A.L. and Piantadosi, C.A. (1988) O_2 dependence of in vivo brain cytochrome redox responses and energy metabolism in bloodless rats, *J. Cereb. Blood Flow & Metab.*, **8**, pp163-172.

249. Tamura, M., Hazeki, O., Nioka, S., Chance, B. and Smith, D.S. (1988) The simultaneous measurements of tissue oxygen concentration and energy state by near infrared and nuclear magnetic resonance spectroscopy, *Adv. Exp. Med. Biol.*, **222**, Plenum Press (N.Y.), pp359-363.

250. Bashford, C.L., Barlow, C.H., Chance, B., Haselgrove, J. and Sorge, J. (1982) Optical measurements of oxygen delivery and consumption in gerbil cerebral cortex, *Am. J. Physiol.*, **242**, ppC265-C271.

251. Milito, S.J., Raffin, C.N., Rosenthal, M. and Sick, T.J. (1988) Potassium ion homeostasis and mitochondrial activity in brain: relative changes as indicators of hypoxia, *J. Cereb. Blood Flow and Metab.*, **8**, pp155-162.

252. Kreisman, N.R., LaManna, J.C., Rosenthal, M. and Sick, T.J. (1981) Oxidative metabolic responses with recurrent seizures in rat cerebral cortex: role of systemic factors, *Brain Res.*, **218**, pp175-188.

253. Brand, M.D. and Murphy, M.P. (1987) Control of electron flux through the respiratory chain in mitochondria and cells, *Biol. Rev.*, **62**, pp141-193.

254. FC-43 Technical Information, The Green Cross Corporation, 1-15-1, Imabashi Higashi-ku, Osaka, Japan.

255. Clark, L.C., Wesseler, E.P., Kaplan, S., Miller, M.L., Becker, C., Emory, C., Stanley, L., Becattini, F. and Obrock, V. (1975) Emulsions of perfluorocarbonated solvents for intravascular gas transport, *Fed. Proc.*, **34**, pp1468-1477.

256. Ferrari, M., Giannini, I., Carpi, A. and Fasella, P. (1983) Non-invasive near infrared spectroscopy of brain in fluorocarbon exchange-transfused rats, *Physiol. Chem. Phys. Med. NMR*, **15**, pp107-113.

257. Jöbsis-VanderVliet F.F., Piantadosi, C.A., Sylvia, A.L., Lucas, S.K. and Keiser, H.H. (1988) Near-infrared monitoring of cerebral oxygen sufficiency: I Spectra of cytochrome c oxidase, *Neurol. Res.*, **10**, pp7-17.

258. Cope, M., Delpy, D.T., Wray, S., Wyatt, J.S. and Reynolds, E.O.R. (1989) A CCD spectrometer to quantitate the concentration of chromophores in living tissue utilising the absorption peak of water at 975 nm, *Adv. Exp. Med. Biol.*, **247**, Plenum Press (N.Y.), pp33-40.

259. Cope, M., van der Zee, P., Essenpreis, M., Arridge, S.R. and Delpy, D.T. (1991) Data analysis methods for near infrared spectroscopy of tissue: problems in determining the relative cytochrome aa_3 concentration, *Proc. SPIE*, **1431**, SPIE (Bellingham, USA), In press.

260. Araki, R., and Nashimoto, I. (1989) Multicomponent analysis of near infrared spectra of anaesthetized rat head: (I) Estimation of component spectra by principal component analysis, *Adv. Exp. Med. & Biol*, **248**, Plenum Press (N.Y., USA), pp. 3-10.

261. Rawlings, J.O. (1988) *Applied regression analysis: a research tool*, Wadsworth & Brooks (Belmont, USA).

262. Everett, N.B., Simmons, B. and Lasher, E.P. (1956) Distribution of blood (Fe^{59}) and plasma (I^{131}) volumes of rats determined by liquid nitrogen freezing, *Circ. Res.*, **4**, pp419-424.

263. Millichap, J.G., Balter, M. and Hernandez, P. (1958) Development of susceptibility to seizures in young animals III. Brain water, electrolyte and acid base metabolism, *Proc. Soc. Exp. Biol.*, **99**, pp6-11.

264. Tsuchiya, Y., Kinoshita, K., Koishi, M., Takeshima, A. and Inagaki, Y. (1984) A new picosecond synchroscan photometer, *Proc SPIE*, **491**, pp224-229.

265. Delpy, D.T., Cope, M., van der Zee, P. and Arridge, S. (1988) Estimation of optical pathlength through tissue from direct time of flight measurement, *Phys. Med. Biol.*, **248**, pp41-46.

266. Bolin, F.P., Preuss, L.E., Taylor, R.C. and Ference, R.J. (1989) Refractive index of some mammalian tissues using a fibre optic cladding method, *Applied Optics*, **28**, pp2297-2303.

267. Gahn, T. and Witte, S. (1986) Measurement of the optical thickness of transparent tissue layers, *J. Microsurgery*, **141**, pp101-111.

268. Delpy, D.T., Arridge, S.R., Cope, M., Edwards, D., Reynolds, E.O.R., Richardson, C.E., Wray, S., Wyatt, J. and van der Zee, P. (1989) *Adv. Exp. Med. Biol.*, **248**, (Plenum Press, NY) pp41-46.

269. van der Zee, P., Cope, M., Arridge, S.R., Essenpreis, M., Potter, L.A., Edwards, A.D., Wyatt, J.S., McCormick, D.C., Roth, S.C., Reynolds, E.O.R. and Delpy, D.T. (1991) Experimentally measured optical pathlengths for the adult head, calf and forearm and the head of the newborn infant as a function of inter optode spacing, *Adv. Exp. Med. Biol.*, (Plenum Press, NY) In Press.

270. Chance, B., Maris, M., Sorge, J. and Zhang, M.Z. (1990) A phase modulation system for dual wavelength difference spectroscopy of haemoglobin deoxygenation in tissues, *Proc. SPIE*, **1204**, pp481-491.

271. Case, M.C. and Zwiefell, P.F. (1967) *Linear Transport Theory*, (Addison-Wesley, N.Y.).

272. Patterson, M.S., Chance, B. and Wilson, B.C. (1989) Time resolved reflectance and transmittance for the noninvasive measurement of tissue optical properties, *Appl. Optics*, **28**, pp2331-2336.

273. P. van der Zee, "Measurement and modelling of the optical properties of human tissue in the near infrared", *PhD Thesis, University of London*, (In preparation).

274. Martins-Ferreeira, H. (1983) Spreading depression in the chicken retina. *In: The Brain and Behaviour of the Fowl. Ed: T. Ookawa.* Japan Scientific Societies Press (Tokyo), pp317-333.

275. Tedeschi, H. and Harris, D.L. (1955) The osmotic behaviour and permeability to non-electrolytes of mitochondria, *Archs. Biochem. Biophys.*, **58**, pp52-67.

276. Orskov, S.L. (1935) Untersuchungen über den Influss von Kohlensäure und Blei auf die Permeabilität der Blutkörperchen für Kalium und Rubidium, *Biochem Z.*, **279**, pp250-261.

277. Hill, K.D. (1950) The effect of stimulation on the opacity of a crustacean nerve trunk and its relation to fibre diameter, *J. Physiol.*, **111**, pp283-303.

278. Hill, D.K. and Keynes, R.D. (1949) Opacity changes in stimulated nerve, *J. Physiol.*, **108**, pp278-281.

279. Tasaki, I., Watanabe, A., Sandlin, R. and Carnay, I. (1968) Changes in fluorescence, turbidity, and birefringence associated with nerve excitation, *Proc. Natl. Acad. Sci.*, **61**, pp883-888.

280. Cohen, L.B. and Keynes, R.D. (1971) Changes in light scattering associated with the action potential in crab nerves, *J. Physiol.*, **212**, pp259-275.

281. Cohen, L.B., Keynes, R.D. and Landowne, D. (1972) Changes in light scattering that accompany the action potential: Current dependent components, *J. Physiol.*, **224**, p727-752.

282. Cohen, L.B., Keynes, R.D. and Landowne, D. (1972) Changes in light scattering that accompany the action potential in squid giant axons: Potential-dependent components, *J. Physiol.*, **224**, pp701-725.

283. Hansen, A.J. (1985) Effect of anoxia on ion distribution in the brain, *Physiol. Rev.*, **65(1)**, pp101-148.

284. Edwards, A.D., Wyatt, J.S., Richardson, C.E., Delpy, D.T., Cope, M., and Reynolds, E.O.R. (1988) Cotside measurement of cerebral blood flow in ill newborn infants by near infrared spectroscopy. *Lancet*, **ii**, pp770-771.

285. Chance, B., Leigh, J.S., Miyake, H., Smith, D.S., Nioka, S., Greenfeld, R., Finander, M., Kaufmannn, K., Levy, W., Young, M., Cohen, P., Yoshioka, H. and Boretsky, R. (1988) Comparison of time-resolved and -unresolved measurements of deoxyhaemoglobin in brain, *Proc. Nat. Acad. Sci.*, **85**, pp4971-4975.

286. Sevick, E.M. and Chance, B. (1991) Photon migration in a model of the head measured using time- and frequency- domain techniques, *Proc. SPIE*, **1431**, In Press.

287. Arridge, S.R., Cope, M., van der Zee, P., Hillson, P.J. and Delpy, D.T. (1986) Near infrared transillumination as a method of visualisation and measurement of the oxygenation state of brain and muscle in newborn infant, In: *Recent developments in medical and physiological imaging*, Eds: R.P. Clark and M.R. Goth, Taylor & Francis (London), pp24-31.

288. Arridge, S.R., Cope, M., van der Zee, P., Hillson, P.J. and Delpy, D.T. (1986) Visualisation of the oxygenation state of brain and muscle in newborn infants by near infrared transillumination, In: *Information processing in medical imaging*. Ed: S.L. Bacharach, Martinus Nijhoff (N.Y.), pp155-176.

289. Arridge, S., van der Zee, P., Delpy, D. T. and Cope, M. (1990) Aspects of clinical infrared absorption imaging, In: *The Formation, Handling and Evaluation of Medical Images*, Eds: A. Todd Pokropek, M. A. Viergever, Nato ASI series F, pp407-418.

290. Arridge, S.R., van der Zee, P., Cope, M. and Delpy, D.T. (1990) New results for the development of infrared absorption imaging, *Proc. SPIE*, **1245**, pp91-103.

291. Singer, J.R., Grünbaum, F.A., Kohn, P. and Zubelli, J.P. (1990) Image reconstruction of the interior of bodies that diffuse radiation, *Science*, **248**, pp990-993.

292. Arridge, S.R., van der Zee, P., Cope, M. and Delpy, D.T. (1991) Reconstruction methods for infra-red absorption imaging, *Proc. SPIE*, **1431**, In press.